SAKARYA ÜNİVERSİTESİ

FEN BİLİMLERİ ENSTİTÜSÜ DERGİSİ

Sakarya University Journal of Science (SAUJS)

SAKARYA
ÜNİVERSİTESİ
e-issn: 2147-835X

SAÜ Fen Bil Der/SAUJS

Cilt/Volume: 25

Sayı/Issue: 6

Aralık/December 2021

Sakarya Üniversitesi Fen Bilimleri Enstitüsü Dergisi
(Sakarya University Journal of Science)
Cilt/Volume: 25 No/ Issue:6 Aralık/December 2021
Editör Kurulu/Editorial Boards

Editor-in-Chief

Davut Avcı, Pyhsics, Sakarya University (Turkey)

Editors

Alparslan Serhat Demir, Industrial Engineering, Sakarya University (Turkey)
Asude Ateş, Environmental Engineering, Sakarya University (Turkey)
Aysun Eğrisöğüt Tiryaki, Mechanical Engineering, Sakarya University (Turkey)
Ertan Bol, Civil Engineering, Sakarya University (Turkey)
Hüseyin Aksoy, Biology, Sakarya University (Turkey)
M. Hilmi Nişancı, Electrical and Electronics Engineering, Sakarya University (Turkey)
Mehmet Uysal, Metallurgical and Materials Engineering, Sakarya University (Turkey)
Mehmet Nebioğlu, Chemistry, Sakarya University (Turkey)
Muhammed Fatih Adak, Computer Engineering, Sakarya University (Turkey)
Mustafa Gülfen, Chemistry, Sakarya University (Turkey)
Murat Güzeltepe, Mathematics, Sakarya University (Turkey)
Ömer Tamer, Physics, Sakarya University (Turkey)

Editorial Board

Aliye Suna Erses Yay, Environmental Engineering, Sakarya University (Turkey)
Aslı Uçar, Faculty of Health Sciences, Nutrition and dietetics, Ankara University (Turkey)
Aykut Astam, Physics, Erzincan Binali Yıldırım University (Turkey)
Burak Erkayman, Industrial Engineering, Atatürk University (Turkey)
Cansu Akbulut, Biology, Sakarya University (Turkey)
Caner Erden, International Trade and Finance, Sakarya University of Applied Sciences (Turkey)
Can Serkan Keskin, Chemistry, Sakarya University (Turkey)
Elif Büyük Öğüt, Mechanical and Metal Technologies, Kocaeli University (Turkey)
Emrah Bulut, Chemistry, Sakarya University (Turkey)
Emre Dil, Energy Systems Engineering, Beykent University (Turkey)
Emre Tabar, Physics, Sakarya University (Turkey)
Fahrettin Horasan, Computer Engineering, Kırıkkale University (Turkey)
Faruk Fırat Çalım, Civil Engineering, Alparslan Türkeş University (Turkey)
Gülnur Arabacı, Chemistry, Sakarya University (Turkey)

İrfan Yazıcı, Electrical and Electronics Engineering, Sakarya University (Turkey)
İsmail Hakkı Demir, Architecture, Sakarya University (Turkey)
Latif Kelebekli, Chemistry, Ordu University (Turkey)
Mahmud Tokur, Metallurgical and Materials Engineering, Sakarya University (Turkey)
Mevlüt Sami Aköz, Civil Engineering, Çukurova University (Turkey)
Miraç Alaf, Metallurgical and Materials Engineering, Bilecik Şeyh Edebali University (Turkey)
Muhammed Maruf Öztürk, Computer Engineering, Süleyman Demirel University (Turkey)
Murat Sarduvan, Mathematics, Sakarya University (Turkey)
Murat Tuna, Chemistry, Sakarya University (Turkey)
Murat Utkucu, Geophysical Engineering , Sakarya University (Turkey)
Mustafa Akpınar, Software Engineering, Sakarya University (Turkey)
Nazan Deniz Yön Ertuğ, Biology, Sakarya University (Turkey)
Nükhet Sazak, Electrical and Electronics Engineering, Sakarya University (Turkey)
Osman Kırtel, Civil Engineering, Sakarya University of Applied Sciences (Turkey)
Öznur Özkan Kılıç, Mathematics, Başkent University (Turkey)
Rıfkı Terzioğlu, Electrical and Electronics Engineering, Bolu Abant İzzet Baysal University, (Turkey)
Sibel Güneş, Mechanical Engineering, Erciyes University (Turkey)
Soley Ersoy, Mathematics, Sakarya University (Turkey)
Tuğrul Çetinkaya, Metallurgical and Materials Engineering, Sakarya University (Turkey)
Turgay Şişman, Biology, Atatürk University (Turkey)

English Language Editor

Ömer Tamer, Physics, Sakarya University (Turkey)

SAKARYA ÜNİVERSİTESİ FEN BİLİMLERİ ENSTİTÜSÜ DERGİSİ
(SAKARYA UNIVERSITY JOURNAL OF SCIENCE)
İÇİNDEKİLER/CONTENTS
Cilt/Volume: 25 – No/Issue6: (ARALIK/DECEMBER-2021)

RESEARCH ARTICLES

SAKARYA ÜNİVERSİTESİ

FEN BİLİMLERİ ENSTİTÜSÜ
DERGİSİ

Sakarya University Journal of Science
SAUJS

e-ISSN 2147-835X Founded 1997 Period Bimonthly Publisher Sakarya University
http://www.saujs.sakarya.edu.tr/en/

Title: Isolation and Identification of Listeria spp. from White Cheese Samples Presented for Consumption in Istanbul

Authors: Nil KAYA, Elif Özlem ARSLAN AYDOĞDU, Ayten KİMİRAN

Recieved: 2021-08-22 00:00:00

Accepted: 2021-10-03 00:00:00

Article Type: Research Article

Volume: 25
Issue: 6
Month: December
Year: 2021
Pages: 1253-1262

How to cite
Nil KAYA, Elif Özlem ARSLAN AYDOĞDU, Ayten KİMİRAN; (2021), Isolation and Identification of Listeria spp. from White Cheese Samples Presented for Consumption in Istanbul. Sakarya University Journal of Science, 25(6), 1253-1262, DOI: https://doi.org/10.16984/saufenbilder.985810
Access link
http://www.saujs.sakarya.edu.tr/tr/pub/issue/66341/985810

Sakarya University Journal of Science 25(6), 1253-1262, 2021

SAKARYA ÜNİVERSİTESİ

Isolation and Identification of *Listeria* spp. from White Cheese Samples Presented for Consumption in Istanbul

Nil KAYA[1], Elif Özlem ARSLAN AYDOĞDU*[2], Ayten KİMİRAN[2]

Abstract

In this study, 119 feta cheese samples taken from different vendors in Istanbul were examined for the presence of *Listeria monocytogenes*. Isolates were confirmed by the PCR method using *iap* and *hlyA* primers, and the antibiotic susceptibility of the identified strains was performed by the Kirby-Bauer protocol. Seven *Listeria* spp. were isolated from three (2.52%) of 119 cheese samples analyzed. The seven *Listeria* spp. obtained from these three samples were found to contain the *iap* gene region but not the *hlyA* gene region. As a result of the sequence analysis using the 16S rRNA gene region, it was determined that these isolates were *L. seeligeri*. As a result of antibiotic susceptibility tests, it was observed that *L. seeligeri* isolates showed ciprofloxacin (85.71%) and penicillin (42.85%) resistance. All strains were susceptible to amikacin, amoxicillin/clavulanic acid, chloramphenicol, rifampin, gentamicin, cefaclor, ampicillin, trimethoprim-sulfamethoxazole, tetracycline, vancomycin, and clarithromycin antibiotics. The detection of *Listeria spp.* isolates in feta cheese samples made with pasteurized milk revealed that packaging, distribution, and storage practices following the pasteurization process should be followed more strictly. It is recommended to apply controls at each stage to prevent contamination.

Keywords: *L. monocytogenes*, Feta cheese, *iap*, *hlyA*, Antibiotic sensitivity

1. INTRODUCTION

Gram-positive, non-spore-forming, facultative anaerobe, rod-shaped *Listeria* bacteria, due to their tolerance to low pH, low temperature and high salt concentration, can be found in various environments such as water, silage, soil, foods and sewage [1-5] The *Listeria* genus has 20 different species, included *L. innocua*, *L. seeligeri*, *L. ivanovii*, *L. fleischmannii*, *L. welshimeri*, *L. marthii*, *L. grayi*, *L. rocourtiae*, *L. weihenstephanensis*, *L. cornellensis*, *L. floridensis*, *L. riparia*, *L. grandensis*, *L. aquatica*, *L. booriae*, *L. newyorkensis*, *L. costaricensis*, *L. goaensis*, and *L. thailandensis*. Among these bacteria, the *L. monocytogenes* and *L. ivanovii* are pathogenic to animals and humans.

L. monocytogenes, the causative agent of listeriosis, is an important foodborne pathogen [6-

---

* Corresponding author: eoarslan@istanbul.edu.tr

[1] Istinye University, Faculty of Pharmacy, Department of Basic Pharmaceutical Sciences.
E-Mail: nilkaya7@outlook.com
ORCID: https://orcid.org/0000-0002-1444-4935

[2] Istanbul University, Faculty of Science, Department of Biology
E-Mail: kimiran@istanbul.edu.tr
ORCID: https://orcid.org/0000-0003-1294-7376, https://orcid.org/0000-0002-0210-2751

8] This infection can occur through the consumption of cheese, milk, cooked and ready-to-eat foods, pork, fermented sausage, meat and meat products such as beef, unwashed raw vegetables and fruits contaminated by *L. monocytogenes* [6, 9, 10] Although *L. monocytogenes* infection is less common than other foodborne diseases, it is the bacterium with the second-highest mortality rate among all foodborne pathogens [11, 12] Despite effective antibiotic treatments, Listeriosis, which has a mortality rate of 30%, seems to be a problem that threatens public health [6, 13].

Cheese is a food product that is widely consumed in the world and has many varieties. Feta cheese, in case of ignoring factors such as pasteurization, business hygiene etc. that need to be considered during production, can be a convenient source for the contamination and reproduction of *L. monocytogenes* bacteria. Pathogenic bacteria found in cheese because of contamination can also cause ailments up to food poisoning. Among these pathogenic bacteria, *L. monocytogenes* due to resistance to temperature and pH changes, the ability to growing at high salt concentration, can survive the production and ripening stages of cheese. The growth of this bacterium can be slowed down by lactic starter cultures in cheese milk but is not completely inhibited. Therefore, to avoid outbreaks from *L. monocytogenes*, the strict control of this food from the production stage until it reaches the consumer is important [9, 14].

Examination of cheese, which has an important consumption rate in our country, in terms of *L. monocytogenes* is important for public health. In the present study, we aimed to detect *Listeria* contamination in white cheese, sold in İstanbul, and determine the risks in terms of public health of the contamination.

2. MATERIAL AND METHOD

2.1. Bacteria Strains

In the study, *Staphylococcus aureus* ATCC 25923 and *L. monocytogenes* RSKK 475 were used as positive control.

2.2. Isolation and Identification of *Listeria* spp.

119 white cheeses made from pasteurized milk obtained from different districts in Istanbul province were examined according to FDA (Food and Drug Administration) standard culture method [15]. The culture method was carried out in three stages. For the primary enrichment process, after a 2-minute homogenization step, a 25 g sample in 225 ml Listeria Enrichment Broth (HiMedia, India) was incubated at 30 ° C for 4 h. After the incubation, the selective additive was added to the culture and incubation was continued. Liquid cultures were kept for 1 and 2 weeks in addition to the incubation period recommended in the standard protocol, and at the end of all periods, they were inoculated onto the PALCAM (Polymyxin-Acriflavin Lithium Chloride-Ceftazidime- Aesculin-Mannitol Agar; HiMedia, India) media by streak plate method. After 48 h incubation at 30 °C, five *Listeria* suspicious colonies, which were grey-green colonies surrounding a black halo growing on the medium, were inoculated on the TSA-YE (Trypticase soy agar with yeast extract; HiMedia, India) media for obtaining pure cultures.

Listeria suspicious colonies growing on TSA-YE medium has been evaluated for biochemical tests such as Gram staining, oxidase, catalase, movement in the medium of Sulphate Indole Motility (SIM), hemolysis, nitrate reduction, Methyl Red (MR) -Voges-Proskauer (VP), acid production from sugar (rhamnose, mannitol, ribose, xylose, and α-methyl-D-mannocide), and Christie Atkins and Munch-Petersen (CAMP) factor [16].

2.3. Antibiotic Susceptibility Test

Antibiotic susceptibilities of *Listeria* spp. isolates were investigated by the Kirby Bauer test protocol [17]. In the study, ampicillin (10 µg), amoxicillin-clavulanic acid (30 µg), penicillin (10 units), cefaclor (30 µg), vancomycin (30 µg), gentamicin (10 µg), amikacin (30 µg), clarithromycin (15 µg), ciprofloxacin (5 µg), tetracycline (30 µg), trimetprim-sulfamethoxazole (25 µg), chloramphenicol (30 µg), and rifampin (5 µg), antibiotics were used.

2.4. Verification of isolates by PCR application

2.4.1. DNA Isolation

Chromosomal DNA was extracted from the *Listeria* suspicious isolates using the IDPURE Universal Spin Column Genomic DNA Mini Kit (IDLabs, Canada).

2.4.2. PCR Amplification

Listeria spp. isolates were verified by PCR method using *iap* (IAP1: 5′ACAAGCTGCACCTGTTGCAG3′ and IAP2: 5′TGACAGCGTGTGTAGTAGCA3′) and *hlyA* (PCRGO: 5′GAATGTAAACTTCGGCGCAATCAG3’ and PCRDO: 5′GCCGTCGATGATTTGAACTTCATC3′) primers [18, 19]. Primers of the *iap* and *hlyA* genes used in the experiment were prepared following the manufacturer's instructions.

The PCR mix was prepared with MyTaq^{TM} Mix (Bioline, Germany). After 0.5 µl (20 µM) of each reverse and forward primer, 1 µl (10 nmol) template DNA, 5 µl MyTaq Reaction Buffer, 0.5 µl MyTaq DNA polymerase was mixed into 0.2 ml microtubes was added, the final volume was completed to 25 µl with sterile ultrapure water. All procedures were repeated using L. monocytogenes RSKK 475 template DNA and ultrapure water as positive and negative control, respectively.

The reaction was performed in the Thermal Cycler (TC-PLUS, Techne, England) device without losing time. The PCR protocol set up following: 95 °C for 1 min for initial denaturation; 35 cycles, 15 s at 95 °C for denaturation, 15 s annealing at 65 °C or 55 °C for *hlyA* or *iap* primers respectively and 10 s extension at 72 °C. The PCR products obtained were visualized on a 1.2% agarose gel, stained with GelRed (Biotium, Hayward, CA, USA), for 45 minutes at 90 volts for electrophoresis. The band lengths of the PCR products obtained were determined using a 100 bp DNA Ladder (Bioline, Singapore) and imaged in a UV imaging system (Wisedoc, South Korea).

2.4.3. Molecular Identification

The phylogenetic analysis of the isolates was performed using bacterial universal primers, 1492R (5’-GGYTACCTTGTTACGACTT-3’) and 27F (5’-AGAGTTTG ATCMTGGCTCAG-3’) described by Lane (1991) using a thermal cycler (TC-PLUS, Techne, England) under the following conditions: 95 °C for 1 min initial denaturation; 35 cycles, at 95 °C for 15 s denaturation, 15 s annealing at 60 °C, 10 s extension at 72 °C.

The reaction mixture (25 µl) contained 0.5 µl (20 µM) of each reverse and forward primer, 1 µl (10 ng) template DNA, 5 µl MyTaq Reaction Buffer, 0.5µl MyTaq DNA polymerase. The PCR products obtained were carried out on a 1.2% agarose gel for 45 minutes at 90 volts for electrophoresis. The band lengths of the PCR products obtained were determined using a 100 bp DNA Ladder (Bioline, Singapore) and imaged in a UV imaging system (Wisedoc, South Korea).

Sanger sequence analyzes of the PCR products were made by BM Laboratory Systems (Ankara, Turkey). The 16S rRNA sequences obtained were aligned against the GenBank database using the BLAST program of the National Centre for Biotechnology Information.

3. RESULTS AND DISCUSSION

In the current study, using the culture method recommended by the FDA, 119 feta cheese samples were analyzed. The pure cultures of suspicious colonies, which appeared grey-green colored with a black halo on PALCAM medium, were obtained by inoculation into TSA-YE medium. According to the phenotypical examinations, 19 isolates obtained from eight cheese samples, which were Gram-positive rod or coccobacillus, catalase positive and oxidase reaction negative, were accepted as *Listeria* spp. suspicious.

19 *Listeria* spp. suspect isolates were examined in terms of motility, hemolysis, nitrate reduction, MR-VP, carbohydrate fermentation and CAMP tests, and 7 of them were found to have similar

biochemical results, except carbohydrate fermentation, with *L. monocytogenes* in all tests (Table 1). Seven *Listeria* spp. were isolated from three (2.52%) cheese samples by the traditional culture method.

Table 1. Biochemical test results of *Listeria* spp. suspicious isolates

	Biochemical Tests										
Isolate	**MR**	**VP**	**Nitrate Reduction**	**Motilitv**	**Rhamnose**	**α-methyl-D-**	**Mannitol**	**Ribose**	**Xylose**	**CAMP**	**β -hemolysis**
N1	-	-	-	-	-	-	-	-	-	-	-
N2	-	-	-	-	-	-	-	-	-	-	-
N3	-	-	-	-	-	-	-	-	-	-	-
N4	-	-	-	-	-	-	-	-	-	-	-
N5	-	-	-	-	-	-	-	-	-	-	-
N6	-	-	-	-	-	-	-	-	-	-	-
N7	-	-	-	-	-	-	-	-	-	-	-
N8	-	-	-	-	-	-	-	-	-	-	-
N9	-	-	-	-	-	-	-	-	-	-	-
N10	-	-	-	-	-	-	-	-	-	-	-
N11	-	-	-	-	-	-	-	-	-	-	-
N12	-	-	+	-	-	-	-	-	-	-	-
N13	+	+	-	+	-	-	-	-	+	+	+
N14	+	+	-	+	-	-	-	-	+	+	+
N15	+	+	-	+	-	-	-	-	+	+	+
N16	+	+	-	+	-	-	-	-	+	+	+
N17	+	+	-	+	-	-	-	-	+	+	+
N18	+	+	-	+	-	-	-	-	+	+	+
N19	+	+	-	+	-	-	-	-	+	+	+
S.B.	+	+	-	+	+	+	-	-	-	+	+

S.B.: *L. monocytogenes* RSKK 475

As a result of the PCR experiment, it was determined that the 7 strains isolated by the culture method only have the *iap* gene region which was specific for the *Listeria* genus, but not the *hlyA* gene that was specific for *L. monocytogenes* (Figure 1).

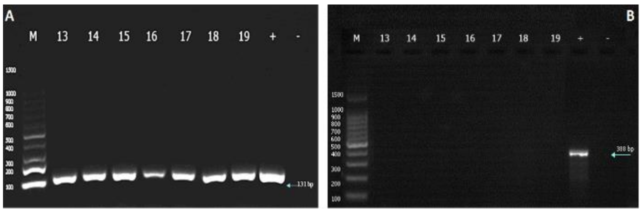

Figure 1. Gel electrophoresis images of the *iap* (A) and *hlyA* (B) gene carried by *Listeria* bacteria isolated from cheese samples [M: 100 bp DNA ladder 13-19: *Listeria* suspected bacteria (N13- N19). +: Positive control -: Negative control]

3.1. Identification of Isolates by Phylogenetic Analysis

It was confirmed that 7 isolates obtained according to the sequence analysis were *L. seeligeri*. The 16S rRNA sequences of the samples obtained from this study were recorded in GenBank under the accession numbers in Table 2. It was determined that the sequence similarity for 16S rRNA was 95-99%. Considering the sequence similarity, the seven isolates obtained were found to be closely related to *L. seeligeri*.

Table 2. Accession numbers of strains obtained from cheese samples

Sample No	**Isolate**	**Similarity**	**Accession No**
	N17	% 95	MK490993
P51	N18	% 98	MK490994
	N19	% 99	MK490995
P53	N15	% 99	MK490991
	N13	% 99	MK490989
P54	N14	% 99	MK490990
	N16	% 97	MK490992

3.2. Determination of Antibiotic Sensitivity of *Listeria* Bacteria

Six (85.71%) of seven *Listeria spp.* isolates obtained from white cheese were found to be resistant to ciprofloxacin and three (42.85%) to penicillin. Besides, 28.57% of the isolates were resistant to both ciprofloxacin and penicillin. All the isolates were sensitive to cefaclor, ampicillin, amikacin, chloramphenicol, rifampin, gentamicin, trimethoprim-sulfamethoxazole, tetracycline, amoxicillin/clavulanic acid, vancomycin, and clarithromycin antibiotics (Table 3).

Table 3. Antibiotic susceptibilities of *Listeria* bacteria

Antibiotic	Isolates						
	N13	N14	N15	N16	N17	N18	N19
Ciprofloxacin	R	I	R	R	R	R	R
Amikacin	S	S	I	I	S	S	S
Penicillin	R	R	S	S	R	S	S
Chloramphenicol	S	S	S	S	S	S	S
Rifampin	S	S	I	I	S	S	S
Gentamicin	S	S	S	S	S	S	S
Cefaclor	S	S	S	I	S	S	S
Ampicillin	S	S	S	S	S	S	S
Amoxicillin/ clavulanic acid	S	S	S	S	S	S	S
Trimethoprim-sulfamethoxazole	S	S	I	I	S	S	S
Tetracycline	S	S	S	S	S	S	S
Clarithromycin	S	S	S	S	S	S	S
Vancomycin	S	S	S	S	S	S	S

L. monocytogenes was not detected in our study, in which 2.52% (3/119) of *L. seeligeri* was detected in the white cheeses examined within the scope. Similar to the results we obtained, Elmas [20] indicated in her study that only one *L. seeligeri* was detected. In many studies [21, 22, 23] reporting that they did not encounter *L. monocytogenes* bacteria in white cheese samples are consistent with our findings.

Failure to report a foodborne listeriosis outbreak in Turkey until today and the infrequency of foodborne *Listeria* infection rate is in line with our findings.

Unlike our results, Çetin et al. [24] did not find *Listeria* spp. in any of the 40 white cheese samples. Although Atıl et al. [25] isolated *L. seeligeri* (0.19%) and *L. innocua* (0.19%) in 106 milk samples, they could not isolate *Listeria* spp. in 28 cheese samples. In the other study, Rahimi et al [26] found the rate of *Listeria spp*. as 7.2% in their study with dairy products in Iran. The researchers stated that the species they obtained were *L. innocua*, *L. monocytogenes*, *L. murrayi*, and *L. seeligeri* (66.7, 23.8, 4.8, and 4.8%, respectively). In a study conducted with 100 white cheeses purchased from neighbourhood markets, 6% of the cheeses were found to be contaminated with *L. monocytogenes* [27]. Aygün and Pehlivanlar [28] found that 8.23% of samples contained *Listeria* spp. In the mentioned study, *L. seeligeri* (2.35%), *L. ivanovii* (3.52%), *L. monocytogenes* (2.35%), *L. innocua* (3.52%) species were detected in white cheese samples. Ceylan and Demirkaya [29] indicated that *L. monocytogenes* was isolated from one (3.45%) white cheese sample. Elshinaway et al. [30], in their study with 240 dairy products, determined that the presence of *Listeria* spp. in kareish cheeses and buttered milk cheeses were 20% and 12.5%, respectively. *Listeria* spp. distribution in butter milk cheese was five (5%) *L. monocytogenes*, one (2.5%) *L. welshimeri*, two (5%) *L. grayii*, while in Kareish cheese was one (2.5%) *L. welshimeri*, one (2.5%) *L. monocytogenes* three (7.5%) *L. grayii*. In a study, investigating to the *L. monocytogenes* and *Listeria* spp. contamination of the 142 homemade cheese samples, conducted in Bolu [31] the presence of bacteria was reported as 9.2% and 33.1%, respectively. Kevenk and Gülel [32], in their study with 210 milk and dairy samples, indicated that *Listeria* spp. were detected in the raw milk samples (12%) and the white cheese samples (25%), and 5% of them were harboured *L. monocytogenes*.

When the results obtained in the current study were compared with the results obtained by other researchers, it was determined that isolation and identification rates of *Listeria* species in cheese samples vary differ. These differences are thought to be caused by the methods used for cheese production, the contamination rates of the milk, the environmental differences and geographical conditions, and also the insufficient hygiene rules. The presence of *L. seeligeri* in the white cheese samples we examined indicates possible contamination after pasteurization. Failure to comply with hygiene rules during the production, distribution and sale of cheese and cross-contamination during the sale and storage of these products are considered as other sources of contamination.

Within the scope of our study, the susceptibility of *L. seeligeri* isolates was determined by the Kirby-Bauer method. In 1988, the first multi-resistant *L. monocytogenes* was discovered in France [33]. After this date, many *Listeria* spp.

strains isolated from different environments have been determined to be resistant to one or more antibiotics [34-40]. It was determined that six (85.71%) of the seven *L. seeligeri* bacteria were resistant to ciprofloxacin and three (42.85%) to penicillin. At the same time, it was detected that five (71.42%) of the bacteria were resistant to one antibiotic and two (28.57%) to two antibiotics. All strains were found to be amikacin, chloramphenicol, rifampin, gentamicin, cefaclor, ampicillin, amoxicillin/ clavulanic acid, trimethoprim-sulfamethoxazole, tetracycline, clarithromycin and vancomycin sensitive. Our results on penicillin and ciprofloxacin resistance are similar to the study of Rahimi et al. [26]. In a study about *Listeria* spp. isolated from dairy products in Iran, it was detected that 28.6% of the isolates were resistant to one antibiotic and 23.8% to two antibiotics. At the same time, they found that 66.7% of them were resistant to nalidixic acid, 42.9% to penicillin, 23.8% to ciprofloxacin and 19% to tetracycline antibiotics. The resistance of the isolates we obtained from our study against penicillin antibiotics is in line with the findings of other researchers. Arslan and Özdemir [31] reported that similar to our study, 47 *Listeria spp.* isolates from white cheese showed resistance to penicillin (12.8%), at the same time these isolates had cefaclor (2.1%), tetracycline (2.1%), amikacin (4.3%), clarithromycin (6.4%), and chloramphenicol (8.5%) resistance.

When Aksoy et al. [41] examined the 15 *L. monocytogenes* isolates in their study, it was found that 26.7% of the isolates were resistant to at least one antibiotic. At the same time, they found that 6.7% of the isolates had multiple antibiotic resistance, and the most resistance was shown against trimethoprim-sulfamethoxazole (26.7% of the isolates). It was determined that 6.7% of isolates were resistant to meropenem, vancomycin, penicillin G, and amikacin at the same rate. In the other study, it was found that most of the isolates were resistant to ampicillin, rifampicin, and florfenicol (92%, 84%, and 66% respectively) and some of them were resistant to tetracycline, penicillin G, and chloramphenicol (45%, 40%, and 32% respectively) [42]. Harakeh et al. [43] when investigated antibiotic profile of *L. monocytogenes* isolated from soft white cheese varieties it was determined that the most resistance against oxacillin, penicillin, and ampicillin (93%, 90%, and 60% respectively). Jamali et al. [44] reported that 83 isolates obtained from raw milk in Malaysia were tetracycline and penicillin G resistance.

Resistance to ciprofloxacin we observed in the study was also reported in different studies. Conter et al. [45], in their study with *L. monocytogenes* strains which were obtained from food and food production areas, found that 10 (8.3%) isolates were resistant to one, three (2.5%) isolates to two and one (0.8%) isolates to five antibiotics. It was determined that the highest antibiotic resistance was against clindamycin and linezolid antibiotics with a ratio of 3.2%. In Ireland, 207 *Listeria* spp. isolates were found to be resistant to gentamicin (5%), sulfamethoxazole-trimethoprim (2%), ciprofloxacin and tetracycline (1.5%) [46]. Unlike the results we obtained, when 1001 *Listeria* spp. strains isolated from food (549 *L. innocua,* 39 *L. welshimeri,* 351 *L. monocytogenes,* 62 *L. seeligeri*) were examined in terms of antibiotic sensitivity, it was reported that *L. seeligeri* bacteria were not resistant to any antibiotics [47].

4. CONCLUSION

It is a known fact that redundant or excessive antibiotic usage in animals and humans also increases the resistance of bacteria to antibiotics. Development of antibiotic resistance not only in terms of pathogenic species of *Listeria* but also in non-pathogenic species, due to the transfer of resistance genes between *Listeria* species, constitutes risks to human health. Although the antibiotics recommended for the treatment of listeriosis are still effective, it is known that the isolated *Listeria* strains exhibit an increasing resistance day by day. On the other hand, resistance to broad-spectrum antibiotics may lead to rapid depletion of antibiotic alternatives, such as penicillin, ampicillin, tetracycline and gentamicin, that can be used for treatment in the future [45]. The increased resistance of *L. monocytogenes* to penicillin and ampicillin is apprehension for public health due to using these antibiotics in the treatment of listeriosis.

It is known that *L. seeligeri* is not a pathogenic *Listeria* species, but there is a case of meningitis due to *L. seeligeri* infection in the literature [48]. Although no other cases have been encountered, these bacteria may also pose a public health risk. For this reason, it is an essential precaution to control the steps such as inadequate pasteurization or post-pasteurization packaging/ distribution and the entire process. It is recommended that strict follow-ups are carried out to take food safety measures and implement HACCP guidelines in food establishments, also local producers do not use non-pasteurized milk.

Funding

This study is supported by Istanbul University Scientific Research Projects Coordination Unit. Project Number: 22416.

The Declaration of Conflict of Interest/ Common Interest

No conflict of interest or common interest has been declared by the authors.

Authors' Contribution

Under this heading, "The authors contributed equally to the study" or "The first author contributed 60%, the second author 40%." expressions such as should be included.

The Declaration of Ethics Committee Approval

This study does not require ethics committee permission or any special permission.

The Declaration of Research and Publication Ethics

The authors of the paper declare that they comply with the scientific, ethical and quotation rules of SAUJS in all processes of the paper and that they do not make any falsification on the data collected. In addition, they declare that Sakarya University Journal of Science and its editorial board have no responsibility for any ethical violations that may be encountered, and that this study has not been evaluated in any academic publication environment other than Sakarya University Journal of Science.

REFERENCES

[1] J. R. Junttila, S. Niemelä, and J. Hirn, “Minimum growth temperatures of *Listeria monocytogenes* and non-haemolytic *Listeria*,” J. Appl. Microbiol., vol. 65, no. 4, pp. 321–327, Oct. 1988, doi: 10.1111/j.1365-2672.1988.tb01898.x.

[2] M. E. Parish and D. P. Higgins, “Survival of *Listeria monocytogenes* in low pH model broth systems,” J. Food Prot., vol. 52, no. 3, pp. 144–147, Mar. 1989.

[3] S. Galsworthy, S. Girdler and S. Koval, “Chemotaxis in *Listeria monocytogenes*,” Acta Microbiol. Hung., vol. 37, no. 1, pp. 81–85, 1990.

[4] S. M. George and B. M. Lund, “The effect of culture medium and aeration on growth of *Listeria monocytogenes* at pH 4.5,” Lett. Appl. Microbiol., vol. 15, no. 2, pp. 49–52, Aug. 1992, doi:10.1111/j.1472-765X.1992.tb00722.x.

[5] J. M. Farber and C. Addison, “RAPD typing for distinguishing species and strains in the genus *Listeria*,” J. Appl. Bacteriol., vol. 77 no. 3, pp. 242–250, Sept. 1994, doi: 10.1111/j.1365-2672.1994.tb03070.x

[6] J. Farber and P. Peterkin, “*Listeria monocytogenes*, a food-borne pathogen,” Microbiol Rev., vol. 55, no. 3, pp. 476–511, Sept. 1991, doi: 10.1128/mr.55.3.476-511.1991.

[7] Schuchat, B. Swaminathan and C. V. Broome, “Epidemiology of human listeriosis,” Clin Microbiol Rev., vol. 4, no. 2, pp. 169–183, Apr. 1991. doi: 10.1128/CMR.4.2.169.

[8] R.W. Pinner, *et al*., “Role of Foods in Sporadic Listeriosis: II. Microbiologic and Epidemiologic Investigation,” Jama, vol. 267, no. 15, pp. 2046–2050, Apr. 1992.

[9] J. Rocourt and P. Cossart, "*Listeria monocytogenes*," in *Food Microbiology Fundamentals and Frontiers*, M. P. Doyle, L. R. Beuchat, T. J. Montville, Eds., Washington, DC, USA: ASM, 1997, pp. 237–352.

[10] B. Gudbjörnsdottir, L. Suihkob, P. Gustavssonc, G. Thorkelssona, S. Salob, A. M. Sjöbergb, O. Niclasend, and S. Bredholte, "The incidence of *Listeria monocytogenes* in meat, poultry and seafood plants in the Nordic countries," Food Microbiol., vol. 21, no. 2, pp. 217–225, Apr. 2004, doi: 10.1016/S0740-0020(03)00012-1.

[11] P.S. Mead, L. Slutsker, V. Dietz, L.F. McCaig, J.S Bresee, C. Shapiro, P.M. Griffin, and R.V. Tauxe, "Food-related illness and death in the United States," Emerg. Infect. Dis., vol. 5, no. 5, pp. 607, Sept. 1999, doi: 10.3201/eid0505.990502.

[12] P. S. Mead *et al.*, "Nationwide outbreak of listeriosis due to contaminated meat," Epidemiol. Infect., vol. 134, no. 4, pp. 744–751, Aug. 2006, doi: 10.1017/S09502688 05005376.

[13] E. Jones and A. MacGowan, "Antimicrobial chemotherapy of human infection due to *Listeria monocytogenes,"* Eur J Clin Microbiol Infect Dis., vol. 14, no. 3, pp. 165–175, Mar. 1995, doi: 10.1007/BF02310351.

[14] P. Kaynar, "Ülkemiz Peynirleri Üzerine Mikrobiyolojik Araştırmalar," Turk Mikrobiyol Cem Derg., vol. 41, no. 1, pp. 1–8, 2011, doi:10.5222/TMCD.2011.001.

[15] FDA, "*Listeria* isolation; revised method of analysis: notice, Bacteriological analytical manual," *Chapter 29*, U.S. Food and Drug Administration, pp. 44147-44153, 1988.

[16] A.D. Hitchins, "*Listeria monocytogenes*," *in Bacteriological Analytical Manual Revision A*, G.J. Jackson, Ed., Gaithersburg, MD, USA: AOAC International, 1995, pp. 1001–1013.

[17] *NCCLS–National Committee for Clinical Laboratory Standards, Performance Standards for Antimicrobial Disk Susceptibility Tests, Approved Standard*, M2-A6, NCCLS Publications, Wayne, PA, USA, 1997.

[18] S. Köhler, M. Leimeister-Wächter, T. Chakraborty, F. Lottspeich and W. Goebel, "The gene coding for protein p60 of *Listeria monocytogenes* and its use as a specific probe for *Listeria monocytogenes*," Infect. Immun., vol. 58, no. 6, pp. 1943–1950, Jun. 1990, doi: 10.1128/iai.58.6.1943-1950.1990.

[19] M. Bohnert, F. Dilasser, C. Dalet, J. Mengaud and P. Cossart, "Use of specific oligonucleotides for direct enumeration of *Listeria monocytogenes* in food samples by colony hybridization and rapid detection by PCR," Res Microbiol., vol. 143, no. 3, pp. 271–280, Mar. 1992, doi: 10.1016/0923-2508(92)90019-k.

[20] S. Elmas, "Aydın ilindeki semt pazarlarında satışa sunulan beyaz, tulum ve lor peynirlerinde *Listeria monocytogenes* ve *Salmonella* spp. varlığının araştırılması," M.S. thesis, Dept. Food Hygiene and Technol., Adnan Menderes Univ., Aydın, Turkey, 2014.

[21] M. Gülmez, A. Güven, and A. Çetinkaya, "Kars'ta tüketime sunulan taze ve salamura beyaz peynirlerin bazı mikrobiyolojik ve kimyasal özellikleri," Kafkas Üniv. Vet. Fak. Derg., vol. 7, no. 1, pp. 55–62, 2001.

[22] Z. Kaynar, P. Kaynar and C. Koçak, Ankara piyasasında tüketime sunulan beyaz peynirlerin hijyenik kalitelerinin belirlenmesi üzerine bir araştırma. Turk Hij Den Biyol Derg., vol. 62, no. 1, pp. 1–10, 2005.

[23] Z. T. Alas, "Ankara piyasasında tüketime sunulan beyaz peynir ve sade dondurmada

*Listeria monocytogenes, Bacillus cereu*s, fekal koliform ve *E. coli* varlığı," M.S. thesis, Dept. Biol., Gazi Univ., Ankara, Turkey, 2004.

[24] B. Çetin, S. Karasu, A. Atik and M. Z. Durak, "Investigation of Microbiological Quality of Some Dairy Products in Kirklareli: Detection of *Salmonella* spp. and *Listeria monoctyogenes* by Real Time PCR,," J. Tekirdag Agric. Fac., vol. 12, no. 1, pp. 74–80, 2015.

[25] E. Atil, H. Ertas and G. Ozbey, "Isolation and molecular characterization of *Listeria spp.* from animals, food and environmental samples," VetMed, vol. 56, no. 8, pp. 386–394, 2011, Doi:10.17221/1551-VETMED

[26] E. Rahimi, M. Ameri and H. Momtaz, "Prevalence and antimicrobial resistance of *Listeria* species isolated from milk and dairy products in Iran," Food Cont., vol. 21, no. 11, pp. 1448–1452, 2010.

[27] L. Akkaya and M. Alişarlı, "Afyonkarahisar'da tüketime sunulan peynirlerde *Listeria monocytogenes* ve *Salmonella* spp. varlığının belirlenmesi," YYU Vet Fak Derg., vol. 17, no. 1, pp. 87–91, 2006.

[28] O. Aygun and S. Pehlivanlar, "*Listeria* spp. in the raw milk and dairy products in Antakya, Turkey," Food Cont., vol. 17, no. 8, 676–679, 2006.

[29] Z. G. Ceylan and A. K. Demirkaya, "Erzurum piyasasından temin edilen salamura beyaz peynirlerde *Listeria monocytogenes* varlığı ve bazı mikrobiyolojik özeliklerinin belirlenmesi," Atatürk Üniv. Ziraat Fak. Derg, vol. 38, no. 2, 137–141, 2007.

[30] S. H. Elshinaway, A. M. Meshref, M. M. Zeinhom and D. A. Hafez, "Incidence of *Listeria* species in some dairy products Inbeni-Suef Governorate," Assiut Vet. Med. J, vol. 63, no. 152, pp. 5–13, Jan. 2017, Doi: 10.21608/AVMJ.2016.169210.

[31] S. Arslan and F. Özdemir, "Prevalence and antimicrobial resistance of *Listeria* spp. in homemade white cheese," Food Cont., vol. 19 no. 4, pp. 360–363, 2008.

[32] T. O. Kevenk and G. T. Gülel. "Prevalence, antimicrobial resistance and serotype distribution of *Listeria monocytogenes* isolated from raw milk and dairy products," J. Food Saf., vol. 36, no. 1, pp. 11–18, Feb. 2016, doi: 10.1111/jfs.12208.

[33] C. Poyart-Salmeron, C. Carlier, P. Trieu-Cuot, P. Courvalin and A, Courtieu, "Transferable plasmid-mediated antibiotic resistance in *Listeria monocytogenes*," The Lancet, vol. 335, no. 8703, pp. 1422–1426, Jun. 1990, doi: 10.1016/0140-6736(90)91447-i.

[34] P. J. Slade and D. L. Collins-Thompson, "*Listeria* plasmids antibiotic resistance and food," Lancet, vol. 336, no. 8721, pp. 1004, Oct. 1990, doi: 10.1016/0140-6736(90)92464-s.

[35] B. Facinelli, E. Giovanetti, P. Varaldo, P. Casolari and U. Fabio, "Antibiotic resistance in foodborne *Listeria*," Lancet, vol. 338, no. 16, pp. 1272, Nov. 1991, doi: 10.1016/0140-6736(91)92138-r.

[36] B. Facinelli, M. Roberts, E. Giovanetti, C. Casolari, U. Fabio and P. Varaldo, "Genetic basis of tetracycline resistance in food-borne isolates of *Listeria innocua*," Appl. Environ. Microbiol., vol. 59, no. 2, pp. 614–616, Feb. 1993, doi: 10.1128/aem.59.2.614-616.1993.

[37] K. Hadorn, H. Hächler, A. Schaffner and F. Kayser, "Genetic characterization of plasmid-encoded multiple antibiotic resistance in a strain of *Listeria monocytogenes* causing endocarditis" Eur. J. Clin. Microbiol. Infect. Dis., vol. 12, no.

12, pp. 928–937, Dec. 1993, doi: 10.1007/BF01992167.

[38] C. F. Abuín, E. Q. Fernández, C. F. Sampayo, J. R. Otero, L. D. Rodríguez and A. C. Sáez, “Susceptibilities of *Listeria* species isolated from food to nine antimicrobial agents, ” Antimicrob. Agents Chemother., vol. 38, no. 7, pp. 1655–1657, Jul. 1994, doi: 10.1128/aac.38.7.1655.

[39] E. Charpentier, G. Gerbaud, C. Jacquet, J. Rocourt and P. Courvalin, “Incidence of antibiotic resistance in *Listeria* species,” J. Infect. Dis., vol. 172, no. 1, pp. 277–281, Jul. 1995, doi: 10.1093/infdis/172.1.277.

[40] E. Charpentier and P. Courvalin, “Antibiotic Resistance in *Listeria spp.,”* Antimicrob. Agents Chemother., vol. 43, no. 9, pp. 2103–2108, Sep. 1999.

[41] A. Aksoy, Ç. Sezer, L. Vatansever and G. Gülbaz, “Presence and Antibiotic Resistance of *Listeria monocytogenes* in Raw Milk and Dairy Products,” Kafkas Üniv. Vet. Fak. Derg., vol. 24, no. 3, pp. 415–421, 2018.

[42] V. Srinivasan, H. Nam, L. Nguyen, B. Tamilselvam, S. Murinda and S. Oliver, “Prevalence of antimicrobial resistance genes in *Listeria monocytogenes* isolated from dairy farms,” Foodborne Pathog. Dis., vol. 2, no. 3, pp. 201–211, 2005, doi: 10.1089/fpd.2005.2.201.

[43] S. Harakeh, I. Saleh, O. Zouhairi, E. Baydoun, E. Barbour and N. Alwan, “Antimicrobial resistance of *Listeria monocytogenes* isolated from dairy-based food products” Sci. Total Environ., vol. 407, no. 13, pp. 4022–4027, Jun. 2009, doi: 10.1016/j.scitotenv.2009.04.010.

[44] H. Jamali, B. Radmehr and K. L. Thong, “Prevalence, characterisation, and antimicrobial resistance of *Listeria* species and *Listeria monocytogenes* isolates from raw milk in farm bulk tanks,” Food Cont., vol. 34, no. 1, pp. 121–125, 2013.

[45] M. Conter, D. Paludi, E. Zanardi, S. Ghidini, A. Vergara and A. Ianieri, “Characterization of antimicrobial resistance of foodborne *Listeria monocytogenes*,” Int. J. Food Microbiol., vol. 128, no. 3, pp. 497–500, Jan. 2009, doi: 10.1016/j.ijfoodmicro.2008.10.018.

[46] L. O’Connor *et al*., “The characterization of *Listeria* spp. isolated from food products and the food-processing environment,” Lett. Appl. Microbiol., vol. 51, no. 5, pp. 490–498, Nov. 2010, doi: 10.1111/j.1472-765X.2010.02928.x.

[47] D. Walsh, G. Duffy, J. Sheridan, I. Blair and D. McDowell, “Antibiotic resistance among *Listeria*, including *Listeria monocytogenes*, in retail foods,” J. Appl. Microbiol., vol. 90, no. 4, pp. 517–522, Apr. 2001, doi: 10.1046/j.1365-2672.2001.01273.x.

[48] J. Rocourt, H. Hof, A. Schrettenbrunner, R. Malinverni and J. Bille, “Acute purulent *Listeria seelingeri* meningitis in an immunocompetent adult,” Schweiz Med Wochenschr., vol. 116, no. 8, pp. 248–251, Feb. 1986.

SAKARYA ÜNİVERSİTESİ

FEN BİLİMLERİ ENSTİTÜSÜ
DERGİSİ

Sakarya University Journal of Science
SAUJS

e-ISSN 2147-835X Founded 1997 Period Bimonthly Publisher Sakarya University
http://www.saujs.sakarya.edu.tr/en/

Title: Numerical Assessment of Symmetric and Non-Symmetric Kernel Functions on Second Order Non-Homogenous Volterra Integro-Differential Equations

Authors: Kazeem Iyanda FALADE, Ismail Gboyeka BAOKU, Abdulgafar Tunde TIAMIYU

Recieved: 2020-01-01 00:00:00

Accepted: 2021-10-04 00:00:00

Article Type: Research Article

Volume: 25
Issue: 6
Month: December
Year: 2021
Pages: 1263-1274

How to cite
Kazeem Iyanda FALADE, Ismail Gboyeka BAOKU, Abdulgafar Tunde TIAMIYU; (2021), Numerical Assessment of Symmetric and Non-Symmetric Kernel Functions on Second Order Non-Homogenous Volterra Integro-Differential Equations. Sakarya University Journal of Science, 25(6), 1263-1274, DOI: https://doi.org/10.16984/saufenbilder.668299
Access link
http://www.saujs.sakarya.edu.tr/tr/pub/issue/66341/668299

Sakarya University Journal of Science 25(6), 1263-1274, 2021

SAKARYA ÜNİVERSİTESİ

Numerical Assessment of Symmetric and Non-Symmetric Kernel Functions on Second Order Non-Homogenous Volterra Integro-Differential Equations

Kazeem Iyanda FALADE*[1], Ismail Gboyeka BAOKU[2], Abdulgafar Tunde TIAMIYU[3]

Abstract

In this paper, we present numerical assessment of symmetric and non-symmetric kernel functions on non-homogenous Volterra integro-differential equations. Simple MAPLE 18 software commands codes procedures are employ based on newly introduced techniques: exponentially fitted collocation approximation method and Adomian decomposition method for the numerical solutions of the non-homogenous Volterra integro-differential equations. The procedures are sought to obtain convergent point of the problems. Considering the property of symmetric and non-symmetric kernel ($K(t,\ s) = K(s,\ t)$ and $K(t,\ s) \neq K(s,\ t)$), the computational lengths are considered to archive the best numerical solutions for the four examples considered. The reliability and efficiency of the proposed techniques are demonstrated using some examples available in literature.

Keywords: symmetric and non-symmetric kernel functions, non-homogenous Volterra integro-differential equations, exponentially fitted collocation approximate method, Adomian decomposition method.

1. INTRODUCTION

The Volterra integro-differential equation appeared after its establishment by Volterra. It then appeared in many physical applications such as glass forming process, nanohydrodynamics, heat transfer and diffusion process in general, neutron diffusion and biological species coexisting together with increasing and decreasing rates of generating and wind ripple in the desert. It gained a lot of interest in many applied mathematical sciences, such as modelling of physical phenomenon: thermodynamics, solid mechanics, rocketing sciences, biological models and chemical kinetics**.** As such, the solution of integro-differential equations has a major role in the fields of applied sciences. Therefore, they received special attention of scientists and researchers [1-5]. When a physical system is modelled under the differential sense, it finally gives a differential equation, an integral equation or an integro-differential equation. There are various techniques for solving an integral or integro differential equation, e.g, wavelet Galerkin, Taylor expansion method, Haar functions method, variational iteration method and differential transform method [6-10]. Homotopy perturbation method (HPM) [11], linear multi step methods [12] and just to mention a few.

---

* Corresponding author: faladekazeem2013@gmail.com
[1] Kano University of Science and Technology, Department of Mathematics, Faculty of Computing and Mathematical Sciences, Wudil, P.M.B, Nigeria
ORCID: https://orcid.org/0000-0001-7572-5688
[2] Federal University, Department of Mathematical Sciences, Dutsin-Ma, Katsina State, Nigeria
E-Mail: ibaoku@fudutsinma.edu.ng
ORCID: https://orcid.org/0000-0002-8323-5977
[3] Federal University of Technology, Department of Mathematics, Minna Niger State, Nigeria
E-Mail: abdgafartunde@yahoo.com
ORCID: https://orcid.org/0000-0003-1641-7196

The purpose of this article is to extend the numerical method proposed by [13] and compare the results obtain with analytical solutions and the Adomian decomposition method discussed by [14] for the assessment of symmetric and non-symmetric kernel functions on second order non-homogenous Volterra intgro-differential equations of the form:

$$\frac{d^2u(t)}{dt^2} = g(t) + \int_a^t K(t,s)u(s)ds, t\epsilon[a,b] \quad (1)$$

subject to initial conditions:

$$u(a) = \beta \qquad u'(a) = \gamma \qquad (2)$$

where β and γ are constants, $g(t)$ is the source inhomogeneous term, a and b are limit of function $u(t)$, $K(t,s) = K(s,t)$ symmetric kernel, $K(t,s) \neq K(s,t)$ non-symmetric kernel.

2. DEFINITION AND THEOREM [15]

Definition 2.1. A kernel $K(t,s)$ is said to be symmetric (real) if

$$K(t,s) = K(s,t) \qquad (3)$$

otherwise is non-symmetric i.e

$$K(t,s) \neq K(s,t) \qquad (4)$$

Theorem 2.2. If the kernel $K(t,s) = K(s,t)$ is symmetric and real then

$$(Ku,v) = (u,Kv) \qquad (5)$$

Proof. We take the general case where

$$(u,v) = \int_a^b \int_a^b \left(u(t)\underline{v}(t)dt\right) \quad Now$$

$$(Ku,v) = \int_a^b \left(\int_a^b (k(t,s)u(s)ds)\right)\underline{v}(t)dt$$

$$(Ku,v) = \int_a^b \int_a^b k(t,s)u(s)\underline{v}(t)dsdt$$

$$re - labelling\ of\ variables$$

$$(Ku,v) = \int_a^b \int_a^b k(s,t)u(s)\underline{v}(t)dtds$$

$$symmetric\ kernel$$

$$(Ku,v) = \int_a^b u(s)\left(\underline{\int_a^b k(s,t)v(t)dt}\right)ds$$

$$real\ kernel$$

$$(Ku,v) = (u,Kv) \qquad (6)$$

3. DESCRIPTION OF THE METHODS

3.1. Adomian decomposition method (ADM)

The Adomian decomposition method [14,16, 17] gives the solution in an infinite series of components that can be recurrently determined. The obtained series may give the exact solution if such a solution exists. Otherwise, the series gives an approximation for the solution that gives high accuracy level.

Consider equation (1) and integrating both sides of from a to t twice lead to:

$$u(t) = a_0 + a_1 t + L^{-1}(g(t)) + L^{-1}\left(\int_a^t K(t,s)u(s)ds\right) \quad (7)$$

where the initial conditions $u(a)$ and $u'(a)$ are used and L^{-1} is a two-fold integral operator.

We then use the decomposition series:

$$u(t) = \sum_{p=0}^{\infty} u_p(t) \qquad (8)$$

Integrate both sides of (7) to obtain:

$$\sum_{p=0}^{\infty} u_p(t) = a_0 + a_1 t + L^{-1}\big(g(t)\big) + L^{-1}\left(\int_a^t K(t,s)\left(\sum_{p=0}^{\infty} u_p(s)\right)ds\right) \quad (9)$$

Simply equation (9), we have:

$$\{u_0(t) + u_1(t) + u_2(t) + u_3(t) + \cdots = a_0 + a_1 t + L^{-1}\big(g(t)\big) + L^{-1}\left(\int_a^t K(t,s)u_0(s)ds\right) + L^{-1}\left(\int_a^t K(t,s)u_1(s)ds\right) L^{-1}\left(\int_a^t K(t,s)u_2(s)ds\right) + \cdots \quad (10)$$

To determine the unknown $u_0(t), u_1(t), u_2(t), u_3(t)$ .... of the solution $u(t)$, we set the recurrence relation

$$\{u_0(t) = a_0 + a_1 t + L^{-1}\big(g(t)\big) \quad u_1(t) = L^{-1}\left(\int_a^t K(t,s)u_0(s)ds\right) \quad u_2(t) = L^{-1}\left(\int_a^t K(t,s)u_1(s)ds\right) \quad (11) \quad u_3(t) = L^{-1}\left(\int_a^t K(t,s)u_2(s)ds\right) \quad \vdots \quad \vdots \quad u_{m+1}(t) = L^{-1}\left(\int_a^t K(t,s)u_m(s)ds\right)$$

where $m \geq 0$ *and* $L^{-1} = \int_a^t \int_a^t (.)dtdt.$

Having determined the components $u_i(t), i \geq 0$ the solution $u(t)$ of equation (1) is then obtained in a series form. Using equation (8), the obtained series converges to exact solution.

3.2. Exponentially fitted collocation approximation method (EFCAM)

Exponentially fitted collocation method was proposed by [13]. The whole idea is that we employ derivative of power series function $u(t)$, then substitute into second order integro-differential equation (1). Perturbation was slightly carried out which eventually collocate perturbed equation and form system of equations. Eventually, the unknown $a_0, a_1, a_2, a_3 \ldots \ldots a_N$ are determine using MAPLE 18 software.

Consider finite power series of the form:

$$u(t) = \sum_{k=0}^{N} a_k t^k \quad (12)$$

and exponentially fitted approximate solution

$$u(t) = \sum_{k=0}^{N} a_k t^k + \tau_2 e^t \quad (13)$$

Here $k \geq 0$, τ is a free parameter and 2 is the order of equation (1) and N is a finite computational length.

Taking derivative of (12) twice and substitute in equation (1), lead to:

$$\{\sum_{k=2}^{N} k(k-1)a_k t^{k-2} = g(t) + + \int_a^t K(t,s)\left(\sum_{k=0}^{N} a_k s^k\right)ds$$

$$\{\sum_{k=2}^{N} k(k-1)a_k t^{k-2} - + \int_a^t K(t,s)\left(\sum_{k=0}^{N} a_k s^k\right)ds = g(t) \quad (14)$$

Expand and collect the like terms, we have:

$$
\begin{aligned}
&\{-\left(\int_a^t K(t,s)\left(\sum_{k=0}^{N} s^0\right)ds\right)a_0\\
&-\left(\int_a^t K(t,s)\left(\sum_{k=0}^{N} s^1\right)ds\right)a_1\left(2\right.\\
&\left.-\left(\int_a^t K(t,s)\left(\sum_{k=0}^{N} s^2\right)ds\right)\right)a_2\\
&+\left(6t-\left(\int_a^t K(t,s)\left(\sum_{k=0}^{N} s^3\right)ds\right)\right)a_3+\\
&\vdots+\left(N(N-1)t^{N-2}\right.\\
&\left.-\left(\int_a^t K(t,s)\left(\sum_{k=0}^{N} s^N\right)ds\right)\right)a_N = g(t) \quad (15)
\end{aligned}
$$

Slightly perturb and collocate equation (15), leads to:

$$
\begin{aligned}
&\{-\left(\int_a^t K(t,s)\left(\sum_{k=0}^{N} s^0\right)ds\right)a_0\\
&-\left(\int_a^t K(t,s)\left(\sum_{k=0}^{N} s^1\right)ds\right)a_1\left(2\right.\\
&\left.-\left(\int_a^t K(t,s)\left(\sum_{k=0}^{N} s^2\right)ds\right)\right)a_2\\
&+\left(6t-\left(\int_a^t K(t,s)\left(\sum_{k=0}^{N} s^3\right)ds\right)\right)a_3+\\
&\vdots+\left(N(N-1)t^{N-2}\right.\\
&\left.-\left(\int_a^t K(t,s)\left(\sum_{k=0}^{N} s^N\right)ds\right)\right)a_N - H(t)\\
&= g(t)
\end{aligned}
$$

$$
\begin{aligned}
&\{-\left(\int_a^t K(t_i,s)\left(\sum_{k=0}^{N} s^0\right)ds\right)a_0\\
&-\left(\int_a^t K(t_i,s)\left(\sum_{k=0}^{N} s^1\right)ds\right)a_1\left(2\right.\\
&\left.-\left(\int_a^t K(t_i,s)\left(\sum_{k=0}^{N} s^2\right)ds\right)\right)a_2\\
&+\left(6t-\left(\int_a^t K(t_i,s)\left(\sum_{k=0}^{N} s^3\right)ds\right)\right)a_3+\\
&\vdots+\left(N(N-1){t_i}^{N-2}\right.\\
&\left.-\left(\int_a^t K(t_i,s)\left(\sum_{k=0}^{N} s^N\right)ds\right)\right)a_N - T_N(t_i)\tau_1\\
&- T_{N-1}(t_i)\tau_2 = g(t_i) \quad (16)
\end{aligned}
$$

Here τ_1 and τ_2 are free tau parameters to be determined, $T_N(t_i)$ and $T_{N-1}(t_i)$ are the Chebyshev polynomials of degree N define in [16] and $t_i = a + \frac{(b-a)i}{N+2}$, $i = 1,2,\ldots.N+1$.

Evaluating the integrals at the right side (16) and using few terms from both sides and collecting the coefficients, equation (16) gives rise to (*N*+*2*) algebraic linear system of equations in (*N*+*2*) unknown constants. Two extra equations are obtained from the given initial conditions.

Thus, MAPLE 18 software is used to obtain the unknown constants: $a_0, a_1, a_2, a_3, \ldots, a_N$ and τ_1, τ_2.

This is then substitute into the exponential fitted approximate solution (13).

4. NUMERICAL EXPERIMENT

In this section, four examples are presented to show the applicability of the proposed methods for the numerical assessment of symmetric and non-symmetric kernel functions on second order non homogenous Volterra integro-differential equations.

Example 1: Consider symmetric kernel function of second order non-homogenous Volterra integro-differential equation [14].

$$\{\frac{d^2u(t)}{dt^2} = -\frac{1}{2}t^2 - \frac{2}{3}t^3 + \int_0^t K(t,s)u(s)ds \qquad (17)$$

subject to initial conditions:

$$u(0) = 1, \quad u'(0) = 4 \qquad (18)$$

when $K(t,s) = K(s,t) = \{(t-s)^2\ (s-t)^2$.

ADM

Consider algorithm (10), we obtain the following:

$$\{u_0(t) = 1 + 4t - \frac{1}{24}t^4 - \frac{1}{30}t^5 \quad u_1(t) = \frac{1}{60}t^5 + \frac{1}{90}t^6 - \frac{1}{181440}t^9 - \frac{1}{453600}t^{10} \quad u_2(t) = \{\frac{1}{907200}t^{10} + \frac{1}{2494800}t^{11} - \frac{1}{21794572800}t^{14} + \frac{1}{81729648000}t^{15}$$

The solution in closed form is given as

$$u(t) \approx u_0(t) + u_1(t) + u_2(t) \ldots.$$

$$u(t) \approx \{1 + 4t - \frac{1}{24}t^4 - \frac{1}{30}t^5 + \frac{1}{60}t^5 + \frac{1}{90}t^6 - \frac{1}{181440}t^9 - \frac{1}{907200}t^{10} + \frac{1}{907200}t^{10} + \frac{1}{2494800}t^{11} - \frac{1}{21794572800}t^{14} + \frac{1}{81729648000}t^{15}$$
(19)

EFCAM

Consider equation (16), we obtain the following:

$$\{a_0 = 0.99999999. \quad a_1 = 4.000000000 \ a_2 = -1.43341437\ 10^{-8}, \ a_3 = 2.527456460\ 10^{-7} \ a_4 = -0.041669441\ , \ a_5 = -0.01664654052 \ a_6 = 0.01101120870\ , \ a_7 = 0.0003472824498 \ a_8 = -0.0008566083\,, a_9 = 0.001498756008 \ a_{10} = -0.00186646807\,, a_{11} = 0.001595032809 \ a_{12} = -0.0008935941, \ a_{13} = 0.0002953130446 \ a_{14} = -0.000043614257\,, \tau_1 = 1.90579645\ 10^{-10} \ \tau_2 = 1.520953686\ 10^{-10}$$

Substitute into equation (13) while computational length *N*=14, the solution is given in closed form:

$$u(t) \approx \{0.99999999 + 4.000000000t - 1.43341437\ 10^{-8}t^2 + 2.527456460\ 10^{-7}t^3 - 0.041669441\ t^4 - 0.0166465405t^5 + 0.01101120870t^6 + 0.0003472824t^7 - 0.0008566083t^8 + 0.001498756008t^9 - 0.00186646807t^{10} + 0.001595032809t^{11} - 0.0008935941t^{12} + 0.0002953130446t^{13} - 0.000043614257t^{14}\ 1.520953686\ 10^{-10}e^t \qquad (20)$$

Table 1. Symmetric kernel on Volterra integro-differential Equation

t	Analytical	ADM	EFCAM
0	1.000000000	1.000000000	1.000000000
0.1	1.399995322	1.399995677	1.399995678
0.2	1.799916622	1.799928711	1.799928711
0.3	2.199532900	2.199630100	2.199630102
0.4	2.598375823	2.598808176	2.598808176
0.5	2.995659736	2.997048599	2.997048599
0.6	3.390193677	3.393822338	3.393822340
0.7	3.780285445	3.788501632	3.788501632
0.8	4.163637751	4.180383887	4.180383888
0.9	4.537236514	4.568723507	4.568723505
1.0	4.897231441	4.952771565	4.952771565

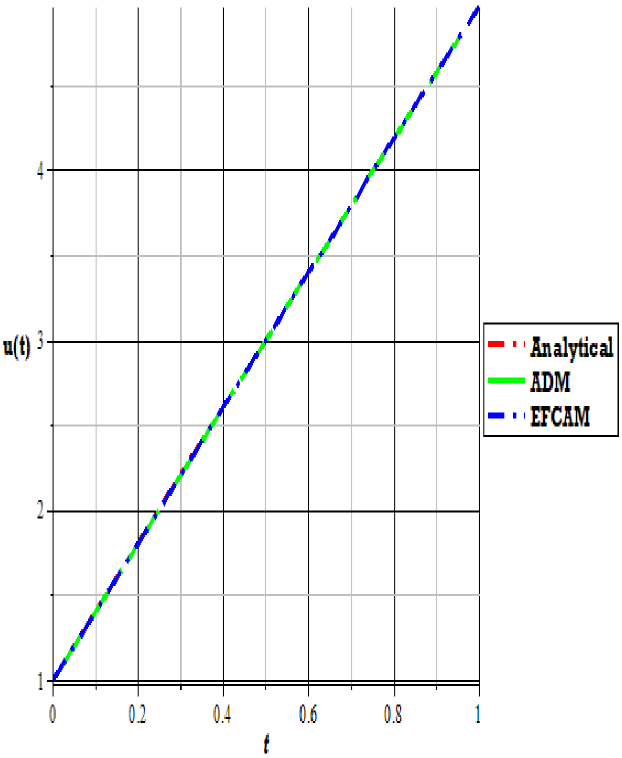

Figure 1. Symmetric kernel function for Example 1

Example 2: Consider symmetric kernel function of second order non-homogenous Volterra integro-differential equation [14]

$$\{\frac{d^2u(t)}{dt^2} = 6t^2 + t + 1 + \int_0^t K(t,s)u(s)ds \qquad (21)$$

subject to initial conditions:

$$u(0) = 0, \quad u'(0) = 2 \qquad (22)$$

when $K(t,s) = K(s,t) = \{s^2t^2 + st + 1\ t^2s^2 + ts + 1$

ADM

Consider algorithm (10), we obtain the following:

$$\{u_0(t) = 2t + \frac{1}{2}t^4 + \frac{1}{6}t^3 + \frac{1}{2}t^2\ u_1(t) = \{\frac{1}{12}t^4 + \frac{1}{120}t^5 + \frac{17}{720}t^6 + \frac{3}{560}t^7 + \frac{1}{105}t^8 + \frac{11}{4320}t^9 + \frac{1}{3240}t^{10} + \frac{1}{1540}t^{11}\ u_2(t) = \{\frac{1}{40}t^5 + \frac{1}{120}t^7 + \frac{1}{40320}t^8 + \frac{17}{362880}t^9 + \frac{1}{134400}t^{10} + \frac{1}{103950}t^{11} + \frac{1}{518400}t^{12} + \frac{1}{5559840}t^{13} + \frac{1}{3363360}t^{14}$$

The solution in closed form is given as:

$$u(t) \approx u_0(t) + u_1(t) + u_2(t) \ldots.$$

$$u(t) \approx \{2t + \frac{1}{2}t^2 + \frac{1}{6}t^3 + \frac{7}{12}t^4 + \ + \frac{1}{30}t^5 + \frac{17}{720}t^6 + \frac{23}{1680}t^7 + \frac{11}{1152}t^8 + \frac{941}{362880}t^9 \qquad (23) \qquad \frac{1147}{3628800}t^{10} + \frac{137}{207900}t^{11} + \frac{1}{518400}t^{12} + \frac{1}{5559840}t^{13} + \frac{1}{3363360}t^{14}$$

EFCAM

Consider equation (16), we obtain the following:

$$\{a_0 = 3.41029653510^{-9}, \quad a_1 = 2.000000002\ a_2 = 0.499999766, \quad a_3 = 0.1666704294\ a_4 = 0.5832961941, \quad a_5 = 0.008572137303\ a_6 = 0.02257332574\,, \ a_7 = 0.008873873203\ a_8 = 0.0029836925, a_9 = 0.01245032147\ a_{10} = -0.009466627967, a_{11} = 0.007364861819\ a_{12} = -0.002654643617, a_{13} = 0.0005423347641\ \tau_1 = -3.410296535\ 10^{-9}\,, \tau_2 = -2.306787544\ 10^{-9}$$

Substitute into equation (13) while computational length *N*=13, the solution is given in closed form:

$$u(t) \approx$$

$$\{3.410296535\ 10^{-9} + 2.000000002t\ 0.4999997661\ t^2 + 0.1666704294t^3 + 0.5832961941\ t^4 + 0.008572137303\ t^5 + 0.02257332574\ t^6 + 0.008873873203t^7\quad 0.002983692582\ t^8 + 0.01245032147\ t^9 \quad (24) \quad - 0.009466627967\ t^{10} + 0.007364861819\ t^{11} - 0.002654643617t^{12} + 0.0005423347641\ t^{13} - 2.306787544\ 10^{-9}e^t$$

Table 2. Symmetric kernel on Volterra integro-differential Equation

t	Analytical	ADM	EFCAM
0	0.0000000000	0.0000000000	0.0000000000
0.1	0.2052251076	0.2052253584	0.2052251080
0.2	0.4222709439	0.4222790453	0.4222709435
0.3	0.6542644055	0.6543268872	0.6542644044
0.4	0.9057985281	0.9060674732	0.9057985261
0.5	1.1830094170	1.183852209	1.183009413
0.6	1.4937040730	1.495867665	1.493704072
0.7	1.8475656370	1.852409718	1.847565655
0.8	2.2564756030	2.266290682	2.256475787
0.9	2.7350108960	2.753436687	2.735012043
1.0	3.3011998730	3.333754134	3.301205663

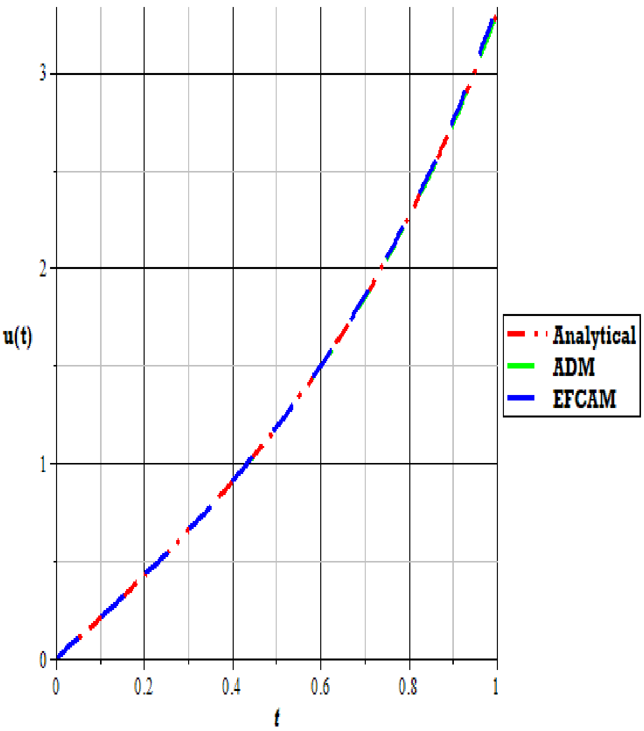

Figure 2. Symmetric kernel function for Example 2

Example 3: Consider non-symmetric kernel function of second order non-homogenous Volterra integro-differential equation [14].

$$\{\frac{d^2u(t)}{dt^2} = t + 1 + \int_0^t K(t,s)u(s)ds \tag{25}$$

subject to initial conditions:

$$u(0) = 1, \quad u'(0) = 1 \tag{26}$$

when

$$\{\ K(t,s) = (t-s)\ K(s,t) = (s-t)$$

Consider equation (10), we obtain the following:

$$\{k(t,s) = \{u_0(t) = 1 + t + \frac{1}{2!}t^2 + \frac{1}{3!}t^3\ u_1(t) = \frac{1}{4!}t^4 + \frac{1}{5!}t^5 + \frac{1}{6!}t^6 + \frac{1}{7!}t^7\ u_2(t) = \frac{1}{8!}t^8 + \frac{1}{9!}t^9 + \frac{1}{10!}t^{10} + \frac{1}{11!}t^{11}\quad k(s,t) = \{\quad u_0(t) = 1 + t + \frac{1}{2!}t^2 + \frac{1}{3!}t^3 \quad u_1(t) = -\frac{1}{4!}t^4 - \frac{1}{5!}t^5 - \frac{1}{6!}t^6 - \frac{1}{7!}t^7\ u_2(t) = \frac{1}{8!}t^8 + \frac{1}{9!}t^9 + \frac{1}{10!}t^{10} + \frac{1}{11!}t^{11}$$

The solution in closed form is given as:

$$u(t) \approx u_0(t) + u_1(t) + u_2(t) \ldots.$$

$$\{k(t,s) = u(t) \approx \{1 + t + \frac{1}{2!}t^2 + \frac{1}{3!}t^3 + \frac{1}{4!}t^4 + \frac{1}{5!}t^5 + \frac{1}{6!}t^6 + \frac{1}{7!}t^7 + \frac{1}{8!}t^8 + \frac{1}{9!}t^9 + \frac{1}{10!}t^{10} + \frac{1}{11!}t^{11}\ k(s,t) = u(t) \approx \{1 + t + \frac{1}{2!}t^2 + \frac{1}{3!}t^3 - \frac{1}{4!}t^4 - \frac{1}{5!}t^5 - \frac{1}{6!}t^6 - \frac{1}{7!}t^7 - \frac{1}{8!}t^8 - \frac{1}{9!}t^9 - \frac{1}{10!}t^{10} - \frac{1}{11!}t^{11} \quad (27)$$

EFCAM

Consider equation (16), we obtain the following:

$$\begin{aligned}k(t,s) = \{a_0 = 1.000000004\,,\ a_1 = 1.000000000\ a_2 &= 0.4999998473, a_3\\ &= 0.1666685047\ a_4\\ &= 0.04165385733,\ a_5\\ &= 0.008388697652\ a_6\\ &= 0.00123467016, a_7\\ &= 0.0004796759526\ a_8\\ &= -0.0003086880157,\ a_9\\ &= 0.0002502211379\ a_{10}\\ &= -0.0001040673428,\ a_{11}\\ &= 0.00001910346056\ \tau_1\\ &= -3.757219228\ 10^{-9}\,.\tau_2\\ &= -4.290656975\ 10^{-10}\end{aligned}$$

$$\begin{aligned}k(s,t) = \{a_0 = 1.000000006\,,\ a_1 = 1.000000000\ a_2 &= 0.499999751, a_3 = 0.1666696625\ a_4\\ &= -0.0416875595,\ a_5\\ &= -0.008243120393\ a_6\\ &= -0.001639615056, a_7\\ &= 0.0002574463432\ a_8\\ &= -0.0005136976419, a_9\\ &= 0.0004006094653\ a_{10}\\ &= -0.0001665747911, a_{11}\\ &= 0.00003029601045\ \tau_1\\ &= -6.254569677\ 10^{-9}.\tau_2\\ &= -3.393171724\ 10^{-10}\end{aligned}$$

Substitute into equation (13) while computational length N=11, the solution is given in close form

$$\begin{aligned}&\{k(t,s) = u(t)\\ &\approx \{1.000000004 + t + 0.4999998473\,t^2\ 0.166668506t^3\\ &+ 0.04165385733\,t^4\ 0.00838869765t^5\\ &+ 0.0012346701\,t^6\ 0.00047967595t^7\\ &- 0.00030868803\,t^8\ 0.000250221138t^9\\ &- 0.00010406734t^{10}\ \ 0.00001910346t^{11}\\ &- \ 4.29065698\,10^{-10}e^t\ \ k(s,t) = u(t)\\ &\approx \{1.000000006 + t\\ &+ 0.4999997515t^2 \qquad (29)\ 0.1666696625t^3\\ &- 0.04168755958t^4\ - 0.008243120393t^5\\ &- 0.001639615056t^6\ 0.000257446343t^7\\ &- 0.000513697642t^8\ 0.000400609465t^9\\ &- 0.000166574791\,t^{10}\ 0.000030296012t^{11}\\ &- 3.393171724\,10^{-10}\ e^t\end{aligned}$$

Table 3. Non- symmetric kernel on Volterra integro-differential Equation

T	Analytical	ADM	EFCAM
0	1.000000000	1.000000000	1.000000000
0.1	1.105170918	1.105170918	1.105170921
0.2	1.221402758	1.221402759	1.221402759
0.3	1.349858808	1.349858808	1.349858809
0.4	1.491824698	1.491824698	1.491824699
0.5	1.648721271	1.648721270	1.648721270
0.6	1.822118800	1.822118801	1.822118800
0.7	2.013752707	2.013752707	2.013752705
0.8	2.225540928	2.225540929	2.225540925
0.9	2.459603111	2.459603111	2.459603109
1.0	2.718281828	2.718281828	2.718281825

Table 4. Non-symmetric kernel n Volterra integro-differential Equation

t	Analytical	ADM	EFCAM
0	1.000000000	1.000000000	1.000000006
0.1	1.105162415	1.105162416	1.105162421
0.2	1.221263909	1.221263907	1.221263912
0.3	1.349141196	1.349141196	1.349141199
0.4	1.489508669	1.489508670	1.489508669
0.5	1.642945601	1.642945600	1.642945600
0.6	1.809882092	1.809882093	1.809882090
0.7	1.990583724	1.990583725	1.990583722
0.8	2.185134863	2.185134863	2.185134859
0.9	2.393420585	2.393420585	2.393420577
1.0	2.615107221	2.615107224	2.615107202

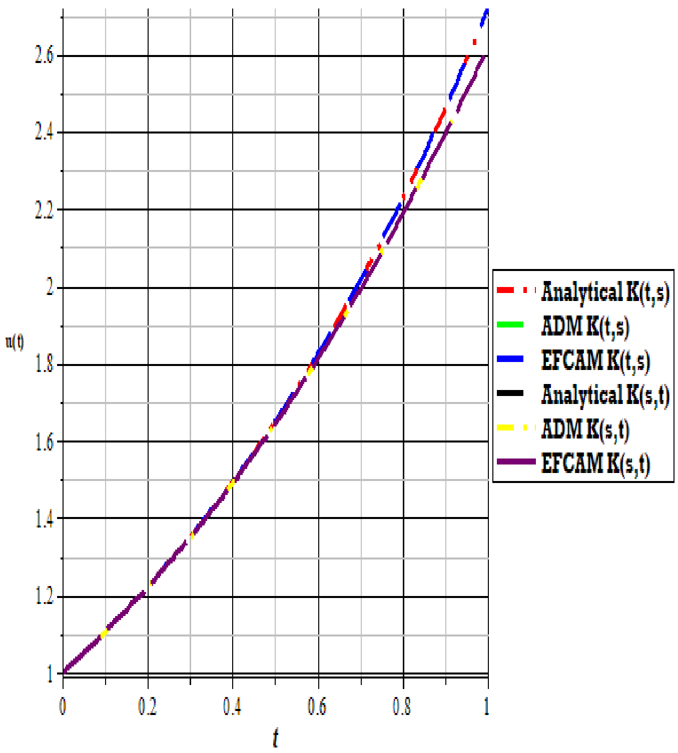

Figure 3. Non-symmetric kernel function for Example 3

Example 4: Consider non-symmetric kernel function of second order non-homogenous Volterra integro-differential equation [14].

$$\{\frac{d^2u(t)}{dt^2} = 1 + t - \frac{t^3}{31} + \int_0^t K(t,s)u(s)ds \qquad (30)$$

$$subject\ to\ initial\ conditions:$$

$$u(0) = 0 \qquad u^{/}(0) = 2 \qquad (31)$$

$$\{\ K(t,s) = t^3s^2 + 1\ K(s,t) = s^3t^2 + 1$$

ADM

Consider equation (10), we obtain the following:

$\{k(t,s) = \{u_0(t) = \{2t + \frac{1}{2}t^2\ + \frac{1}{6}t^3 - \frac{1}{620}t^5\ \ u_1(t) = \{\frac{1}{12}t^4 + \frac{1}{120}t^5 + \frac{1}{720}t^6\ - \frac{1}{208320}t^8 + \frac{1}{180}t^9 + \frac{t^{10}}{1080}\ + \frac{1}{4620}t^{11} - \frac{1}{870480}t^{13}\ \ k(s,t) = \{u_0(t) = \{2t + \frac{1}{2}t^2\ + \frac{1}{6}t^3 - \frac{1}{620}t^5\ \ u_1(t) = \{\frac{1}{12}t^4 + \frac{1}{120}t^5 + \frac{1}{720}t^6\ - \frac{1}{208320}t^8 + \frac{1}{144}t^9 + \frac{1}{900}t^{10}\ + \frac{1}{3960}t^{11} - \frac{1}{773760}t^{13}$

The solution in close formed is given as

$$u(t) \approx u_0(t) + u_1(t) + \cdots.$$

$$\{k(t,s) = u(t) \approx \{2t + \frac{1}{2}t^2 + \ + \frac{1}{6}t^3 - \frac{1}{620}t^5 + \frac{1}{12}t^4 + \frac{1}{120}t^5 + \frac{1}{720}t^6 - \frac{1}{208320}t^8 + \frac{1}{180}t^9 + \frac{t^{10}}{1080} + \frac{1}{4620}t^{11} - \frac{1}{870480}t^{13}\ \ k(s,t) = u(t) \approx \{ \quad 2t + \frac{1}{2}t^2 + \quad (32)\ \frac{1}{6}t^3 - \frac{1}{620}t^5 + \frac{1}{12}t^4 + \frac{1}{120}t^5 + \frac{1}{720}t^6 - \frac{1}{208320}t^8 + \frac{1}{144}t^9 + \frac{1}{900}t^{10} + \frac{1}{3960}t^{11} - \frac{1}{773760}t^{13}$$

EFCAM

Consider equation (16), we obtain the following:

$$k(s,t) = \{a_0 = -3.24787640710^{-9}\ , a_1 = 2.000000007\ a_2 = 0.5000003604, a_3 = 0.1666613521\ a_4 = 0.0833789638, a_5 = 0.006476916042\ a_6 = 0.00222628486, a_7 = -0.001476579128\ a_8 = 0.002670665105,\ \ a_9 = 0.003464478311\ a_{10} = \ 0.00129650136, a_{11} = 0.001096040923\ a_{12} = -0.000707666673, a_{13} = 0.000231470098\ \tau_1 = 3.24787640710^{-9}, \tau_2 = -6.59335272310^{-9}$$

Substitute into equation (13) while computational length N=13, the solution is given in closed form

$$
\begin{aligned}
&\{k(t,s) = u(t) \\
&\approx \{1.17645503810^{-10} + 2.000000010t \\
&+ 0.5000001012\,t^{2} + 0.1666654340t^{3} \\
&+ 0.08333942803t^{4} + 0.006727115765t^{5} \\
&+ 0.00115497992t^{6} + 0.00169299751t^{7} \\
&+ -0.003871054346t^{8} + 0.01424531284t^{9} \\
&- 0.00772113217t^{10} + 0.007014853163t^{11} \\
&- 0.00291650618t^{12} + 0.000611187901t^{13} \\
&- 1.17645503810^{-10}e^{t} \;. \qquad\qquad\qquad . \\
&= u(t) \\
&\approx \{-3.24787640710^{-9} + 2.000000007t \\
&+ 0.5000003604t^{2} + 0.1666613521t^{3} \\
&+ 0.08337896382t^{4} + 0.006476916042t^{5} \\
&+ 0.00222628487t^{6} - 0.00147657913t^{7} \\
&+ 0.002670665105t^{8} + 0.0034644783t^{9} \\
&+ 0.001296501364\,t^{10} + 0.00109604092t^{11} \\
&+ -0.0007076667t^{12} + 0.000231470092t^{13} \\
&+ 3.24787640710^{-9}e^{t}
\end{aligned}
$$

Table 5. Non- symmetric kernel on Volterra Integro-differential Equation

t	Analytical	ADM	EFCAM
0	0.000000000	0000000000	0.000000000
0.1	0.205175086	0.205175069	0.205175070
0.2	0.421470011	0.421468909	0.421468918
0.3	0.650205199	0.650192458	0.650192579
0.4	0.892948544	0.892876066	0.892877125
0.5	1.151564198	1.151285222	1.151291369
0.6	1.428286475	1.427449669	1.427476700
0.7	1.725830112	1.723722238	1.723819881
0.8	2.047555014	2.042895706	2.043199983
0.9	2.397713108	2.388422212	2.389267401
1.0	2.781817795	2.764801302	2.766942728

Table 6. Non- symmetric kernel on Volterra Integro-differential Equation

t	Analytical	ADM	EFCAM
0	0.000000000	0.000000000	0.000000000
0.1	0.205175069	0.205175069	0.205175071
0.2	0.421468914	0.421468909	0.421468919
0.3	0.650192547	0.650192487	0.650192554
0.4	0.892876734	0.892876451	0.892876743
0.5	1.151288446	1.151288132	1.151288459
0.6	1.427461417	1.427464916	1.427461431
0.7	1.723757695	1.723784226	1.723757717
0.8	2.042989624	2.043105095	2.042989691
0.9	2.388649276	2.389036150	2.388649643
1.0	2.765316717	2.766411307	2.765318799

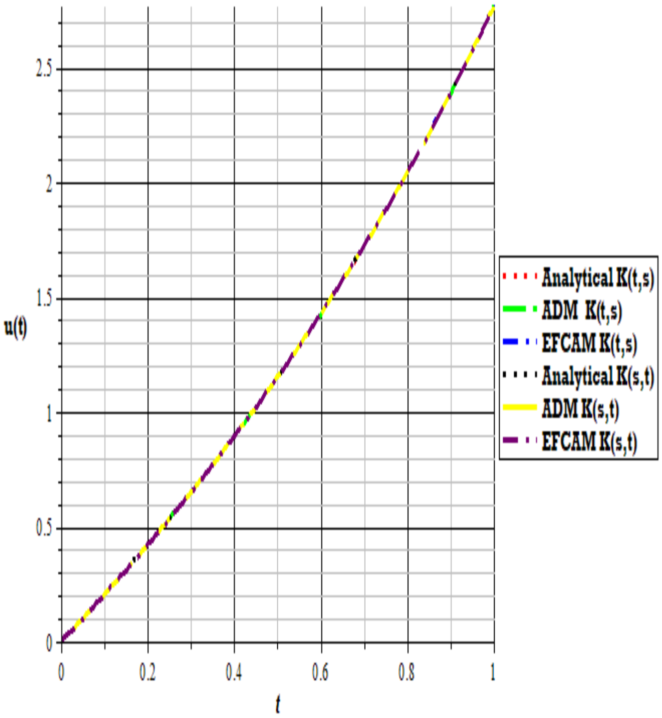

Figure 4. Non-symmetric kernel function for Example 4

5. DISCUSSION AND CONCLUSION

In this paper, we present two numerical techniques for numerical solutions of symmetric and non-symmetric kernel functions on Volterra non homogenous second order integro-differential equations. Table 1, Table 2, Figure 1 and Figure 2 depict no significant difference on symmetric kernels $K(t,s) = K(s,t)$ while Table 3, Table 4, Table 5, Table 6, Figure 3, Figure 4, Figure 5 and Figure 6 depict non- symmetric kernels $K(t,s) \neq K(s,t)$ which established in definition (1). From numerical solutions obtained it was demonstrated that proposed methods are powerful and efficient in given approximation solutions in closed form. However, comparison certified that EFCM gives closed numerical solutions to that of analytical solutions as evident in all Tables of numerical solutions obtained. Therefore recommend for solving similar problems in applied sciences.

Funding

None.

The Declaration of Conflict of Interest/ Common Interest

Authors of this article declared no conflict of interest or common interest.

Authors' Contribution

K.I.F: Conceptualization and carry out all computation works of all examples considered.

I.G.B: Vetting the literature searches and typing the article.

A.T.T: Validate the methods and coordinate the final write up.

The Declaration of Ethics Committee Approval

This article does not require ethics committee

permission or any special permission.

The Declaration of Research and Publication Ethics.

Authors of the article declare that they comply with the scientific, ethical and quotation rules of SAUJS in all processes of the paper and that they do not make any falsification on the data collected. In addition, they declare that Sakarya University Journal of Science and its editorial board have no responsibility for any ethical violations that may be encountered, and that this study has not been evaluated in any academic publication environment other than Sakarya University Journal of Science.

REFERENCES

[1] P. Linz, “Analytic and Numerical Methods for Volterra Equations”, SIAM, Philadelphia, Pa, USA, Pp 132-139, 1985.

[2] T. H. Christopher Baker, “Structure of recurrence relations in the study of stability in the numerical treatment of Volterra integral and integro-differential equation”, Journal of Integral Equations, 2 (1980) 11-29.

[3] R. Kanwall, K. Liu. “A Taylor expansion approach for solving integral equations”. International Journal of Mathematical Education in Science and Technology, 20 (2006), 411–414, 1989.

[4] S. Yuzbasi, N. Sahin, M. Sezer. “Bessel polynomial solutions of high-order linear Volterra integro-differential equations”. Computers & Mathematics with Applications, 62, 1940–1956, 2011.

[5] Jalil Rashidinia and Ali Tahmasebi “Approximate solution of linear integro-differential equations by using modified Taylor expansion method” World Journal of Modelling and Simulation, 9(4), 300, 2013.

[6] A. Avudainayagam, C. Vani, “Wavelet-Galerkin method for integro-differential equations”, Applied Numerical Mathematics, 32 (2000) 247-254.

[7] J. Rashidinia, A. Tahmasebi, “Approximate solution of linear integro-differential equations by using modified Taylor expansion method”, World Journal of Modelling and Simulation, 9 (4) (2013), 289-301.

[8] K. Maleknejad, F. Mirzaee and S. Abbasbandy, “Solving linear integro-differential equations system by using rationalized Haar functions method”, Applied Mathematical and Computation,155(2004), 317–328.

[9] S.Q. Wang and J.H. He, “Variational iteration method for solving integro-differential equations”, Phys. Lett. A, 367 (2007), 188-191.

[10] M. Mohseni Moghadam, H. Saeedi “Application of Differential Transforms for solving the Volterra Integro-Partial Differential Equations”, Iranian Journal of Science & Technology, Transaction A, Vol. 34, 2010

[11] J.H. He, “Homotopy perturbation technique”, Computation Meth. Appl. Mech. Eng., 178, 257-262 1999.

[12] P. Linz, “Linear multi step methods for Volterra integro-differential equations”, Journal of the ACM (JACM), 16 (1969), 295-301.

[13] Falade K.I “Solving Integro-Differential equations using exponentially fitted collocation approximate technique” Middle East Journal of Science 5(1) (2019), 73-85.

[14] Abdul-Majid Wazwaz. “Linear and Nonlinear Integral Equations Methods and Applications” Saint Xavier University Chicago, IL 60655 April 20, 2011 pp 65-72.

[15] Ramesh Kumar Vat, “M.SC. Mathematics MAL-644 Integral equation and symmetric kernel“ (2005) pp239-245.

[16] G. Adomian, “Solving Frontier problems of physics: The decomposition method” Kluwer Pp 123-134, 1994.

[17] K. Maleknejad and M. Hadizadeh, “A New computational method for Volterra-Fredholm integral equations”, Comput. Math. Appl., 37 (1999), 1–8.

SAKARYA ÜNİVERSİTESİ
FEN BİLİMLERİ ENSTİTÜSÜ
DERGİSİ

Sakarya University Journal of Science
SAUJS

e-ISSN 2147-835X Founded 1997 Period Bimonthly Publisher Sakarya University
http://www.saujs.sakarya.edu.tr/en/

Title: The Effect of Derived Features on Art Genre Classification with Machine Learning

Authors: Didem ABİDİN

Recieved: 2021-03-29 00:00:00

Accepted: 2021-10-07 00:00:00

Article Type: Research Article

Volume: 25
Issue: 6
Month: December
Year: 2021
Pages: 1275-1286

How to cite
Didem ABİDİN; (2021), The Effect of Derived Features on Art Genre Classification with Machine Learning. Sakarya University Journal of Science, 25(6), 1275-1286, DOI: https://doi.org/10.16984/saufenbilder.904964
Access link
http://www.saujs.sakarya.edu.tr/tr/pub/issue/66341/904964

Sakarya University Journal of Science 25(6), 1275-1286, 2021

The Effect of Derived Features on Art Genre Classification with Machine Learning

Didem ABİDİN*[1]

Abstract

Classification of the artwork according to their genres is being done for years. Although this process was used to be done by art experts before, now artificial intelligence techniques may help people manage this classification task. The algorithms used for classification are already improved, and now they can make classifications and predictions for any kind of genre classification. In this study, two different machine learning algorithms are used on an artwork dataset for genre classification. The primary purpose of this study is to show that the derived features about the artwork have a remarkable effect on correct genre classification. These features are derived from the metadata of the dataset. This metadata contains information about the nationalities and the period that the artist lived. Image filters are also applied to the images but the results show that applying only image filters on the dataset used in the study did not perform well. Instead, adding derived features extracted from the metadata increased the classification performances dramatically.

Keywords: genre classification, machine learning, Random Forest, J48.

List of Symbols and Abbreviations

Machine Learning	ML
Artificial Neural Networks	ANN
Deep Neural Networks	DNN
Support Vector Machines	SVM
Convolutional Neural Network	CNN
Random Forest	RF
Deep Learning	DL

1. INTRODUCTION

Genre classification is a very popular study on which researchers work on different data sets with growing amounts of data. These data may consist of numerical values as well as images. Artificial intelligence techniques have been widely used for genre classification for many years on these types of data. When dealing with image data, researchers also use various filtering methods to obtain better classification results. Machine Learning (ML) is a branch of artificial intelligence, which is used for data science applications on a formatted data. Among the ML techniques, Artificial Neural Networks (ANN) play an important role on the classification of image data. ANN can be defined as a simulation of the working principles of neurons in human body, that takes one input, processes it and gives an output while learning the data. ANN techniques are developed by applying hidden layers of neurons between the input and output layers to obtain more accurate results in learning process. Because of its high learning capability, it can be used in various application areas like classification [1], prediction [2][3], recognition in general (including pattern, handwriting

---

* Corresponding author: doktem@hotmail.com
[1] Manisa Celal Bayar University, Faculty of Engineering, Computer Engineering
ORCID: https://orcid.org/0000-0001-5966-7537

recognition) [4] and so on. ANN with more than three hidden layers between input and output layers is called Deep Neural Networks (DNN). Although the use of deep learning techniques for the processing and classification of visual data is becoming widespread, other ML techniques can still be used on visual data, and many ML algorithms can yield efficient results. In particular, the application of image filters on visual data makes the data ready for a classification problem application. In addition to filters, textual or numerical data that can be obtained from images also contribute to successful classification. The data that can be extracted from the images can be called as "derived features" and this study aimed to show that more efficient genre classification is possible on a data set where image filtering is used together with calculated fields. The values of the calculated fields can easily be included to the image filters' data and they together generate a stronger input to train any ML algorithm in use.

The layout of the paper is as follows: Section 2 explains the related work listed in literature about art genre classification, where Section 3 explains the proposed methodology with the details of the dataset used. Section 4 gives the results for the experiments of the study and Section 5 is the conclusion.

2. RELATED WORK

Machine Learning has been a very popular classification technique for the past two decades. Using ML algorithms in art genre classification is equally popular as other application areas of ML. below, some studies related with art genre classification with ML algorithms are listed. [5] studied on art genre classification for five genres of paintings (abstract expressionism, cubism, impressionism, popart and realism) and used Naïve Bayes [6], k-Nearest Neighbor [7], ANN [8], Support Vector Machines (SVM) [9] and AdaBoost [10] algorithms. The best performing algorithm appeared to be the AdaBoost with 68.3% accuracy.

In some studies, self-organizing maps are used for art genre classification. For example, [11] proposed a methodology that classifis painting styles by extracting some features from the paintings. They achieved their goal by using self-organizing maps. Another study extracted the light, line and color features and classified the art paintings by using k-Nearest Neigbor [12]. In this study, self-organizig maps also took place in the analysis of the classification process. [13] used dual-tree complex wavelet transforms and Hidden Markov Trees for the stylistic analysis of the paintings, where [14] used Genetic Algorithm (GA), to classify paintings into two and three classes. They used nearest neighbor algorithm for the training step and obtained better solutions than a classical nearest neighbor algorithm. In another study, a method to recognize painters having styles Impressionism, Expressionism, and Surrealism as a genre is proposed [15]. A study that derives features from a deep Convolutional Neural Network (CNN) obtained a performance of 77.57% in the classification of seven genre categories [16]. [17] worked on classification of fine-art paintings by using SVM and CNN [18]. They worked on the performances of different visual features in fine-art paintings. [19] worked on the classification of paintings with CNN and they were successful on the discovery of over 250,000 new object annotations across 93,000 paintings.

In a relatively new study compared to the above-mentioned studies, [20] handled the classification of painting styles problem with transfer learning. In [21], they used CNN the classification of the paintings and also used the timeframe feature as done in our study.

Some recent studies used DNN to classify the styles in paintings like [22], where they obtained successful results in a large scale collection of paintings. [23]worked on Wikipaintings dataset with 25 different styles. They used DNN to perform a classification with an accuracy of 62%. [24] trained and classified fine-art paintinds with Deep Convolutional Neural Network. They used three different pretrained CNNs and three of them showed a remarkable improvement over the others.

In the studies listed, very few of them have dealt with deriving calculated fields for the art paintings datasets. This study focuses on the importance of derived features in genre classification.

3. PROPOSED METHODOLOGY

3.1. The Dataset

The dataset used contains artworks of 50 artists with 8355 pieces in total. It has been obtained from Kaggle [25] with a .csv file with the artist's information. This file contains the following columns: Id, name, years (birth-death), genre, nationality, bio (biography), Wikipedia (Wikipedia link), and paintings (number of paintings in the dataset). There are 21 genres in the dataset which are listed as: Abstract expressionism, Baroque, Byzantine art, Cubism, Early Renaissance, Expressionism, High Renaissance, Impressionism, Mannerism, Neoplasticism, Northern Renaissance, Pop art, Post-impressionism, Primitivism, Proto-Renaissance, Realism, Romanticism, Social Realism, Suprematism, Surrealism and Symbolism. The .csv file for artist information is given in Figure 1.

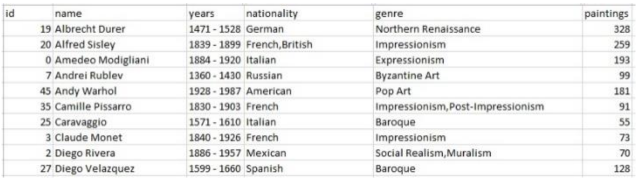

id	name	years	nationality	genre	paintings
19	Albrecht Durer	1471 - 1528	German	Northern Renaissance	328
20	Alfred Sisley	1839 - 1899	French,British	Impressionism	259
0	Amedeo Modigliani	1884 - 1920	Italian	Expressionism	193
7	Andrei Rublev	1360 - 1430	Russian	Byzantine Art	99
45	Andy Warhol	1928 - 1987	American	Pop Art	181
35	Camille Pissarro	1830 - 1903	French	Impressionism,Post-Impressionism	91
25	Caravaggio	1571 - 1610	Italian	Baroque	55
3	Claude Monet	1840 - 1926	French	Impressionism	73
2	Diego Rivera	1886 - 1957	Mexican	Social Realism,Muralism	70
27	Diego Velazquez	1599 - 1660	Spanish	Baroque	128

Figure 1 Artists.csv file

The artworks are given in 50 folders for 50 artists and the resized files are also available for the same paintings in another folder. In this study, the resized files are used.

3.2. Data Preprocessing

Classification algorithms are executed on the dataset in the WEKA environment [26]. WEKA can use .arff file format and the preprocessing steps on the data to be used for classification are given below:

Generating the initial .arff file: For image filtering, two main attributes are needed for the instances in the .arff file. These attributes are the file name and class information. In addition to the aforementioned columns, year, nationality and genre columns are added for every instance in the dataset to be used after the filtering process. To add these columns, the artist.csv file is used. In this file, year, nationality and genre columns are first converted to encoded values with Python using LabelEncoder library [27]. This is done to give numeric values to categorical features. The source code and the numeric values for year, nationality, and genre fields are given in Figure 2 below.

```
In [5]:
from sklearn.preprocessing import LabelEncoder
var_mod = ['years','genre','nationality']
le = LabelEncoder()
for i in var_mod:
    df[i] = le.fit_transform(df[i])
df.dtypes

df
```

Out[5]:

	id	name	years	genre	nationality	bio
0	0	Amedeo Modigliani	5	5	8	Amedeo Cl (Italian pror
1	1	Vasiliy Kandinskiy	5	5	11	Wassily W Kandinsky
2	2	Diego Rivera	5	17	9	Diego Marí Juan Nepo
3	3	Claude Monet	5	7	6	Oscar-Clau [klod mɔnɛ]
4	4	Rene Magritte	5	19	2	René Fran Magritte (Fr

Figure 2 Artists.csv file after LabelEncoder

The meanings of encoded values for genres and nationalities are given in Table 1 and Table 2 respectively.

Table 1 Genre encoding

No	Genre
0	Abstract Expressionism
1	Baroque
2	Byzantine Art
3	Cubism
4	Early Renaissance
5	Expressionism
6	High Renaissance
7	Impressionism
8	Mannerism
9	Neoplasticism
10	Northern Renaissance
11	Pop Art
12	Post-impressionism
13	Primitivism

14	Proto-Renaissance
15	Realism
16	Romanticism
17	Social Realism
18	Suprematism
19	Surrealism
20	Symbolism

Table 2 Nationality encoding

No	Nationality
1	Austrian
2	Belgian
3	British
4	Dutch
5	Flemish
6	French
7	German
8	Italian
9	Mexican
10	Norwegian
11	Russian
12	Spanish

Detecting artists' era: The years attribute is encoded according to the timeframes which the artists had lived and it has values from 0 to 30. The period from 1275 to 2000, including the life periods of all artists, is divided into 25 years' timeframes and every timeframe is encoded. Then the timeframes corresponding to the birth and death dates of the artists are represented with two numeric values for more accuracy. The timeframe encoding is done according to the scale shown in Figure 3. For example, the birth and death dates of Pablo Picasso (1881-1973) fall into timeframes 25-28.

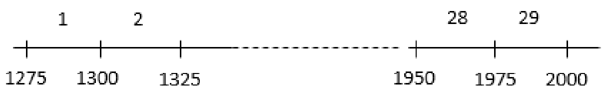

Figure 3 The timeframe scale

Adding derived features: To add these three encoded columns to .arff file, a small Java program is implemented. For every artist, the derived year, nationality, and genre data is read from .csv file to initial .arff file. The final .arff file is given in Figure 4 with *borns*, *dies*, and *nationality* attributes. Genre is already represented with the class column.

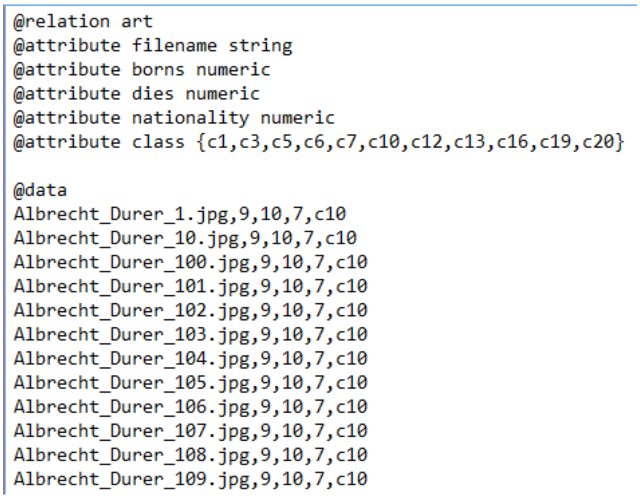

```
@relation art
@attribute filename string
@attribute borns numeric
@attribute dies numeric
@attribute nationality numeric
@attribute class {c1,c3,c5,c6,c7,c10,c12,c13,c16,c19,c20}

@data
Albrecht_Durer_1.jpg,9,10,7,c10
Albrecht_Durer_10.jpg,9,10,7,c10
Albrecht_Durer_100.jpg,9,10,7,c10
Albrecht_Durer_101.jpg,9,10,7,c10
Albrecht_Durer_102.jpg,9,10,7,c10
Albrecht_Durer_103.jpg,9,10,7,c10
Albrecht_Durer_104.jpg,9,10,7,c10
Albrecht_Durer_105.jpg,9,10,7,c10
Albrecht_Durer_106.jpg,9,10,7,c10
Albrecht_Durer_107.jpg,9,10,7,c10
Albrecht_Durer_108.jpg,9,10,7,c10
Albrecht_Durer_109.jpg,9,10,7,c10
```

Figure 4 .arff file with birth, death, nationality and genre data

Applying image filters: Filtering is applied to transform pixel intensity values of images to obtain some numeric data [28]. By doing so, features are extracted from image data and this data is written to the dataset. The arff files generated are used as input in WEKA and several algorithms are used to find the best performing one in classifying the paintings by genre. In [29], the best image filter combination to classify art images was found as the combination of EdgeHistogramFilter [30] and SimpleColorHistogramFilter [31]. EdgeHistogramFilter focuses on the edges of an image and takes shape information of the image into consideration for image indexing [32]. SimpleColorHistogramFilter extracts color histogram features. It has three histograms for red, green and blue, each one having 32 bins. Each bin has the count of pixels that fall to that bin. These two image filters are applied on .arff files and image filter data is merged with existing and derived columns. The .arff file after applying image filters is given in Figure 5. The same filter combination is applied to both versions of the data used in this study.

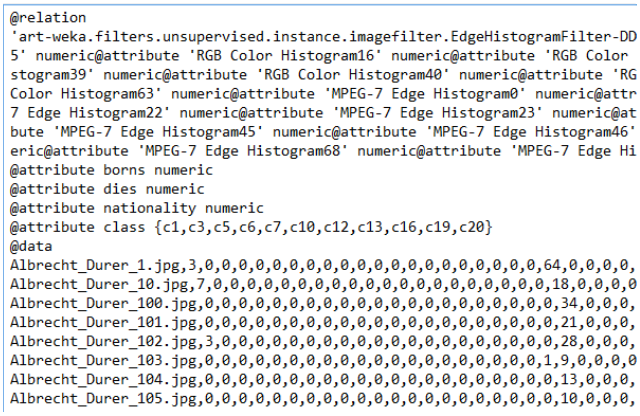

```
@relation
'art-weka.filters.unsupervised.instance.imagefilter.EdgeHistogramFilter-DD
5' numeric@attribute 'RGB Color Histogram16' numeric@attribute 'RGB Color
stogram39' numeric@attribute 'RGB Color Histogram40' numeric@attribute 'RG
Color Histogram63' numeric@attribute 'MPEG-7 Edge Histogram0' numeric@attr
7 Edge Histogram22' numeric@attribute 'MPEG-7 Edge Histogram23' numeric@at
bute 'MPEG-7 Edge Histogram45' numeric@attribute 'MPEG-7 Edge Histogram46'
eric@attribute 'MPEG-7 Edge Histogram68' numeric@attribute 'MPEG-7 Edge Hi
@attribute borns numeric
@attribute dies numeric
@attribute nationality numeric
@attribute class {c1,c3,c5,c6,c7,c10,c12,c13,c16,c19,c20}
@data
Albrecht_Durer_1.jpg,3,0,0,0,0,0,0,0,0,0,0,0,0,0,0,0,0,0,0,0,0,64,0,0,0,0,
Albrecht_Durer_10.jpg,7,0,0,0,0,0,0,0,0,0,0,0,0,0,0,0,0,0,0,0,0,18,0,0,0,0
Albrecht_Durer_100.jpg,0,0,0,0,0,0,0,0,0,0,0,0,0,0,0,0,0,0,0,0,0,34,0,0,0,
Albrecht_Durer_101.jpg,0,0,0,0,0,0,0,0,0,0,0,0,0,0,0,0,0,0,0,0,0,21,0,0,0,
Albrecht_Durer_102.jpg,3,0,0,0,0,0,0,0,0,0,0,0,0,0,0,0,0,0,0,0,0,28,0,0,0,
Albrecht_Durer_103.jpg,0,0,0,0,0,0,0,0,0,0,0,0,0,0,0,0,0,0,0,0,1,9,0,0,0,0
Albrecht_Durer_104.jpg,0,0,0,0,0,0,0,0,0,0,0,0,0,0,0,0,0,0,0,0,0,13,0,0,0,
Albrecht_Durer_105.jpg,0,0,0,0,0,0,0,0,0,0,0,0,0,0,0,0,0,0,0,0,0,10,0,0,0,
```

Figure 5 .arff file with image filters applied

The artists and the number of paintings they have in the dataset are given in Table 3. Among these, the ones that have paintings from the rarest genres (shaded ones in Table 1) are excluded and 39 artists' paintings are used. The excluded artists are also shown in shades in the table.

Table 3 Artists and the number of paintings

Name	**paintings**
Albrecht Durer	328
Alfred Sisley	259
Amedeo Modigliani	193
Andrei Rublev	99
Andy Warhol	181
Camille Pissarro	91
Caravaggio	55
Claude Monet	73
Diego Rivera	70
Diego Velazquez	128
Edgar Degas	702
Edouard Manet	90
Edvard Munch	67
El Greco	87
Eugene Delacroix	31
Francisco Goya	291
Frida Kahlo	120
Georges Seurat	43
Giotto di Bondone	119
Gustav Klimt	117
Gustave Courbet	59
Henri de Toulouse-Lautrec	81
Henri Matisse	186
Henri Rousseau	70
Hieronymus Bosch	137
Jackson Pollock	24
Jan van Eyck	81
Joan Miro	102
Kazimir Malevich	126
Leonardo da Vinci	143
Marc Chagall	239
Michelangelo	49
Mikhail Vrubel	171
Pablo Picasso	439
Paul Cezanne	47
Paul Gauguin	311
Paul Klee	188
Peter Paul Rubens	141
Pierre-Auguste Renoir	336
Piet Mondrian	84
Pieter Bruegel	134
Raphael	109
Rembrandt	262
Rene Magritte	194
Salvador Dali	139
Sandro Botticelli	164
Titian	255
Vasiliy Kandinsky	88
Vincent van Gogh	877
William Turner	66

3.3. Input Data

The input dataset contains the following columns:

- Attributes of SimpleColorHistogram (64 columns)
- Attributes of EdgeHistogram (80 columns)
- borns: It is the corresponding 25-year interval (timeframe) in which the artist's date of birth coincides (values from 1 to 30).
- dies: It is the corresponding 25-year interval (timeframe) in which the artist's date of death coincides (values from 1 to 30).
- nationality: Encoding values given in Table 2.

Class column is the output for the proposed system. Genre encoding values are given in Table 1. Additionally, image filters' features are added to the dataset automatically when any of the filters are applied in WEKA.

3.4. Proposed System

To classify artworks into genres, supervised learning techniques are used. In supervised techniques, the class information for every instance is given to the algorithm and the algorithm "learns" and generates a model with this data on the training set. Later, the generated model is used for testing. Among all ML algorithms, this study uses Random Forest (RF) and J48 algorithms.

RF builds many classification trees as a forest of random decision trees [33] and these trees are then merged to obtain a more accurate prediction. Each tree uses a specific subset of the input features. Each tree outputs a classification (vote) and the algorithm chooses the one having most votes among all the trees in the forest [34]. As the number of trees in the forest increases, the generalization error for the forests converges to a limit value. This error value depends on the strength of the individual trees in the forest and the correlation between them [35]. RF algorithms can be used for both classification and regression problems. It adds additional randomness to the model while the trees grow. It searches for the best feature among a subset of features selected randomly. This means a wide diversity that generally results in a better model [36].

ID3 was the first version of the C4.5 algorithm of Quinlan [37] and J48 [38] is the Java implementation of C4.5 [39]. C4.5 is a classifier that accepts nominal classifiers and can use both discrete and continuous attributes. Also training data with missing attribute values is accepted. J48 adds some more features to C4.5 like processing for missing values, decision tree pruning, continuous attribute value ranges, and derivation of rules. C4.5 classifiers are also considered as decision trees and they can construct classifiers in a more comprehensible rule set form [40].

After the preprocessing step for the dataset is completed, it is used for executing classification algorithms.

4. EXPERIMENTAL RESULTS

The results were obtained for two versions of the dataset. In the first version (V1), all 50 artists from 21 genres were included. In the second version (V2) rare genres and their instances were excluded since they have very few examples. V2 dataset has 39 artists from 11 genres. These 11 genres are Baroque, Cubism, Early Renaissance, Expressionism, High Renaissance, Impressionism, Northern Renaissance, Post-impressionism, Primitivism, Romanticism, Surrealism and Symbolism. The genres which are already in the original dataset but not included in the second version are shaded in grey in Table 1. Table 4 shows the properties of both versions of the dataset for comparison.

Table 4 Artists and the number of paintings

	V1	**V2**
# genres	21	11
# instances	8355	7252
# artists	50	39
# attributes	148	148
Image filters	EdgeHistogram SimpleColorHistogram	EdgeHistogram SimpleColorHistogram
Algorithms	RF J48	RF J48

For both versions of datasets, the same image filters and the same classification algorithms were used. Among the classification algorithms, RF and J48 had the best performances.

RF and J48 results for dataset V1 are given in Table 5 and Table 6 and RF and J48 results for dataset V2 are given in Table 7 and Table 8 respectively.

Table 5 RF Results for V1

Time taken to build model : 6.76 seconds
Correctly Classified Instances: 82.9823 %
Kappa statistic : 0.8101
Mean absolute error : 0.0557
Root mean squared error : 0.1455
Relative absolute error : 64.3106 %
Root relative squared error : 69.9367 %
Total Number of Instances : 8355

Precision	Recall	F-Measure	Class
0.629	0.676	0.975	c0
0.928	0.923	0.998	c1
0.857	0.863	0.997	c2
0.855	0.849	0.997	c3
0.477	0.548	0.993	c4
0.835	0.827	0.992	c5
0.857	0.853	0.997	c6
0.827	0.793	0.982	c7
0.709	0.727	0.999	c8
0.473	0.554	0.985	c9
0.921	0.914	0.985	c10
0.84	0.845	0.996	c11
0.896	0.882	0.988	c12
0.761	0.754	0.975	c13
0.91	0.911	0.997	c14
0.183	0.315	0.982	c15
0.959	0.957	1	c16
0.289	0.396	0.984	c17
0.564	0.609	0.988	c18
0.795	0.785	0.983	c19
0.708	0.704	0.972	c20
0.83	0.816	0.811	W. Avg.

Table 6 J48 Results for V1

Number of Leaves :155
Size of the tree : 309
Time taken to build model : 0.92 seconds
Correctly Classified Instances : 94.6386 %
Kappa statistic : 0.941
Mean absolute error : 0.0056
Root mean squared error : 0.0696
Relative absolute error : 6.4555 %
Root relative squared error : 33.4437 %
Total Number of Instances : 8356

Precision	Recall	F-Measure	Class
1	1	1	c0
1	1	1	c1
1	1	1	c2
1	1	1	c3
1	1	1	c4
1	1	1	c5
1	1	1	c6
0.877	0.847	0.938	c7
1	1	1	c8
1	1	1	c9
1	1	1	c10
1	1	1	c11
0.963	0.957	0.983	c12
0.892	0.886	0.96	c13
1	1	1	c14
0.868	0.865	0.977	c15
1	1	1	c16
1	1	1	c17
1	1	1	c18
1	1	1	c19
0.766	0.748	0.905	c20
0.946	0.946	0.938	W. Avg.

Table 7 RF Results for V2

Time taken to build model : 11.59 seconds
Correctly Classified Instances : 88.7204 %
Kappa statistic : 0.8709
Mean absolute error : 0.0941
Root mean squared error : 0.1831
Relative absolute error : 58.6993 %
Root relative squared error : 64.681 %
Total Number of Instances : 7252

Precision	Recall	F-Measure	Class
0.943	0.939	0.998	c1
0.915	0.91	0.998	c3
0.888	0.88	0.995	c5
0.978	0.977	0.999	c6
0.867	0.832	0.983	c7
0.92	0.912	0.988	c10
0.91	0.895	0.99	c12
0.824	0.824	0.977	c13
0.956	0.954	1	c16
0.844	0.836	0.99	c19
0.716	0.713	0.972	c20
0.887	0.885	0.872	W. Avg.

Table 8 J48 Results for V2

Number of Leaves : 144
Size of the tree : 287
Time taken to build model : 1.09 seconds
Correctly Classified Instances : 94.2774 %
Kappa statistic : 0.9351
Mean absolute error : 0.0114
Root mean squared error : 0.0983
Relative absolute error : 7.1129 %
Root relative squared error : 34.7342 %
Total Number of Instances : 7252

Precision	Recall	F-Measure	Class
1	1	1	c1
1	1	1	c3
1	1	1	c5
1	1	1	c6
0.886	0.853	0.947	c7
1	1	1	c10
0.964	0.958	0.985	c12
0.884	0.877	0.957	c13
1	1	1	c16
1	1	1	c19
0.767	0.746	0.911	c20
0.943	0.943	0.932	W. Avg.

The confusion matrices for the best performing algorithm on V1 and V2 are given in Table 9 and Table 10 below respectively. The confusing genres are marked in grey on both tables.

Table 9 Confusion Matrix for V1 with J48 Algorithm

c0	**c1**	**c2**	**c3**	**c4**	**c5**	**c6**	**c7**	**c8**	**c9**	**c10**	**c11**	**c12**	**c13**	**c14**	**c15**	**c16**	**c17**	**c18**	**c19**	**c20**	
24	0	0	0	0	0	0	0	0	0	0	0	0	0	0	0	0	0	0	0	0	**c0**
0	495	0	0	0	0	0	0	0	0	0	0	0	0	0	0	0	0	0	0	0	**c1**
0	0	99	0	0	0	0	0	0	0	0	0	0	0	0	0	0	0	0	0	0	**c2**
0	0	0	439	0	0	0	0	0	0	0	0	0	0	0	0	0	0	0	0	0	**c3**
0	0	0	0	164	0	0	0	0	0	0	0	0	0	0	0	0	0	0	0	0	**c4**
0	0	0	0	0	469	0	0	0	0	0	0	0	0	0	0	0	0	0	0	0	**c5**
0	0	0	0	0	0	556	0	0	0	0	0	0	0	0	0	0	0	0	0	0	**c6**
0	0	0	0	0	0	0	1458	0	0	0	0	22	23	0	18	0	0	0	0	126	**c7**
0	0	0	0	0	0	0	0	87	0	0	0	0	0	0	0	0	0	0	0	0	**c8**
0	0	0	0	0	0	0	0	0	84	0	0	0	0	0	0	0	0	0	0	0	**c9**
0	0	0	0	0	0	0	0	0	0	748	0	0	0	0	0	0	0	0	0	0	**c10**
0	0	0	0	0	0	0	0	0	0	0	181	0	0	0	0	0	0	0	0	0	**c11**
0	0	0	0	0	0	0	32	0	0	0	0	1005	7	0	0	0	0	0	0	4	**c12**
0	0	0	0	0	0	0	40	0	0	0	0	6	376	0	0	0	0	0	0	7	**c13**
0	0	0	0	0	0	0	0	0	0	0	0	0	0	119	0	0	0	0	0	0	**c14**
0	0	0	0	0	0	0	21	0	0	0	0	0	0	0	128	0	0	0	0	0	**c15**
0	0	0	0	0	0	0	0	0	0	0	0	0	0	0	0	388	0	0	0	0	**c16**
0	0	0	0	0	0	0	0	0	0	0	0	0	0	0	0	0	70	0	0	0	**c17**
0	0	0	0	0	0	0	0	0	0	0	0	0	0	0	0	0	0	126	0	0	**c18**
0	0	0	0	0	0	0	0	0	0	0	0	0	0	0	0	0	0	0	435	0	**c19**
0	0	0	0	0	0	0	127	0	0	0	0	7	8	0	0	0	0	0	0	457	**c20**

Table 10 Confusion Matrix for V1 with J48 Algorithm

c1	**c3**	**c5**	**c6**	**c7**	**c10**	**c12**	**c13**	**c16**	**c19**	**c20**	
495	0	0	0	0	0	0	0	0	0	0	**c1**
0	439	0	0	0	0	0	0	0	0	0	**c3**
0	0	469	0	0	0	0	0	0	0	0	**c5**
0	0	0	556	0	0	0	0	0	0	0	**c6**
0	0	0	0	1468	0	27	28	0	0	124	**c7**
0	0	0	0	0	747	0	0	0	0	0	**c10**
0	0	0	0	28	0	1008	6	0	0	6	**c12**
0	0	0	0	41	0	6	373	0	0	9	**c13**
0	0	0	0	0	0	0	0	388	0	0	**c16**
0	0	0	0	0	0	0	0	0	435	0	**c19**
0	0	0	0	129	0	3	8	0	0	459	**c20**

Image filters on their own did not perform well for the two datasets. However, with the addition of the derived features, the classification process became more significant. Table 11 and Table 12 show the classification performances with only the image filters, and the image filters together with the derived features for both datasets.

Table 11 Classification performances without/with derived features in V1

Condition	Algorithm	Performance (%)
Only Filters	RF	42.13
	J48	26.24
Filters + derived features	RF	82.63
	J48	94.63

Table 12 Classification performances without/with derived features in V2

Condition	Algorithm	Performance (%)
Only Filters	RF	47.13
	J48	21.67
Filters + derived features	RF	88.18
	J48	94.27

5. CONCLUSION AND DISCUSSION

In this study, the art genre classification with ML algorithms is done by using derived features of the artwork in the dataset with the best performing image filters. Here, not the images, but the information about the images is in question, that is why no CNN or DL techniques are used. Instead, classical ML algorithms were enough to make proper classification on image data including.the derived features.

The two version of the same dataset is used in two different sizes, one with 21 different genres of work and the smaller one with 11 genres of artwork image data. Some of these genres are close to each other in terms of the time period they were used. One genre may be following the other one as a slight developed/transformed version of the previous. For this reason, it is possible to confuse the genres of some othe pieces in the dataset. The most confusing genres are identified as symbolism, impressionism, and post-impressionism.

Although reducing the number of genres affects the performance in a positive way for both of the algorithms, this effect is more evident for RF. On both datasets, J48 performs better than RF, but the size of the dataset does not affect the performance of J48. With V1, as the greater dataset, the performance is measured as 95.81%; where it is 95.34% with V2. Less number of genres and fewer attributes do not affect the performance. Contrarily, more instances in the dataset played a positive role in the accuracy of the result.

What is meant to be emphasized here, together with the best performance values obtained for the proposed system, are the performance values obtained for the genres that are more difficult to classify. For example, symbolism genre has emerged as the one with the worst performance value among genres confused with each other for both data sets. 70.8%, which is the worst performance value for this genre, is not a bad performance value when compared with the art genre classification studies in the literature.

Funding

The author has no received any financial support for the research, authorship or publication of this study.

The Declaration of Conflict of Interest/ Common Interest

No conflict of interest or common interest has been declared by the authors.

Authors' Contribution

The author contributed 100%.

The Declaration of Ethics Committee Approval

This study does not require ethics committee permission or any special permission.

The Declaration of Research and Publication Ethics

The authors of the paper declare that they comply with the scientific, ethical and quotation rules of SAUJS in all processes of the paper and that they do not make any falsification on the data collected. In addition, they declare that Sakarya University Journal of Science and its editorial board have no responsibility for any ethical violations that may be encountered, and that this study has not been evaluated in any academic publication environment other than Sakarya University Journal of Science.

In addition, the RESEARCH AND PUBLICATION ETHICS DECLARATION FORM regarding this statement should be signed by the corresponding author and uploaded as an additional file when submitting the article.

REFERENCES

[1] Sengupta, N., Sahidullah, M., Saha, G., 2016. "Lung sound classification using cepstral-based statistical features". Computers in Biology and Medicine. Vol. 75(1), pp.118–129. doi:10.1016/j.compbiomed.2016.05.013.

[2] Işık, E., İnallı, M., 2018. “Artificial neural networks and adaptive neuro-fuzzy inference systems approaches to forecast the meteorological data for HVAC: The case of cities for Turkey”. Energy, Vol. 154, pp. 7-16.

[3] Işık, E., İnallı, M., Celik, E., 2019. “ANN and ANFIS Approaches to Calculate the Heating and Cooling Degree Day Values: The Case of Provinces in Turkey”. Arab J Sci Eng, Vol.44, pp. 7581–7597. https://doi.org/10.1007/s13369-019-03852-4.

[4] Maitra, D.S., Bhattacharya, U., Parui, S.K., 2015. "CNN based common approach to handwritten character recognition of multiple scripts". 13th International Conference on Document Analysis and

Recognition (ICDAR), pp. 1021–1025. doi:10.1109/ICDAR.2015.7333916.

[5] Zujovic, J., Gandy, L., Friedman, S., Pardo, B., Pappas, T. N., 2009, “Classifying paintings by artistic genre: An analysis of features & classifiers”, 2009 IEEE International Workshop on Multimedia Signal Processing, 5-7 Oct. 2009, Rio de Janeiro, Brazil. DOI: 10.1109/MMSP.2009.5293271.

[6] Bayes, M., Price, M., 1763, "An Essay Towards Solving a Problem in The Doctrine of Chances. By the Late Rev. Mr. Bayes, F. R. S. Communicated by Mr. Price, in a Letter to John Canton, A. M. F. R. S.", Philosophical Transactions, Vol. 53, pp. 370–418.

[7] Fix, E., Hodges, J. L., 1951, “Discriminatory Analysis. Nonparametric Discrimination: Consistency Properties” USAF School of Aviation Medicine, Randolph Field, Texas.

[8] Caudill, M., 1989, "Neural Network Primer: Part I", AI Expert

[9] Cortes, C., Vapnik, V., 1995, "Support Vector Networks", Machine Learning, Vol. 20, pp. 273-297.

[10] Kégl, B., 2013, "The return of AdaBoost.MH: multi-class Hamming trees". arXiv:1312.6086.

[11] Lee, S. G., Cha, E. Y., 2016, “Style classification and visualization of art painting’s genre using self-organizing maps”, Human-Centric Computing and Information Sciences, 6:07. DOI: 10.1186/s13673-016-0063-4.

[12] Lombardi, T. E., 2005, “The classification of style in fine-art painting”, PhD thesis, Pace University, New York.

[13] Jafarpour, S., Polatkan, G., Brevdo, E., Hughes, S., Brasoveanu, A., Daubechies, I., 2009, "Stylistic analysis of paintings using wavelets and machine learning," In 17th European Signal Processing Conference, pp. 1220–1224.

[14] Levy, E., David, O., Netanyahu, N. S., 2013, “Painter Classification Using Genetic Algorithms”, 2013 IEEE Congress on Evolutionary Computation, pp. 3027-3034, June 20-23, Cancún, México.

[15] Shamir, L., Macura, T., Orlov, N., Eckley, D.M., Goldberg, I.G., 2010, “Impressionism, expressionism, surrealism: automated recognition of painters and schools of art”, Transact Appl Percept 7:8.

[16] Cetinic, E., Grgic, S., 2016, “Genre Classification of Paintings”, Proceedings of 58th International Symposium ELMAR, pp. 201-204, 12-14 September 2016, Zadar, Croatia.

[17] Saleh, B., Elgammal, A., 2015, “Large-scale Classification of Fine-Art Paintings: Learning The Right Metric on The Right Feature”, arXiv:1505.00855. DOI: 10.11588/dah.2016.2.23376.

[18] Fukushima, K., 2007, "Neocognitron", Scholarpedia, 2(1), 1717. DOI:10.4249/scholarpedia.1717.

[19] Crowley, E. J., 2016, “Visual Recognition in Art using Machine Learning”, PhD Thesis, Department of Engineering Science, University of Oxford.

[20] Oomen, E., 2018, “Classification of painting style with transfer learning”, Master Thesis, School of Humanities and Digital Science of Tilburg University, Tilburg, The Netherlands.

[21] Zhao, W., Zhou, D., Qiu, X., Jiang, W., 2021, “How to Represent Paintings: A Painting Classification Using Artistic Comments”, Sensors, 21, 1940. https://doi.org/10.3390/s21061940.

[22] Bar, Y., Levy, N., Wolf, L., “Classication of Artistic Styles using Binarized Features

Derived from a Deep Neural Network", 2015, Workshop at the European Conference on Computer Vision. DOI: 10.1007/978-3-319-16178-5_5.

[23] Lecoutre, A., Negrevergne, B, Yger, F., 2017, "Recognizing Art Style Automatically in painting with deep learning", Proceedings of Machine Learning Research, 77, pp. 327-342.

[24] Sandoval, C., Pirogova, E., Lech, A. M., 2019, "Two-Stage Deep Learning Approach to the Classification of Fine-Art Paintings", IEEE Access, 7. DOI: 10.1109/ACCESS.2019.2907986.

[25] Kaggle, Best Artworks of All Time, https://www.kaggle.com/ikarus777/best-artworks-of-all-time. Accessed 08.10.2019.

[26] Hall, M., Frank, E., Holmes, G., Pfahringer, B., Reutemann, P., Witten, I. H., 2009, "The WEKA data mining software: An update," SIGKDD Explorations, vol. 11, 2009. http://www.cs.waikato.ac.nz/ml/weka/

[27] SciKit Learn, Label Encoder, https://scikit-learn.org/stable/modules/generated/sklearn.preprocessing.LabelEncoder.html. Accessed 10.10.2019.

[28] Voutsakis, E., Petrakis, E.G.M., and Milios, E. 2006. IntelliSearch: Intelligent Search for Images and Text on the Web. In Proceedings of International Conference on Image Analysis and Recognition (Povoa de Varzim, Portugal, September 18-20, 2006). ICIAR 2006, 697-708.

[29] Abidin, D., "Effects of Image Filters on Various Image Datasets". Proceedings of the 2019 5th International Conference on Computer and Technology Applications. April 2019. Pages 1–5. https://doi.org/10.1145/3323933.3324056

[30] Balasubramani, R., Kannan, V., 2009, "Efficient use of MPEG-7 Color Layout and Edge Histogram Descriptors in CBIR Systems", Global Journal of Computer Science and Technology. 9, 5 (2009), 157-163.

[31] SimpleColorHistogramFilter, WEKA unsupervised instance image filter, URL:https://github.com/mmayo888/ImageFilter/blob/master/ImageFilter/src/weka/filters/unsupervised/instance/imagefilter/SimpleColorHistogramFilter.java.

[32] Shim S. O., Choi, T. S., 2002, "Edge color histogram for image retrieval", In Proceedings of International Conference on Image Processing (Rochester, NY, USA, September 22-25, 2002). IEEE, pp. 957-960. DOI: 10.1109/ICIP.2002.1037942.

[33] Ho, T. K., 1995, "Random Decision Forests". Proceedings of the 3rd International Conference on Document Analysis and Recognition, 278-282, Montreal, QC, Canada.

[34] Fontana, F.A., Mäntylä, M.V., Zanoni, M., Marino, A., 2016, "Comparing and Experimenting Machine Learning Techniques for Code Smell Detection", Empirical Software Engineering, Vol. 21, pp. 1143-1191.

[35] Breiman, L., 2001, "Random Forests". Machine Learning, 5–32. doi: 10.1023/A:1010933404324.

[36] Donges N., 2018, "The Random Forest Algorithm". https://machinelearning-blog.com/2018/02/06/the-random-forest-algorithm/#more-375 (03.09.2018).

[37] Quinlan, J. R., 1986, "Induction of Decision Trees". Machine Learning 1, 81-106.

[38] Witten, L. H., Frank, E., 2005, Data Mining: Practical Machine Learning Tools and Techniques. 2nd ed. San Francisco, USA. Morgan Kaufmann Publishers.

[39] Quinlan, J. R., 1993, C4.5 Programs for Machine Learning. San Francisco, USA. Morgan Kaufmann Publishers.

[40] Salama, A. A., Eisa, M., ELhafeez, S. A., Lotfy, M. M., 2015, “Review of Recommender Systems Algorithms Utilized in Social Networks based e-Learning Systems & Neutrosophic System”, Neutrosophic Sets and Systems, Vol. 8, pp. 33.

SAKARYA ÜNİVERSİTESİ

FEN BİLİMLERİ ENSTİTÜSÜ
DERGİSİ

Sakarya University Journal of Science
SAUJS

e-ISSN 2147-835X Founded 1997 Period Bimonthly Publisher Sakarya University
http://www.saujs.sakarya.edu.tr/en/

Title: In-Plane Buckling of Open-section Shell Segments

Authors: Haluk YILMAZ, İbrahim KOCABAŞ

Recieved: 2021-03-08 00:00:00

Accepted: 2021-10-11 00:00:00

Article Type: Research Article

Volume: 25
Issue: 6
Month: December
Year: 2021
Pages: 1287-1294

How to cite
Haluk YILMAZ, İbrahim KOCABAŞ; (2021), In-Plane Buckling of Open-section Shell Segments. Sakarya University Journal of Science, 25(6), 1287-1294, DOI: https://doi.org/10.16984/saufenbilder.893343
Access link
http://www.saujs.sakarya.edu.tr/tr/pub/issue/66341/893343

Sakarya University Journal of Science 25(6), 1287-1294, 2021

In-Plane Buckling of Open-section Shell Segments

Haluk YILMAZ*[1], İbrahim KOCABAŞ[1]

Abstract

The present study investigates elastic buckling behavior of open-section shell segments under action of a central radial load. A design parameter is expressed to characterize the influence of fillet radius on load-bearing capacity. A reduction factor equation is developed as a multivariate function of shell parameters, which evaluates the amount of decrease in load-bearing capacity of the structure caused by the corner fillet. In addition, an expression to predict limit load of the shell structure under clamped end conditions is introduced. Furthermore, a parametric study is performed to reveal the influence of fillet radius and radius-to-thickness ratio on the limit load as well as deformation patterns of the open-section shells. Results show that corner fillets have a significant effect on the limit load of the open-section shell segments under in-plane loading.

Keywords: buckling, open-section shell, radial load, load-bearing capacity

1. INTRODUCTION

Buckling of open-section shell segments is a classical stability problem and exact solutions are only available for limited cases, based on certain assumptions. Major practical application of this kind of structures are rigid-concreate pavement substructure for highways, open foundations for buildings, laterally and vertically loaded piles, tunnels in soil profile etc. Since the open-section shell is a special type of an arch profile with an opening angle of 90 degrees, the arch structures in the design of bridges, roofs and applications concerning structural engineering and architecture may be shown as the other examples. A shell-segment with an open section, which is under a central radial load, is also a buckling problem and the shell structure may suddenly lose its stability in a non-linear fashion. For this reason, exact solutions are generally incapable of capturing deformation patterns and load-bearing capacities of these structures. To resolve this issue, the use of numerical analysis is an effective tool because it considers the role of non-linear geometry on the buckling behavior. In addition, geometric parameters of the shell segments play an important role in the load-bearing capacity and equilibrium paths as well as material properties, boundary conditions and loading types. This is because the geometric stiffness is highly dependent to the geometry of the shell structures and the system may lose its stability before reaching the yield point of the material. To analyze the stability of the open-shell segments under radial loading cases, researchers are proposed several analytical approaches. For example, a new theory for the buckling and nonlinear analysis of the thin-walled structures is developed by Chengyi et al., [1] to reflect the

---

* Corresponding author: halukyilmaz@eskisehir.edu.tr
[1] Eskisehir Technical University, Vocational School of Transportation
E-mail: ibrahimkocabas@eskisehir.edu.tr
ORCID: https://orcid.org/0000-0002-6750-3708, https://orcid.org/0000-0003-0600-2034

influence of shear deformation on the critical load. However, various assumptions based on the Galerkin method are made to obtain analytical solutions of the critical loads. Open or close section shells are the most employed components in many structures. Rao et al. [2] investigate influence of cap fillet of tubular sections on deformation and energy-absorbing characteristics under lateral loading. Their findings emerge that the end fillet details have a strong effect on the deformation patterns and final shape profiles of the tested specimens [2]. This clearly indicates that the buckling response of a shell segment is highly affected by the presence of fillets and their dimensions. A similar study is conducted by Wang et al. [3], to examine vertical shear buckling capacity of steel beams with fillet corner hexagonal web openings. They compared buckling modes and buckling capacities of the beams with hexagonal and circular openings. As a result of their parametric analysis, buckling behavior of the beam is affected by the opening shape, the opening dimension, the opening distance, and thickness [3]. Shell profiles are also an important geometric factor for buckling load evaluations as well as fillet details of corners. Tang et al. [4] are investigated parabolic profiles for buckling load evaluation considering vertical loading cases. A modified eigen-buckling algorithm based on eigenvalue analysis is presented to assess buckling strength of a steel bridge structure regarding to inelastic buckling method and elastic buckling method. They result that influences of the geometric parameters of parabolic arches are taken into account by modifying slenderness parameter [4]. There are several methods to improve buckling loads of thin-walled structures through implementing different geometrical cross-sections. Yang et al. [5] are tried to enhance the local buckling strength of open-section beam segments using some stiffeners in different geometrical forms. They successfully increase the buckling strength up to 207%. This shows importance of geometrical configurations to obtain higher load-bearing capacities in thin-walled structures. On the other hand, type of loading also plays an important role in determining the buckling load of an open-section shell. Pi et al. [6] perform an analytical investigation to reveal significance of pre-buckling behavior of open-section thin-walled arches under uniform radial load. Their numerical results show that the pre-buckling deformations of shallow arches are substantial and neglecting the effects of the pre-buckling deformations will lead to incorrect predictions of the buckling load of the arches. Szychowski [7] apply a warping torsion in an open-section thin-walled structure to investigate the geometry of the cross-section on the buckling characteristics. Pi and Bradford [8] examine stability of circular arches under a sudden uniform radial load. Similar loading case is considered by ref. [9] which takes a radial central load into account to formulate elasto-plastic buckling of arch structures, numerically. A different loading type, which is axial and end moment, is studied by Asadi et al. [10] to investigate buckling behavior of both open and closed section beams. As a result, it is reported that changes in geometrical details and loading types should be precisely considered to develop efficient buckling relations.

This paper aims prediction of in-plane buckling load of an open-section shell segment with different corner fillet radius values subjected to a central radial load, accounting for non-linear geometry. In this case, it would be possible to estimate limit load and reduction factor as a reference to the semi-cylinder profile for a simple open-section shell structure application. For this purpose, buckling load equations under clamped end conditions are developed to predict load-carrying capacities of open-section shell segments. A reduction factor is also proposed to evaluate influence of the corner fillet radius, ranging from a reference circular profile to a rectangular profile, on the load-carrying capacity. In this respect, the present study will have a contribution to the current literature in the field of open-section shell structures.

2. NUMERICAL BUCKLING ANALYSIS

2.1. Open-section Shell Geometry

Geometry of an open-section shell structure is schematically illustrated in Fig. 1. There are four independent geometric parameters in construction of an open-section shell segment which are denoted as shell width L, shell thickness t, fillet radius r and shell height h. A reference circular open-shell profile of radius R as shown in Fig. 1 may be proposed to evaluate the influence of the fillet radius r on the limit load. In this case, for the open-section shell segment, the half-width $L/2$ and the height h are equal to the radius of the reference circular profile ($L=2h=2R$). It enables the buckling load comparisons of the shells with different fillet radius values as a basis of reference shell profile. For general buckling expressions, it is useful to consider normalized geometry parameters. Therefore, normalized parameters, such as ratio of the fillet radius to the radius of reference profile r/R, and radius-to-thickness ratioR/t are chosen for buckling evaluation. The r/R parameter is a geometric shape factor which varies between zero and unity. Several shell configurations are presented in Fig. 2 for different values of r/R. If r/R equals to 1, reference open-section shell profile is constructed. In the case of $r/R=0$, a rectangular shell section is yielded. A parametric study is conducted to derive buckling expressions for the geometrical open-section shell segment parameters, as can be seen in Table 1.

The geometrical parameters have an extensive range to develop efficient buckling expressions. For this reason, R/t is chosen in the range of 25 and 1000. This is a quite feasible interval considering practical applications of the open-section shells. Similarly, r/R is reasonably taken as between zero and unity with an increment size of 0.1.

Table 1 Range of open-section shell segments for parametric study.

Radius-to-thickness ratio (R/t)	Fillet radius-to-radius of reference profile (r/R)	Young's Modulus E [GPa]
25	0	200
↓	↓	
1000	1	

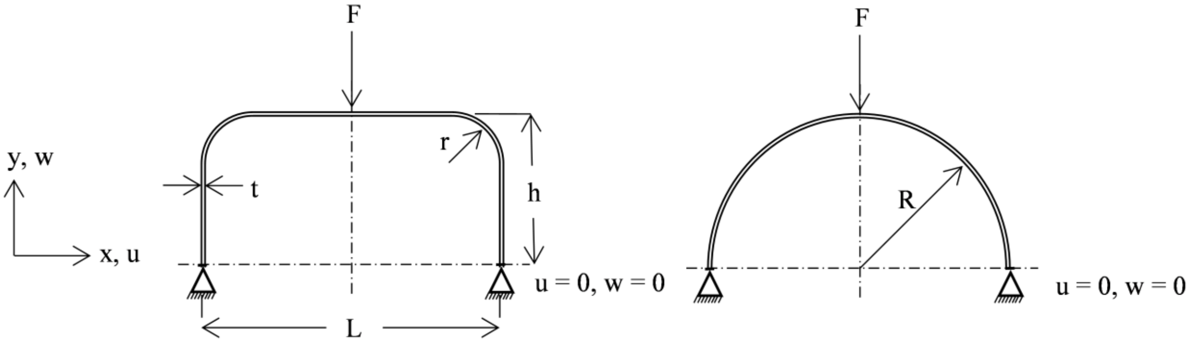

Figure 1 Schematic illustration of an open-section shell geometry with a fillet radius (on left) and reference circular profile (on right).

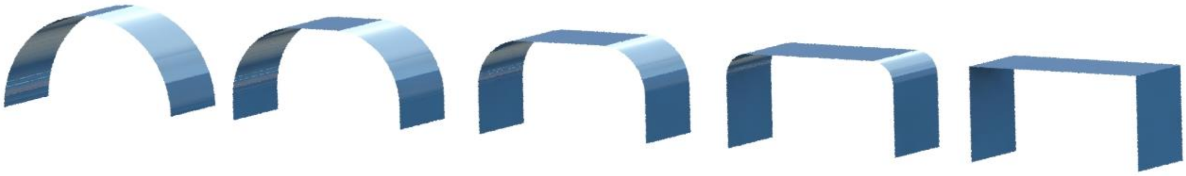

Figure 2 Various open-section shell segment configurations between $r/R=1$ and $r/R=0$

2.2. Numerical Model Details

This section gives the details of the finite element model, boundary conditions and numerical analysis. A numerical model is constructed in ANSYS Workbench package program considering static analysis. Fig. 1 displays the boundary conditions employed in the numerical model for fixed (clamped) case. Ends of the shell models are constrained to move in *u* and *w* direction, and a central radial load *F* is applied progressively until the buckling occurrence to simulate in-plane buckling conditions, as shown in Fig 1. The open-section shell system can be modelled as a plane strain problem because the length of the shell is enough large thus out-of-plane buckling is ignored. In this case, the limit load can be expressed as the load per unit depth of the shell in the *z*-direction. A mesh sensitivity analysis is conducted to decide optimal element size considering the accuracy of the numerical analysis. As a result, an element size of 0.25 mm gives reasonably sufficient accuracy because the deviation in the buckling loads does not change considerably for smaller values of the element size. The numerical analysis takes nonlinear geometry referred to GNA (geometrically nonlinear analysis) into account in this study. An elastic material model is considered since the elastic buckling behavior of the shells is investigated. Shell181, four-node quadrilateral shell element with large deflection capability, is selected for the numerical analysis.

The numerical model is validated with the experimental test results in the literature. For this purpose, the experimental test results of limit loads of two semi-cylinder configurations are considered in the validation process [11]. The semi-cylinder dimensions are R=62.5 mm, t=3.2 mm and R=62.5 mm, t=2.4 mm for the first and second test samples, respectively with a depth of 125mm in the *z*-axis. Multilinear material model is implemented in the validation and mechanical properties of the samples are given in ref. [11]. The comparison of numerical and experimental test results is given in Table 2. It is seen that the amount of deviation from the test data is found out to be 10.9% and 5.11% for the first and second semi-cylinder configurations, respectively. Therefore, the proximity between the test data and numerical model is in the acceptable limits.

Table 2 The proximity between experimental and numerical limit load results.

C1	Experimental Limit Load [N/mm]	8.137
	Numerical Limit Load [N/mm]	9.027
	Deviation [%]	10.9
C2	Experimental Limit Load [N/mm]	4.045
	Numerical Limit Load [N/mm]	4.252
	Deviation [%]	5.11

3. RESULTS AND DISCUSSION

The results of numerical analysis of the open-section shell configurations are presented to examine effects of corner fillets on the limit load. Equilibrium paths (load-deflection curves) is an important tool to understand general buckling behavior of a shell structure. For this reason, the load-deflection curves of the shells are plotted in Fig. 3 for the r/R values changing between zero and unity. In the parametric study, R/t varies in the range of 25 and 1000. To demonstrate general buckling behavior, R/t=100 is considered in the construction of the load-deflection diagram in Fig. 3. As can be seen in Fig. 3, a smooth vertical deflection response occurs in which no sharp drops in load-bearing capacity are observed for r/R=0 (rectangular open-section shell segment). As r/R increases up to 0.5, a similar deformation pattern trend is recorded, and relatively higher fluctuations in the load-deflection curve are observed, as shown in Fig. 3. It can be said that the shell structure does not exhibit a significant buckling behavior for the r/R values up to 0.5, which means that the structure almost keeps its load-bearing capacity during loading history. However, a visible reduction is yielded in load-bearing capacity for the r/R values larger than 0.5. Major reason is that the geometric stiffness of the structure does not change considerably up to the limit point in comparison with the configurations where r/R is lower than 0.5, and a membrane stress dominant system is achieved for r/R is greater than 0.5. However, a bending stress dominant system exhibits in the other configurations (r/R<0.5) from beginning of the loading, naturally. In this interval where r/R is between 0.5 and 1, the open-section shell loses its stability, and a limit load value can be directly determined from the diagram. Otherwise, at lower values of r/R, the limit load can be determined considering the minimum slope of the equilibrium path. It is notable that the fillet radius r has a great impact on the limit load of open-section shells and should be considered as a design factor in the constructions.

Deformation patterns of some selected open-section shell configurations are given in Figs. 4a, 4b and 4c for r/R=0, r/R=0.5 and r/R=1, respectively. The labels in Fig. 4 represents the total deformation at the buckling instant of the structure. It is seen that the amount of vertical deflection depends on the r/R parameter.

However, it is difficult to reach a direct correlation between the limit load and corresponding deflection because r/R emerges a nonlinear contribution in terms of buckling behavior. As a result, the mode shapes of the shell configurations are quite similar.

A reference limit load equation is required to measure the amount of reduction in the limit load of the shell structure with a fillet. For this reason, r/R=1, which corresponds to a circular shell section, is taken as a reference profile. The limit load of the reference profile, denoted as F_{ref}, is plotted against R/t, as shown in Fig. 5. F_{ref} is observed to decrease tremendously as R/t increases from 25 to 1000. F_{ref} is apparently a multivariate function of R/t, R and Young's modulus E. Therefore, as a result of the regression process, which is applied to the parametric analysis results, Eq. 1 may be introduced to calculate the limit load of the reference profile per unit depth:

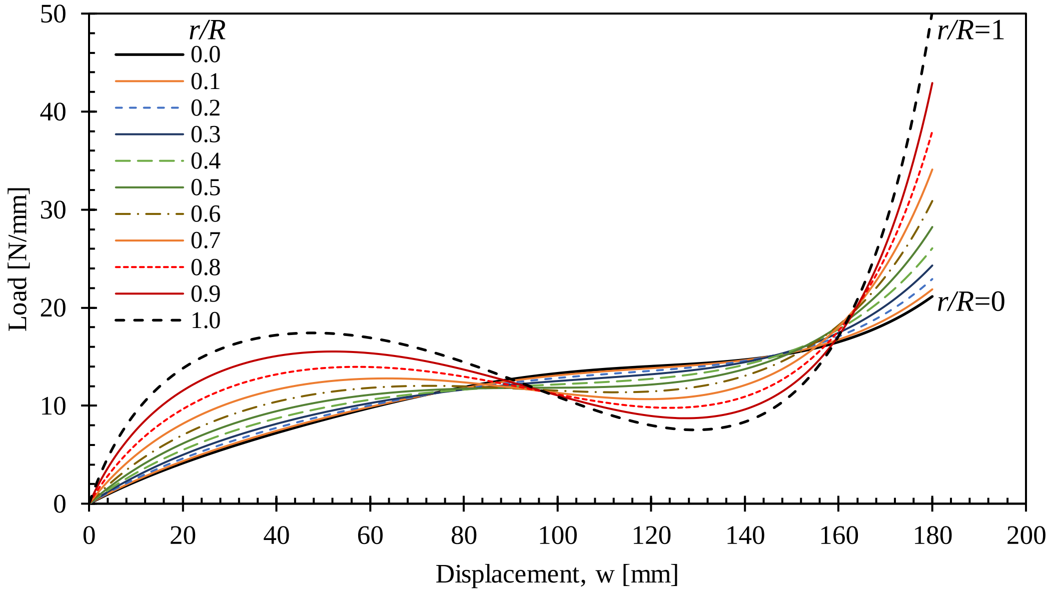

Figure 3 Equilibrium paths (load-deflection diagram) of the open-section shell segment configurations at R/t=100.

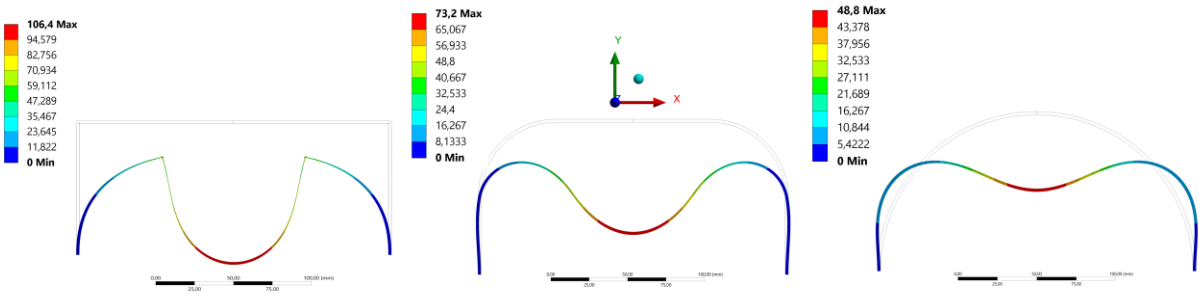

Figure 4 Deformation patterns of the open-section shells for (a) r/R=0, (b) r/R=0.5 and (c) r/R=1.

$$F_{ref} = ER(R/t)^{-3.03} \qquad (1)$$

where E is Young's modulus, R is the radius of the reference shell profile and t is the shell thickness.

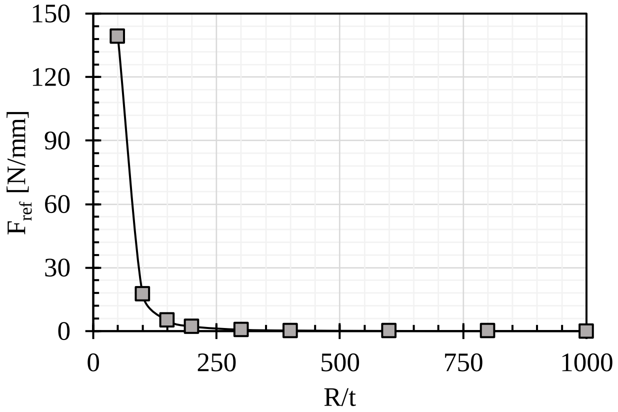

Figure 5 Limit load (F_{ref}) versus *R/t* for the reference open-section shell profile

A reduction factor parameter, which is denoted as φ, is introduced to measure the amount of reduction in the limit load as a basis of reference profile. The reduction factor can be described as $\varphi = F_{lim}/F_{ref}$, where F_{lim} is the limit load of the shell segment for which r/R is lower than unity. To produce an expression, the variation of φ is plotted against *r/R* in the range of 0 to 1, as shown in Fig. 6. The reduction factor φ is calculated based on the limit load values obtained from the numerical analysis. The results emphasize that φ decreases slightly for the increasing values of *r/R* from zero (corresponding to rectangular open-section shell) to 0.5. For 0.5< *r/R* <1, a visible buckling response appears and φ continuously increases as the shell section approaches to reference profile (*r/R* =1). It can be reported that there is a critical region, at around *r/R* =0.5, at which φ reaches some local minima. It means that the maximum decrement appears in the limit load, which is caused by the corner fillets. Although *R/t* is an important parameter in buckling evaluations, it results that there is no considerable influence of *R/t* on the reduction factor. For this reason, an expression for φ may be produced as only a function of *r/R* in the following polynomial form:

$$\varphi = F_{lim}/F_{ref} = 0.9(r/R)^2 - 0.7(r/R) + 0.8 \qquad (2)$$

Eq. 2 is proposed as an efficient tool to evaluate the amount of reduction in the limit load of an open-section shell segment which caused by the radius of the corner fillets. Substituting Eq. 1 into Eq.2 and solving for F_{lim} gives the following expression to calculate the limit load of an arbitrary shell configuration:

$$F_{lim} = ER(R/t)^{-3.03}[0.9(r/R)^2 - 0.7(r/R) + 0.8] \qquad (3)$$

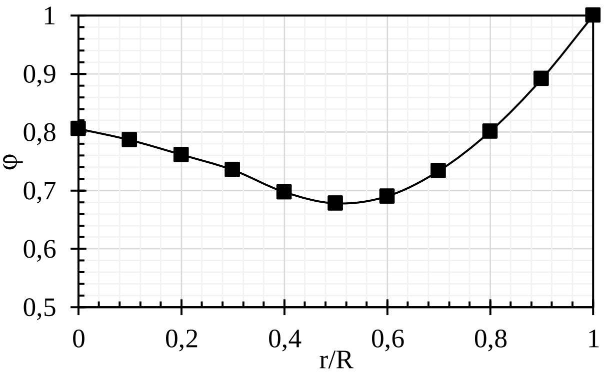

Figure 6 Reduction factor versus *r/R* diagram at *R/t*=100.

A residual estimator approach is implemented as a measure of the accuracy of Eq. 3 as a reference to numerical data. The residual denoted as $\Delta\Phi$ is used as an error indicator. It is expressed as $\Delta\Phi = (F_{num} - F_{eq})/F_{num}$ where F_{eq} and F_{num} are the limit loads obtained from the Eq. 3 and numerical analysis, respectively. $\Delta\Phi$ is presented in Fig. 7 for the *r/R* values in the range of 0 and 1 considering all of the *R/t* values given in Table 1. The horizontal line where $\Delta\Phi$ is equal to zero represents that the predictions obtained from Eq. 3 and numerical analysis are identical. It is concluded that the residuals mostly lay between a lower and upper bound of -0.1 and 0.05, respectively. The higher residuals for each *r/R* ratio are especially obtained at higher *R/t* values. Therefore, the proposed equations give more accurate predictions at lower *R/t* values. However, good proximity is achieved at higher *R/t* with a maximum deviation of +5% and -10%, which is accepted to be in the feasible regions.

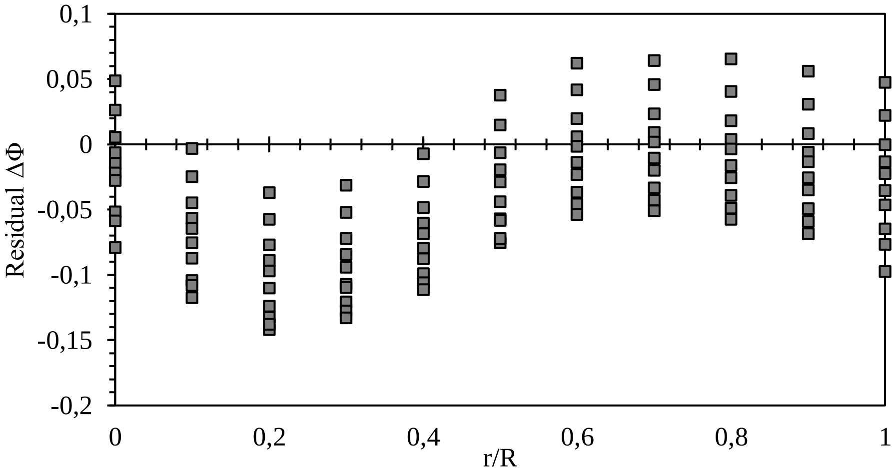

Figure 7 Residual $\Delta\phi$ versus *r/R* at different *R/t* values in the range of 25 and 1000

4. CONCLUDING REMARKS

In this study, influence of corner fillet radius on the buckling behavior of open-section shell segments under a central radial load is investigated, numerically. The effects of the geometrical parameters on the load-bearing capacity of the open-section shells are studied. Additionally, a parametric study is performed for a wide range of geometry configurations considering clamped boundary conditions. A reduction factor and a limit load equation are developed and compared with the numerical results to examine the accuracy of the equations. Finally, the results that can be drawn from the present study are as follows:

- The load-bearing capacity of an open section shell segment under a radial load varies, which is proportional to (*R/t*)-3.03 for a certain r/R ratio.
- No sudden drop in the load-bearing capacity of the open-section shells is observed for which r/R is lower than 0.5. However, slopes of the equilibrium paths approach to zero just before reaching the stiffening region depending on the change of geometric stiffness
- Limit load attains a maximum value at the semi-circular configuration (reference config.) and a snap-through occurs beyond the limit point as the nature of this kind of structures. It results in a sudden reduction in the load-bearing capacity after the limit point. This is because the geometric stiffness of the semi-circular profile is greater than the other configurations during the loading history.
- Geometric stiffness decreases as the structure turns into to rectangular profile then the severity of the loss of stability diminishes or completely disappears. Nevertheless, the load-bearing capacity of the structure still decreases.
- The limit load may reduce up to 25% depending on *r/R* in connection with the reference profile. It is formulated by a second-order polynomial which evaluates the elastic limit load of the structure without needing a numerical analysis. Therefore, it provides a guide for the selection of an open-section shell geometry with corner fillets according to production and service conditions.

Acknowledgments

The authors are greatly thankful to Eskisehir Technical University, Turkey for providing the facilities in developing the paper.

The Declaration of Conflict of Interest

No conflict of interest or common interest has been declared by the authors.

REFERENCES

[1] C. Chengyi, T. Genshu, and Z. Lei, “In-plane nonlinear buckling analysis of circular arches considering shear deformation,” J. Constr. Steel Res., vol. 164, p. 105762, 2020.

[2] M. Gowthamuneswara Rao, A. Praveen Kumar, C. Nagaraj, and L. Ponraj Sankar, “Investigations on the lateral impact behaviour of combined geometry tubular structures and its effect of cap fillet radius,” Mater. Today Proc., vol. 27, pp. 1912–1916, 2020.

[3] P. Wang, X. Wang, and N. Ma, “Vertical shear buckling capacity of web-posts in castellated steel beams with fillet corner hexagonal web openings,” Eng. Struct., vol. 75, pp. 315–326, 2014.

[4] Z. Tang, W. Zhang, J. Yu, and S. Pospíšil, “Prediction of the elastoplastic in-plane buckling of parabolic steel arch bridges,” J. Constr. Steel Res., vol. 168, 2020.

[5] J. Q. Yang, T. Q. Liu, and P. Feng, “Enhancing flange local buckling strength of pultruded GFRP open-section beams,” Compos. Struct., vol. 244, p. 112313, 2020.

[6] Y. L. Pi and M. A. Bradford, “Nonlinear dynamic buckling of shallow circular arches under a sudden uniform radial load,” J. Sound Vib., vol. 331, no. 18, pp. 4199–4217, 2012.

[7] A. Szychowski, “A theoretical analysis of the local buckling in thin-walled bars with open cross-section subjected to warping torsion,” Thin-Walled Struct., vol. 76, pp. 42–55, 2014.

[8] Y. L. Pi and M. A. Bradford, “Elasto-plastic buckling and postbuckling of arches subjected to a central load,” Comput. Struct., vol. 81, no. 18–19, pp. 1811–1825, 2003.

[9] Y. L. Pi, M. A. Bradford, and F. Tin-Loi, “Flexural-torsional buckling of shallow arches with open thin-walled section under uniform radial loads,” Thin-Walled Struct., vol. 45, no. 3, pp. 352–362, 2007.

[10] A. Asadi, A. H. Sheikh, and O. T. Thomsen, “Buckling behaviour of thin-walled laminated composite beams having open and closed sections subjected to axial and end moment loading,” Thin-Walled Struct., vol. 141, pp. 85–96, 2019.

[11] İ. Kocabaş and H. Yılmaz, “In-plane buckling of semi-cylindrical shells with elastic edge restraints under a central radial load,” Thin-Walled Struct., vol. 167, pp. 148141, 2021.

SAKARYA ÜNİVERSİTESİ

FEN BİLİMLERİ ENSTİTÜSÜ
DERGİSİ

Sakarya University Journal of Science
SAUJS

e-ISSN 2147-835X Founded 1997 Period Bimonthly Publisher Sakarya University
http://www.saujs.sakarya.edu.tr/en/

Title: Determination of Multiple Antibiotic Resistance Profiles of Enterococcus Species Isolated From Fermented Meat Products Consumed in Ankara

Authors: Meryem Burcu KÜLAHCI, Sumru ÇITAK, Zehra ŞAHİN

Recieved: 2021-09-23 00:00:00

Accepted: 2021-10-12 00:00:00

Article Type: Research Article

Volume: 25
Issue: 6
Month: December
Year: 2021
Pages: 1295-1303

How to cite
Meryem Burcu KÜLAHCI, Sumru ÇITAK, Zehra ŞAHİN; (2021), Determination of Multiple Antibiotic Resistance Profiles of Enterococcus Species Isolated From Fermented Meat Products Consumed in Ankara. Sakarya University Journal of Science, 25(6), 1295-1303, DOI: https://doi.org/10.16984/saufenbilder.999958
Access link
http://www.saujs.sakarya.edu.tr/tr/pub/issue/66341/999958

SAKARYA ÜNİVERSİTESİ
FEN BİLİMLERİ ENSTİTÜSÜ DERGİSİ
Sakarya University Journal of Science (SAUJS)
SAKARYA ÜNİVERSİTESİ
e-issn: 2147-835X
SAÜ Fen Bil Der/SAUJS
Cilt/Volume: 25
Sayı/Issue: 6
Aralık/December 2021

Sakarya University Journal of Science 25(6), 1295-1303, 2021

SAKARYA ÜNİVERSİTESİ

Determination of Multiple Antibiotic Resistance Profiles of *Enterococcus* Species Isolated From Fermented Meat Products Consumed in Ankara

Meryem Burcu KÜLAHCI*[1], Sumru ÇITAK[1], Zehra ŞAHİN[1]

Abstract

The aim of this study was to determine the multiple antibiotic resistance profiles of *Enterococcus* spp. isolated from the fermented meat products consumed in Ankara, Turkey. A total of 134 *Enterococcus* spp. were isolated and identified from 80 fermented meat samples. The highest prevalence of enterococci in the fermented food samples was found in sucuk (a Turkish fermented sausage) samples (50%), followed by sausage (25.4%), pastirma (a Turkish dry-cured meat product) (18.6%), and salami, respectively. Of a total of 134 *Enterococcus* isolates, 110 (82.1%) were found to be resistant to one or more of the antibiotics tested. The highest resistance rate was seen against rifampicin (73.2%), streptomycin (36.5%) and erythromycin (20.2%), and 28 (20.9%) of Enterococcus isolates were resistant to multiple antibiotics. The presence of multiple antibiotic resistant *Enterococcus* in foods of animal origin raises alarm because of the risk of carrying these bacteria to humans via the food chain.

Keywords: *Enterococcus*, fermented meat products, multiple antibiotic resistance

1. INTRODUCTION

Enterococcus species are found in many environments such as soil, food and water and they are also found in the microbiota of the gastrointestinal system of humans and warm-blooded animals [1]. They have also shown to be present in some ripened cheeses and fermented salami as part of established starter cultures and are used in the production of some meat and dairy products because of their important contribution in the process and fermentation of flavors and their probiotic properties. Therefore by intestinal and/or environmental exposure, enterococci can colonize raw foods of animal origin (milk, meat) where they can survive and reproduce during fermentation processes. Due to their tolerance to environmental conditions (temperature, pH, salinity), they are often isolated from both fermented and heat treated meat products [2].

Enterococcus species have been shown to be among the most common nosocomial pathogens, important cause of multiple antibiotic resistance as well as urinary tract, central nervous system, intraabdominal and pelvic infections, endocarditis, bacteremia and infections [3, 4]. There is no consensus, however, on the importance of their existence in food items. In the field of veterinary medicine, antibiotics are commonly used to control and treat infections and

---

* Corresponding author: meryemburcu@gazi.edu.tr
[1] Gazi University, Faculty of Science, Department of Biology
E-Mail: scitak@gazi.edu.tr, zehrakarabiyik@gmail.com
ORCID: https://orcid.org/0000-0002-5007-5209, https://orcid.org/0000-0003-1925-0483, https://orcid.org/0000-0003-3483-9528

feed additives to promote growth results in the selection of resistant enterococci in the animal intestinal flora. The ingestion of antibiotic-resistant bacteria through foods is a potential mechanism for the transition of antibiotic resistance determinants to human or animal adapted strains [5, 6].

The present study was designed to determine the multiple antibiotic resistance profiles of enterococci isolated from fermented meat products mainly derived from sucuk (a Turkish fermented sausage), sausage, salami, and pastirma (a Turkish dry-cured meat product) in Turkey.

2. MATERIAL AND METHODS

2.1. Sampling

Eighty samples of fermented meat (20 sucuk, 20 sausages, 20 salami, and 20 pastirma) were collected from markets in Ankara between February 2017 and December 2017. All the samples were kept at 4^0C before analysis and transported to the laboratory, immediately.

2.2. Isolation and Identification

The fermented meat samples were transferred to the laboratory under cold chain conditions, diluted 1:10 with sterile buffered peptone water (BPW) (Oxoid, CM 509, Basingstoke, UK) and homogenized for about 10 min. Isolation was done by selecting typical pink and purple colonies on Slanetz Bartley Agar (SBA; Oxoid, CM 377), selective medium for *Enterococcus*. Estimated identification of isolates was performed by Gram staining, production of catalase and oxidase, growth at 10 °C and 45 °C, growth in the presence of 6.5% NaCl, growth at pH 9.6, determination of esculin hydrolysis on bile-esculin agar (Merck, 48300).

The species identification was confirmed with Becton Dickinson (BD) BBL Crystal Identification Systems and Gram-Positive ID kit (Becton, Dickinson and Company, USA [7].

2.3. Antimicrobial Susceptibility Testing

Antimicrobial susceptibility of the isolates was determined using the disc diffusion method following Clinical and Laboratory Standard Institute guidelines, 2012 [8] on Muller Hinton Agar (MHA) plates (Becton Dickinson Microbiology Systems, Cockeysville, USA). All strains were incubated at 37^0C for 48 h. The antimicrobials and their concentrations (BBL Microbiology Systems, Cockeysville, USA) were as follows: ampicillin chloramphenicol (C, 30 µg), ciprofloxacin (CIP, 5 µg), erythromycin (E, 15 µg), gentamicin (CN, 120 µg), nitrofurantoin (F, 300 µg), penicillin (P, 10 µg), rifampicin (RF, 5 µg), streptomycin (S, 300 µg), teicoplanin (TEC, 30 µg), tetracycline (TE, 30 µg), vancomycin (VA, 30 µg). *Enterococcus faecalis* ATCC 29211 was used as a control strain. The MAR (multiple antibiotic resistance) indexes were calculated as described by Krumperman [9].

3. RESULTS

3.1. Isolation and Identification

Overall, one hundred thirty-four *Enterococcus* spp. were isolated from the eighty fermented meat samples (twenty sucuk, twenty sausages, twenty salami, twenty pastirma). In this study, the highest prevalence of enterococci in the fermented food samples was found in sucuk samples (50%), followed by sausage (25.4%), pastirma (18.6%) and salami (6%), respectively (Table 1).

Table 1 Distribution in the 134 *Enterococcus* strains isolated from the fermented meat samples

Types of fermented meat	*Enterococcus* isolated from fermented meat						Total
	E. faecium	*E. faecalis*	*E. gallinarum*	*E. durans*	*E. avium*	*E. hirae*	
	n (%)	n (%)	n (%)	n (%)	n (%)	n (%)	n (%)
sucuk	48 (71.6%)	6 (8.9%)	9 (13.4%)	3 (4.5%)	1 (1.5%)	-	67 (50%)
sausage	11 (32.3%)	20 (58.8%)	3 (8.8%)	-	-	-	34 (25.4%)
salami	6 (75%)	1 (12.5%)	1 (12.5%)	-	-	-	8 (6%)
pastirma	14 (56%)	8 (32%)	-	2 (8%)	-	1 (4%)	25 (18.6)

n: Number of Enterococcus isolates

E. faecium (59%) and *E faecalis* (26.1%) strains were predominantly isolated from all the fermented meat classes in this study (Table 2).

Table 2 Distribution of the *Enterococcus* strains isolated from the fermented meat samples

Enterococcus species	Fermented meat samples	
	Number of	%
E.faecium	79	59
E.faecalis	35	26.1
E.gallinarum	13	9.7
E.durans	5	3.7
E.avium	1	0.7
E.hirae	1	0.7
Total	134	100

3.2. Antimicrobial Susceptibility Testing

The prevalence of antibiotic resistance determined in Enterococcus species isolated from fermented meat samples in our study is shown in Table 3.

Table 3 Antimicrobial resistance in *Enterococcus* isolates

Antibiotics	Resistant isolates (%)						
	E. faecium n=79	*E. faecalis* n=35	*E. gallinarum* n=13	*E. durans* n=5	*E. avium* n=1	*E. hirae* n=1	Total n=134
	n (%)	n (%)	n (%)	n (%)	n (%)	n (%)	n (%)
Ampicillin	1 (%1.3)	-	-	-	-	-	1 (%0.8)
Chloramphenicol	-	2 (%5.7)	-	-	-	-	2 (%1.5)
Ciprofloxacin	4 (%5)	4 (%11.4)	-	-	-	-	8 (%6)
Erythromycin	19 (%24)	6 (%17.1)	1 (%7.7)	1 (%20)	-	-	27 (%20.2)
Gentamicin	1 (%1.3)	1 (%2.8)	1 (%7.7)	-	-	-	3 (%2.3)
Nitrofurantoin	12 (%15.1)	3 (%8.5)	4 (%30.7)	1 (%20)	-	-	20 (%15)

Penicillin	1 (%1.3)	-	-	-	-	-	1 (%0.8)
Rifampicin	59 (%74.6)	27 (%77.1)	8 (%61.5)	2 (%40)	1 (%100)	1 (%100)	98 (%73.2)
Streptomycin	32 (%40.5)	12 (%34.2)	4 (%30.8)	-	-	1 (%100)	49 (%36.5)
Teicoplanin	2 (%2.5)	-	1 (%7.7)	-	-	-	3 (%2.3)
Tetracycline	5 (%6.3)	3 (%8.5)	-	-	-	-	8 (%6)
Vancomycin	-	-	-	-	-	-	-

Of a total of 134 *Enterococcus* isolates, 110 (82.1%) were found to be resistant to one or more of the antibiotics tested. Multiple antibiotic resistance status of *Enterococcus* isolates are given in Table 4.

Table 4 Antimicrobial resistance pattern and multiple resistance of *Enterococcus* isolates from the fermented meat

Antibiotics	Number of resistant *Enterococcus* isolates (%)	MAR Index
AM	1 (0.7%)	0.08
CIP	1 (0.7%)	0.08
E	1 (0.7%)	0.08
F	3 (2.2%)	0.08
RF	34 (25.3%)	0.08
S	2 (1.5%)	0.08
S-RF	19 (14.2%)	0.17
CIP-RF	4 (3%)	0.17
RF-E	9 (6.7%)	0.17
S-F	2 (1.5%)	0.17
TE-RF	4 (3%)	0.17
CIP-F	1 (0.7%)	0.17
S-E	1 (0.7%)	0.17
S-RF-F	9 (6.7%)	0.25
S-RF-TEC	1 (0.7%)	0.25
S-RF-E	7 (5.2%)	0.25
S-CIP-RF	1 (0.7%)	0.25
TE-RF-E	1 (0.7%)	0.25
RF-F-E	1 (0.7%)	0.25
S-E-TEC	1 (0.7%)	0.33
S-RF-F-E	2 (1.5%)	0.33
C-CIP-TE-E	1 (0.7%)	0.33
S-RF-CN-E	1 (0.7%)	0.33
S-TE-RF-CN	1 (0.7%)	0.33
S-RF-F-P-E	1 (0.7%)	0.42
S-RF-F-CN-TEC	1 (0.7%)	0.42

AM (Ampicillin), C (Chloramphenicol), CIP (Ciprofloxacin), CN (Gentamicin), E (Erythromycin), F (Nitrofurantoin), P (Penicillin), RF (Rifampicin), S (Streptomycin), TE (Tetracycline), TEC (Teicoplanin).

4. DISCUSSION AND CONCLUSION

In Turkey, *E. feacalis* and *E. faecium* were isolated as the dominant species in meat and meat products [10]. Likewise, *E. faecalis* and *E. faecium* were dominant species isolated from naturally fermented Turkish foods [11]. In other studies conducted on fermented meat products from Turkey [12], Canada [13] and North of Portugal [14] the researchers reported predominant isolation of *E. faecalis* and *E. faecium*. However, other species such as *E. gallinarum, E. durans, E. avium, E. hirae* are less frequently identified in our study (Table 2). Nevertheless, other studies have found *E. faecalis* as the predominant species [15, 16, 17], and the low occurrence of other *Enterococcus* species in fermented food samples resembled other research that had previously been published [10, 14, 16]. A higher prevalence of enterococci in fermented foods during the removal of the internal organs can be considered as an indicator of fecal contamination in the slaughterhouse. Due to their heat sensitivity, *Enterococcus* species can be found in many different fermented foods during fermentation without starter or in meat products processed after baking [18]. Cross-contamination can also occur at the final stages of processing, such as cutting and packaging of produce [19].

It is known that *Enterococcus* spp. is naturally resistant to many antibiotics used in treatment. In addition, they have the ability to develop genetic resistance and transfer it to commensal bacteria by genes carried by plasmids or transposons [20]. In the present study, the prevalence of antibiotic resistance was higher for *E. faecium* when compared to *E. faecalis* (Table 3). *E. faecium* showed resistance to rifampicin (74.6 %), streptomycin (40.5%), erythromycin (24%), and nitrofurantoin (15.1%). A high percentage of rifampicin resistance (73.2%) was detected among our enterococcal isolates. About 77.1% of *E. faecalis,* 74.6 % of *E. faecium* and 60% of other *Enterococcus* spp (*E. gallinarum, E. durans, E. avium and E. hirae)* presented resistance to rifampicin. Rifampicin is used nearly solely for the treatment of tuberculosis. Very significant research with enterococci was conducted in Northern Portugal using enterococcal strains isolated from traditional fermented meat products [21]. Rifampicin resistance was shown by a high proportion of strains (60%) from 182 enterococcal isolates.

Gentamicin and streptomycin are the most effective antibiotics used in the treatment of enterococcal infections in high-level aminoglycoside resistance situations. In our study among 134 *Enterococcus* isolates, 49 (36.5%) were resistant to streptomycin, 3 (2.3%) were resistant to gentamicin. For the erythromycin, a high percentage of (20.2%) fermented food isolates was reported as resistant. Similarly, a high frequency of erythromycin resistance has been shown among enterococcal isolates from different sources [22, 23]. Resistance to erythromycin, an important representative of macrolides, is a concern because erythromycin-resistant plasmids and transposons are often found in enterococci [24]. In this study, we found low percentages of ß-lactams resistant enterococcal strains (ampicillin resistance 0.8% and penicillin resistance 0.8%), which is not in line with the generalization that enterococci are intrinsically resistant to ß-lactams [25]. Similar results were obtained by other authors [26, 27].

Vancomycin, one of the few substitutes in the treatment of enterococcal infections, has been recognized as increasingly significant in human medicine, and in the last decade, vancomycin-resistant enterococci have arisen as a common source of nosocomial infections. [28, 29]. Strong data suggest that the decreased number of VREs has been isolated since 1995 when avoparcin was first forbidden for use in livestock [30]. In this study, none of the studied isolates was resistant to vancomycin and only 2.3% of *Enterococcus* species was found resistant to teicoplanin (Table 3). Similar results have been obtained for food isolates in many studies [22, 31].

In cases where there is uncontrolled use of antibiotics in livestock, it has been determined that high and multiple resistance is seen in food and human isolates as a result of cross-resistance. The potential of fermented foods as a source for human transmission of multiple antibiotic-resistant strains of enterococci or as the cause of horizontal transfer of resistance genes between strains is particularly noteworthy [32]. The MAR index is a value determined as a result of a calculation to determine the risk of multiple antibiotic resistance of an isolate in the sample. MAR index values greater than 0.2 indicate that the samples are contaminated from sources where antibiotics are frequently used. MAR index values equal to or less than 0.2 indicate a strain originating from animals for which antibiotics are rarely or never used [33]. Because of its infamous ability to obtain and transfer resistance genes, multiple antibiotic resistance has frequently been reported for enterococci [34, 35]. The multiple antibiotic resistance index calculated for all resistant *Enterococcus* isolates and the ratio ranged from 0.08 to 0.42 values; 25.4% of the strains had a MAR index higher than 0.2 (Table 4), indicating a high risk of contamination for the consumer. This MAR index level is lower than that of the index’s found in in other studies from 0.25 to 0.87 [36] and from 0.2 to 0.6 [37]. The results of this study indicated that resistance to multiple antibiotics was spread among *Enterococcus* isolates.

Enterococcus is commonly present in the digestive tract of humans and animals, with very high numbers of various species of *Streptococcus* and *Listeria monocytogenes* harboring conjugal plasmids and transposons. This information supports the notion that the intestinal tract is the most favorable ecosystem for the direct sharing of genetic information between these bacterial genera [38]. The inclusion of antibiotics in animal feed and inadequate control of prescription medications lead to the proliferation of antibiotic resistance, like enterococci, in the natural flora of healthy humans and livestock. Although antibiotic-resistant enterococci as nosocomial pathogens from clinical environments, especially *E. faecium* [39, 40] and raw food samples from livestock have been extensively studied, little is known about the antibiotic resistance of enterococci strains isolated from fermented food samples.

In conclusion, our findings suggest that the hygienic nature of raw meat may be important as a source of enterococci in the fermentation of meat. It may also provide the correct physical and biochemical conditions for the growth of enterococci during fermentation. This study, therefore, suggests the need for continuous surveillance of enterococci in meat products, considering their importance as vectors for the spread of microorganisms from animals to humans via the food chain. In addition, enterococci obtained from animal foods should be handled carefully for antimicrobial resistance. Fermented meat products are enterococcal reservoirs of antibiotic resistance. This provides useful risk assessment information indicating that foods containing antibiotic-resistant enterococci are likely to pose a potential public health risk to consumers.

Acknowledgments

The authors would like to thank Gazi University Academic Writing Application and Research Center for checking this article.

Funding

The authors have no received any financial support for the research, authorship or publication of this study.

The Declaration of Conflict of Interest/ Common Interest

No conflict of interest or common interest has been declared by the authors.

Authors' Contribution

The authors contributed equally to the study. MBK: Literature research, conducting experiments, writing the article, SÇ: Literature research, writing the article, ZŞ: Literature research, conducting experiments

The Declaration of Ethics Committee Approval

This study does not require ethics committee permission or any special permission.

The Declaration of Research and Publication Ethics

The authors of the paper declare that they comply with the scientific, ethical and quotation rules of SAUJS in all processes of the paper and that they do not make any falsification on the data collected. In addition, they declare that Sakarya University Journal of Science and its editorial board have no responsibility for any ethical violations that may be encountered, and that this study has not been evaluated in any academic publication environment other than Sakarya University Journal of Science.

REFERENCES

[1] A.M. Hammerum, “Enterococci of animal origin and their significance for public health,” Clinical Microbiology and Infection, vol.18, no.7, pp. 619-625, 2012.

[2] L.M. Cintas, P. Casaus, L.S. Håvarstein, P.E. Hernandez, and I. Nes, “Biochemical and genetic characterization of enterocin P, a novel sec-dependent bacteriocin from Enterococcus faecium P13 with a broad antimicrobial spectrum,” Appl Environ Microbiol., vol. 63, no. 11, pp. 4321-4330, 1997.

[3] H.L. Leavis, M.J. Bonten, and R.J. Willems, “Identification of high-risk enterococcal clonal complexes: global dispersion and antibiotic resistance,” Current opinion in microbiology, vol. 5, pp. 454-460, 2006.

[4] S. Ali, I. A. Mirza, S. Yaqoob, A. Hussain, I. Khan, and M. Y. Rafiq, “Antimicrobial susceptibility pattern of enterococcus species isolated from patients with urinary tract infection,” Gomal Journal of Medical Sciences, vol. 12, no. 1, pp. 11-14, 2014.

[5] M. Sparo, L. Urbizu, M.V. Solana, G. Pourcel, A. Delpech, Confalonieri and S.F. Sanchez Bruni, High-level resistance to gentamicin: genetic transfer between *Enterococcus faecalis* isolated from food of animal origin and human microbiota. Letters In Applied Microbiology, vol. 54, no. 2, pp. 119-125, 2012.

[6] C. Vignaroli, G. Zandri, L. Aquilanti, S. Pasquaroli, and F. Biavasco, “Multidrug-resistant enterococci in animal meat and faeces and co-transfer of resistance from an *Enterococcus durans* to a human *Enterococcus faecium*,” Current Microbiology, vol. 62, no. 5, pp. 1438-1447, 2011.

[7] J. M. T. Hamilton-Miller, and S. Shah, “Identification of clinically isolated vancomycin-resistant enterococci: comparison of API and BBL Crystal systems,” Journal of Medical Microbiology, vol. 48, no. 7, pp. 695-696, 1999.

[8] Clinical and Laboratory Standards Institute (CLSI), P. A. Wayne, M07-A9 Methods for dilution antimicrobial susceptibility tests for bacteria that grow aerobically; approved standard – ninth edition, 2012.

[9] P. H. Krumperman, “Multiple antibiotic resistance indexing of Escherichia coli to identify high-risk sources of fecal contamination of foods,” Applied and Environmental Microbiology, vol. 46, no. 1, pp. 165-170, 1983.

[10] T. Elal Mus, F. Cetinkaya, R. Cibik, G. E. Soyutemiz, H. Simsek, and N. Coplu, “Pathogenicity determinants and antibiotic resistance profiles of enterococci from foods of animal origin in Turkey,” Acta Veterinaria Hungarica, vol. 65, no. 4, pp. 461-474, 2017.

[11] S. Özmen Toğay, A. Çelebi Keskin, L. Açık, and A. Temiz, “Virulence genes, antibiotic resistance and plasmid profiles of Enterococcus faecalis and Enterococcus faecium from naturally fermented Turkish foods,” Journal Of Applied Microbiology, vol. 109, no. 3, pp. 1084-1092, 2010.

[12] M. Gökmen, N. Ektik, R. Kara, E. Torlak, and M. Metli, “Detection of prevalence, antibiotic resistance and virulence factors of

Enterococcus spp. isolated from ready to eat foods,” Kocatepe Veteriner Dergisi, vol.10, no. 2, pp. 76-82, 2017.

[13] M. Jahan, D. O. Krause, and R. A. Holley, “Antimicrobial resistance of Enterococcus species from meat and fermented meat products isolated by a PCR-based rapid screening method,” International Journal of Food Microbiology, vol. 163, no. 2-3, pp. 89-95, 2013.

[14] J. Barbosa, P.A. Gibbs, and P. Teixeira, “Virulence factors among enterococci isolated from traditional fermented meat products produced in the North of Portugal,” Food Control, vol. 21, no. 5, pp. 651-656, 2010.

[15] F. M. Aerestrup, Y. AgersØ, P. Ahrens, J. C. Østergaard Jørgensen, M. Madsen, and L. B. Jensen, “Antimicrobial susceptibility and presence of resistance genes in staphylococi from poultry,” Veterinary Microbiology, vol. 74, pp. 353–364, 2000.

[16] N. Klibi, L. B. Said, A. Jouini, K.B. Slama, M. López, R. B. Sallem, and C. Torres, “Species distribution, antibiotic resistance and virulence traits in enterococci from meat in Tunisia,” Meat science, vol. 93, no.3, pp. 675-680, 2013.

[17] S. A. P. Fracalanzza, E. M. D. Scheidegger, P. F. D. Santos, P. C. Leite, and L. M. Teixeira, “Antimicrobial resistance profiles of enterococci isolated from poultry meat and pasteurized milk in Rio de Janeiro, Brazil,” Memórias do Instituto Oswaldo Cruz, vol. 102, no. 7, pp. 853-859, 2007.

[18] G. Giraffa, “Enterococci from foods,” FEMS microbiology reviews, vol. 26, no. 2, pp. 163-171, 2002.

[19] M. Hugas, M. Garriga, and M. T. Aymerich, “Functionality of enterococci in meat products,” International journal of food microbiology, vol. 88, no. 2-3, pp. 223-233, 2003.

[20] B. Martin, M. Garriga, M. Hugas, and T. Aymerich, “Genetic diversity and safety aspects of enterococci from slightly fermented sausages,” Journal of Applied Microbiology, vol. 98, no. 5, pp. 1177-1190, 2005.

[21] J. Barbosa, V. Ferreira, and P. Teixeira, “Antibiotic susceptibility of enterococci isolated from traditional fermented meat products,” Food Microbiology, vol. 26, no. 5, pp. 527-532, 2009.

[22] L. Mannu, A. Paba, E. Daga, R. Comunian, S. Zanetti, I. Duprè, and L. A. Sechi, “Comparison of the incidence of virulence determinants and antibiotic resistance between *Enterococcus faecium* strains of dairy, animal and clinical origin,” International journal of food microbiology, vol. 88, no. 2-3, pp. 291-304, 2003.

[23] J. Peters, K. Mac, H. Wichmann-Schauer, G. Klein, and L. Ellerbroek, “Species distribution and antibiotic resistance patterns of enterococci isolated from food of animal origin in Germany.” International journal of food microbiology, vol. 88, no. 2-3, pp. 311-314, 2003.

[24] B. E. Murray, “The life and times of the Enterococcus,” Clinical microbiology reviews, vol. 3, no. 1, pp. 46-65, 1990.

[25] V. Kak, and J. W. Chow, “Acquired antibiotic resistances in enterococci. In: The enterococci: pathogenesis, molecular biology, and antibiotic resistance,” ASM Press, pp. 355-383, 2002.

[26] L. L. McGowan-Spicer, P.J. Fedorka-Cray, J. G. Frye, R. J. Meinersmann, J. B. Barrett, and C. R. Jackson, “Antimicrobial resistance and virulence of Enterococcus faecalis isolated from retail food,” Journal of food protection, vol. 71, no. 4, pp. 760-769, 2008.

[27] A. S. Valenzuela, N. B. Omar, H. Abriouel, R. L. López, E. Ortega, M. M. Cañamero, and A. Gálvez, “Risk factors in enterococci

isolated from foods in Morocco: determination of antimicrobial resistance and incidence of virulence traits," Food and chemical toxicology, vol. 46, no. 8, pp. 2648-2652, 2008.

[28] World Health Organization (WHO). Critically important antimicrobials for human medicine-3rd revision. WHO Advisory Group on Integrated Surveillance of Antimicrobial Resistance (AGISAR), 978924 1504485, WHO Press, Geneva, Switzerland, 2011.

[29] L. B. Rice, "Emergence of vancomycin-resistant enterococci," Emerging infectious diseases, vol. 7, no.2, pp. 183, 2001.

[30] K. Borgen, G. S. Simonsen, A. Sundsfjord, Y. Wasteson, Ø. Olsvik, and H. Kruse, "Continuing high prevalence of VanA-type vancomycin-resistant enterococci on Norwegian poultry farms three years after avoparcin was banned." Journal of Applied Microbiology, vol. 89, no. 3, pp. 478-485, 2000.

[31] P. Messi, E. Guerrieri, S. De Niederhaeusern, C. Sabia, and M. Bondi, "Vancomycin-resistant enterococci (VRE) in meat and environmental samples." International journal of food microbiology, vol. 107, no. 2, pp. 218-222, 2006.

[32] A. K. Olawale, R. J. Salako, A. O. Olawale, and O. Famurewa, "Antibiotic-Resistant *Enterococcus faecalis* isolated from food canteens in Osun States, Nigeria," Microbiology Research Journal International, vol. 6, no. 4, pp. 196-206, 2015.

[33] Son R, Nimita F, Rusul G, Nasreldin E, Samuel L, Nishibuchi M. Isolation and molecular characterization of vancomycin-resistant *Enterococcus faecium* in Malaysia. Letters In Applied Microbiology, vol. 29, no. 2, pp. 118-122, 1999.

[34] S. Citak, N. Yucel, and S. Orhan, "Antibiotic resistance and incidence of *Enterococcus* species in Turkish white cheese. International Journal of Dairy Technology, vol. 57, no.1, pp. 27-31, 2004.

[35] S. M. McBride, V. A. Fischetti, D. J. LeBlanc, R. C. Moellering Jr, and M. S. Gilmore, "Genetic diversity among *Enterococcus faecalis*," PloS One, vol. 2, no. 7, e582, 2007.

[36] E. M. Carvalho, R. A. Costa, A. J. Araujo, F. A. C. Carvalho, S. P Pereira, O. V. Sousa, and R. H. Vieira, "Multiple antibiotic-resistance of *Enterococcus* isolated from coastal water near an outfall in Brazil," African Journal of Microbiology Research, vol. 8, no. 17, pp. 1825-1831, 2014.

[37] A. Bouymajane, F. R. Filali, S. Oulghazi, A. Ed-dra, F. Benhallam, A. El Allaoui, J. Anissi, K. Sendide, B. Ouhmidou, and M. Moumni, "Occurrence, molecular and antimicrobial resistance of *Enterococcus* spp. isolated from raw cow's milk trade by street trading in Meknes city, Morocco," Germs, vol. 8, no. 2, pp. 77, 2018.

[38] E. Charpentier, and P. Courvalin, "Antibiotic resistance in *Listeria* spp.," Antimicrobial Agents and Chemotherapy, vol. 43, no. 9, pp. 2103-2108, 1999.

[39] P. Linden, and C. Miller, "Vancomycin-resistant enterococci: the clinical effect of a common nosocomial pathogen," Diagnostic Microbiology And Infectious Disease, vol. 33, no. 2, pp. 113-120, 1999.

[40] M. Y. Yoon, Y. J. Kim, and H.J. Hwang, "Properties and safety aspects of *Enterococcus faecium* strains isolated from Chungkukjang, a fermented soy product," LWT-Food Science and Technology, vol. 41, no. 5, pp. 925-933, 2008.

SAKARYA ÜNİVERSİTESİ

FEN BİLİMLERİ ENSTİTÜSÜ
DERGİSİ

Sakarya University Journal of Science
SAUJS

e-ISSN 2147-835X Founded 1997 Period Bimonthly Publisher Sakarya University
http://www.saujs.sakarya.edu.tr/en/

Title: Electromagnetic Shielding Properties of Pack Borided MirraxTM Steel

Authors: İbrahim ALTINSOY

Recieved: 2021-01-14 00:00:00

Accepted: 2021-10-13 00:00:00

Article Type: Research Article

Volume: 25
Issue: 6
Month: December
Year: 2021
Pages: 1304-1312

How to cite
İbrahim ALTINSOY; (2021), Electromagnetic Shielding Properties of Pack Borided MirraxTM Steel. Sakarya University Journal of Science, 25(6), 1304-1312, DOI: https://doi.org/10.16984/saufenbilder.860759
Access link
http://www.saujs.sakarya.edu.tr/tr/pub/issue/66341/860759

Sakarya University Journal of Science 25(6), 1304-1312, 2021

Electromagnetic Shielding Properties of Pack Borided Mirrax^{TM} Steel

İbrahim ALTINSOY*[1]

Abstract

In this study, it was aimed to investigate the electromagnetic interference shielding (EMI-SE) as well as some physical and mechanical properties of pack borided Mirrax tool steel. Boriding process was carried out at 900, 950 and 1000°C for 2, 5, 8h, respectively. Optical images showed that borides layer have smooth morphology and flat interface with matrix. XRD analysis revealed that main phases in the layer were FeB and Fe_2B. Intensity of FeB phases increased with increment of process temperature and time. Depending on process time and temperature, the thickness of borides layer was ranged from 10 µm to 87.80 µm. Microhardness of layer was between 1700 and 2400 HV. EMI-SE measurements conducted within Ku band (12-20 GHz) indicated that EMI-SE efficiency increased by increasing of process time and temperature and it was ranged from 52dB to 75dB. It is possible to claim that borided Mirrax steel performed good EMI-SE and when boriding time reached to 5h, remarkable EMI-SE (electromagnetic interference shielding) (over 60dB) was observed on the samples borided at 900°C.

Keywords: pack boriding, borides, EMI-SE, microhardness, layer thickness.

1. INTRODUCTION

The rapid proliferation of diverse electro/electrical products and technology has resulted in the increase of electromagnetic pollution known as electromagnetic interference (EMI) to greater levels. This ever-increasing electromagnetic pollution can produce severe interference effects and may cause detrimental effects on device performance and human health [1, 2]. Therefore, the issues caused by electromagnetic interference are exposed to people accompanied by the transmission of high-energy electromagnetic radiation, and have become critical problems needed to be addressed. Electromagnetic interference (EMI) and electromagnetic wave pollution will not only cause interference and serious impact on electronic equipment, but also cause harm to human health. Also, in national defense and military fields, electromagnetic wave leakage will seriously harm national defense information security and state secret protection [2, 3]. EMI can be shielded by mechanisms involving reflection and absorption of electromagnetic (EM) radiation. Reflection occurs through interactions of incident EM waves with mobile charge carriers (electrons or holes) of an electrically conductive material [2]. To minimize these issues arising due to EMI, effective shielding materials are in need to protect the efficient operation of electro/electrical systems. And they are widely employed to prolong the service life of equipment, improve the electromagnetic

---

* Corresponding author: ialtinsoy@sakarya.edu.tr

[1] Sakarya University, Engineering Faculty, Department of Metallurgy and Materials Engineering, Turkey.

ORCID: https://orcid.org/0000-0003-4284-5397

compatibility (EMC) and security of biological systems, whilst reduce the impact and harm in electromagnetic radiation on the human body or the equipment being interfered [1,3]. As a result, searching for high performance EMI shielding materials has become a burgeoning field of research. Currently, the most commonly used materials for EMI shielding are metals, such as stainless steel, copper, aluminum, silver, etc. due to good electrical conductivity, metals exhibit excellent EMI shielding performance. However, many metals come across problems of high specific weight, susceptibility to corrosion, and easy oxidation [4]. Among these materials, the diffusion of hydrogen into steels results in a number of problems such as; hydrogen-induced cracking, hydrogen stress cracking, sulfide stress corrosion cracking and hydrogen embrittlement [5]. With the increasing demand for EMI shielding in various applications, such as high temperature and corrosion circumstances, as well as hydrogen infiltration, there exists a growing interest in exploring suitable materials [4]. For this purpose, boriding of steel substrates should be promising approach and there is limited reports in open literature about EMI shielding effectiveness of borided steels.

Boriding, being a kind of thermo-chemical surface hardening process by which boron is introduced onto the surface of the steels and its alloys at elevated temperature and generally applied to engineering components to increase the superficial hardness, enhance their oxidation, abrasion, and erosion resistance [6,7, 8]. The formation borides such as FeB and Fe_2B depends on the process temperature, the chemical composition of the substrate steel, the boron potential of the medium and the duration of the boriding [9, 10]. The material alloy composition also plays an important role in the morphology and properties of the boride layer [10]. Borided surfaces can maintain their hardness, wear properties up to 1000 °C. One of the most important features of the borided surface is to retain its hardness even after additional heat treatment [11]. Various boriding techniques such as powder-pack boriding, liquid boriding, plasma boriding and gas boriding have been developed [12,13]. Pack boriding method is frequently used because of having technical favors and cost efficiency [11, 12]. The process consists of packing the samples in a powder mixture rich in boron inside of a stainless steel box [14]. Ferrous and non-ferrous materials are commonly borided in temperature range of 850–1000 °C and with treatment time range of 1–10 h or more in pack boriding process [11].

The aim of this study, to enhance surface properties such as ~~high~~ increasing hardness of Mirrax tool steel, by pack boriding method and investigate EMI shielding properties of the borided surface formed on the studied steel sample within the Ku band range. The main driving force of this report is there are limited reports about EMI-SE effectiveness of borided steels in open literature and therefore, it was focused on EMI-SE tests as well as the mechanical , morphological properties of borides formed on the Mirrax steel surface.

2. MATERIALS and METHOD

Mirrax steel samples with dimensions of 20x15x10 mm were ground with 240,320, 400 and 600 number SiC papers and at each grinding stage, grinding papers were lubricated with stream of water. Then, all samples were washed and dried. After drying, samples were taken to polishing wheel and polished with 1 μm diamond past in order to clean surface and enhance the boron diffusion efficiency prior to boriding process. Pack boriding was realized at 900, 950, 1000°C for 2, 5, 8h, respectively by sealing samples within steel container with Ekabor® as boronizing source and Ekrit® powders, for preventing possible oxidation. Chemical properties of the Mirrax steel was given in Table 1.

After boronizing, samples were grinded with SiC abrasive paper up to1000 grid and then polished with 1 μm alumina suspension. Polished samples were etched with 3 % of Nital (vol. 3% HNO_3-vol. 97%Ethanol) in order to carried out optical microscopy observation. The borides layer formed on the surface of steel substrate were examined via Nikon Eclipse L200 optical microscope. Layer thickness was measured with image analysis from the optical micrographs as-taken. XRD analysis was conducted by Rigaku PC2200 using CuKα with a wavelength of 1.54 nm between 20-90° range in order to detect boride phases in the borided layer. Microhardness of borides and variation of hardness from borides to matrix were measured by Nikon VM-HTMod with a load of 50g. Electromagnetic Interference Shielding test was carried out via Vector Network Analyzer (Agilent ENA E5071C) according to ASTM D4935 within the Ku band (12-20 GHz). Thickness of borided samples was reduced to 2 mm in order to elude the shielding efficiency of metallic matrix before EMI-SE test.

Table 1 Chemical composition of Mirrax® Steel

Elements/Chemical Composition, wt.%						
C	**Si**	**Mn**	**Cr**	**Mo**	**Ni**	**V**
0.25	0.35	0.55	13.3	0.35	1.35	0.35

3. RESULTS AND DISCUSSIONS

3.1. Optical Microstructure

Optical images of Mirrax sample borided at 900-1000°C for 2-8h were illustrated in Figure 1-3 (a-c). As it can be seen from optical micrographs, borided layer had smooth morphology and flat interface between layer and matrix. It was resulted from alloying elements of Cr, Ni due to high amount of Cr and Ni in the Mirrax steel matrix restricted the growing of borides layer [9, 15, 16, 17]. These elements, especially Cr, also has higher dissolution ability in the layer according to iron matrix because of atomic number of Cr was lower than that of Fe and therefore, higher porosity can be seen towards surface of the borides layer. It was probably resulted from more Cr promoted towards the surface of the borides layer by boriding temperature and time increased (Fig.1-3 a-c)[15]. On the other hand, Ni tends to accumulate at the end of borides layer during boriding process [16] and it can be claimed that grayish-black coloured zone beneath the layer indicated Ni and also Cr rich region. Ni elements pushed towards the tips of borides also formed the complex (Fe,Ni)B [16] as well as some Cr-borides with grayish-green coloured particle morphology at the grain boundaries and some of them can take place in the steel matrix observed as grayish-green colored small bright particles (Fig. 2-3b-c). As boronizing time and temperature progress, the borides layer became more porous as more alloying elements take place of iron during boriding and it leaded to more porosity formation [16].

It can be seen from optical micrographs, borided layer thickness increased with decreased growing rate by boriding progress and temperature raised (Fig. 1-3a-c). This is well-known diffusion phenomenon and in the presence of high alloying elements (Cr), growing of the borides layer become difficult. The nature of borides layer had polyphase morphology and consisted of FeB/Fe_2B (Fig. 2b). This polyphase nature was obviously seen in the samples borided at 950 and 1000 °C. At the beginning of the boriding process, boron diffusing occurs first, and Fe_2B phase is formed by the reaction of boron with iron. By increasing the thickness of this boride layer, the boron diffusion towards the end of borides and matrix is reduced and the FeB phase, which has higher boron content, starts to form on the Fe_2B phase by reaction of B with outer section Fe_2B (Fig. 2-3a-c) [9, 18].

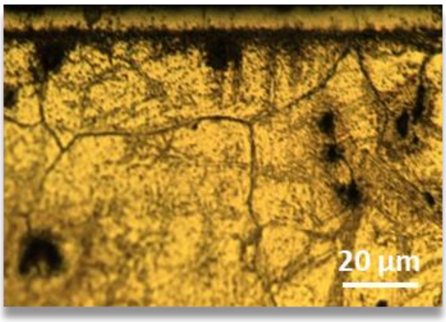

a)

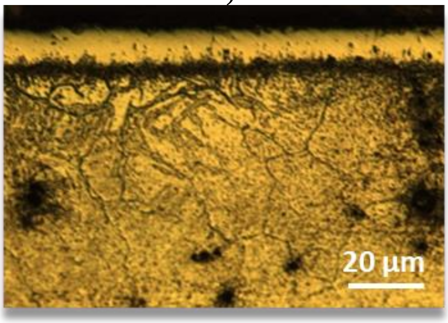

b)

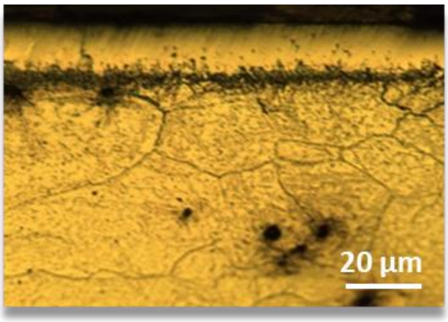

c)

Figure 1 Optical micrographs of Mirrax steel borided at 900°C, **a)** 2h, **b)** 5h, **c)** 8h.

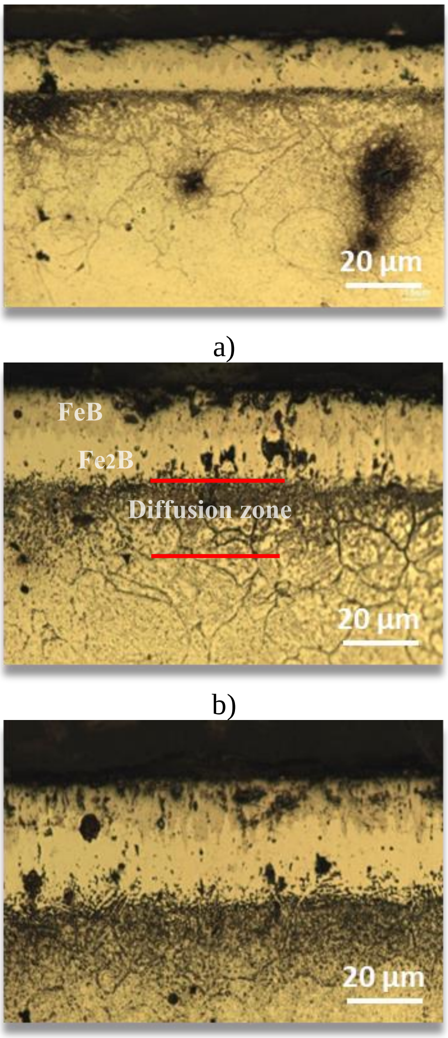

a)

b)

c)

Figure 2 Optical micrographs of Mirrax steel borided at 950°C, **a)** 2h, **b)** 5h, **c)** 8h.

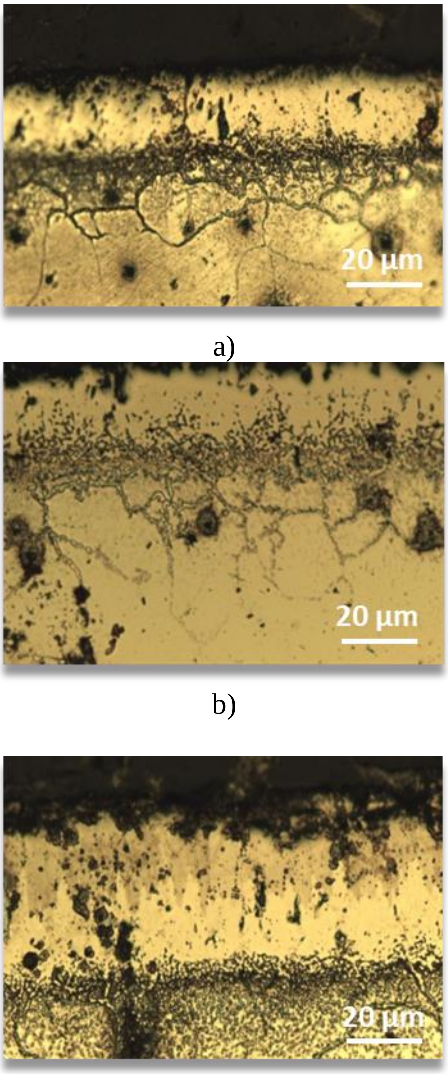

a)

b)

c)

Figure 3 Optical micrographs of Mirrax steel borided at 1000°C, a) 2h, b) 5h, c) 8h.

3.2. Layer Thickness

Variation of borides layer thickness was presented in Table 2 and it can be seen from Table 2, when boriding temperature increased, the thickness of borides layer rapidly growth for the short process time, 2h. So that, four time higher thickness for sample borided at 1000°C, 2h was measured compared to that of sample borided 900°C, 2h and the growing rate of borides reduced from four times to three and two-half times in the samples borided for 5 and 8h, respectively by increasing temperature. The growing of layer got slower when the process time increased for increasing temperatures. On the other hand, boriding temperatures was more dominant factor for growth of the borides layer. The obtained results was coming from nature of diffusion phenomenon as boronizing is diffusion base process, and results were similar to reports related to boriding of AISI 420 steel [16, 19]. Mirrax steel was derivated and developed from AISI 420 steel, thus similar but lower layer thickness was measured in Mirrax steel than that of AISI 420 due to higher amount of Cr and Ni according to AISI 420 steel.

Table 2 Borides Layer thickness depending on boriding time and temperature

Boriding Time (h)	Boride Layer Thickness (µm)		
	Boriding Tempereature (°C)		
	900	950	1000
2	11,55	32,06	43,85
5	21,32	46,50	66,63
8	33,51	62,20	86,15

3.3. XRD Analysis

XRD analysis of the boride samples were shown in Figure 4a-c.

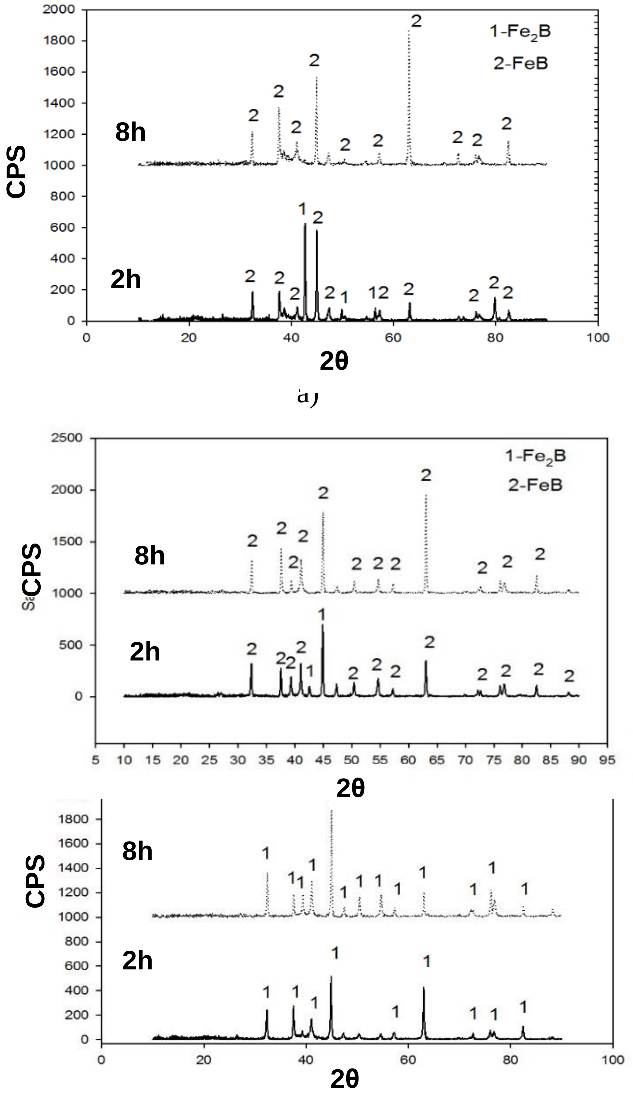

Figure 4 XRD analysis of borided Mirrax Steels according to boriding temperature, a) 900°C, b) 950°C, c) 1000°C.

When boriding process have just started, Fe_2B initially formed followed by saturation of matrix with boron. As boronizing process progressed, Fe_2B layer growth restrictly due to high amount of Cr as well as some Ni in the steel matrix and FeB started to form by reaction of boron rich Fe_2B on outer side of Fe_2B phase. Therefore, remarkable amount of FeB was detected in the sample even borided at 900°C for 2h (Fig. 4a). According to XRD analysis, FeB formation accelerated with increasing temperature and time. for 8h This led to detection of only FeB on the surface of borided matrix as thickness of FeB layer which took place outer zone of the borides increased with increment in boronizing time and tempearature. (Fig. 4b-c). It was reported that double phase (FeB/Fe_2B) was common for high alloy steels. [14, 17] Althogh there was high amount of Cr in the samples, there was no CrB detected due to possible a relative low intensity and a low volume fraction of the chromium boride phases within the borides layer [17].

3.4. Microhardness

Microhardness of borides formed on the steel samples was ranged from 1672 HV to 2215 HV by increasing of boriding temperature and times. Microhardness of the borided samples was four times higher than that of Mirrax steel matrix (500HV) which was higher than that of annealed Mirrax steel (250 HV) [20] (Fig. 5a-c). It was reported that AISI 420 steel could be air quenched and hardness of air quenched AISI 420 steel was approximately 500 HV. Mirrax have similar heat treatment characterizations with AISI 420 steel and identical results obtained for Mirrax steel [20, 21]. During boriding process, steel matrix was possibly exposed to air quenching and that matrix hardness was measured.

It can be observed from the Figure 5a-c, penetration of high hardness continued towards more inner section of matrix due to increasing of borides layer consisting of FeB and Fe_2B with increment in the process time and temperature. It can be said that microhardness of over 1800 HV was measured in max. 20 μm range in the samples borided at 900°C for 8h. There was also limited Ni rich diffusion zone having 600-1000HV microhardness observed in the same borided samples.

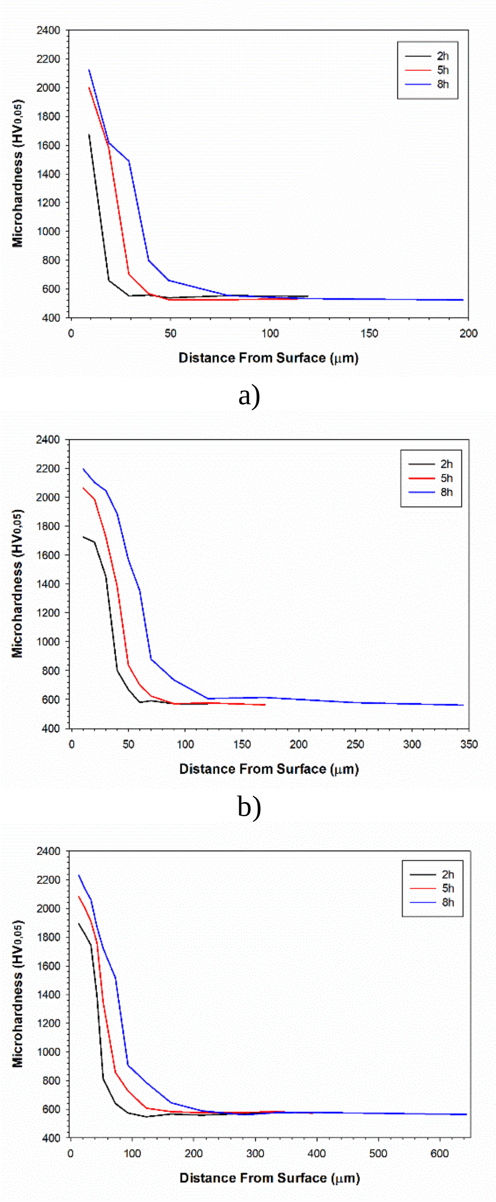

a)

b)

c)

Figure 5 Variation of microhardness from surface to interior of sample in the samples borided at a) 900°C, b) 950°C, c) 1000°C.

When boriding temperature raised to 950°C, it was observed that high microhardness of over 1800 HV could be measured up to 50 μm distance from the borides surface. Same phenomenon was seen up to 60 μm in the samples borided at maximum temperature. This was resulted from growing of the layer having FeB phase which is harder. By increasing of layer thickness, microhardness of 1800 HV was measured up to 75 μm, and diffusion zone also enlarged by increment in temperature and times. Microhardness of over 2000 HV measured in the all samples, except that of borided at 900°C for 2h possibly due to complex borides (Fe,Cr)B formation which was resulted from high amount of Cr within the FeB layer formed on the near surface regions (Fig.5a-c).

3.5. EMI-SE Analysis

EMI-SE (total) measurement were carried out within Ku band and results were presented in Figure 6a-c. Also, variation of mean EMI-SE with layer thickness was shown in Figure 7. As Figure 6a was investigated, it was found that at lower boriding temperature maximum EMI-SE was ranged from 60 to 74 dB by increasing process time. As boronizing time raised, variation of EMI-SE within Ku band seen in a narrower range. When boriding temperature increased to 950°C, maximum EMI-SE was measured between 70-79 dB. On the other hand, EMI-SE of sample borided at 950°C for 2h was significantly decreased to 60 dB after 13 GHz band passed and remained within 60-65 dB range up to 20 GHz. However, samples borided at 950°C for 5 and 8h performed higher EMI-SE efficiency and become more stable within the Ku band range. Samples borided at 1000°C had narrower, higher and more stable EMI-SE efficiency in the same band range. Maximum EMI-SE was ranged between 74 and 80 dB and samples caused a lower EMI-SE lost as boronizing time progressed with increased the band frequency (Fig. 6b-c).

When the layer thickness-EMI-SE relationship was examined, mean EMI-SE values reached the desirable maximum, 75 dB, at 46 μm borides layer thickness. After reaching out certain layer thickness, mean EMI-SE was not remarkably changed up to maximum layer thickness of 86 μm which belonged to sample borided at 1000°C for 8h (Fig. 7). It can be claimed that mean EMI-SE was increased by increasing of layer thickness up to 46 μm and certain amount of FeB phase. The borides layer have poly phase (FeB/Fe_2B) and thickness of FeB phase increased with growing of borides layer. The thickness of FeB was lower than half of total thickness of borides layer for the sample borided at 950° C for 5h. The higher boronizing temperature and duration, the higher FeB ratio to Fe_2B in the layer was observed. It was possibly reason of the fixing EMI-SE of around 75 dB.

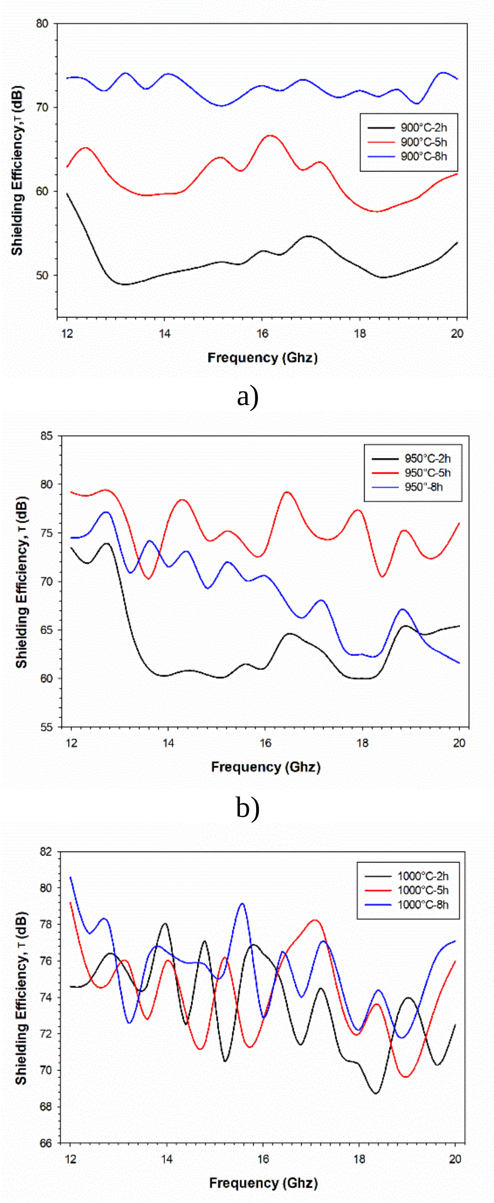

a)

b)

c)

Figure 6 Total EMI-SE in the Ku band of steel samples borided at a) 900°C, b) 950°C, c) 1000°C.

On the other hand, increasing FeB ratio and layer thickness led to narrower and more stable EMI-SE for samples borided at higher temperatures and durations (Fig.7).

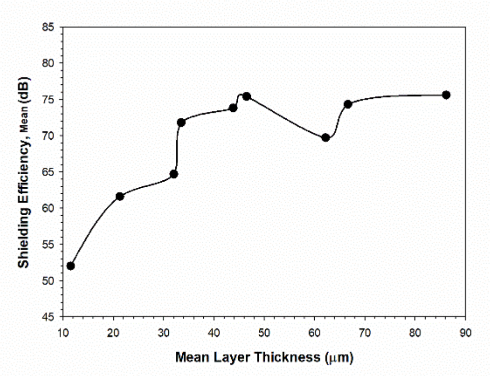

Figure 7 Variation of mean EMI-SE with borided layer thickness

4. CONCLUSIONS

The following results can be derived from this study,

a. The microstructure of borides formed on the surface of Mirrax steel was smooth morphology.
b. The thickness of borides layer, microhardness and penetration of microhardness were increased by increment of boriding temperature and time.
c. XRD revealed that borides layer showed biphasic nature (FeB, Fe_2B).
d. Maximum EMI-SE, total values increased from 50 to 80 dB as boriding time and temperature raised.
e. Mean EMI-SE of samples was increased with certain layer thickness (46 μm) and FeB ratio in the layer and it was found to be maximum 75 dB for sample borided at 950 °C for 5h.
f. It can be expressed that optimum EMI-SE values obtained in sample borided at 950 °C for 5h.
g. Layer thickness was more dominant effect than type of borides on the EMI-SE values. But, by increasing layer thickness and FeB amount made EMI-SE more stable within Ku band range.

ACKNOWLEDGEMENT

I would like to express my deepest thank to Prof. Dr. Cuma Bindal of Sakarya University for his invaluable supports.

REFERENCES

[1] N. Maruthi, M. Faisal and N. Raghavendra, "Conducting polymer based composites as efficient EMI shielding materials: A comprehensive review and future prospects," Synthetic Metals, vol. 272, pp. 1-20, 2021.

[2] G-H. Lim, N. Kwon, E. Han, S. Bok and S-E. Lee S, "Flexible Nanoporous Silver Membranes with Unprecedented High Effectiveness for Electromagnetic Interference Shielding," Journal of Industrial and Engineering Chemistry, Article in press, 2020.

[3] H. Liu, S. Wou, C. You, N. Tian, Y. Li and N. Chopra, "Recent progress in morphological engineering of carbon materials for electromagnetic interference shielding," Carbon, vol. 172, pp. 569–596, 2021.

[4] H. Zhang, B. Zhao, F-Z. Dai, H. Xiang and Z. Zhang, "$(Cr_{0.2}Mn_{0.2}Fe_{0.2}Co_{0.2}Mo_{0.2})B$: A novel high-entropy monoboride withgood electromagnetic interference shielding performance in K-band," Journal of Materials Science & Technology, vol. 77, pp. 58-65, 2021.

[5] N. L. Perrusquia, M. A. Doñu Ruiz, C.R. Torres San Miguel, G.J. Pérez Mendoza, J.V. Cortes Suarez and A. Juanico Loran, "Evaluation of properties in steel with boride coatings under hydrogen," Surface & Coatings Technology, vol. 377, pp. 1-9, 2019.

[6] G. K. Sireli, A. S. Bora and S. Timur, "Evaluating the mechanical behavior of electrochemically borided low carbon steel," Surface & Coatings Technology, vol. 381, pp. 1-10, 2020.

[7] M. Prince, S.L. Arjun, G. Surya Raj and P. Gopalakrishnan, "Experimental Investigations on the Effects of Multicomponent Laser Boriding on steels," Materials Today: Proceedings, vol. 5, pp. 25276-25284, 2018.

[8] S. A. Rosas-Meléndez, M. Elías-Espinosa, J.A. Reyes-Retana and F. Cervantes-Sodi, "Friction and wear of borided AISI O1 steel with carbon nanomaterial deposit," Materials Letters, vol. 282, pp. 1-4, 2021.

[9] A. Erdoğan, "Investigation of high temperature dry sliding behavior of borided H13 hot work tool steel with nanoboron powder," Surface & Coatings Technology, vol. 357, pp. 886-895, 2019.

[10] A. P. Krelling, C. E. da Costa, J.C.G. Milan and E.A.S. Almeida, "Micro-abrasive wear mechanisms of borided AISI 1020 steel," vol. 111, pp. 234-242, 2017.

[11] I. Turkmen, E. Yalamac and M. Keddam, "Investigation of tribological behaviour and diffusion model of Fe_2B layer formed by pack-boriding on SAE 1020 steel," Surface & Coatings Technology", vol. 377, pp. 1-12, 2019.

[12] I. Türkmen and E. Yalamaç, "Growth of the Fe2B layer on SAE 1020 steel employed a boron source of H3BO3 during the powder-pack boriding method," Journal of Alloys and Compounds, vol. 744, pp. 658-666, 2018.

[13] A. Bendoumi, N. Makuch, R. Chegroune, M. Kulka, M. Keddam, P. Dziarski and D. Przestacki, "The effect of temperature distribution and cooling rate on microstructure and microhardness of laser re-melted and laser-borided carbon steels with various carbon concentrations," Surface & Coatings Technology, vol. 387, pp. 1-20, 2020.

[14] E. H. Sanchez and J. C. Valezquez, “Kinetics of Growth of Iron Boride Layers on a Low-Carbon Steel Surface,” Laboratory Unit Operations and Experimental Methods in Chemical Engineering-Chapter 3, pp. 37-55, IntechOpen, 2018.

[15] İ. Güneş, “Investigation of Tribological Properties and Characterization of Borided AISI 420 and AISI 5120 Steels,” Trans Indian Inst Met, vol. 67, no. 3, pp. 359-365, 2014.

[16] N. Barut, D. Yavuz and Y. Kayalı, “Borlanmış AISI 5140 ve AISI 420 Çeliklerinin Difüzyon ve Adhezyon Davranışlarının İncelenmesi,” Afyon Kocatepe Üniversitesi Fen ve Mühendislik Bilimleri Dergisi, vol. 14, pp. 1-8, 2014.

[17] P. Juijerm, “Diffusion kinetics of different boronizing processes on martensitic stainless steel AISI 420,” Kovove Mater., vol. 52, pp. 232-236, 2014.

[18] C. Martini, G. Palombarini and M. Carbucicchio,” Mechanism of thermochemical growth of iron borides on iron,” Journal of Materials Science, vol. 39, pp. 933-937, 2004.

[19] Y. Kayali, “Investigation of the diffusion kinetics of borided stainless steels,” Physics of Metals and Metallography, vol. 114, pp. 161-168, 2013.

[20] https://www.uddeholm.com/app/uploads/sites/40/2017/11/mirrax esr-eng p.1506-1602.pdf, Erişim tarihi: 12.01.2021.

[21] C. J. Scheuera, R. A. Fraga, R. P. Cardoso and S.F. Brunatto, “Effects Of Heat Treatment Condıtıons On Mıcrostructure And Mechanıcal Propertıes Of AISI 420 Steel,” 21º CBECIMAT - Congresso Brasileiro de Engenharia e Ciência dos Materiais, pp. 5857-5867, 2014.

SAKARYA ÜNİVERSİTESİ
FEN BİLİMLERİ ENSTİTÜSÜ
DERGİSİ

Sakarya University Journal of Science
SAUJS

e-ISSN 2147-835X Founded 1997 Period Bimonthly Publisher Sakarya University
http://www.saujs.sakarya.edu.tr/en/

Title: A Comparative Investigation of the Mechanical Properties of Single and Bi Layer MoS2 Structures: Influences of Defect, Strain Rate and Temperature

Authors: Ahmet Emin ŞENTÜRK

Recieved: 2021-02-25 00:00:00

Accepted: 2021-10-15 00:00:00

Article Type: Research Article

Volume: 25
Issue: 6
Month: December
Year: 2021
Pages: 1313-1321

How to cite
Ahmet Emin ŞENTÜRK; (2021), A Comparative Investigation of the Mechanical Properties of Single and Bi Layer MoS2 Structures: Influences of Defect, Strain Rate and Temperature. Sakarya University Journal of Science, 25(6), 1313-1321, DOI: https://doi.org/10.16984/saufenbilder.886377
Access link
http://www.saujs.sakarya.edu.tr/tr/pub/issue/66341/886377

Sakarya University Journal of Science 25(6), 1313-1321, 2021

A Comparative Investigation of the Mechanical Properties of Single and Bi Layer MoS_2 Structures: Influences of Defect, Strain Rate and Temperature

Ahmet Emin ŞENTÜRK*[1]

Abstract

In this paper, the mechanical properties of single and bi layer molybdenum disulfide (MoS_2) structures are investigated using uniaxial tensile molecular dynamics (MD) simulation. According to the results of MD simulations, these structures show superior mechanical properties (failure strain, ultimate tensile strength and Young's modulus) for various applications of nanodevice. The mechanical properties of single and bi layer MoS_2 structures are studied at four different temperatures between 300 K and 900 K and different strain rates from 10^7 s^{-1} to 10^9 s^{-1}. As temperature increases up to 900 K, the mechanical properties of single and bi layer MoS_2 structures gradually decrease, due to the high tempreraturе's weakening effect. Also, changing of temperatures shows more effect on the bi layer MoS_2 structure than single layer MoS_2 structure. Furthermore, MD results show that the mechanical properties of single and bi layer MoS_2 structures demonstrate increasing trend when the strain rate increases. Different strain rates indicate similar effects on the mechanical properties of single and bi layer MoS_2 structures. On the other hand, the mechanical properties of these structures are adversely affected by structural defects. Accordingly, the influences of two different S atom types vacancy defect on the mechanical properties of single and bi layer MoS_2 structures are examined. When the vacancy defect concentrations in MoS_2 structures increase, the mechanical properties of these structures decrease significantly. In addition, S atom bi vacancy defects type exerts more effect on the mechanical properties of single and bi layer MoS_2 structures than S atom single vacancy defect type do by increasing concentration. Additionally, vacancy defects indicate more influence on the bi layer MoS_2 structure than single layer MoS_2 structure. Finally, the results of this study make them excellent candidate for nano-mechanical systems.

Keywords: molecular dynamics, MoS_2 structure, mechanical properties.

1. INTRODUCTION

The discovery of 2D nanomaterials, many investigations have been conducted for the applications in nanodevice. Due to 2D transition metal dichalcogenides' (TMDs) electronic, mechanical, thermal, structural properties and many potential applications [1-5], they have gained increasing attention, recently. For example, molybdenum disulfide (MoS_2), a 2D semiconductor, is promising member of TMDs family with hexagonal lattice structure. Different from graphene, because of its considerable band gap, MoS_2 is proposed as an excellent potential candidate in flexible electronics and optoelectronic devices [6, 7], piezoelectronics [8],

---

* Corresponding author: ahmeteminsenturk@maltepe.edu.tr

[1] Maltepe University / Faculty of Engineering and Natural Sciences /Department of Industrial Engineering

ORCID: https://orcid.org/0000-0003-1493-0965

high-performance field-effect transistors [3], and valleytronics, [9, 10]. MoS_2 can be further manipulated via changing its stacking order [11], number of layer [12], or by application of mechanical strain [13, 14]. MoS_2 is consisting of S_{upper}–Mo–S_{lower} triple thickness layers. During synthesizing or processing, in reality, structural defects, such as, Stone-Wales and vacancy, are unavoidably observed in MoS_2. Structural defect affects the physical, mechanical and chemical properties of MoS_2. Only vacancy defect was examined in this investigation.

The mechanical properties of 2D nanostructures have examined by several researchers using molecular dynamics (MD) simulations, in recent years [15, 16]. The published knowledges regarding the mechanical properties of single and bi layers MoS_2 structures are still limited, despite of the earlier experimental realization of these structures. Comprehensive computational estimates of the mechanical properties of single and bi layers MoS_2 structures are examined, in this investigation. Additionally, understanding the effects of vacancy defect on the mechanical properties of MoS_2 structure are crucial issue. Mamun et al. [17] investigated the effects of different types of vacancy defects, such as, single and bi-vacancy, on thermal properties of single layer MoS_2 structure. They indicated that thermal property of single layer MoS_2 structure is significantly reduced with increasing defect concentrations. However, the effects of vacancy defect on the mechanical properties of MoS_2 structure get less attention from authors. Thus, the influences of single and bi vacancy defects on the single and bi layers MoS_2 structures are studied. In this work, because of problems in experimental characterizations of 2D nanomaterials, MD simulation was used as an alternative of experimental studies.

2. SIMULATION METHODS AND PHYSICAL MODELS

In this investigation, the VNL package [18] was used for visualization, while all MD simulations of MoS_2 structure were conducted by using LAMMPS [19], which is the publicly available simulation code. The physical model of the atomistic structure of MoS_2 was illustrated in Figure 1. Single and bi layer MoS_2 structures consisting of 7500 and 15000 atoms, respectively, were built with almost 13.6 nm in width and 15.8 nm in length.

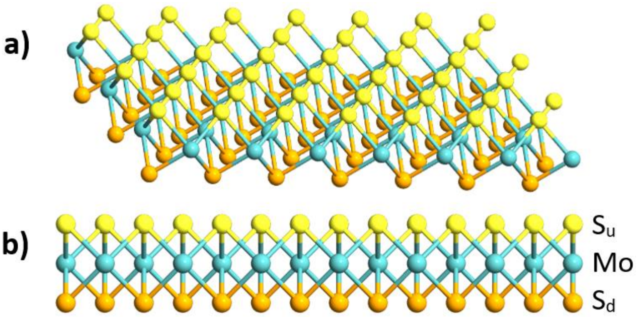

Figure 1 Physical model of the non-defective single layer MoS_2 structure: Mo represents a molybdenum atom and S_d and S_u represent S atom in the lower and upper layer, a) top and b) side views

To compute the mechanical properties of single and bi layer MoS_2 structures, uniaxial tensile test was conducted at room temperature (300 K) for loading condition. Integration scheme of velocity Verlet was used in the calculation to solve the motion-equations with a time step of 0.5 fs. For defining the interatomic interactions of single and bi layer MoS_2 structures, the correctness of force field is so important. There are several potential for use in MD simulations, such as Stillinger-Weber (SW), Tersoff and Brenner. The Tersoff and Brenner bond-order potentials have had particular success for carbon-based materials. Beside these potentials, the SW potential is another successful empirical potential for covalently bonded systems. The SW potential has a simpler form and fewer parameters than the Brenner potential, so it is much faster. One of the practical advantage of the SW potential is that it has been implemented in almost all available MD simulation packages. For these structures, the SW potential is chosen. This potential is simple and contains all possible atomic interactions of S and Mo [20, 21]. Therefore, it is used to describe the interatomic interactions of these structures. Additionally, this potential provides an accurate prediction for the structural parameters of MoS_2. The form of SW potential can be written as,

$$E = \sum_{i}\sum_{j>i} \emptyset_2(r_{ij}) + \sum_{i}\sum_{j\neq i}\sum_{k>j} \emptyset_3(r_{ij}, r_{ik}, \theta_{ijk}) \quad (1)$$

The two-body interaction potential $\emptyset_2$ takes the following form.

$$\emptyset_2(r_{ij}) = A_{ij}\left(\frac{B_{ij}}{r_{ij}^4} - 1\right) \times exp\left[\frac{\rho_{ij}}{r_{ij} - r_{ij}^{max}}\right] \quad (2)$$

The three-body interaction potential $\emptyset_3$ in Equation (1) is modeled as;

$$\emptyset_3(r_{ij}, r_{ik}, \theta_{ijk}) = K_{ijk} exp\left[\frac{\rho_{ij}}{r_{ij} - r_{ij}^{max}} + \frac{\rho_{ik}}{r_{ik} - r_{ik}^{max}}\right] \times \left(cos\theta_{ijk} - cos\theta_{0,ijk}\right)^2 \quad (3)$$

$\emptyset_2$ and $\emptyset_3$ represents the two body (bond stretching) and three body (bond bending) interactions. The pair separations are described by r_{ij} and r_{ik}. The angle between the separation vectors centering on atom-i is denoted by θ_{ijk}. The potential parameters are A, B, K, ρ, along with r^{max} cutoff radii and equilibrium angles and they rely upon on the atoms interacting with each other. Periodic boundary conditions (PBCs) are used to the in-plane directions (x and y directions), in order to minimize edge effects. Single and bi layer MoS_2 structures are uniaxially stretched at strain rate of 10^9 s^{-1}. Virial stresses are computed at each strain's level to acquire a stress–strain response. The Young's modulus (YM) of MoS_2 structure was computed at low level of the strain (up to 0.05) of the linear region. The stress (σ), strain (ε) and YM (E) of single and bi layer MoS_2 structures can be written as:

$$\varepsilon = \frac{l - l_0}{l_0} \quad (4)$$

$$\sigma = \frac{1}{At}\frac{\partial U}{\partial \varepsilon} \quad (5)$$

$$E = \frac{1}{At}\frac{\partial^2 U}{\partial^2 \varepsilon} \quad (6)$$

here, the thickness, surface area and strain energy of single and bi layer MoS_2 structures are expressed by t, A and U, respectively. The final and initial lengths of these structures are denoted by l and l_0, respectively.

3. RESULTS AND DISCUSSION

Firstly, to understand the energetic stability of the MoS_2 structure, per-atom cohesive energy was computed as:

$$E_{coh} = \left(\sum_{i} E_i - E_t\right)/n \quad (7)$$

here n, E_t and E_i denote the total number of atoms in the cell, total energy per cell and the energy of the i-th isolated atom, respectively. MD results indicated that the cohesive energy of MoS_2 structure is negative, -10.41 eV. This result indicate that MoS_2 structure is energetically stable.

3.1. Mechanical Properties

In this section, the MD simulations system was employed to investigate the effects of various temperatures, structural defects and different strain rates on mechanical properties of single and bi layers MoS_2 structures. Firstly, the computed uniaxial stress–strain response for considered single layer MoS_2 structure was showed in Figure

2. The YM, ultimate tensile strength (UTS) and failure strain (FS) of single layer MoS_2 structure were acquired at low strain levels (up to 0.05). At 300 K, the acquired YM, UTS and FS values of single layer MoS_2 structure are 0.202 TPa, 42.7 GPa and 0.155, respectively. These results are in agreement with the previous study [22] on the single layer MoS_2 structure. Also, the mechanical properties of bi layer MoS_2 structure were studied. The YM, UTS and FS of bi layer MoS_2 structure are 0.191 TPa, 40.3 GPa and 0.149, respectively. These results revealed that these structures have outstandingly high mechanical properties.

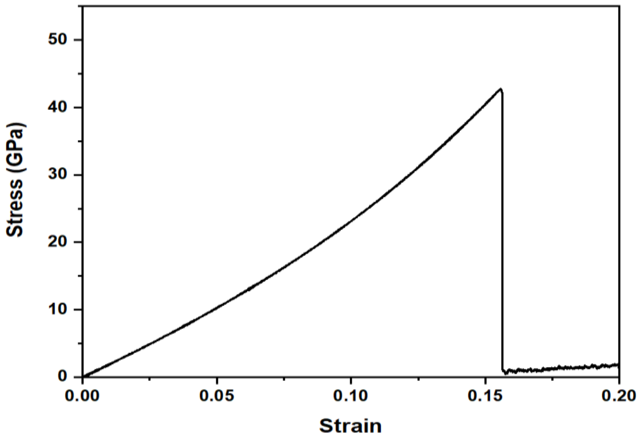

Figure 2 Stress-strain curve of pristine MoS_2 structure at room temperature

3.1.1. Temperature Effects

In this part of this study, the effects of various temperatures on the mechanical properties of single and bi layer MoS_2 structures were examined. Using MD simulations for single and bi layer MoS_2 structures at 300 K, 500 K, 700 K and 900 K, the UTS, FS and YM values of single and bi layer MoS_2 structures are presented in Figure 3. According to these results, by rising the temperatures up to 900 K, the UTS, FS and YM of single and bi layer MoS_2 structures gradually reduce. With increasing temperature, these structures become softer and less stiff. The atomic thermal vibrations get more dramatically robust and the vibrational amplitudes seem to be more tremendous while the temperature is growing up. This growing prompts the interatomic distance expands. When the distances of neighbors atoms increase, the interaction energy of atoms decrease by increasing temperature. Therefore, the UTS of single and bi layer MoS_2 structures reduces. Also, by increasing temperature, the strain energy reduces because of the rising kinetic energy. Hence, high temperatures affect the FS adversely. As temperature is increased, the binding energy between atoms reduces. Thus, the YM values of single and bi layer MoS_2 structures decrease.

According to Figure 3, when the temperature rises from 300 K to 900 K, the maximum variations in the YM of single and bi layer MoS_2 structures are around 23.7% and 27%, respectively. The UTS of single and bi layer MoS_2 structures are 66.3% and 68.3% lower than those at room temperature, respectively, when the temperature is increased to 900K. Similar to other properties, the FS reduction of single and bi layer MoS_2 structures are computed around 55.1% and 59.2%, respectively, as the temperatures rise from 300 K to 900 K. The difference between monolayer and multilayer MoS_2 can be lies in the presence of the van der Waals interlayer interaction. The interlayer van der Waals interaction between adjacent layers is not that strong. Therefore, it cannot boost the mechanical properties for multilayer MoS_2 significantly. As a result, changing of temperatures shows more effect on the bi layer MoS_2 structure than single layer MoS_2 structure. It is important to note that, the van der Waals interaction can be strengthened by various methods such as, chemical functionalization and surface roughness modification.

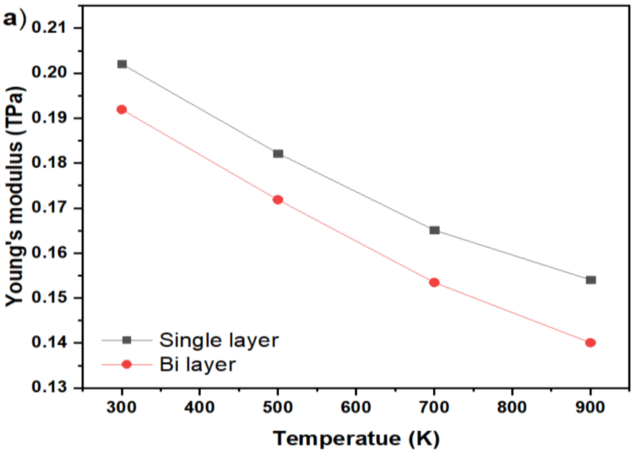

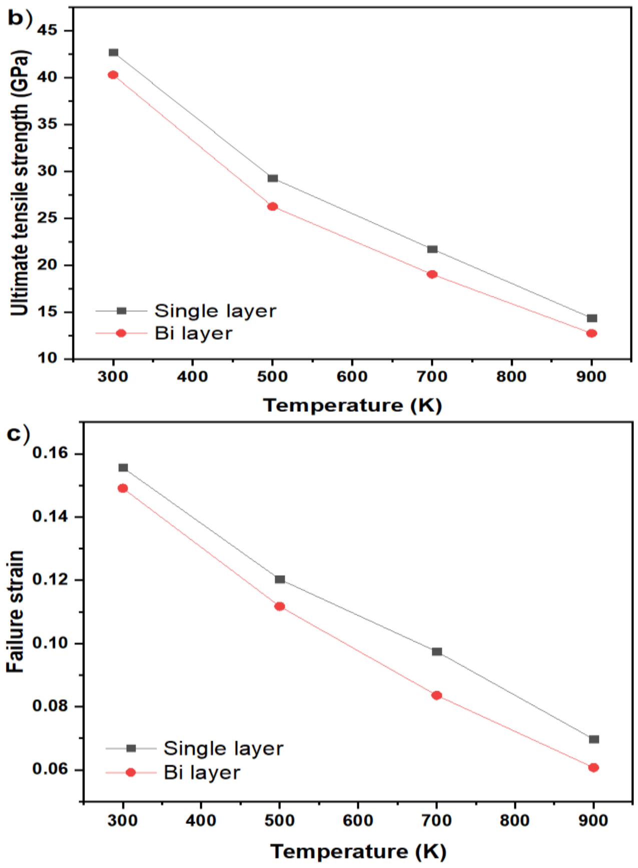

Figure 3 a) Young's modulus b) ultimate tensile strength and c) failure strain of MoS_2 structure as a function of different temperatures

3.1.2. Strain Rate Effects

The effects of different strain rates on the mechanical properties of single and bi layer MoS_2 structures were studied. In Figure 4, the UTS, FS and YM of single and bi layer MoS_2 structures were shown as a function of different strain rate. It can be seen in Figure 4, as the strain rate rises from 10^7 s^{-1} to 10^9 s^{-1}, the YM, UTS and FS of single and bi layer MoS_2 structures show an increasing trend. Additionaly, it can be said that the strain rates influence on the mechanical properties of single and bi layer MoS_2 structures indicate similar behavior. As observed in Figure 4, as the strain rate reduces from 10^9 s^{-1} to 10^7 s^{-1}, the maximum differences in the UTS, FS and YM of single layer MoS_2 structure are around 13.1%, 22.4% and 25.6%, respectively, at 300 K. Additionally, as shown in Figure 4, the UTS, FS and YM reduction of bi layer MoS_2 structure are almost 14.6%, 21.4% and 24.5%, respectively, when the strain rate is decreased to 10^7 s^{-1}, at room temperatue. Also, various strain rates show similar influences on the UTS, FS and YM of single and bi layer MoS_2 structures.

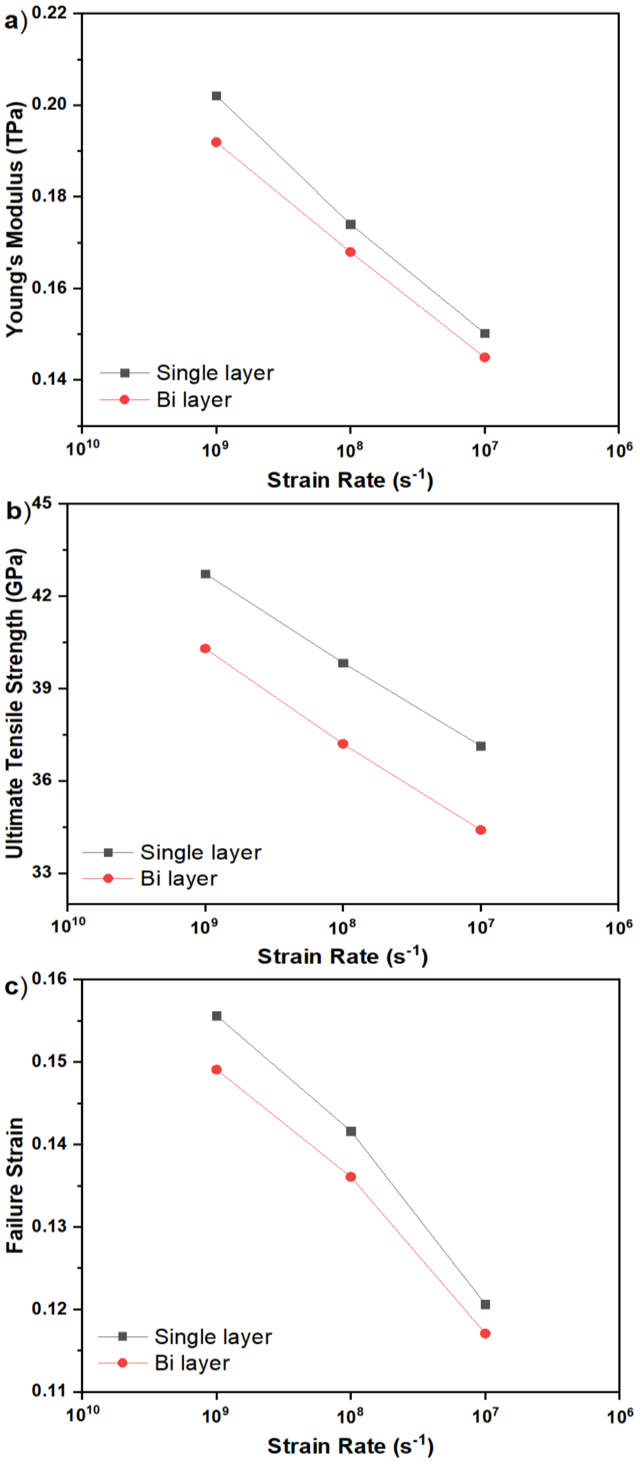

Figure 4 a) Young's modulus b) ultimate tensile strength and c) failure strain of MoS_2 structure as a function of different strain rates

3.1.3. Defect Effects

The influences of two different S atom types vacancy defect (point and bi vacancy) on the mechanical properties of single and bi layer MoS_2 structures were investigated, in this part. It is important to note that experimentally introduce S atom defects into the MoS_2 structures is found to be easier than defects caused by Mo atom defects [23]. Therefore, only S atom vacancy defect was examined, in this study. The atomic structures of the defective MoS_2 with point and bi vacancy defects are shown in Figure 5.

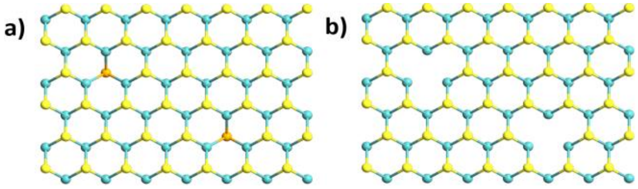

Figure 5 The atomic structure of the defective MoS_2 structures with a) point and b) bi vacancies

As observed in Figure 6, due to the S atom point and bi vacancy defects in the single and bi layer MoS_2 structures at 300 K, the mechanical properties of these structures decrease. Additionally, in Figure 6, the effects of eight various concentrations of S atom vacancy defects on the UTS, FS and YM of single and bi layer MoS_2 structures were investigated. As the point and bi vacancy defects concentration increases up to to 4%, the mechanical properties of single and bi layer MoS_2 structures containing vacancy defects gradually reduce, in Figure 6. The MD simulation results in Fig. indicated that the type of S atom bi vacancy defect exerts more influence on the FS, UTS and YM than other do with increasing concentrations because type of S atom bi vacancy defect occurs a hole in the structure. For single layer MoS_2 structure, the maximum variations in the YM, UTS and FS between the pristine MoS_2 structure and that one with S atom bi vacancy defect type are about 27.9%, 78.3% and 64.1%, respectively, in Figure 6. Furthermore, as shown in Figure 6, the variations of the YM, UTS and FS between the pristine MoS_2 structure and that one with S atom single vacancy defect type are changed between 22.9%, 72.9% and 58.8%, respectively. Also, for bi layer MoS_2 structure, the maximum variations in the YM, UTS and FS between the pristine bi layer MoS_2 structure and that one with S atom bi vacancy defect type are almost 25%, 82% and 65.1%, respectively, in Figure 6. In addition, the differences of the YM, UTS and FS between the pristine bi layer MoS_2 structure and that one with S atom single vacancy defect type are changed between 20%, 77.3% and 60.4%, respectively. For both single and bi layer MoS_2 structures, vacancy defect type's changing indicates more influence on the FS and UTS than YM does by rising defect concentration.

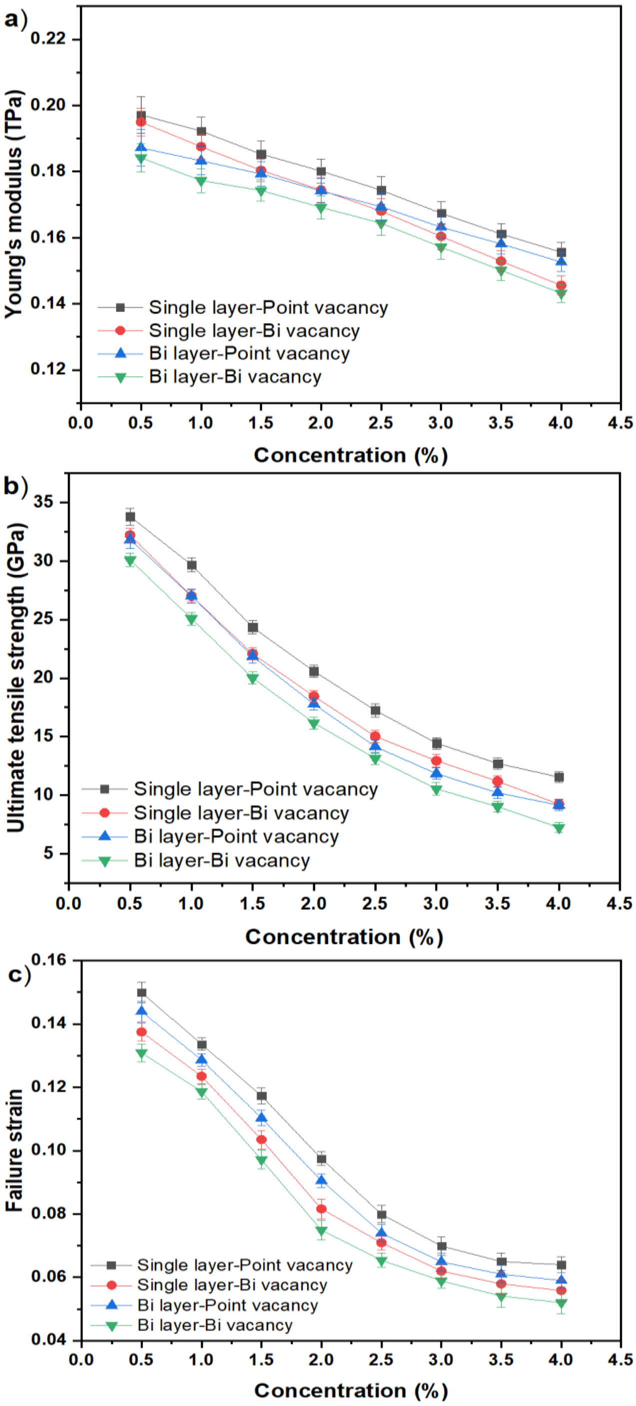

Figure 6 a) Young's modulus b) ultimate tensile strength and c) failure strain of single and bi layer MoS_2 structures as a function of the concentration of point and bi S atoms vacancy defects

4. CONCLUSIONS

In this study, via utilizing MD simulations, the mechanical properties (FS, UTS and YM) of single and bi layer MoS_2 structures are investigated. Also, the influences of various strain rates, vacancy defects and temperatures on the single and bi layer MoS_2 structures are studied. MD simulation results indicated that single and bi layer MoS_2 structures have ultra high mechanical properties. The influences of four various temperatures from 300 K to 900 K on the mechanical properties of single and bi layer MoS_2 structures are examined. As the atomic bonds become weaker at higher temperatures, the lower FS, UTS and YM values occur. In addition, bi layer MoS_2 structure has lower mechanical properties than single layer MoS_2 structure, at high temperature. It is also demonstrated that the existence of point and bi vacancy defects in single and bi layer MoS_2 structures reduce the mechanical properties of these structures remarkably by increasing concentrations of defects. Furthermore, S atom bi vacancy defect type exerts more effect on the mechanical properties of single and bi layer MoS_2 structures than S atom single vacancy defect type do with increasing concentrations. The effects of various strain rates from from 10^7 s^{-1} to 10^9 s^{-1} on the FS, UTS and YM of single and bi layer MoS_2 structures are studied. The FS, UTS and YM of single and bi layer MoS_2 structures indicate increasing trend, as the strain rate increases. Single and bi layer MoS_2 structures, along with superior electronic properties, exhibit ultra high mechanical properties which make it a promising candidate for nano-mechanical system.

Conflict of Interest

No conflict of interest or common interest has been declared by the authors.

Ethics Committee Approval

This study does not require ethics committee permission or any special permission.

Research and Publication Ethics

The author of the paper declare that he complies with the scientific, ethical and quotation rules of SAUJS in all processes of the paper and that he does not make any falsification on the data collected. In addition, he declares that Sakarya University Journal of Science and its editorial board have no responsibility for any ethical violations that may be encountered, and that this study has not been evaluated in any academic publication environment other than Sakarya University Journal of Science.

REFERENCES

[1] S. Das, J. A. Robinson, M. Dubey, H. Terrones and M. Terrones, “Beyond graphene: progress in novel two-dimensional materials and van derWaals solids,” Annual Review of Materials Research, vol. 45, no. 1, pp. 1–27, 2015.

[2] A. Pospischil, M. M. Furchi and T. Mueller, “Solar-energy conversion and light emission in an atomic monolayer p–n diode,” Nature Nanotechnology, vol. 9, pp. 257–261, 2014.

[3] B. Radisavljevic, A. Radenovic, J. Brivio, V. Giacometti and A. Kis, “Single-layer MoS2 transistors,” Nature Nanotechnology, vol. 6, pp. 147–150, 2011.

[4] B. Liu and K. Zhou, “Recent progress on graphene-analogous 2D nanomaterials: properties, modeling and applications,” Progress in Materials Science, vol. 100, pp. 99–169, 2019.

[5] B. Mortazavi, A. Ostadhossein, T. Rabczuk and A. C. T. Van Duin, “Mechanical response of all-MoS2 single-layer heterostructures: a ReaxFF investigation”, Physical Chemistry Chemical Physics, vol. 18, no. 34, pp. 23695–23701, 2016.

[6] H. Chang, S. Yang, J. Lee, L. Tao, W. Hwang, D. Jena, N. Lu and D. Akinwande, “High-performance, highly bendable MoS2

transistors with high-k dielectrics for flexible low-power systems," ACS Nano, vol. 7, no. 6, pp. 5446–5452, 2013.

[7] O. Lopez-Sanchez, D. Lembke, M. Kayci, A. Radenovic and A. Kis, "Ultrasensitive photodetectors based on monolayer MoS2," Nature Nanotechnology, vol. 8, pp. 497–501, 2013.

[8] W. Wu, L. Wang, Y. Li, F. Zhang, L. Lin, S. Niu, D. Chenet, X. Zhang, Y. Hao, T. F. Heinz, J. Hone and Z. L. Wang, "Piezoelectricity of single-atomic-layer MoS2 for energy conversion and piezotronics," Nature, vol. 514, no. 7523, pp. 470–474, 2014.

[9] H. Zeng, J. Dai, W. Yao, D. Xiao and X. Cui, "Valley polarization in MoS2 monolayers by optical pumping," Nature Nanotechnology, vol. 7, pp. 490–493, 2012.

[10] K. F. Mak, K. He, J. Shan and T. F. Heinz, "Control of valley polarization in monolayer MoS2 by optical helicity," Nature Nanotechnology, vol. 7, pp. 494–498, 2012.

[11] K. Liu, L. Zhang, T. Cao, C. Jin, D. Qiu, Q. Zhou, A. Zettl, P. Yang, S.G. Louie and F. Wang, "Evolution of interlayer coupling in twisted molybdenum disulfide bilayers," Nature Communications, vol. 5, no. 4966, 2014.

[12] K. F. Mak, C. Lee, J. Hone, J. Shan and T. F. Heinz, "Atomically thin MoS2: a new direct-gap semiconductor," Physical Review Letters, vol. 105, no. 136805, 2010.

[13] P. Lu, X. Wu, W. Guo and X. C. Zeng, "Strain-dependent electronic and magnetic properties of MoS2 monolayer, bilayer, nanoribbons and nanotubes," Physical Chemistry Chemical Physics , vol. 14, no. 37, pp. 13035-13040, 2012.

[14] S. Bhattacharyya and A. K. Singh, "Semiconductor-metal transition in semiconducting bilayer sheets of transition-metal dichalcogenides," Physical Review B, vol. 86, no. 075454, 2012.

[15] A. E. Senturk, "Outstanding thermo-mechanical properties of graphene-like B3C3 and C3N3," Applied Physics A, vol. 126, no. 8, pp. 1–15, 2020.

[16] A. E. Senturk, A. S. Oktem, A. E. S. Konukman, "Thermal conductivity and mechanical properties of graphene-like BC2, BC3 and B4C3", Molecular Simulation, vol. 46, no. 12, pp. 879–888, 2020.

[17] M. A. Z. Mamun, A. A. Mohaimen and S. Subrina, "Tunable thermal conductivity of single layer MoS2 nanoribbons: an equilibrium molecular dynamics study," Journal of Computational Electronics, vol. 19, no. 13, pp. 957–965, 2020.

[18] S. Smidstrup et al., "QuantumATK: An integrated platform of electronic and atomic-scale modelling tools", Journal of Physics: Condensed Matter, vol. 32, no. 015901, 2020.

[19] S. Plimpton, "Fast parallel algorithms for short-range molecular dynamics," Journal of Computational Physics, vol. 117, no. 1, 1995.

[20] A. Kandemir, H. Yapicioglu, A. Kinaci, T. Cagin and C. Sevik, "Thermal transport properties of MoS2 and MoSe2 monolayers," Nanotechnology, vol. 27, no. 55703, 2015.

[21] M. Wen, S. N. Shirodkar, P. Plech, E. Kaxiras, R. S. Elliott and E. B. Tadmor, "A force-matching Stillinger-Weber potential for MoS2: Parameterization and Fisher information theory based sensitivity analysis," Journal of Applied Physics, vol. 122, no. 244301, 2017.

[22] J.-W. Jiang, H. S. Park and T. Rabczuk, "Molecular dynamics simulations of single-layer molybdenum disulphide (MoS2): Stillinger-Weber parametrization,

mechanical properties, and thermal conductivity," Journal of Applied Physics, vol. 114, no. 064307, 2013.

[23] H. P. Komsa and A. V. Krasheninnikov, "Native defects in bulk and monolayer MoS2 from first principles," Physical Review B, vol. 91, no. 125304, 2015.

SAKARYA ÜNİVERSİTESİ
FEN BİLİMLERİ ENSTİTÜSÜ
DERGİSİ

Sakarya University Journal of Science
SAUJS

e-ISSN 2147-835X Founded 1997 Period Bimonthly Publisher Sakarya University
http://www.saujs.sakarya.edu.tr/en/

Title: Determination of Indoor Air Quality in University Student Canteens

Authors: Gülgün DEDE, Cemile DEDE

Recieved: 2020-01-03 00:00:00

Accepted: 2021-10-18 00:00:00

Article Type: Research Article

Volume: 25
Issue: 6
Month: December
Year: 2021
Pages: 1322-1331

How to cite
Gülgün DEDE, Cemile DEDE; (2021), Determination of Indoor Air Quality in University Student Canteens. Sakarya University Journal of Science, 25(6), 1322-1331, DOI: https://doi.org/10.16984/saufenbilder.669802
Access link
http://www.saujs.sakarya.edu.tr/tr/pub/issue/66341/669802

Sakarya University Journal of Science 25(6), 1322-1331, 2021

Determination of Indoor Air Quality in University Student Canteens

Gülgün DEDE[1], Cemile DEDE*[2]

Abstract

The negative effects of indoor air quality cause a decrease in the working efficiency of people, and health problems. For this reason, monitoring the indoor air quality of the places where students spend time such as canteen, cafeteria and library is important in terms of quality of life. Particulate matter is the leading source of pollutants affecting indoor air quality. For this purpose, the indoor air quality of student canteens in a public university located in Marmara Region, Turkey was examined in terms of temperature, relative humidity, person density, area, particulate matter ($PM_{2.5}$ and PM_{10}) parameters. The relative humidity in canteens was found to be within normal range in terms of comfort conditions, and the temperature was slightly higher depending on seasonal conditions and canteen conditions. According to the results of Spearman's correlation analysis applied, a statistically significant negative correlation between temperature and $PM_{2.5}$ (r=-0.449) and PM_{10} (r=-0.339) measurements, a positive correlation between humidity and $PM_{2.5}$ (r=0.974) and PM_{10} (r=0.440) measurements, and a positive correlation between the number of people and $PM_{2.5}$ (r=0.320) measurements ($p<0.05$), a positive correlation between $PM_{2.5}$ (r=0.454) and PM_{10} were detected ($p<0.01$). It was determined that World Health Organization (WHO) limit values and air pollution regulation limit values were exceeded in canteens except E3 and A1 canteens. Due to the insufficient ventilation of the canteens, it was determined that particulate matter may pose a risk to the students and the employees of the canteen, and recommendations were made to improve the indoor air quality.

Keywords: Indoor air quality, $PM_{2.5}$, PM_{10}, temperature, relative humidity, canteen

1. INTRODUCTION

The air quality within and around buildings and structures, particularly relating the building occupants' health and comfort, is considered as Indoor Air Quality (IAQ) [1]. It has been stated that low IAQ may cause building-related diseases and adversely affect human health. Nowadays, people spend most of their time in indoor environments where there are crowded communities such as houses, workplaces, schools, indoor shopping centers and canteens [2]. However, according to the U.S. Environmental Protection Agency (EPA) pollutants levels in indoor air may be two to five times and sometimes even more than 100 times

---

* Corresponding author: cdede@sakarya.edu.tr

[1] Sakarya University, Faculty of Engineering, Department of Environmental Enginering
E-mail: gulgunk@sakarya.edu.tr
ORCID: https://orcid.org/0000-0003-0302-6508

[2] Sakarya University, Vocational School of Health Sciences
ORCID: https://orcid.org/0000-0003-4040-9137

higher than outdoor air levels [3]. Therefore, IAQ has a significant impact on health. The adverse health effects of indoor air pollutants may be occur immediately after exposure or may show up years later [1]. Both short-term and long-term exposure to IAP can cause a wide variety of diseases. Short-term effects include eye, nose and throat irritation, headache, dizziness and fatigue. Other health effects may occur years after exposure has occurred or only after prolonged or repeated exposure periods. These effects, which include some respiratory diseases, heart disease and cancer, can be fatal [4].

IAQ can be affected by many sources of pollution such as outdoor air, building materials, furniture materials, fuels used in activities such as heating, lighting or cooking, pollutants arising from user activities like cleaning, smoking [5-8]. Some of the indoor air pollutants which are known their hazardousness to health are benzene, carbon monoxide, formaldehyde, naphthalene, nitrogen dioxide, polycyclic aromatic hydrocarbons, radon, trichloroethylene and tetrachloroethylene [9]. In terms of health, one of the most important pollutants in indoor air is particulate matter (PM). The particulate matter, also known as PM or particle pollution, is a complex mixture of airborne solid and / or liquid particles. These particles may exist in different sizes, shapes and compositions [4,10]. PM$_{10}$ refers to particles less than or equal to 10 µm in diameter and PM$_{2.5}$ refers to fine inhalable particles with diameters that are generally 2.5 micrometers and smaller. Particles that are 10 micrometers in diameter or smaller are especially concern because they are inhalable. They can penetrate the upper regions of the body's respiratory defense mechanisms [11, 12]. In a study, it was predicted that the number of deaths attributable to PM$_{2.5}$ is 4.2 million between 1990 and 2015 and 20% increased for the same period [13]. According to World Health Organization (WHO), air quality limit values are 10 µg/m^3 (annual mean) and 25 µg/m^3 (24-hour mean) for PM$_{2.5}$. For PM$_{10}$, the specified limit values are 20 µg/m^3 (annual mean) and 50 µg/m^3 (24-hour mean) (Table 1) [14]. The limit values stated in the Air Quality Assessment and Management Regulation (2008) in our country is 50 µg/m^3 (24-hour mean) for PM$_{10}$ (Table 1) [15]. Limit values recommended in national and international standards on indoor air quality are shown in Table 1 [4, 9, 11, 15, 16, 17].

Table 1. Limit values recommended in national and international standards on indoor air quality

Turkey	PM$_{10}$ <40 µg/m^3 (annual mean) PM$_{10}$ <50 µg/m^3 (24-hour mean)
Canada	PM$_{2.5}$<40 µg/m^3 (8-hour mean) PM$_{2.5}$<100 µg/m^3 (1-hour mean)
China	PM$_{10}$<150 µg/m^3 (24-hour mean)
WHO (World Health Organization)	PM$_{10}$<20 µg/m^3 (annual mean) PM$_{10}$<50 µg/m^3 (24-hour mean) PM$_{2.5}$<10 µg/m^3 (annual mean) PM$_{2.5}$<25 µg/m^3 (24-hour mean)
EPA (Environmental Protection Agency)	PM$_{10}$<150 µg/m^3 (24-hour mean) PM$_{2.5}$<12 µg/m^3 (annual mean) PM$_{2.5}$<35 µg/m^3 (24-hour mean)
England	PM$_{10}$<50 µg/m^3
Norway	PM$_{2.5}$<20 µg/m^3
EU (European Union)	PM$_{10}$<40 µg/m^3 (annual mean) PM$_{10}$<50 µg/m^3 (24-hour mean) PM$_{2.5}$<25 µg/m^3 (annual mean)
Hong-Kong	PM$_{10}$<20 µg/m^3 (Level 1) PM$_{10}$<180 µg/m^3 (Level 2) (8-hour mean)
Belgium	PM$_{2.5}$<15 µg/m^3 (24-hour mean) PM$_{10}$<40 µg/m^3 (annual mean)
Korea	PM$_{10}$<100 µg/m^3 (24-hour mean) PM$_{10}$<100 µg/m^3 (8-hour mean)
Portugal	PM$_{2.5}$<25 µg/m^3 (24-hour mean) PM$_{10}$<50 µg/m^3 (annual mean)

Among the indoor environments canteens are especially important places for students because they may spend long times and be influenced from IAQ inside them. Investigating the inhalable particle concentrations inside them is great significance for human health [18]. The importance of this has been emphasized in many studies in the literature. Slezakova et al. (2019), assessed UFP levels in different indoor school microenvironments including classrooms, canteens, gyms, libraries. They conducted real-time Ultra Fine Particles (UFP) measurements in 20 public primary schools located in Oporto city which is the 2nd largest city in Portugal. Their results showed that canteens were the microenvironment with the highest UFP levels among the investigated indoor school microenvironments [19]. Zhang et al. (2017), measured cooking particle concentrations at university canteens having enclosed and open style cooking units. Their results revealed the cooking style at canteens have significant role in the particle concentrations. They determined that PM_{10} mass concentration in the open-style cafeteria can reach to 450 $\mu g/m^3$ and exceeds maximum allowable concentrations. The researchers recommended the improving ventilation in canteens with open-style dining hall to reduce the detrimental effects of particulate matter on human health [18].

The aim of this study is to determine the indoor air quality in student canteens, especially in terms of particulate matter. Another purpose of this study is to help raise public awareness of the need to provide a better IAQ in student's canteens.

2. MATERIALS AND METHODS

The study was carried out in a total of 9 student canteen in a public university located in Marmara Region, Turkey. The locations and the areas of the canteens were shown in Table 2. The ventilation of the canteens is provided by mechanical ventilation system and the heating and cooling systems are similar. The hardware features of the canteens are as follows; double-glazed windows, floor tiles, interior doors, tables and chairs are standard, walls are standard plastic paint. In addition, the materials of the canteens are standard (oven, rotary cooking stove, tea stove, etc.). The buildings are outside the city and the traffic density is negligible. The measurements were made in spring semester in April, 2019. In each of the selected canteens, measurements were made in the time interval of 10:00 AM and 19:00 PM for one day. Measurements were carried out regularly for nine consecutive days.

As the IAQ parameters, temperature, relative humidity, PM_{10} and $PM_{2.5}$ values were measured simultaneously and meanwhile, the areas of the examined canteens, and the people densities during the measurements were determined. The Particle Measuring Device PCE-MPC 10 was used to determine particulate matter (PM_{10} and $PM_{2.5}$) level, temperature and relative humidity. Temperature and relative humidity were measured at the time of the sampling and the number of people in the cafeteria during the air sampling was counted. The study was carried out by measuring the average 10 hours of $PM_{2.5}$ and PM_{10}. Measurements were carried out at each hour during the day between 10:00 AM-19:00 PM and 1.5 meters above the ground (the height at which the air is inhaled).

Table 2. Locations and the areas of the canteens

Location		Area (m^2)
Faculty of Engineering	E1	75
	E2	30
	E3	30
Faculty of Arts and Sciences	A1	70
	A2	180
Faculty of Theology	T1	200
Faculty of Health Sciences	H1	90
Business School	B1	110
Central cafeteria	C1	5075

The results were statistically analyzed by spearman correlation analysis (Table 3).

3. RESULTS AND DISCUSSION

Temperature It is reported that the ideal temperature for indoors can vary between 15-26 ºC. Although the indoor air temperature is chosen according to the outdoor temperature in summer conditions, the indoor temperature in winter is determined according to the purpose and type of use of the environment. Indoor temperature affects air movement/velocity and clothing selection. It is also a factor that affects distraction and work efficiency. Temperature and humidity form an inseparable relationship. In general, more moisture is retained in the air at lower temperatures and constant barometric pressure. Below these "dew point" temperatures, water can condense on cold surfaces inside a room or building. This can contribute to the collection and accumulation of airborne dust and debris containing fungal spores on wet surfaces, followed by mold growth [16, 20, 21].

Measurements regarding indoor air quality were taken during working hours on certain days in April. Temperature (°C) distribution in canteens were shown in Figure 1. According to the obtained values, it was observed that the indoor temperature ranged between 19.3 °C and 34.2 °C (Fig. 1). In the morning (10:00-11:00), the temperature values determined between 19.3 °C - 25 °C (Fig. 1). The detected values are low and this can be attributed to the coolness of the morning weather and the lack of indoor people due to the class hours. At noon (12:00-14:00) there was a significant rise in temperatures thanks to warming of the air and sunlight. In addition, the frequent use of open style cooking units for crowded and food orders created by the students on lunch breaks in canteens is the main reason for this temperature increase. The highest values were determined during this time period (20.2 °C-34.2 °C) (Fig. 1).

In the afternoon (15:00-19:00) the loss of the sun caused significant reductions in outdoor temperature, and in addition, the density of people in the canteens was reduced due to the fact that the formal education students had finished their classes and left the campus area. In the afternoon (15:00-19:00), the indoor temperatures in the canteens were determined between 20.3 °C and 30.9 °C (Fig. 1). This decrease in temperature can be attributed to the fact that the students of night education are very few and they do not prefer canteens to spend time.

According to the results of the Spearman's correlation analysis applied, a statistically significant negative correlation was found between temperature and $PM_{2.5}$(r=-0.449) and PM_{10} (r=-0.339) (p<0,05) (Table 3).

Tablo 3. Results of Spearman's correlation analysis

		$PM_{2.5}$	PM_{10}
Temperature	r	-0,449	-0,339
	p	0,000*	0,001*
Humidity	r	0,974	0,440
	p	0,000*	0,000*
Number of people	r	0,320	0,036
	p	0,002*	0,736
$PM_{2.5}$	r		0,454**
	p		0,000

*:p<0,05, **: p<0,01

Humidity Relative humidity levels can affect the release rate of many indoor pollutants, their concentration in the air, and the growth of microbial organisms. Relative Humidity also has an impact on human comfort. Areas with 30-70% relative humidity are suitable for human comfort, productivity and health. In general, relative humidity levels below 30% cause drying of the skin, eyes and mucous membranes, while levels above 70% can contribute to mold growth and the growth of pathogenic and allergic organisms [16, 21].

When we examined the relative humidity content, it was observed that it generally varied between 34.8-61.5% (Fig. 2). In the morning (10:00-11:00), the humidity levels determined ranged from 38.1% to 61.5% (Fig. 2). At noon (12:00-14:00) it was found that the amount of moisture decreased and changed in the range of 34.8-53.2% (Fig. 2). In the afternoon (15:00-19:00), an increase in the amount of moisture was observed and it was found to vary between 35.9-55.1% (Fig. 2). According to the results of Spearman's correlation analysis, a statistically significant positive correlation was found between moisture and $PM_{2.5}$ (r=0.974) and PM_{10} (r=0.440) (p<0,05) measurements (Table 3).

Similar to our study, Işık and Çibuk (2015), carried out measurements of parameters related to indoor air quality in a university canteen and cafeteria. As a result of the measurements made in the cafeteria and canteen, which are heated by the central heating system in the winter period, they have determined that the indoor temperature and relative humidity do not pose a significant problem since they are within the desired range in terms of comfort [16].Bulut (2011), investigated indoor air quality in public living spaces in his study. According to the results obtained, the relative humidity remained at low values in terms of comfort (average 36.2%, minimum 14.2%, maximum 68.6%). The low relative humidity is due to the fact that the region is a dry region and the humidification process is not performed in the ambient air conditioning. There is a statistically significant relationship between the number of people and PM_1, temperature, CO, CO_2 and relative humidity. In addition, a significant correlation was found between the relative humidity in the indoor environment and PM values [22].

Menteşe et al. (2018) investigated the potential to improve IAQ of a rotor turbine ventilator (RTV) installed outside the kitchen chimney of a cafeteria. After RTV setup, total TB (Number of airborne bacteria), PM, TVOC (Total volatile organic compounds) and CO_2 were clearly reduced, while ozone and CO levels did not change significantly during the study. In addition to examining the effectiveness of RTV, they found cross-correlations between air pollutants, temperature-relative humidity, and occupancy regardless of RTV setup. In addition, statistically significant correlations ($p<0.05$) were found for the number of people in the cafeteria and both CO_2 and TB levels throughout the study [23].

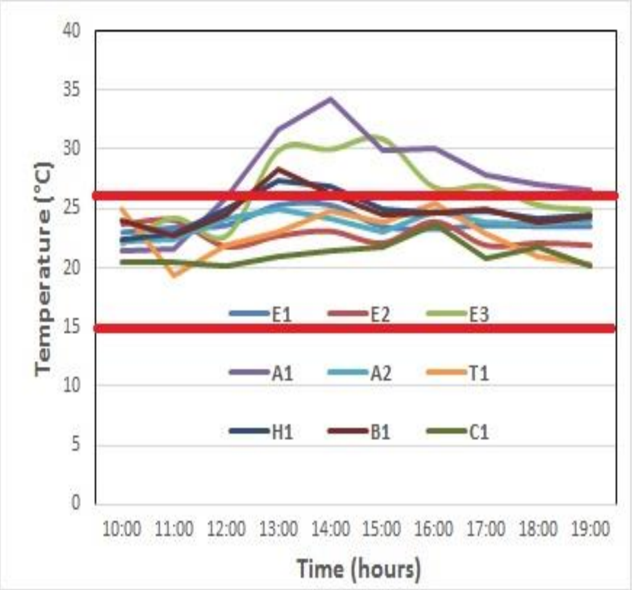

Figure 1. Temperature (°C) distribution in canteens

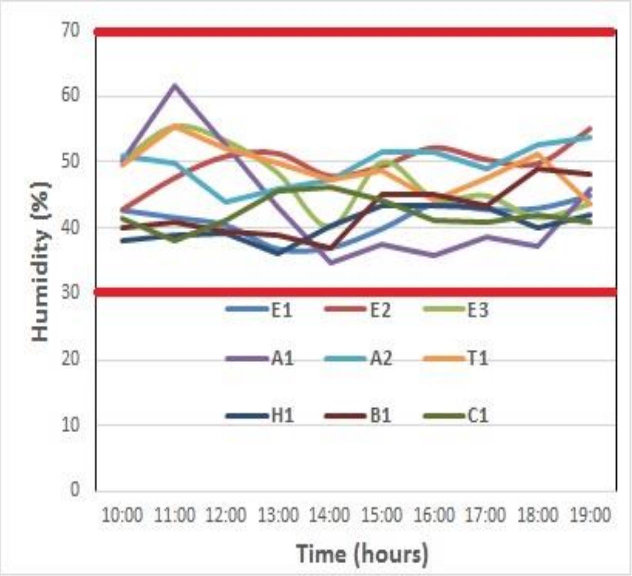

Figure 2. Humidity (%) distribution in canteens

People density When we look at the number of people in the canteens, there is generally a decrease in the morning hours (10:00-11:00) (5-50 people) (Fig. 3). This can be attributed to morning classes. However, with the arrival of the lunch hours (12:00-14:00), the number of people identified in the canteens increased (10-160 people) (Fig. 3). This is of course due to the fact that students eat lunch at the canteens. However, in the case of canteens E1, E3 and A1, this is exactly the opposite. The reason for this is the location of buildings with canteens. The fact that these buildings are close to the student refectory causes the students to eat their meals in the refectory. In the afternoon (15:00-19:00), it is seen that the number of students in the canteens has decreased (3-107 people) (Fig. 3). A positive correlation between the number of people and $PM_{2.5}$ ($r=0.320$) measurements was detected ($p<0.05$) (Table 3).

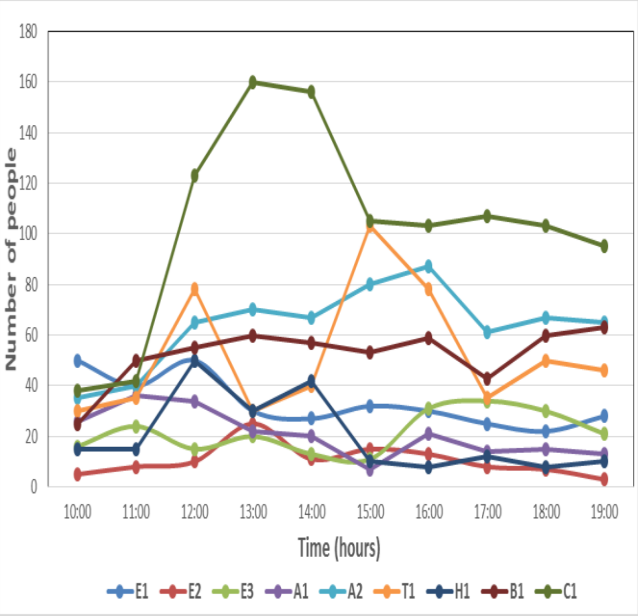

Figure 3. Hourly people density in canteens

$PM_{2.5}$ When the $PM_{2.5}$ measurement results were examined, it was found to be directly proportional to the number of people in the canteens. According to the results of Spearman correlation analysis, a statistically significant positive correlation was found between the number of people and the measurement of $PM_{2.5}$ (r=0.320) ($p<0.05$) (Table 3). $PM_{2.5}$ values generally varied between 3-130 µg/m^3 (Fig. 4). $PM_{2.5}$ values measured in the morning hours (10:00-11:00) were between 3-126 µg/m^3 (Fig. 4). This was especially the case during the morning when students bought toast and tea from the canteens. However, it should be noted that the concentrations of $PM_{2.5}$ detected in canteens are as effective as 1 hour after the concentration of the individual.

At noon (12:00-14:00), $PM_{2.5}$ level increased with the increase in the number of people (3-130 µg/m^3) (Fig. 4). This is an expected rise. However, in the afternoon (15:00-19:00), $PM_{2.5}$ values were also decreased due to the decrease in students, and they were measured in the range of 3-99 µg/m^3 (Fig. 4). When we examine Figure 4, hourly changes of $PM_{2.5}$ levels are similar for all canteens.

During the morning hours (10:00-11:00) $PM_{2.5}$ is at low levels. However, after 11:00, the students had to leave the classes and enter the lunch break and there were intensities in the canteens and therefore the $PM_{2.5}$ values increased. As of 14:00, a decrease was seen again, but this did not last longer at 15:00 with the arrival of night education students increased $PM_{2.5}$ values (Fig. 4). When the $PM_{2.5}$ values in all canteens were examined, it was found that the limit values (<25 µg / m^3) specified in the WHO regulation were exceeded except for the E3 and A1 canteens [14]. The 50 percentage of number of samples is higher than the standard of $PM_{2.5}$ in WHO regulation (<25 µg / m^3).

Zhu (2015) examined the relationship between indoor and outdoor particulate matter concentrations and suggested better measures to improve indoor air quality. Zhu determined that the concentration of particulate matter in campus underground spaces and canteens is quite high. Zhu even determined that the concentration of particulate matter in the external environment can reach two to three times. Therefore, researcher concluded that uncirculated air sometimes increases $PM_{2.5}$ concentration and cooking can be a new source of pollution to some extent [24].

Kumar and Jain measured PM in the student occupants area in India. Among the investigated areas canteen had the highest PM level. In their study, the average PM $_{2.5}$ concentration in canteen was 87 ± 26.45 µg/m^3 [25].

In our study a positive correlation between $PM_{2.5}$ (r=0.454) and PM_{10} was detected ($p<0.01$). In a recent study carried by Liang et al., indoor air chemical contaminants including PM2,5 and PM10 were measured in public buildings in China. Liang et al., also determined a positive correlation between $PM_{2.5}$ and PM_{10} in the canteen that investigated and Pearson correlation coefficient was 0.3. They detected that the $PM_{2.5}$ concentration in the canteen during the cooking periods before breakfast, lunch and dinner, reached extreme values with concentrations of 32.5 µg/m3,, 30.6 µg/m3, and 30.3 µg/m3, respectively [26].

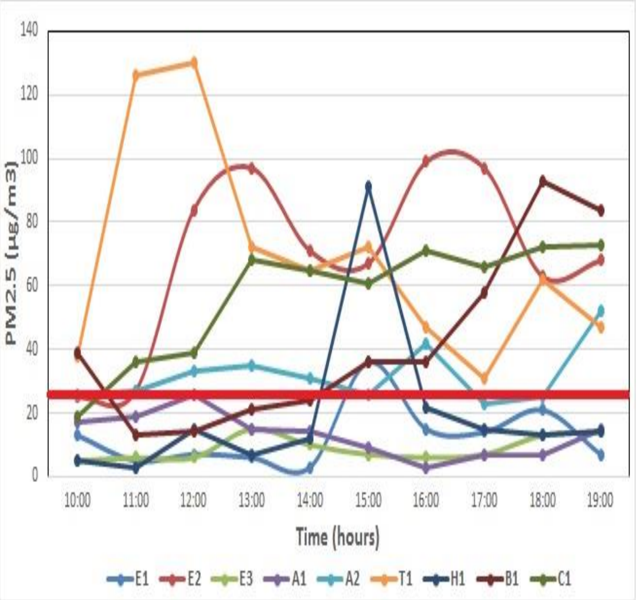

Figure 4. Hourly $PM_{2.5}$ ($\mu g/m^3$) concentrations in canteens

PM_{10} The result show that the average PM_{10} concentrations of 10 hour are in the range of 8-253 $\mu g/m^3$ (Fig. 5). In the morning hours (10:00-11:00), PM_{10} values were between 8-235 $\mu g/m^3$ range (Fig. 5). At noon (12:00-14:00), PM_{10} values were determined in the range of 10-253 $\mu g/m^3$ (Fig. 5). In the afternoon (15:00-19:00), PM_{10} levels in canteens decreased (11-177 $\mu g/m^3$) (Fig. 5). When the canteens where the measurements were made were examined, the highest (253 $\mu g/m^3$) PM_{10} value was determined in the canteen of the faculty of theology at 12:00. When the PM_{10} values in all canteens were examined, it was found that the limit values (<50 $\mu g / m^3$) specified in the WHO and Air Quality Assessment and Management Regulation (2008) were exceeded except for the E3 and A1 canteens [14, 15]. The 42 percentage of number of samples is higher than the standard of PM_{10} in WHO regulation (<50 $\mu g / m^3$).

According to the results of Spearman's correlation analysis applied, a statistically significant negative correlation between temperature and PM_{10} ($r=-0.339$) measurements and a positive correlation between humidity and PM_{10} ($r=0.440$) ($p<0.05$) measurements, and a positive correlation between $PM_{2.5}$ ($r=0.454$) and PM_{10} was detected ($p<0.01$). The correlation between number of people and PM_{10} was not statistically significant (Table 3).

Thongsanit et al. (2017), aimed to investigate the particle size of particles smaller than 10 microns (PM_{10}) in the canteens of a university and determined the 8-hour average PM_{10} concentrations in the range of 49.0 to 294.1 $\mu g/m^3$. The results they obtained supported the results we found, and they stated that there may be many factors affecting the amount of PM_{10} in canteens, including the number of people and their activities, and the cooking process is effective [27].

In the study performed by Liang et al. (2021) the PM_{10} concentration in the canteen peaked to 59 $\mu g/m^3$ [26]. The average $PM_{2.5}$ concentration in canteen was 138 ± 34.19 $\mu g/m^3$ in the study caried by Kumar and Jain. [25].

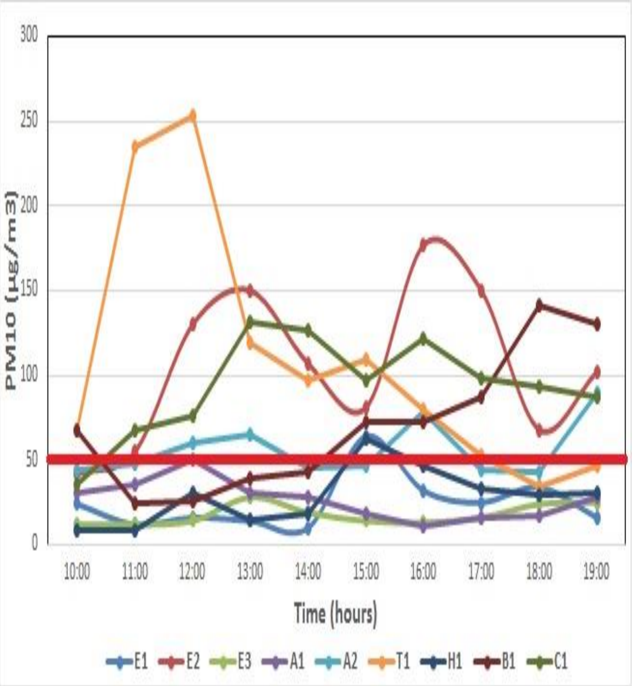

Figure 5. Hourly PM_{10} ($\mu g/m^3$) concentrations in canteens

In our study, it is observed that particulate matter (PM_{10} and $PM_{2.5}$) levels reach its highest value at 15:00 in canteens E1 and H1 (E1; PM_{10}: 64 $\mu g/m^3$; $PM_{2.5}$:36 $\mu g/m^3$) (H1; PM_{10}: 63 $\mu g/m^3$; $PM_{2.5}$:91 $\mu g/m^3$). However, when we look at the densities of people in both canteens, we see the highest student crowd at 12:00 noon. It should be noted that particulate matter concentrations detected in canteens in the literature are effective up to 1 hour after the highest concentration of people. Considering this situation, it is seen that the 1-hour period increases even more (2-3 hours) depending on the high level of activity of the person. Similarly, in the canteen E2, the highest student density was observed at 13:00, while the highest particulate matter levels were detected at 16:00 (approximately 2-3 hours later) following this hour (PM_{10}: 177 μg/m^3; $PM_{2.5}$:99 μg/m^3). In the canteen no. A1, the highest particulate matter levels were measured 1 hour after 11:00, when the person density was highest, in line with the literature data (PM_{10}: 50 μg/m^3; $PM_{2.5}$:26 μg/m^3). When we look at the canteen numbered A2, similar to the canteens E1, E2 and H1, the highest particulate matter levels were observed 2-3 hours after 16:00 when the density of people was highest (PM_{10}: 90 μg/m^3; $PM_{2.5}$:52 μg/m^3). When we examined the values we obtained, we found the highest student density in the central cafeteria no. C1 (160 people). It is expected that the central cafeteria, which is frequented by the students of all faculties, has the highest crowd. However, the highest particulate matter levels were detected in the canteen T1 (PM_{10}: 253 μg/m3; $PM_{2.5}$: 130 μg/m^3). The highest levels were measured at 12:00. This may be due to the fact that the T1 canteen is far from the cafeteria and the central cafeteria. However, while the highest student density in the T1 canteen was expected at 12:00, the most crowded hour was determined at 15:00 (103 people). When we look at 12:00, we see a relatively crowded canteen with a density of 78 people. This crowd, seen at 12:00, was determined as the second highest level of rudeness in the given time period.

4. CONCLUSIONS

Indoor temperature and humidity are the most important parameters of indoor air quality and human comfort. Especially these two parameters are known to affect air quality and influence the growth and sporulation of the present fungi. The indoor temperature is 15-26 ℃ and the relative humidity is recommended between 30% and 70% for different environments [21]. In the canteens where the measurements were made, the temperatures determined were slightly higher (19.3-34.2 ℃) (Fig. 1). However, this situation can be attributed to the increase in outdoor temperature in season, the crowd experienced at certain hours and the increase of indoor air temperature of canteens serving with open style cooking system. The relative humidity levels were consistent with the literature (34.8-61.5%) (Fig. 2). The canteens measured according to the relative humidity values obtained can be considered as the environment with suitable humidity area. Canteens usually have central air conditioning systems, heating and cooling is provided in this way. However, such systems are used for air heating and cooling and use indoor air when performing this operation. Therefore, it is advisable to use heating and cooling systems against high temperatures depending on the weather conditions.

When we look at the $PM_{2.5}$ and PM_{10} concentrations, it was found that both parameters exceed the regulations limit values at certain hours in all canteens except E3 and A1 (Fig 4., Fig. 5). This situation has negative effects on human health and may cause some acute and chronic diseases. In such places, ventilation should be done regularly, cleaning should be repeated frequently, air conditioning systems should be reviewed and their filters should be cleaned and maintained. Performing these routines regularly is essential for a healthy and productive life.

Funding

The authors have no received any financial support for the research, authorship or publication of this study.

The Declaration of Conflict of Interest/ Common Interest

No conflict of interest or common interest has been declared by the authors.

Authors' Contribution

The authors contributed equally to the study.

The Declaration of Ethics Committee Approval

This study does not require ethics committee permission or any special permission.

The Declaration of Research and Publication Ethics

The authors of the paper declare that they comply with the scientific, ethical and quotation rules of SAUJS in all processes of the paper and that they do not make any falsification on the data collected. In addition, they declare that Sakarya University Journal of Science and its editorial board have no responsibility for any ethical violations that may be encountered, and that this study has not been evaluated in any academic publication environment other than Sakarya University Journal of Science.

REFERENCES

[1] https://www.epa.gov/indoor-air-quality-iaq/introduction-indoor-air-quality (Access Date: 02.01.2020).

[2] C.J. Matz, D.M. Stieb, K. Davis, M. Egyed, A. Rose, B. Chou, O. Brion, “Effects of age, season, gender and urban rural status on time-activity: canadian human activity pattern survey2 (chap2).” Int. J. Environ. Res. Public Health, 11, pp. 2108–2124, 2014.

[3] https://www.epa.gov/iaq-schools/why-indoor-air-quality-important-schools (Access Date: 02.01.2020).

[4] https://www.epa.gov/indoor-air-quality-iaq/introduction-indoor-air-quality (Access Date: 02.01.2020).

[5] E. Hollbacher, T. Thomas, R.G., Cornelia, E. Srebotnik, “Emissions of indoor air pollutants from six user scenarios in a model Room”, Atmospheric Environment,150, pp. 389-394, 2017.

[6] T. Salthammer, M. Bahadir, “Occurrence, dynamics and reactions of organic pollutants in the indoor environment”, Clean-Soil, Air, Water 37, pp. 417-435, 2009.

[7] P. Wolkoff, G.D. Nielsen, “Organic compounds in indoor air - their relevance for perceived indoor air quality?” Atmos. Environ. 35, 4407-4417, 2001.

[8] C. Dede, N. Çınar, “Indoor (Household) Air Pollution and Children Health”, Research on Science and Art in 21st Century Turkey, Chapter 68, Editors: Arapgillioğlu H., Atik A., Elliot RL., Turgeon, E., Gece Publishing, Ankara, Turkey, Volume:1, pp:612-620, 2017, ISBN: 978-605-180-771-3.

[9] World Health Organization, “WHO guidelines for indoor air quality. Selected pollutants”. WHO Regional Office for Europe, Copenhagen, 2010.

[10] World Health Organization, “Health effects of particulate matter. Policy implications for countries in eastern Europe, Caucasus and central Asia (2013)”, WHO Regional Office for Europe, Copenhagen, 2013.

[11] https://www.epa.gov/pmpollution/particulate-matter-pm-basics#PM (Access Date: 02.01.2020).

[12] EPA, “The Particle Pollution Report, Current Understanding of Air Quality and Emissions through 2003”, U.S. Environmental Protection Agency Office of Air Quality Planning and Standards Emissions, Monitoring, and Analysis Division Research Triangle Park, North Carolina, EPA 454-R-04-002 December 2004.

[13] P.J. Landrigan, R. Fuller, N.J.R. Acosta, et al. “The lancet commission on pollution and health”, Lancet. 391:462–512, 2018.

[14] World Health Organization, “Air quality guidelines for particulate matter, ozone, nitrogen dioxide and sulfur dioxide, Global update 2005, Summary of risk

assessment”, WHO/SDE/PHE/OEH/06.02, 2006.

[15] T.R. Air Quality Assessment and Management Regulation, 2008.

[16] E. Işık and S. Çibuk, “Yemekhaneler ve kantinlerde iç hava kalitesi ile ilgili ölçüm sonuçları ve analizi -Tunceli Üniversitesi örneği”, Dicle Üniversitesi Mühendislik Fakültesi, Mühendislik Dergisi, Cilt:6, sayı:1, pp. 39-50 , 2015.

[17] ASHRAE, “Standard 62.1-2019. “Ventilation for Acceptable Indoor Air Quality”, American Society of Heating, Refrigerating and Air-Conditioning Engineers, Atlanta, 2019.

[18] D. Zhang, X. Jin, L. Yang, X. Du, Y. Yang, “Experimental study of inhalable particle concentration distribution in typical university canteens”, Journal of Building Engineering, 14, pp. 81–88, 2017.

[19] K. Slezakova, E.O. Fernandes, M.C. Pereira, “Assessment of ultrafine particles in primary schools: Emphasis on different indoor microenvironments”,Environmental Pollution, 246, pp. 885-895, 2019.

[20] OSHA Policy on Indoor Air Quality: Office Temperature/Humidity and Environmental Tobacco Smoke. USDOL/OSHA, Washington DC. 2003

[21] Pennstate, Environmental Health and Safety. EHS Indoor Air Quality Standard Procedures Guide. 2014.

[22] H. Bulut, “İnsan Yoğunluklu Toplu Yaşam Ortamlarında İç Hava Kalitesinin Analizi”, Ulusal İklimlendirme Kongresi-İKLİM 2011 Bildiriler Kitabı, 377-386, Antalya, 2011

[23] S. Mentese, O. Çotuker, B. Selçuk, “Indoor air quality of a cafeteria with a rotor turbine ventilator (RTV) and cross-correlations between indoor air pollutants, occupancy rate and meteorological parameters”, Environmental Engineering and Management Journal, Vol.17, No. 9, 2051-2059, 2018.

[24] Y. Zhu, “A study on the correlation of the indoor and outdoor particulate pollution levels in the university premises”, International Conference on Economics, Social Science, Arts, Education and Management Engineering (ESSAEME 2015).

[25] S. Kumar, M. K. Jain, “Exposure to Particulate Matter and CO2 in indoor conditions at IIT(ISM) Dhanbad”, Article in Press.

[26] X. Liang, Z. Li, H. Zhang, X. Hong, “Study of the characteristics and comprehensive fuzzy assessment of indoor air chemical contamination in public buildings”, Frontiers in Public Health, 9, pp.1-17, 2021, doi: 10.3389/fpubh.2021.579299

[27] P. Thongsanit, N. Kaewvisate, C. Tajumpa, “Particulate Matter in the Cafeterias in Naresuan University, Phitsanulok Province, Lower Northern Part of Thailand”, Advanced Science Letters, 23(5), pp. 3960-3962, 2017.

SAKARYA ÜNİVERSİTESİ

FEN BİLİMLERİ ENSTİTÜSÜ
DERGİSİ

Sakarya University Journal of Science
SAUJS

e-ISSN 2147-835X Founded 1997 Period Bimonthly Publisher Sakarya University
http://www.saujs.sakarya.edu.tr/en/

Title: Examination of Stability Analysis of Sakarya and Turkey Scale Alcohol Use Model

Authors: Recai TARAKÇI, Ömer Faruk GÖZÜKIZIL

Recieved: 2021-06-11 00:00:00

Accepted: 2021-10-18 00:00:00

Article Type: Research Article

Volume: 25
Issue: 6
Month: December
Year: 2021
Pages: 1332-1342

How to cite
Recai TARAKÇI, Ömer Faruk GÖZÜKIZIL; (2021), Examination of Stability Analysis of Sakarya and Turkey Scale Alcohol Use Model. Sakarya University Journal of Science, 25(6), 1332-1342, DOI: https://doi.org/10.16984/saufenbilder.950878 Access link
http://www.saujs.sakarya.edu.tr/tr/pub/issue/66341/950878

Sakarya University Journal of Science 25(6), 1332-1342, 2021

Examination of Stability Analysis of Sakarya and Turkey Scale Alcohol Use Model

Recai TARAKÇI*[1], Ömer Faruk GÖZÜKIZIL[1]

Abstract

This paper is devoted to studying the mathematical model of the alcohol-consuming population. For this purpose, the formulation of the model including the alcohol-consuming population is presented; then the balance points related to non-alcohol use and positive alcohol use are discussed. Hurwitz theorem is used to find the local stability of the model, and Lyapunov function theory is used to investigate the global stability. The same mathematical model with alcohol use is considered for Sakarya and Turkey, individual numerical results are presented, and stability analyzes are examined. Finally, using the numerical data, a simulation is made in Matlab with the Runge-Kutta fourth-order method.

Keywords: alcohol use model, differential equation system, stability analysis, equilibrium model of the mathematical model

1. INTRODUCTION

The mathematical model is a system model, and the terms are conjecture. Mathematical models are used in nature, fundamentals, engineering, and social sciences. Mathematical biology is an interdisciplinary branch in which mathematics is applied to the branch of biology, medicine, and biotechnology. This field is seen as the fastest growing and productive, and enlightening branch of mathematics in today's world. In mathematical biology, Daniel Bernoulli used mathematical tools to describe the impact of smallpox on the human population in the 18th century [1]. Likewise, we use mathematical biology to understand diseases and develop new perspectives for treatment. On an individual scale, it is possible to predict how the patient's immune system might respond to a virus and thus determine the course of treatment. On a larger scale, new methods can be developed to control epidemic diseases such as Ebola. In 1909, Brownlee took responsibility for the development of mathematical biology [1]. In 1912, He presented basic laws for epidemic spreading [2]. Details of epidemic studies were discussed by Kermark and McKendrick in 1927 [3]. Then they discussed different models of many diseases [4-17]. After all these researches, people's health deteriorated, and they became ill due to harmful habits such as alcohol, one of the social habits that spread rapidly to the world like a contagious disease.

Alcohol use causes significant health problems in society. Alcohol use is the main cause of some fatal diseases. Alcohol consumption negatively affects the social and economic lives of societies. The most important reason for the occurrence of

---

* Corresponding author: recai.tarakci@ogr.sakarya.edu.tr
[1] Sakarya University, Faculty of Science and Literature, Department of Mathematics
E-mail: farukg@sakarya.edu.tr
ORCID: https://orcid.org/0000-0001-7569-8974, https://orcid.org/0000-0002-5975-6430

violence and unconscious movements in society is alcohol. Some studies have shown that alcohol use starts at a young age. It is seen that the use as an infectious disease spreads in society. In this study, we created the mathematical model of alcohol use considering the SIR model of epidemic diseases [18-24].

We divided the population who use alcohol in society into five classes as follows:

X(t): Susceptible population,

$H_1(t)$: Alcohol drinkers class,

H_2(t): Irregular alcohol drinkers class,

Y(t): Regular alcohol drinkers class,

Z(t): Alcoholic quitters class.

Here 't' denotes time change. We formalized the alcohol use model according to the assumptions that we obtained. We applied the stability analysis of the model that we created. We examined the local stability of this model using the Hurwitz theorem and discussed its global stability with the help of the Lyapunov function.

2. MATHEMATICAL MODEL

2.1. Formation of the Model

We divided the community of the alcohol users class into five classes as X(t), $H_1(t)$, $H_2(t)$,Y(t), Z(t). Moreover, let λ, β_1, β_2, ω, γ, μ, α, ρ, d, respectively, denote the recruitment rate (birth ve migration), rate of conversion of sensitive populations to alcohol drinkers, rate at which alcohol drinkers become irregular alcohol drinkers, rate of which irregular alcohol drinkers become regular alcohol drinkers, quitting rate, natural death rate, relapse rate, the death rate of alcohol drinkers class due to alcohol use, death due to alcohol drinkers related diseases, then our model has been constructed as follows:

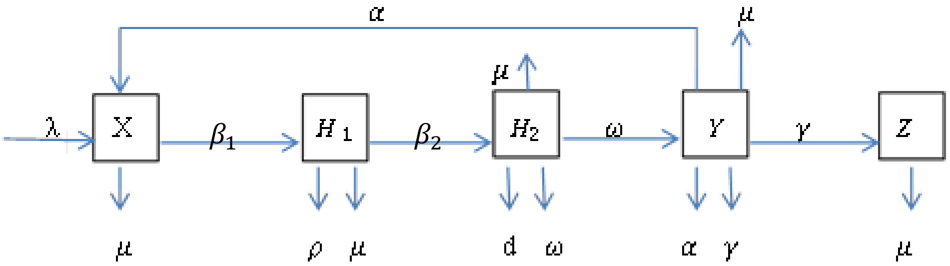

Figure 1 Schematic Diagram of Alcohol Use Pattern

Thus the differential equation system depending on our model has been given by

$$\frac{dX}{dt} = \lambda - \beta_1 X H_1 - \mu X + \alpha Y,$$

$$\frac{dH_1}{dt} = \beta_1 X H_1 - \beta_2 H_1 H_2 - (\rho + \mu) H_1,$$

$$\frac{dH_2}{dt} = \beta_2 H_1 H_2 - (d + \omega + \mu) H_2,$$

$$\frac{dY}{dt} = \omega H_2 - (\alpha + \gamma + \mu) Y,$$

$$\frac{dZ}{dt} = \gamma Y - \mu Z. \qquad (1)$$

In this system, we take the first four equations. We do not take Z(t) because it does not affect the generality. Our new model is converted to the following system:

$$\frac{dX}{dt} = \lambda - \beta_1 X H_1 - \mu X + \alpha Y\ ,$$

$$\frac{dH_1}{dt} = \beta_1 X H_1 - \beta_2 H_1 H_2 - (\rho + \mu) H_1,$$

$$\frac{dH_2}{dt} = \beta_2 H_1 H_2 - (d + \omega + \mu) H_2,$$

$$\frac{dY}{dt} = \omega H_2 - (\alpha + \gamma + \mu) Y.\ (2)$$

3. EQUILIBRIUM POINTS OF THE SYSTEM

3.1. No Alcohol Equilibrium Points

Let $H_1 = H_2 = Y = 0$, the balance point is obtained as $E_0 = (\frac{\lambda}{\mu}, 0,0,0)$. The Jacobian of the system (2) is found as

$$J = \begin{bmatrix} -\beta_1 H_1 - \mu & -\beta_1 X & 0 & \alpha \\ \beta_1 H_1 & \beta_1 X - \beta_2 H_2 - \rho + \mu & -\beta_2 H_1 & 0 \\ 0 & \beta_2 H_2 & \beta_2 H_1 - (d + \omega + \mu) & 0 \\ 0 & 0 & \omega & -(\alpha + \gamma + \mu) \end{bmatrix}.$$

So by considering the balance point in the last Jacobian matrix, we get

$$J(E_0) = \begin{bmatrix} -\mu & -\frac{\beta_1 \lambda}{\mu} & 0 & \alpha \\ 0 & \frac{\beta_1 \lambda}{\mu} - (\rho + \mu) & 0 & 0 \\ 0 & 0 & -(d + \omega + \mu) & 0 \\ 0 & 0 & \omega & -(\alpha + \gamma + \mu) \end{bmatrix}.$$

Concerning the Hurwitz theorem, we find the matrices of F and V as

$$F = \begin{bmatrix} \beta_1 \frac{\lambda}{\mu} & 0 & 0 \\ 0 & 0 & 0 \\ 0 & 0 & 0 \end{bmatrix}$$

and

$$V = \begin{bmatrix} (\rho + \mu) & 0 & 0 \\ 0 & (d + \omega + \mu) & 0 \\ 0 & -\omega & (\alpha + \gamma + \mu) \end{bmatrix}.$$

The dominant eigenvalue of $F.V^{-1}$ is $\frac{\beta_1 \lambda}{\mu(\rho+\mu)}$,

So, $R_0 = \frac{\beta_1 \lambda}{\mu(\rho+\mu)}$ is the value of the required reproductive number defined in [12].

3.2. Alcohol Present Equilibrium Points

Theorem 3.1. If $R_0 > 1$, then the drinking alcohol has a positive equilibrium point.

Proof. Let $R_0 > 1$. Then to determine the equilibrium E^*, we assume the left side of the system (2) is equal to zero.

The third equation of the system (2) implies that

$$H_1^* = \frac{(d+\omega+\mu)}{\beta_2}.$$

From the second equation of the system (2), we have

$$X^* = \frac{\beta_2 H_2^* + (\rho+\mu)}{\beta_1}.$$

Also, the fourth equation implies that

$$Y^* = \frac{\omega H_2^*}{(\alpha+\gamma+\mu)}.$$

Similarly, the first equation reveals that

$$H_2^* = \frac{(\alpha+\gamma+\mu)(\rho+\mu)[\beta_2 \mu (R_0 - 1) - \beta_1 (d+\omega+\mu)]}{(\gamma+\mu)(\beta_1 \beta_2 \omega) + (\alpha+\gamma+\mu)(\beta_1 \beta_2 (d+\mu) + \beta_2^2 \mu)}.$$

We have $\beta_2 \mu (R_0 - 1) > \beta_1 (d + \omega + \mu))$ since $R_0 > 1$. Thus, H_2^* is positive. So, the required positive equilibrium point $E^*$is found as

$$E^*(X^*, H_1^*, H_2^*, Y^*) = \left(\frac{\beta_2 H_2^* + (\rho+\mu)}{\beta_1}, \frac{(d+\omega+\mu)}{\beta_2}, \frac{\omega H_2^*}{(\alpha+\gamma+\mu)}, \frac{(\alpha+\gamma+\mu)\,(\rho+\mu)[\beta_2\mu\,(R_0-1)-\beta_1(d+\omega+\mu)]}{(\boldsymbol{\gamma}+\boldsymbol{\mu})(\boldsymbol{\beta_1\beta_2\omega})+(\alpha+\gamma+\mu)\big(\beta_1\beta_2(d+\mu)+\beta_2^2\mu\big)}\right).$$

4. STABILITY OF THE MODEL

4.1. Local Stability

Theorem 4.1. If $R_0 < 1$, then the system (2) is locally stable, and if $R_0 > 1$, then system (2) is unstable.

Proof. For the local stability at E_0, the Jacobian matrix of the system (2) is given by

$$J(E_0) = \begin{bmatrix} -\mu & -\frac{\beta_1\lambda}{\mu} & 0 & \alpha \\ 0 & \frac{\beta_1\lambda}{\mu} - (\rho+\mu) & 0 & 0 \\ 0 & 0 & -(d+\omega+\mu) & 0 \\ 0 & 0 & \omega & -(\alpha+\gamma+\mu) \end{bmatrix}.$$

The eigenvalues λ_1, λ_2, λ_3 and λ_4 of $J(E_0)$ are obtained as

$\lambda_1 = -\mu < 0,$

$\lambda_2 = (\rho+\mu)\,(R_0-1) < 0,$

$\lambda_3 = -(d+\omega+\mu) < 0,$

$\lambda_4 = -(\alpha+\gamma+\mu) < 0.$

Assuming $R_0 < 1$ implies that that $\lambda_2 < 0$. On the other hand if $R_0 = 1$ then $\lambda_2 = 0$. Finally, if $R_0 > 1$, then $\lambda_2 > 0$.

Theorem 4.2. If $R_0 > \frac{\beta_2\lambda}{(d+\omega+\mu)(\rho+\mu)}$, then the system (2) is locally stable at E^*, otherwise unstable.

Proof. For the local stability at E^*, the Jacobian matrix of the system (2) becomes

$$J(E^*) = \begin{bmatrix} -\beta_1 H_1^* - \mu & -\beta_1 X^* & 0 & \alpha \\ \beta_1 H_1^* & \beta_1 X^* - \beta_2 H_2^* - \rho + \mu & -\beta_2 H_1^* & 0 \\ 0 & \beta_2 H_2^* & \beta_2 H_1^* - (d+\omega+\mu) & 0 \\ 0 & 0 & \omega & -(\alpha+\gamma+\mu) \end{bmatrix}.$$

Under the assumption, we get

$$J(E^*) = \begin{bmatrix} -\beta_1 H_1^* - \mu & -\beta_1 X^* & 0 & \alpha \\ \beta_1 H_1^* & 0 & -\beta_2 H_1^* & 0 \\ 0 & \beta_2 H_2^* & 0 & 0 \\ 0 & 0 & \omega & -(\alpha+\gamma+\mu) \end{bmatrix},$$

$$= \begin{bmatrix} -\beta_1 H_1^* - \mu & -\beta_1 X^* & 0 & \alpha \\ -\mu & -\beta_1 X^* & -\beta_2 H_1^* & \alpha \\ \beta_1 H_1^* & \beta_2 H_2^* & -\beta_2 H_1^* & 0 \\ 0 & 0 & \omega & -(\alpha+\gamma+\mu) \end{bmatrix},$$

$$= \begin{bmatrix} -\beta_1 H_1^* - \mu & -\beta_1 X^* & 0 & \alpha \\ 0 & -\beta_1 X^* + \frac{\mu\beta_2{}'H_2^*}{\beta_1{}'H_1^*} & -\beta_2 H_1^* - \frac{\mu\beta_2 H_1^*}{\beta_1 H_1^*} & \alpha \\ \beta_1 H_1^* & \beta_2 H_2^* & -\beta_2 H_1^* & 0 \\ 0 & 0 & \omega & -(\alpha+\gamma+\mu) \end{bmatrix},$$

$$\mathrm{J}(E^*) = \begin{bmatrix} -\beta_1 H_1^* - \mu & -\beta_1 X^* & \frac{\omega\alpha}{(\alpha+\gamma+\mu)} & 0 \\ 0 & -\beta_1 X^* + \frac{\mu\beta_2 H_2^*}{\beta_1 H_1^*} & -\beta_2 H_1^* - \frac{\mu\beta_2 H_1^*}{\beta_1 H_1^*} + \frac{\omega\alpha}{(\alpha+\gamma+\mu)} & 0 \\ \beta_1 H_1^* & \beta_2 H_2^* & -\beta_2 H_1^* & 0 \\ 0 & 0 & \omega & -(\alpha+\gamma+\mu) \end{bmatrix}.$$

For the sake of simplicity, this matrix can be written as

$$J(E^*) = \begin{pmatrix} A & B \\ C & D \end{pmatrix}$$

where

$$A = \begin{pmatrix} -\beta_1 H_1^* - \mu & -\beta_1 X^* \\ 0 & -\beta_1 X^* + \frac{\mu\beta_2 H_2^*}{\beta_1 H_1^*} \end{pmatrix},$$

$$B = \begin{pmatrix} \frac{\omega\alpha}{(\alpha+\gamma+\mu)} & 0 \\ -\beta_2 H_1^* - \frac{\mu\beta_2 H_1^*}{\beta_1 H_1^*} + \frac{\omega\alpha}{(\alpha+\gamma+\mu)} & 0 \end{pmatrix},$$

$$C = \begin{pmatrix} \beta_1 H_1^* & \beta_2 H_2^* \\ 0 & 0 \end{pmatrix},$$

$$D = \begin{pmatrix} -\beta_2 H_1^* & 0 \\ \omega & -(\alpha+\gamma+\mu) \end{pmatrix}.$$

Since the eigenvalues of $J(E^*)$ depend on the eigenvalues of A and D, the eigenvalues of A are given as follows:

$$\lambda_1 = -\beta_1 H_1^* - \mu < 0,$$

$$\lambda_2 = -(\rho+\mu) + \frac{\mu\beta_2 H_2^*}{\beta_1 H_1^* \lambda}\,(\lambda - H_1^*(\rho+\mu)R_0).$$

If $R_0 > \frac{\beta_2\lambda}{(d+\omega+\mu)(\rho+\mu)}$, then $\lambda_2 < 0$.

Moreover, the eigenvalues of D are

$$\lambda_3 = -\beta_2 H_1^* < 0,$$

$$\lambda_4 = -(\alpha+\gamma+\mu) < 0.$$

This completes the proof.

4.2. Global Stability

Theorem 4.3. If $R_0 < 1$, then the system (2) is globally stable.

Proof. First, we construct the Lyapunov function L as

$$L = \ln\frac{X}{X_0} + \ln\frac{H_1}{H_{1_0}} + H_2 + Y. \qquad (4)$$

Differentiating Eq. (4) with respect to time, we get

$$L' = \frac{\lambda}{X} - \beta_1 H_1 + \frac{\alpha Y}{X} - \mu + \beta_1 X - \beta_2 H_2 - (\rho + \mu) + \beta_1 H_1 H_2 - (d+\omega+\mu)H_2 + \omega H_2 - (\alpha + \gamma + \mu)Y.$$

Using the values E_0 in the above equation, we find

$$L' = \mu - \mu + \frac{\beta_1\lambda}{\mu} - (\rho+\mu).$$

By successive calculation, we obtain that

$$L' = R_0(\rho+\mu) - (\rho+\mu),$$

$$L' = (\rho+\mu)(R_0 - 1).$$

Therefore, if $R_0 < 1$, then $L' < 0$, which implies that the system (2) is globally stable.

5. NUMERICAL RESULTS

Table 1 Parameters of the model

Parameter	Definition	Rates in Turkey	Rates in Sakarya
λ	Recruitment rate (birth ve migration)	0,0022	0,0018
β_1	Rate of conversion of sensitive populations to alcohol drinkers	0,003	0,003
β_2	Rate at which alcohol drinkers become irregular alcohol drinkers	0,004	0,004
ω	Rate of which irregular alcohol drinkers become regular alcohol drinkers	0,002	0,002
γ	Quitting rate	0,086	0,084
μ	Naturel death rate	0,005	0,006
α	Relapse rate	0,002	0,002
ρ	The death rate of alcohol drinkers class due to alcohol use	0,003	0,003
d	Death due to alcohol drinkers related diseases	0,003	0,003

Table 2 The classes of the population who use alcohol

Classes	Explanations	Turkey data	Sakarya data
$X(t)$	Sensitive Alcohol Drinkers	47.236.000 (%78)	420.550 (%65)
$H_1(t)$	Alcohol Consumers	13.324.075 (%22)	226.450 (%35)
$H_2(t)$	Irregular Alcohol Consumers	9.145.435 (%15.1)	163.044 (%25,2)
Y(t)	Regular Alcohol Consumers	4.178.640 (%6,9)	63.406 (%9,8)
Z(t)	Those Who Quit Alcohol	111.914 (%8,4)	19.021 (%8,4)

Turkey's population in 2019 is approximately 83 million and over 18 years old is 60 million 560 thousand 75.

The population of Sakarya in 2019 is approximately 1 million 45 thousand and over the age of 18 is 647 thousand [25-28]

Graphics 1. MatLab simulations of the Turkey alcohol use model (system 1), that are plotted according to the approximate parameters given in Table 1 and the numerical data presented in Table 2. They are scaled to 1/1.000.000.

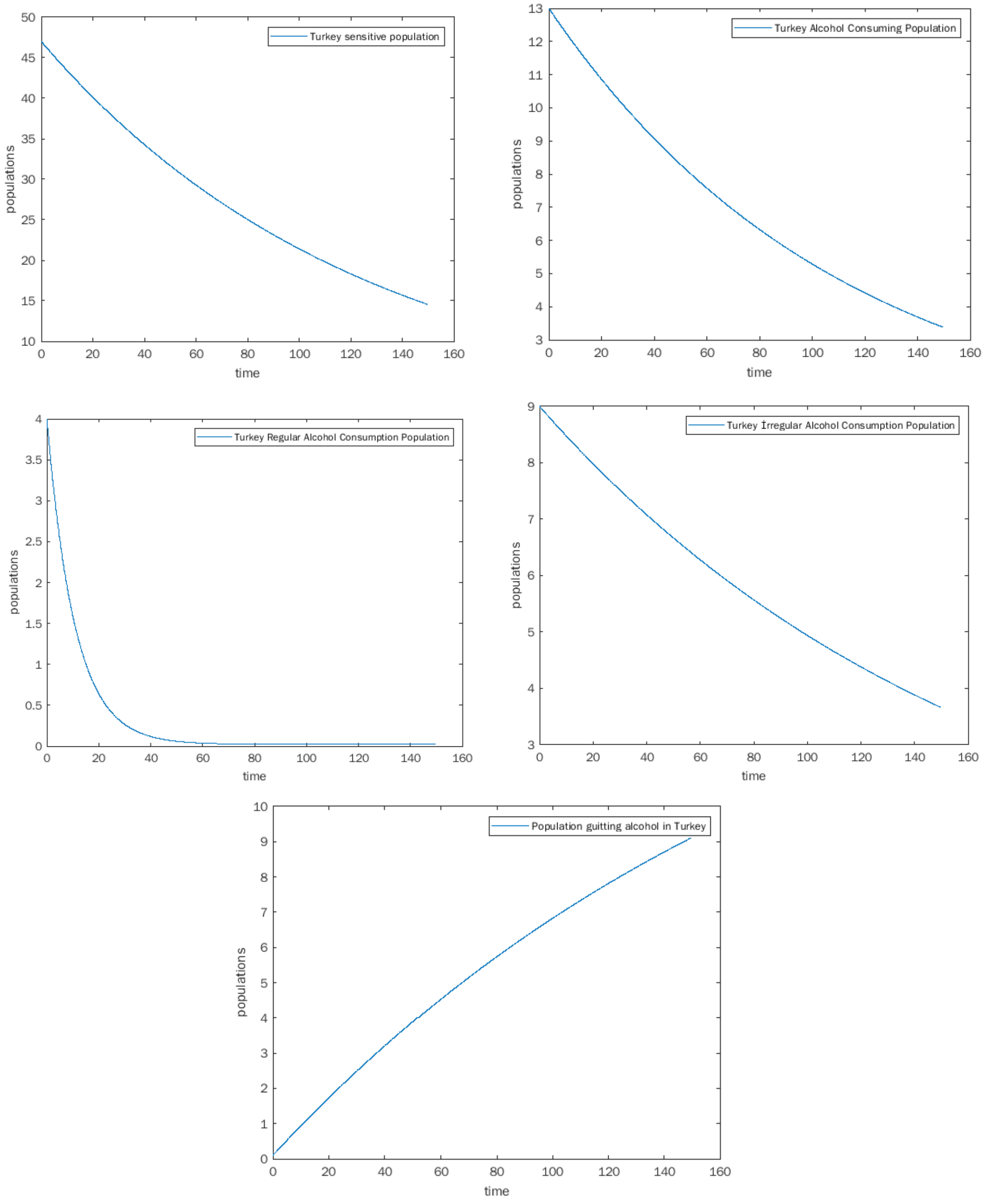

Graphics 2 MatLab simulations of the Sakarya alcohol use model (system 1), that are plotted according to the approximate parameters given in Table 1 and the numerical data presented in Table 2. They are scaled to 1/1.000.000.

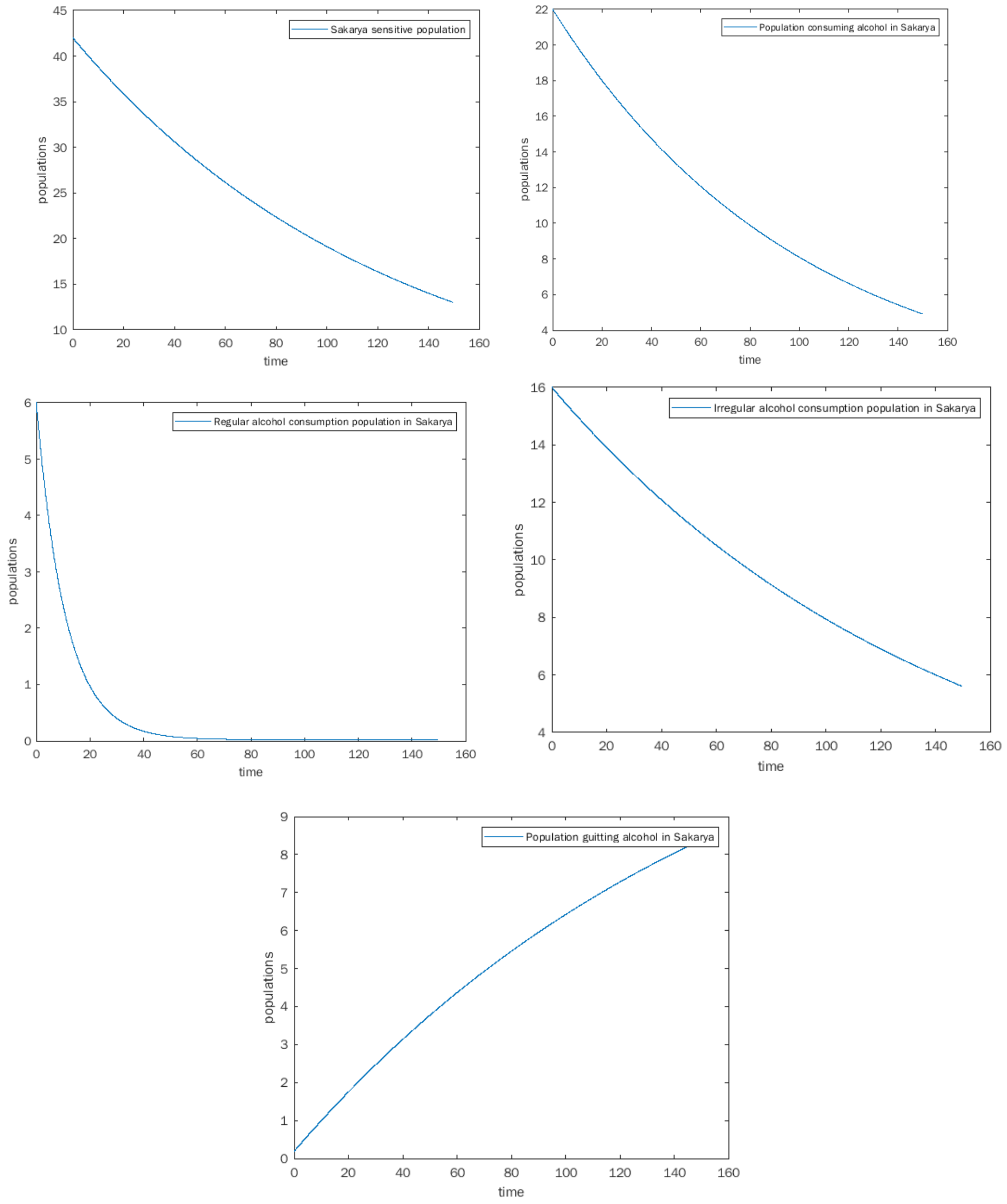

6. CONCLUSION AND DISCUSSION

The ratio R_0 of a mathematical model gives us information about the increase or decrease of an incident. R_0 consists of the parameters of the model. In our model, if R_0 =1, the prevalence of alcohol use is stable. It never disappears. If R_0>1, the prevalence of alcohol use increases, and if R_0 < 1, the prevalence of alcohol use decreases over time.

6.1. Non-Alcohol Equilibrium Points

Since R_0= 0.165 < 1 for Turkey, the balance point is found as $(E_0) = (0{,}44\,;0;0;0)$. This means that the social spread of alcohol use is decreasing. Alcohol use will decrease over time.

Similarly, since R_0= 0.1 < 1 for Turkey, the balance point is found as $(E_0) = (0{,}3\,;0;0;0)$. This can be interpreted that the social spread of alcohol use is decreasing. Alcohol use will decrease over time.

6.2. Alcohol Use Equilibrium Points

If R_0> 1, the equilibrium point is positive. Since we found R_0< 1 for Turkey, alcohol consumption does not have a positive equilibrium point. Since we found R_0< 1 for Sakarya, alcohol consumption does not have a positive equilibrium point, too.

Acknowledgments

I would like to thank my esteemed referees and editors for their help during the publication of this article.

Funding

No financial support was received for the research, authorship, or publication of this work.

The Declaration of Conflict of Interest/ Common Interest

No conflict of interest or common interest has been declared by the authors.

Authors' Contribution

The first author contributed 70%, and the second author contributed 30%.

The Declaration of Ethics Committee Approval

This study does not require ethics committee approval or any special permission.

The Declaration of Research and Publication Ethics

I declare that I have complied with the scientific, ethical, and attribution rules of SAUJS in all processes of the article and have not made any falsifications on the data collected. I accept that I am not responsible for ethical violations that may be encountered, and this study has not been evaluated in any academic publication environment other than Sakarya University Journal of Science.

REFERENCES

[1] Brownlee, J. (1909). Certain considerations on the causation and course of epidemics. Proc. R. Soc. Med. 2: 243–258

[2] Brownlee, J. (1912). The mathematical theory of random migration and epidemic distribution. Proc. R. Soc. Edinb. 31: 262–289

[3] Kermack, W.O., McKendrick, A.G. (1927). Contributions to the mathematical theory of epidemics, part 1. Proc. R. Soc. Edinb., Sect. A., Math., 115: 700–721

[4] Song, S., Wang, K., Wang, W. (2008). Dynamics of an HBV model with diffusion and delay. J. Theor. Biol. 253(1): 36–44

[5] Huo, H.F., Ma, Z.P. (2010). Dynamics of a delayed epidemic model with non-monotonic incidence rate. Commun. Nonlinear Sci. Numer. Simul. 15(2): 459–468

[6] McCluskey, C.C. (2010). Complete global stability for an SIR epidemic model with

delay distributed or discrete. Nonlinear Anal., Real World Appl. 11(1): 55–59

[7] Ma, Z., Xu, R. (2009). Global stability of a SIR epidemic model with nonlinear incidence rate and time delay. Nonlinear Anal., Real World Appl. 10(5): 3175–3189

[8] Ma, Z., Xu, R. (2009). Stability of a delayed SIRS epidemic model with a nonlinear incidence rate. Chaos Solitons Fractals 41(5): 2319–2325

[9] Cheng, S., Song, X. (2005). A delay-differential equation model of HIV infection of CD4+ T-cells. J. Korean Math. Soc. 42(5): 1071–1086

[10] Guglielmi N., Hairer, E. (2001). Implementing Radau IIA methods for stiff delay differential equations. J. Comput. Math. 67(1): 1–12

[11] Beretta, E., Ma, W., Takeuchi, Y. (2010). Global asymptotic properties of a delay SIR epidemic model with finite incubation times. Nonlinear Anal., Theory Methods Appl. 42(6): 931–947

[12] Van den Driessche, P., Watmough, J. (2008). Further notes on the basic reproduction number. In: Mathematical Epidemiology. Lecture Notes in Mathematics, vol. 1945, pp. 159–178. Springer, Berlin

[13] D’Onofrio, A., Manfredi, P., Salinelli, E. (2007). Bifurcation thresholds in an SIR model with information-dependent vaccination. Math. Model. Nat. Phenom. 2(1),: 26–43

[14] Yi, N., Zhao, Z., Zhang, Q. (2009). Bifurcations of an SEIQS epidemic model. Int. J. Inf. Syst. Sci. 5(3–4): 296–310

[15] Anwar, M.N., Fathalla, A.R. (2012). Qualitative analysis of delayed SIR epidemic model with saturated incidence rate. Int. J. Differ. Equ. 2012, Article ID 408637

[16] Hethcote, H.W. (1976). Qualitative analyses of communicable disease models. Math. Biosci. 7: 335–356

[17] Alzahrani, E., Zeb, A. (2020). Stability analysis and prevention strategiesa of tobacco smoking model,/ doi.org./10.1186/s13661-019-01315-1

[18] Okongo, O.M. (2015). The local and global stability of the disease free eguilibrium in a coinfection model of HIV7AIDS, Tuberculosis and malaria, IOSR Journal of Mathematics/ISSN:2319-764X.Volume 11.,pp 1-13

[19] Bhattacharjee, A. (2015). A transmission model for HIV/AIDS in the presence of treatment, IOSR Journal of Mathematics/ISSN:2319-764X.Volume 11.,pp. 72-80

[20] Momani, S., Zaman, G., Zeb, A. (2013). Dynamics of a giving up smoking model, Elsevier, Applied mathematical modelling , 37.7: 5326-5334

[21] Adu , I.K. ,Mojeeb Al-Rahman El-Nur, O. , Yang, C. (2017). mathematical model of drinking epidemic, British journal of mathematics & Computer science, 22(5):1-10, ISSN:2231-0851

[22] Balatif, O., Khajii, B., Labzai,A., Rachik ,M. (2020).Mathematical modeling and analysis of an alcohol drinking model with the ınfluence of alcohol treatment centers, International journal of Mathematics and Matematical sciences, Volume 2020,ID:4903168, pp.12

[23] Röst, G., Tekeli, T. (2020). Stability and oscillations of multistage SIS models depend on the number of stages,Elsevıer :Applied mathematics and computation,380, DOI: 10.1016 / j.amc.2020.12525

[24] Alzzahrani, E., Beleanu, D., El-Desoky, M.M. (2021).Mathematical modeling and analysis of the novel coronavirus using

atangana-Baleanu derivative, Elsevıer: Results in Physics, 25, 104240

[25] https://dosyasb.saglik.gov.tr/Eklenti/36134,siy2018trpdf.pdf (Access Date:01.02.2021)

[26] https://tuikweb.tuik.gov.tr/UstMenu.do.(Access Date:01.02.2021)

[27] Demirci, M., Eker, E. (2017). Üniversite öğrencilerinin madde bağımlılığı sıklığı ve madde kullanım özellikleri, Anadolu bil Meslek Yüksekokulu Dergisi, Cilt:12,s.10

[28] https://www.milliyet.com.tr/gundem/iste-turkiyenin-alkol-haritasi-1714739 (Access Date:15.01.2021)

SAKARYA ÜNİVERSİTESİ

FEN BİLİMLERİ ENSTİTÜSÜ
DERGİSİ

Sakarya University Journal of Science
SAUJS

e-ISSN 2147-835X Founded 1997 Period Bimonthly Publisher Sakarya University
http://www.saujs.sakarya.edu.tr/en/

Title: A New Game Value Approach for Infinite Interval Matrix Games

Authors: Aykut OR, Gönül Selin SAVAŞKAN

Recieved: 2021-09-06 00:00:00

Accepted: 2021-10-21 00:00:00

Article Type: Research Article

Volume: 25
Issue: 6
Month: December
Year: 2021
Pages: 1343-1351

How to cite
Aykut OR, Gönül Selin SAVAŞKAN; (2021), A New Game Value Approach for Infinite Interval Matrix Games. Sakarya University Journal of Science, 25(6), 1343-1351, DOI: https://doi.org/10.16984/saufenbilder.991897
Access link
http://www.saujs.sakarya.edu.tr/tr/pub/issue/66341/991897

Sakarya University Journal of Science 25(6), 1343-1351, 2021

A New Game Value Approach for Infinite Interval Matrix Games

Aykut OR[1], Gönül Selin SAVAŞKAN*[1]

Abstract

The purpose of this paper is to determine when and under which conditions the solution and game value of the infinite interval matrix games will exist. Firstly, the concept of a reasonable solution defined in interval matrix games was extended to infinite interval matrix games. Then, the solution and game value were characterized by using sequences of interval numbers defined by Chiao ["Fundamental Properties of Interval Vector Max-Norm", Tamsui Oxf J Math Sci, 18(2):219-233, 2002.] and their concept of convergence of interval numbers. Considering that each row or column of the payoff matrix is a sequence of interval numbers, we assume that each row converges to the same interval number $\tilde{\alpha} = [\alpha_l, \alpha_r]$ and each column to the same interval number $\tilde{\beta} = [\beta_l, \beta_r]$. In a conclusion, the existence of the solution of $\tilde{G}$ is shown.

Keywords: infinite matrix games, interval matrix games, reasonable solution

1. INTRODUCTION

Game theory is a branch of mathematics that studies the interaction between players with mathematical methods, in which all parties engage in a game to maximize the payoffs (for a specific goal) making rational decisions (Barron, 2006). John von Neumann laid the mathematical foundations of game theory with the Minimax Theorem in 1928. Moreover, "Game Theory and Economics Behavior" known as the first book in the field of game theory, was published by von Neumann and Morgenstern in 1944. Different mathematical concepts such as matrix, differential equation, and graphs are used to create mathematical model of the game.

On the other hand, the games are classified according to payoff functions, players' numbers, and strategy sets. In this context, games played with two players in which one's loss is equal to the other's gain and the payoff function is represented by a matrix called matrix games (Owen, 1995).

Generally, in matrix games, all payoff matrix entries are supposed to be certain. However, we often encounter cases with imprecise information such as interval matrices or uncertain environments in real-life situations.

In this paper, we count infinite interval matrix games, a generalized form of interval matrix games, allowing players to have infinite strategies. As in the finite games, $\tilde{g}_{ij}$ is the payoff of player I when players I and II choose ith and jth pure strategies, respectively.

---

* Corresponding author: aykutor@comu.edu.tr
[1] Çanakkale Onsekiz Mart University, Faculty of Arts and Sciences, Department of Mathematics
E-mail: savaskan@comu.edu.tr
ORCID: https://orcid.org/0000-0001-5279-0057, https://orcid.org/0000-0002-9978-6941

A mixed strategy for Player I, in this case, will be a sequence $(x_1, x_2, \ldots)$ satisfying

$$\sum_{i=1}^{\infty} x_i = 1, x_i \geq 0.$$

Similarly, for player II will be a sequence $(y_1, y_2, \ldots)$ defined similarly (Owen, 1995). The game value in mixed strategies is denoted by $h(x, y)$, i.e.,

$$h(x, y) = \sum_{i,j=1}^{\infty} x_i \, \tilde{g}_{ij} y_j.$$

Marchi (1967) found a necessary and sufficient condition for the existence of game value in an infinite matrix game. However, it wasn't easy to verify this condition. Tijs (1975), Cegielski (1991) ve Mendez Naya (1996, 1998, 2001) obtained different results regarding the existence of game value in infinite matrix games. Li et al. (2012) defined the "reasonable solution" and notions of solution for infinite matrix games, developing a bi-objective linear programming method to solve the game. In this paper, we account for a reasonable solution and notions of solution for infinite interval matrix games. Also, we present sufficient conditions for an exact or reasonable solution by using the convergence of sequences of rows or columns.

2. PRELIMINARIES

In this section, we refer to the definition, theorem, and the notions concerning interval matrices (Moore, 1979; Sengupta and Pal, 1997, 2000, 2009) and concerning interval matrix games (Collins and Hu, 2008; Nayak and Pal, 2009). The most extensive work on interval analysis was done by Moore (1979). First of all, we introduced the definitions used in interval matrix games.

2.1. Interval Numbers

Definition 2.1.1 [8] An interval $\tilde{a}$ is the bounded, closed subset of the real number set $\mathbb{R}$, defined by

$$\tilde{a} = [a_L, a_R] = \{x \in \mathbb{R}: a_L \leq x \leq a_R\},$$

where $a_L, a_R \in \mathbb{R}$ and $a_L \leq a_R$. All interval number set is denoted by $\mathbb{R}^i$. If $a_L = a_R$, then $\tilde{a}$ is a degenerate interval.

The following definition describes the basic arithmetic operations for intervals.

Definition 2.1.2 [8] Let $\tilde{a} = [a_L, a_R]$ and $\tilde{b} = [b_L, b_R]$ be two interval numbers, and α is a real number, then

(1) $\tilde{a} = \tilde{b} \Leftrightarrow a_L = b_L$ ve $a_R = b_R$

(2) $\tilde{a} + \tilde{b} \Leftrightarrow [a_L + b_L, a_R + b_R]$

(3) $\tilde{a} - \tilde{b} \Leftrightarrow [a_L - b_R, a_R - b_L]$

(4) $\tilde{a}.\tilde{b} \Leftrightarrow [\min S, \max S]$ such that

$$S = \{a_L b_L, a_L b_R, a_R b_L, a_R b_R\}$$

(5) $\tilde{a}/\tilde{b} \Leftrightarrow [\min K, \max K]$ where

$$K = \{\frac{a_L}{b_L}, \frac{a_L}{b_R}, \frac{a_R}{b_L}, \frac{a_R}{b_R}\} \text{ such that } 0 \notin \tilde{b}$$

(6) For $\alpha \in \mathbb{R}, (\alpha \neq 0)$

$$\alpha\tilde{a} = \begin{cases} [\alpha a_L, \alpha a_R], \alpha \geq 0 \\ [\alpha a_R, \alpha a_L], \alpha < 0. \end{cases}$$

The midpoint, and the radius of the interval $\tilde{a}$ was defined by Moore (1979) as follows respectively,

$$m(\tilde{a}) = \frac{a_L + a_R}{2}, \qquad \omega(\tilde{a}) = \frac{a_R - a_L}{2}.$$

The ordering between intervals is a difficult problem. Firstly, Moore (1979) introduced an order relation to order two discrete interval numbers. Then, Ishibuchi and Tanaka (1990) defined different order relations, which cannot strictly explain ranking interval numbers. Then, an index was defined by Sengupta et al. (2001) and Sengupta et al. (2009), which can order two intervals in terms of value.

Definition 2.1.3 [17] Let $\mathbb{R}^i$ denote the set of all closed intervals on the real line $\mathbb{R}$. Then, an acceptability function $\phi: \mathbb{R}^i \times \mathbb{R}^i \to [0,\infty)$ is defined by

$$\phi\left(\tilde{a} \prec \tilde{b}\right) = \frac{m\left(\tilde{b}\right) - m(\tilde{a})}{\omega(\tilde{a}) + \omega\left(\tilde{b}\right)}$$

where $\omega(\tilde{a}) + \omega\left(\tilde{b}\right) \neq 0$. $\phi\left(\tilde{a} \prec \tilde{b}\right)$ may be interpreted as the grade of acceptability of the "second interval to be superior to the first interval".

The grade of acceptability of $\phi\left(\tilde{a} \prec \tilde{b}\right)$ can be further classified and interpreted based on comparison interval $\tilde{b}$ with respect to the interval $\tilde{a}$ as follows:

$$\phi(\tilde{a} \prec \tilde{b}) = \begin{cases} 0 & m(\tilde{a}) = m(\tilde{b}) \\ > 0, < 1 & m(\tilde{a}) < m\left(\tilde{b}\right) \text{ ve } a_R > b_L \\ \geq 1 & m(\tilde{a}) < m\left(\tilde{b}\right) \text{ ve } a_R \leq b_L. \end{cases}$$

(1) If $\phi\left(\tilde{a} \prec \tilde{b}\right) = 0$, then the premiss "$\tilde{a}$ inferior to $\tilde{b}$" is not accepted.
(2) If $0 < \phi\left(\tilde{a} \prec \tilde{b}\right) < 1$, then the interpreter accepts the premiss $\tilde{a} \prec \tilde{b}$ with different grades of satisfaction ranging from zero to one.
(3) If $\phi\left(\tilde{a} \prec \tilde{b}\right) \geq 1$, the interpreter is satisfied with the premiss $\tilde{a} \prec \tilde{b}$.

For each interval number, the terms supremum and infimum are defined further below:

Definition 2.1.4 For each $\tilde{a}, \tilde{b} \in \mathbb{R}^i$

$$\sup\left\{\tilde{a}, \tilde{b}\right\} = [\sup\{a_L, b_L\}, \sup\{a_R, b_R\}]$$

$$\inf\left\{\tilde{a}, \tilde{b}\right\} = [\inf\{a_L, b_L\}, \inf\{a_R, b_R\}].$$

2.2. Interval Matrix Games

Let us consider an interval matrix game. Suppose that $S_I = \{I_1, I_2, \ldots, I_m\}$ and $S_{II} = \{II_1, II_2, \ldots, II_n\}$ are the sets of pure strategies for Players I and II. If Players I and II choose their pure strategies $I_i \in S_I$ and $II_j \in S_{II}$, respectively, then the payoff for Player I is stated by $\tilde{g}_{ij} = [g_{ijL}, g_{ijR}]$. Interval matrix G is denoted as follows:

$$\begin{array}{c} \\ I_1 \\ I_2 \\ \vdots \\ I_m \end{array} \begin{array}{c} \begin{array}{cccc} II_1 & II_2 & \cdots & II_n \end{array} \\ \begin{bmatrix} [g_{11L}, g_{11R}] & [g_{12L}, g_{12R}] & \cdots & [g_{1nL}, g_{1nR}] \\ [g_{21L}, g_{21R}] & [g_{22L}, g_{22R}] & \cdots & [g_{2nL}, g_{2nR}] \\ \vdots & \vdots & \cdots & \vdots \\ [g_{m1L}, g_{n1R}] & [g_{m2L}, g_{m2R}] & \cdots & [g_{mnL}, g_{mnR}] \end{bmatrix} \end{array}$$

X and Y below represent sets of mixed strategies for Players I and II,

$$X = \left\{x = (x_1, x_2, \ldots, x_m) \mid \sum_{i=1}^{m} x_i = 1, x_i \geq 0, (i = 1,2, \ldots, m)\right\}$$

$$Y = \left\{y = (y_1, y_2, \ldots, y_n) \mid \sum_{j=1}^{n} y_i = 1, y_j \geq 0, (j = 1,2, \ldots, n)\right\}.$$

Taking into account (2) and (6) of Definition 2.1.2, the payoff function of Player I can be given as follows:

$$h(x,y) = \sum_{i=1}^{m} \sum_{j=1}^{n} \tilde{a}_{ij} x_i y_j = \left[\sum_{i=1}^{m} \sum_{j=1}^{n} a_{ijL} x_i y_j, \sum_{i=1}^{m} \sum_{j=1}^{n} a_{ijR} x_i y_j\right],$$

which is an interval (Li et al., 2012).

Definition 2.2.1 [6] Let G be an interval matrix. The lower and upper values of the game are defined below

$$V_L = \max_{1 \leq i \leq m} \min_{1 \leq j \leq n} \left\{\left[a_{ijL}, a_{ijR}\right]\right\}$$

$$V_U = \min_{1 \leq j \leq n} \max_{1 \leq i \leq m} \left\{\left[a_{ijL}, a_{ijR}\right]\right\}.$$

If $[a_{krL}, a_{krR}] = V_L = V_U$, then (k,r) element of interval matrix G is called an equilibrium point and $[a_{krL}, a_{krR}]$ is called the game value in pure strategies.

Example 2.2.2 Let us consider an interval matrix game given by G

$$G = \begin{array}{c} \\ I_1 \\ I_2 \\ I_3 \end{array} \begin{array}{c} \begin{array}{cccc} II_1 & II_2 & II_3 & II_4 \end{array} \\ \begin{pmatrix} [-12,-1] & [-10,5] & [-6,5] & [-8,5] \\ [-11,6] & [-3,5] & [1,6] & [6,7] \\ [-5,-4] & [-3,3] & [-4,0] & [-5,5] \end{pmatrix} \end{array}.$$

$g_{23} = [1,6]$ is the minimum value of the second row and the maximum value of the third column at the same time, namely

$$\max\min g_{ij} = \min\max g_{ij} = [1,6].$$

It means that [1,6] is the game value.

Example 2.2.3 Let us consider the game given by

$$G = \begin{array}{c} \\ I_1 \\ I_2 \end{array} \begin{array}{c} \begin{array}{cc} II_1 & II_2 \end{array} \\ \begin{pmatrix} [-1,1] & [1,3] \\ [0,2] & [-2,0] \end{pmatrix} \end{array}$$

Here, we compute

$$\min\max g_{ij} = [-1,1]$$

$$\max\min g_{ij} = [0,2].$$

Then, we get the following,

$$\max\min g_{ij} \neq \min\max g_{ij}.$$

Now, in pure strategies, there cannot always be the game value of the interval matrix game. In this case, Li et al. (2012) defined the reasonable solution and the concepts of solution for interval matrix games, as follows.

Definition 2.2.4 [6] Let $\tilde{v} = [v_L, v_R]$ and $\tilde{w} = [w_L, w_R]$ be interval numbers on $\mathbb{R}$. Assume that there exist $x^* \in X$ and $y^* \in Y$. Then, $(x^*, y^*, \tilde{v}, \tilde{w})$ is called a reasonable solution of the interval matrix game G if $\forall\, x \in X, y \in Y$; $(x^*, y^*, \tilde{v}, \tilde{w})$ satisfies both conditions following

$$x^* G y^T \geq \tilde{v} \text{ and } x G {y^*}^{\mathrm{T}} \leq \tilde{w}.$$

If $(x^*, y^*, \tilde{v}, \tilde{w})$ is a reasonable solution for the interval matrix game G then $\tilde{v}$ is called a reasonable value for Player I and $\tilde{w}$ is called reasonable value for Player II. In this case, x^* and y^* represent reasonable strategies for Player I and II, respectively. In other words, a reasonable solution for the interval matrix game is not an exact solution, which is conceptually defined below.

Definition 2.2.5 [6] Let V and W be the sets of reasonable values $\tilde{v}$ *and* $\tilde{w}$ for Players I and II, respectively. Assume that there exist $\tilde{v}^* \in V, \tilde{w}^* \in W$. If there does not exist any $\tilde{v}' \in V(\tilde{v}' \neq \tilde{v}^*)$ and $\tilde{w}' \in W(\tilde{w}' \neq \tilde{w}^*)$ such that they satisfy either

$$\tilde{v}^* \preccurlyeq \tilde{v}' \quad or \quad \tilde{w}^* \succcurlyeq \tilde{w}',$$

then $(x^*, y^*, \tilde{v}^*, \tilde{w}^*)$ is called a solution of the interval matrix game G, with x^* and y^* being optimal strategies for Player I and II. $\tilde{v}^*$ is called the value of interval matrix game G for Player I and similarly, $\tilde{w}^*$ is for Player II.

2.3. A Sequence of Interval Numbers

Definition 2.3.1 [3] Let $\tilde{x}_i = \{\tilde{x}: \tilde{x}_{iL} \leq x \leq \tilde{x}_{iR}, \tilde{x}_{iL},\ \tilde{x}_R \in \mathbb{R}\}$ be a real closed interval. Then, an ordered n-tuple of intervals

$$\begin{aligned} \tilde{x} &= (\tilde{x}_1, \tilde{x}_2, \dots, \tilde{x}_m) \\ &= ([x_{1L}, x_{1R}], [x_{2L}, x_{2R}], \dots, [x_{nL}, x_{nR}]) \end{aligned}$$

is called an n-dimensional interval vector.

Definition 2.3.2 [8] Let f be a function defined below

$$\begin{array}{rcl} f: \mathbb{N} & \to & \mathbb{R}^i \\ n & \to & f(n) := \tilde{x}_k \end{array}$$

Then, f is called a sequence of interval numbers and denoted by $(\tilde{x}) = (\tilde{x}_k)$. Also $\tilde{x}_k$ is the kth term of $(\tilde{x}_k)$.

Let $\mathbb{R}^i$ be the sets of all intervals and $\tilde{a}, \tilde{b} \in \mathbb{R}^i$. The distance between $\tilde{a}$ and $\tilde{b}$ intervals are represented by

$$d(\tilde{a}, \tilde{b}) = max\{|a_L - b_L|, |a_R - b_R|\}.$$

Moreover, d is a metric on $\mathbb{R}^i$ and $(\mathbb{R}^i, d)$ is a metric space (Moore, 1979).

Definition 2.3.3 [3] A sequence $(\tilde{x}_k)$ of $(\mathbb{R}^i, d)$ is said to be convergent to the interval number $\tilde{x}_0$ if for each $\varepsilon > 0$ there exists a positive integer k_ε such that $d(\tilde{x}_k, \tilde{x}_0) < \varepsilon$ for all $k \geq k_\varepsilon$ and denoted by

$$\lim_{k\to\infty} \tilde{x}_k = \tilde{x}_0.$$

Thus,

$$\lim_{k\to\infty} \tilde{x}_k = \tilde{x}_0 \Leftrightarrow \lim_{k\to\infty} x_{kL} = x_{0L} \text{ ve } \lim_{k\to\infty} x_{kR} = x_{0R}.$$

Theorem 2.3.4 [3] Let $(\tilde{x}_k)$ be a convergent sequence of intervals with limit interval $\tilde{x}_0$ then

$$\lim_{k\to\infty} \tilde{x}_k = \tilde{x}_0 \Leftrightarrow \lim_{k\to\infty} d(\tilde{x}_k, \tilde{x}_0) = 0.$$

Example 2.3.5 Let us consider a sequence of interval $(\tilde{x}_k) = \left(\left[\frac{1}{k}, 1^k\right]\right)$ and denote its convergent to the interval number [0,1].

$$\begin{aligned}
\lim_{k\to\infty} d(\tilde{x}_k, \tilde{x}_0) &= \lim_{k\to\infty} \max\{|x_{kL} - x_{0L}|, |x_{kR} - x_{0R}|\} \\
&= \lim_{k\to\infty} \max\left\{\left|\frac{1}{k} - 0\right|, |1 - 1|\right\} \\
&= \lim_{k\to\infty} \frac{1}{k} = 0
\end{aligned}$$

Thereby, the sequence of interval $(\tilde{x}_k)$ is convergent to the interval number [0,1].

2.4. Infinite Interval Matrix Games

In this paper, we have considered finite interval matrix games till this part. In this section, we focus on the case where the pure strategy sets of both players have infinite elements. We investigate the concepts of game value and solution of infinite interval matrix games generalized to finite interval matrices. Given $\tilde{g}_{ij} = [\tilde{g}_{ijL}, \tilde{g}_{ijR}]$ denotes the payoff of Player I when Player I chooses $i\ th$ strategy and Player II chooses $j\ th$ strategy.

Let $\tilde{G} = [g_{ij}]_{i,j\in\mathbb{N}}$ be an infinite interval matrix. Also denoted by

$$\tilde{G} = [g_{ij}]_{i,j\in\mathbb{N}} = \begin{bmatrix} [g_{11L}, g_{11R}] & [g_{12L}, g_{12R}] & \cdots \\ [g_{21L}, g_{21R}] & [g_{22L}, g_{22R}] & \cdots \\ \vdots & \vdots & \vdots \end{bmatrix}$$

where the set of strategies of both players is defined by

$$S = \{(x_1, x_2, \dots): \sum_{i=1}^{\infty} x_i = 1,\ \ x_i \geq 0,\ \ \forall i \in \mathbb{N}\}$$

Naya (2001). The payoff function of Player I is given below,

$\forall\ (x, y) \in S \times S,$

$$\tilde{h}(x, y) = X\tilde{G}Y^T = \sum_{j=1}^{\infty}\sum_{i=1}^{\infty} x_i\, [g_{ijL}, g_{ijR}] y_j^T.$$

Definition 2.4.1 [11] Let $\tilde{G} = [g_{ij}]_{i,j\in\mathbb{N}}$ be the payoff matrix of the infinite interval matrix game. For each $(x, y) \in S \times S$, the superior and inferior values of $\tilde{G}$, $\overline{V}(\tilde{G})$ and $\underline{V}(\tilde{G})$ respectively, are defined by

$$\overline{V}(\tilde{G}) = \inf_{y\in S} \sup_{x\in S} \tilde{h}(x, y)$$

and

$$\underline{V}(\tilde{G}) = \sup_{x\in S} \inf_{y\in S} \tilde{h}(x, y),$$

respectively.

Assume that the payoff matrix is denoted by

$$\tilde{G}_{i'} = (g_{ij})_{1\leq i\leq i';1\leq j<\infty}$$

in which the Player I has a finite strategy but Player II has infinite strategy while the payoff matrix is stated by

$$\tilde{G}^{j'} = (g_{ij})_{\substack{1\leq i<\infty \\ 1\leq j\leq j'}}$$

in which the rows are infinite, and the columns are finite. Such games are called semi-infinite interval matrix games (Tijs, 1975).

3. RESULTS

This section contains the results obtained and a new definition and theorem based on the approach in this paper.

Definition 3.1 Let $\tilde{v} = [v_l, v_r]$ and $\tilde{w} = [w_l, w_r]$ be elements of $\mathbb{R}^i$. Assume that $x^*, y^* \in S$ and $(x^*, y^*, \tilde{v}, \tilde{w})$ is a reasonable solution to the infinite interval matrix game $\tilde{G}$. If $(x^*, y^*, \tilde{v}, \tilde{w})$ satisfies both the conditions

$$x^*\tilde{G}y^T \succcurlyeq \tilde{v} \text{ and } x\tilde{G}{y^*}^T \preccurlyeq \tilde{w}, \forall x, y \in S\,.$$

If $(x^*, y^*, \tilde{v}, \tilde{w})$ is a reasonable solution to the infinite interval matrix game $\tilde{G}$, then $\tilde{v}$ and $\tilde{w}$ are called reasonable values for each player, where x^* is a reasonable strategy of Player I and y^* is a reasonable strategy for Player II.

Let V and W be the sets of reasonable values for Players I and II, respectively, which does not imply a solution for the infinite interval matrix game. Consequently, the solution to the infinite interval matrix game is defined below.

Definition 3.2 Given that there are $\tilde{v}^* \in V$ and $\tilde{w}^* \in W$. If there are no $\tilde{v}' \in V(\tilde{v}' \neq \tilde{v}^*)$ and $\tilde{w}' \in W(\tilde{w}' \neq \tilde{w}^*)$ such that they satisfy

$$\tilde{v}^* \preccurlyeq \tilde{v}' \; or \; \tilde{w}^* \succcurlyeq \tilde{w}'$$

then $(x^*, y^*, \tilde{v}^*, \tilde{w}^*)$ is called a solution of the infinite interval matrix game $\tilde{G}$, x^* and $y^*$are optimal strategies for Players I and II, respectively, $\tilde{v}^*$ is called the value of infinite interval matrix game $\tilde{G}$ for Player I and $\tilde{w}^*$is called the value of the game for Player II.

Definition 3.3 Let $\tilde{G} = (\tilde{g}_{ij})_{i,j\in\mathbb{N}}$ be a bounded infinite interval matrix. Limit superior of row sequences and limit inferior of column sequences of an infinite interval matrix are described as follows:

$$T_i = \inf_{\mathrm{m}\geq 1}\sup_{\mathrm{j}\geq\mathrm{m}} \tilde{g}_{ij}\,, \forall j \in \mathbb{N}, T = (T_i)_{i\in\mathbb{N}}$$

and

$$K_j = \sup_{\mathrm{m}\geq 1}\inf_{\mathrm{i}\geq\mathrm{m}} \tilde{g}_{ij}\,, \forall i \in \mathbb{N}, K = (K_j)_{j\in\mathbb{N}}\,,$$

respectively.

Theorem 3.4 Let $\tilde{v} = \inf_{\mathrm{j}\in\mathbb{N}} K_j$ be infimum of K_j and $\tilde{w} = \sup_{\mathrm{i}\in\mathbb{N}} T_i$ be supremum of T_i, $x^*, y^* \in S$ and $(x^*, y^*, \tilde{v}, \tilde{w})$ be a reasonable solution. If $\tilde{G} = (\tilde{g}_{ij})_{i,j\in\mathbb{N}}$ is a bounded infinite interval matrix such that

$$\tilde{v} \succ \tilde{w},$$

then $\tilde{G}$ does not have a value.

Proof. First,

$$\inf x\tilde{G}y^T \preccurlyeq xT, \forall x \in S.$$

Suppose otherwise. Then, there exist $z \in S$ and $\epsilon > 0$ such that

$$\inf_{y\in S} z\tilde{G}y^T \succ zT + \epsilon.$$

Therefore,

$$z\tilde{G}e_j^T \prec zT + \epsilon \Rightarrow z\left(T - \tilde{G}e_j^T\right) \prec -\epsilon, \forall j \in \mathbb{N}.$$

But this is a contradiction.

Hence,

$$\inf_{\mathrm{y}\in\mathrm{S}} x\tilde{G}y^T \preccurlyeq xT, \forall x \in S.$$

Thereby,

$$\sup_{\mathrm{x}\in\mathrm{S}}\inf_{\mathrm{y}\in\mathrm{S}} x\tilde{G}y^T \preccurlyeq \sup xT = \sup_{\mathrm{i}\in\mathbb{N}} T_i = \tilde{w}$$
$$\Rightarrow V_L(\tilde{G}) \preccurlyeq \tilde{w}.$$

Similarly,

$$V^U(\tilde{G}) \succcurlyeq \tilde{v}.$$

Thus, game $\tilde{G}$ does not have a value.

Example 3.5 Payoff matrix $\tilde{G}$ is given as follows

$$\tilde{G} = \left(\tilde{g}_{ij}\right)_{i,j\in\mathbb{N}} = \begin{cases} [-1,1] & i < j, \\ [0,0] & i = j, \\ [1,1] & i > j. \end{cases}$$

Given Theorem 3.4, the fact that $\tilde{G}$ has no value is an immediate result, since it is obvious that for this matrix $T_i = [-1,1]$ for all $i,j \in \mathbb{N}$ and $K_j = [1,1]$.

Theorem 3.6 Let $\tilde{G} = \left(\tilde{g}_{ij}\right)_{i,j\in\mathbb{N}}$ be a bounded infinite interval matrix game such that all its column converges to $\tilde{\alpha} = [\alpha_l, \alpha_r]$ and all its rows converge to $\tilde{\beta} = [\beta_l, \beta_r]$. If $\tilde{\alpha} \preccurlyeq \tilde{\beta}$ then,

$$\tilde{\alpha} \preccurlyeq \underline{V}(\tilde{G}) \preccurlyeq \overline{V}(\tilde{G}) \preccurlyeq \tilde{\beta}.$$

Proof. Let us consider $\tilde{G} = \left(\tilde{g}_{ij}\right)_{i,j\in\mathbb{N}}$ as a separate payoff matrix taking into account the lower and upper values of the intervals, as follows:

$$\begin{aligned}\tilde{G} &= \left[g_{ij}\right]_{i,j\in\mathbb{N}} \\ &= \begin{bmatrix} [g_{11L}, g_{11R}] & [g_{12L}, g_{12R}] & \cdots \\ [g_{21L}, g_{21R}] & [g_{22L}, g_{22R}] & \cdots \\ \vdots & \vdots & \vdots \end{bmatrix}\end{aligned}$$

$$G_L = \left[g_{ijL}\right]_{i,j\in\mathbb{N}} = \begin{bmatrix} g_{11L} & g_{12L} & \cdots \\ g_{21L} & g_{22L} & \cdots \\ \vdots & \vdots & \vdots \end{bmatrix}$$

$$G_R = \left[g_{ijR}\right]_{i,j\in\mathbb{N}} = \begin{bmatrix} g_{11R} & g_{12R} & \cdots \\ g_{21R} & g_{22R} & \cdots \\ \vdots & \vdots & \vdots \end{bmatrix}$$

where G_L and G_R are infinite interval matrices whose entries are real numbers. Assume that each of G_L and G_R is an infinite matrix game and in the payoff matrix G_L the sequence of rows (or columns) converges to the real number β_L (or α_L). Similarly, in the payoff matrix G_R the sequence of rows (or columns) converges to the real number β_R (or α_R).

Since $\tilde{\alpha} \preccurlyeq \tilde{\beta}$

then,

$$\alpha_L \leq \beta_L \; and \; \alpha_R \leq \beta_R.$$

Therefore,

$$\alpha_L \leq V_L(G_L) \leq V^U(G_L) \leq \beta_L$$

$$\alpha_R \leq V_L(G_R) \leq V^U(G_R) \leq \beta_R.$$

the above inequalities hold (Naya, 2001). Given these inequalities when the nested intervals are ignored

$$\begin{aligned}[\alpha_L, \alpha_R] &\preccurlyeq [V_L(G_L), V_L(G_R)] \\ &\preccurlyeq [V^U(G_L), V^U(G_R)] \preccurlyeq [\beta_L, \beta_R]\end{aligned}$$

the above inequality is obtained.

On the other hand, it means that

$$\tilde{\alpha} \preccurlyeq \underline{V}(\tilde{G}) \preccurlyeq \overline{V}(\tilde{G}) \preccurlyeq \tilde{\beta}.$$

Namely, the proof is completed.

4. CONCLUSIONS

The concepts of game value and solution of the game are two main characteristics of the research-related matrix games. Currently, interval matrix games, which play a crucial part in dealing with uncertainties in the real world, are gaining attention. Studies on interval matrix games and their solution methods play an essential role in the game theory since their applicability to daily life practices is high. Consequently, within the scope of this paper, we extend an interval matrix game to an infinite interval matrix game, and we state some definitions and theorems for finite interval matrix games. The results obtained from the present work will significantly contribute to future works since the infinite interval matrix game is an emerging topic. After this work, research on the convergence of either row or column sequence to a different interval number for a matrix game with infinite payoffs is an open problem.

Acknowledgments

We would like to thank the reviewers, editors, and Canakkale Onsekiz Mart University Scientific Research Projects Coordination Unit, who supported the work.

Funding

“This study is supported by the Office of Scientific Research Projects Coordination at Canakkale Onsekiz Mart University, Grant Number: FBA-2019-2807.”

The Declaration of Conflict of Interest/ Common Interest

No conflict of interest or common interest has been declared by the authors.

Authors' Contribution

The authors contributed equally to the study and approved the last version of the manuscript.

The Declaration of Ethics Committee Approval

This study does not require ethics committee permission or any special permission.

The Declaration of Research and Publication Ethics

The authors of the paper declare that they comply with the scientific, ethical and quotation rules of SAUJS in all processes of the paper and that they do not make any falsification on the data collected. In addition, they declare that Sakarya University Journal of Science and its editorial board have no responsibility for any ethical violations that may be encountered, and that this study has not been evaluated in any academic publication environment other than Sakarya University Journal of Science.

REFERENCES

[1] E. N. Barron, Game Theory an Introduction, John Wiley & Sons Inc., New Jersey, 1-108, 2008.

[2] A. Cegielski, “Approximation of some zero-sum noncontinuous games by a matrix game”, Comment. Math., 2261-267, 1991.

[3] K.P. Chiao, “Fundamental Properties of Interval Vector Max-Norm”, Tamsui Oxf J Math Sci, 18(2):219-233, 2002.

[4] D.W. Collins and C. Hu, “Studying interval valued matrix games with fuzzy logic” Soft Comput, 12(2):147-155, 2008.

[5] H. Ishibuchi and H. Tanaka, “Multi-objective Programming in Optimization of the Interval Objective Function”, European Journal of Operational Research, 48: 219-225, 1990.

[6] D.F. Li, J.X. Nan and M.J. Zhang, “Interval programming models for matrix games with interval payoffs”, Optimization Methods and Software, 27(1), 1-16, 2012.

[7] E. Marchi, “On the minimax theorem of the theory of games”, Ann. Mat. Pura Appl. 77, 207-282, 1967.

[8] R.E. Moore, Method and Application of Interval Analysis, SIAM, Philadelphia, 1979.

[9] L.M. Naya, “Zero-sum continuous games with no compact support”, International J. Game Theory, 25(1), 93-111, 1996.

[10] L.M. Naya, “Weak topology and infinite matrix games”, Int J Game Theory, 27, pp:219-229, 1998.

[11] L.M. Naya, “On the Value of Some Infinite Matrix Games”, Mathematics of Operation Research, 26(1): 82-88, 2001.

[12] P.K. Nayak and T.K. Pal, “Linear Programming Technique To Solve Two-Person Matrix Games With Interval Payoffs”, Asia Pacific J of Operation Research, 26(2), 285-305, 2009.

[13] V.J Neuman and O. Morgenstern, “Theory of Games and Economic Behavior”, New York, Science Editions, John Wiley and Sons, Inc. third edition, 85-165, 1944.

[14] G., Owen, Game Theory, Third Edition Academic Press, 1995.

[15] A. Sengupta and T.K. Pal, “A-index for ordering interval numbers”, Presented in

Indian Science Congress. Delhi University, January 3-8, 1997.

[16] A. Sengupta and T.K. Pal, “On comparing interval numbers”, European Journal of Operational Research, 27: 28-43, 2000.

[17] A. Sengupta, T.K. Pal and D. Chakraborty, “Interpretation of Inequality Constraints Involving Interval Coefficients and a Solution to Interval Linear Programming”, Fuzzy Sets and Systems, 119: 129-138, 2001.

[18] A. Sengupta and T.K. Pal, “Fuzzy Preference Ordering of Interval Numbers in Decision Problems”, Studies in Fuzziness and Soft Computing 238, Springer, Berlin, 2009.

[19] S.H Tijs, “Semi Infinite and infinite matrix and bimatrix games”, Ph.D. thesis, University of Nijmegan, 1975.

SAKARYA ÜNİVERSİTESİ

FEN BİLİMLERİ ENSTİTÜSÜ
DERGİSİ

Sakarya University Journal of Science
SAUJS

e-ISSN 2147-835X Founded 1997 Period Bimonthly Publisher Sakarya University
http://www.saujs.sakarya.edu.tr/en/

Title: The Leaf and Stem Anatomy of Two Endemic Salvia (Section Salvia, Lamiaceae) from Turkey: S. aucheri subsp. canascens and S. Heldreichiana

Authors: Gülnur EKŞİ, Gülderen YILMAZ

Recieved: 2021-10-02 00:00:00

Accepted: 2021-10-27 00:00:00

Article Type: Research Article

Volume: 25
Issue: 6
Month: December
Year: 2021
Pages: 1352-1365

How to cite
Gülnur EKŞİ, Gülderen YILMAZ; (2021), The Leaf and Stem Anatomy of Two Endemic Salvia (Section Salvia, Lamiaceae) from Turkey: S. aucheri subsp. canascens and S. Heldreichiana. Sakarya University Journal of Science, 25(6), 1352-1365, DOI: https://doi.org/10.16984/saufenbilder.1003862
Access link
http://www.saujs.sakarya.edu.tr/tr/pub/issue/66341/1003862

Sakarya University Journal of Science 25(6), 1352-1365, 2021

The Leaf and Stem Anatomy of Two Endemic *Salvia* (Section *Salvia*, Lamiaceae) from Turkey: *S. aucheri* subsp. *canascens* and *S. heldreichiana*

Gülnur EKŞİ*[1], Gülderen YILMAZ[2]

Abstract

Salvia L. has a wide variety of traditional usages as digestive, appetizer, carminative, antiseptic, stimulant, pain reliever, antipyretic, diuretic, antitussive and for bronchitis, asthma and cold. Anatomical features are extremely important for the taxonomy of *Salvia* species, especially leaf and stem represent many specific characteristics. The aim of this study is to determine the distinctive anatomical structures of *S. aucheri* subsp. *canascens* (Boiss. & Heldr.) Celep, Kahraman & Doğan and *S. heldreichiana* Boiss. comparatively. The transverse-sections were taken from the leaf and stem to determine the anatomical features of two *Salvia* species. They differ in many anatomical characters like leaf type, which is bifacial and hypostomatic for *S. aucheri* subsp. *canascens* and monofacial and amphistomatic for *S. heldreichiana*. Besides, the leaf surfaces of both species are covered by different types of glandular trichomes. The midrib contains a big vascular bundle in *S. aucheri* subsp. *canascens* and has three big vascular bundles in *S. heldreichiana*. Additionally, the stem surface of *S. aucheri* subsp. *canascens* is glabrous while the stem is pilose in *S. heldreichiana*. In conclusion, our anatomical results were contributed to the taxonomy of *S. aucheri* subsp. *canascens* and *S. heldreichiana* and confirmed the importance of anatomy in the species level for the genus.

Keywords: anatomy, Lamiaceae, *Salvia aucheri* subsp. *canascens*, *S. heldreichiana*.

1. INTRODUCTION

Salvia L. is the largest genus of Lamiaceae consisting of ca. 1000 species worldwide. The genus is distributed mainly in Central and South America and Asia [1–3]. It has more than 100 species in Turkey, half of which are endemic demonstrating that Turkey is a possible diversity centre for *Salvia* in Asia [4, 5]. The members of the genus are herbaceous, suffruticose or shrubby, generally perennials and often strongly aromatic. Stems erect or procumbent and glandular to glabrous. Leaves undivided and lyrate or pinnatisect. Inflorescence verticillaster. Calyx and corolla are bilabiate [6]. *Salvia* species have many usages worldwide, not only for medicinal purposes but also for food, in cosmetics, perfumery and pharmaceutical industry [7–9]. The genus is one of the most well-known medicinal plant group in Turkey since ancient times with its various traditional use such as diuretic, stimulant, laxative and for abdominal

---

* Corresponding author: gulnur_eksi@yahoo.com

[1] Istanbul Medipol University, Department of Basic Pharmaceutical Sciences, Deparment of Pharmacognosy
ORCID: https://orcid.org/0000-0002-6869-8703

[2] Ankara University, Faculty of Pharmacy, Department of Pharmaceutical Botany
E-mail: gulderen_yilmaz@yahoo.com
ORCID: https://orcid.org/0000-0002-6569-4766

pain, cold, flatulence, rheumatism, stomach ache, wounds [1, 10–18]. Recent bioactivity studies proved that *Salvia* species contain bioactive secondary metabolites efficient as antioxidant, antimicrobial, antialzheimer, anticancer, antidiabetic, antitumor, antiplasmodial, antiinflammatory [19–25]. Besides, numerous anatomical studies have been conducted on *Salvia* species [2, 12, 26–29]. *Salvia aucheri* subsp. *canescens* (Boiss. & Heldr.) Celep, Kahraman & Doğan and *S. heldreichiana* Boiss. (Lamiaceae) are both belong to sect. *Salvia* (Figure 1).

In the present study, the anatomical characteristics of these two endemic species have been studied for the first time. The results are presented by photographs. The characteristic elements of anatomical structures have been determined and these results compared to other studies in the literature. This study aims to contribute to the taxonomy of examined *Salvia* species and the genus.

2. MATERIALS AND METHODS

Aerial parts of *S. aucheri* subsp. *canascens* and *S. heldreichiana* were collected from Karaman province at the flowering time on 27th of June 2019 from Yeşildere Village at an elevation of 1300 m by the second author and the specimens were stored in Ankara University, Pharmacy Faculty Herbarium with the numbers of AEF 28920 and AEF 28919, respectively. For anatomical studies, living materials were kept in 70% alcohol. Transverse-sections of leaf and stem were taken by hand and examined using Sartur and chloral hydrate reagents. The measurements (Table 1) and photos (Figures 2, 3, 4, 5) of characteristic elements were photographed by a binocular light microscope with a Leica DFC280 camera at 4x, 10x and 40x magnifications.

3. RESULTS

3.1. S. aucheri subsp. canescens

S. aucheri subsp. *canescens* (Boiss. & Heldr.) Celep, Kahraman & Doğan, Distribution: Southern Turkey. Habitat: Stony slopes, rocky areas. Flowering: July to October. Phytogeographical Region: East Mediterranean element.

3.1.1. Stem

The stem is quadrangular in transverse-section (Figure 2. A, C). The epidermis is covered by a cuticle layer and consists of a single layer of elliptical to rectangular cells (Figure 2. F, I). The collenchyma tissue is in one or two rows, thicker at the edges (Figure 2. A, C, F, I). Parenchyma is three to five layered in the cortex. Starches are visible in parenchymatic cells (Figure 2. G). Sclerenchyma cell groups in the cortex are above the phloem. The cambium is distinctive (Figure 2. A, C). The pith consists of lignified and unlignified parenchymatic cells which are large, polygonal or orbicular in shape (Figure 2.E, H).

3.1.2. Leaf

In the transverse-section of the leaf lamina including the midrib, the epidermis is covered by a cuticle layer on both sides of the leaf (Figure 3. B, C). The epidermis consists of a single layer of elliptical to rectangular cells which are larger at upper surface. The multicellular non-glandular and glandular trichomes are present on both sides of the leaves (Figure 3. B, C). The non-glandular multicellular trichome consists of two or three cells (Figure 3. F, G, I). Two types of glandular trichome are present. The first one is a larger glandular trichome that has two or three cells including a neck cell in the stalk with unicellular heads (Figure 3. G, H). The second one is a small glandular trichome containing one or two cells including a neck cell in the stalk with one or two celled heads (Figure 3. F, H, I). The midrib has a big vascular bundle covered with 5-6 layers of polygonal to circular collenchyma cells from the adaxial and 3-4 layers from the abaxial (Figure 3. D, E). The stomata type is diacytic and they present on the lower epidermis (Figure 3. K, L). The leaf is hypostomatic and bifacial (Figure 3. B, C). The palisade parenchyma cells are rectangular elongated, 4-6 layered and 1–3 layers of intercellular spaced spongy parenchyma cells (Figure 3. B, C). The vascular bundle is the collateral type (Figure 3. D, E).

3.2. *Salvia heldreichiana*

Salvia heldreichiana Boiss., Prodr. 17: 320, (1873). Distribution: Southern Turkey. Habitat: Stony slopes, rocky places. Flowering: July-October. Phytogeographical Region: East Mediterranean element.

3.2.1. Stem

The stem is quadrangular to circular in transverse-section (Figure 4. A, B). The epidermis is covered by a cuticle layer and non-glandular trichomes consisted of one to three cells (Figure 4. A, B, H, I). The epidermis is composed of uniseriate, thick walled, elliptical to rectangular cells (Figure 4. G, H, I). Cortex exhibits three different layers. The first layer has thick walled, flattened, collenchyma cells in two to six rows under the epidermis. The second layer is three to five rows of bigger and ovoid parenchyma cells. At the third layer, cells are smaller and without intercellular spaces cells (Figure 4. G, H, I). Sclerenchyma cells are in the third layer of the cortex above the phloem cells (Figure 4. E, G). The cambium is distinctive cells (Figure 4. A, B). The pith consists of lignified parenchyma cells, which are larger and polygonal or orbicular in shape (Figure 4. D).

3.2.2. Leaf

In the transverse-section of the leaf lamina, the upper and the lower epidermis are covered with a cuticle layer cells. The epidermis is composed of a single layer of elliptical to rectangular cells which are thick walled (Figure 5. E, F, G, H, I). The multicellular non-glandular and glandular trichome are on both sides of the leaves. The non-glandular multicellular trichome consist of two or three cells. Two types of glandular trichome are distinguished. One has a unicellular stipe with one or two celled heads, second has a unicellular stipe with multicellular heads (Figure 5. F, G, I). The midrib contains three big vascular bundles covered with four to six layers of collenchyma cells from the adaxial and six to nine layers of collenchyma cells from the abaxial (Figure 5. A, B, C, D, E). The collenchyma cells are polygonal to circular in shape. The vascular bundle is the collateral type (Figure 5. D). The leaf is monofacial (Figure 5. A, B, C, H). The palisade parenchyma cells are elongated rectangular as 6-8 layers in the mesophyll. The spongy parenchyma cells are one or two layers on both sides of the palisade parenchyma (Figure 5. H, I). On the surface, the stomata cells are located on both sides of the leaf The leaf is amphistomatic and the stomata type is diacytic (Figure 5. J, K, L).

4. DISCUSSION

Salvia species have non-glandular and glandular trichomes characteristic to Lamiaceae [2, 4, 12, 30–34] (Table 3). In the leaf transverse and the leaf superficial sections, upper and lower epidermis of *S. aucheri* subsp. *canascens* and *S. heldreichiana* were both covered by non-glandular and glandular trichomes. The trichome characteristics are very important for the classification of *Salvia* species [2, 4, 32, 33]. The non-glandular trichome in Lamiaceae could be erect, triangular, unicellular to multicellular and variable in shape and length [30, 35]. *S. heldreichiana* has long and non-glandular multicellular trichome on the stem surface in contrast to *S. aucheri* subsp. *canascens* (Figure 2. A, C, G, I; Figure 4. A, B, H, I; Table 3). Glandular trichome in *Salvia* displays variability among species [32, 33]. Capitate and peltate are the two main types of glandular trichome based on the shape of secretory heads [2, 4, 35]. The capitate trichome contains short or long stalks with unicellular heads. The peltate trichome is formed of short stalks with a broad multicellular secretory head. *S. heldreichiana* has both. The peltate trichome in *S. heldreichiana* comprises of a glandular head with eight cells in a row (Figure 5. L). The capitate trichome in *S. heldreichiana* has one to two celled stalks with spherical secretory heads (Figure 5. F, G, I,). *S. aucheri* subsp. *canascens* has two main types of capitate trichome, one is short capitate (the short stalk consists of one or two cells-if two cells, one of them is neck cell-) and the other is long capitate (the long stalk contains two or more cells including neck cell). *S. aucheri* subsp. *canascens* has the long capitate trichome with two to three cells in stalk and the short capitate trichome with a round unicellular secretory head and a stalk with two cells including a neck cell. The leaf epidermis of both *S. aucheri* subsp. *canascens* and *S. heldreichiana* consist of a single layer of the oval to rectangular thick-walled epidermis cells covered with a cuticle. The leaf of *S. aucheri* subsp. *canascens* is bifacial like *S. potentillifolia* Boiss. & Heldr. ex Benth., *S. nydeggeri* Hub.-Mor. [12], *S. quezelii* Hedge & Afzal-Rafii[2] and *S. divaricata* Montbret & Aucher ex Benth. [28] (Table 2). The leaf of *S. heldreichiana* is monofacial like *S. macrochlamys* Boiss. & Kotschy [36], *S. ballsiana* (Rech.f.) Hedge [37] (Table 2). In both *S. aucheri* subsp. *canascens* and *S. heldreichiana*, mesophyll consists of elongated rectangular palisade parenchyma and nearly isodiametric spongy parenchyma cells. In *S. aucheri* subsp. *canascens*, the midrib has a single large vascular bundle in the middle (Figure 3. A, D) like in *S. macrochlamys* [36], *S. ballsiana* [37], *S. potentillifolia*, *S. nydeggeri* [12] and *S. divaricata* [28]. In *S. heldreichiana* three large vascular bundles were in the midrib (Figure 5. D, E) like in *S. indica* L. [38] and *S. vermifolia* Hedge & Hub.-Mor. [39]. The midrib comprises multilayers of collenchyma cells around vascular bundles in both species. *S. aucheri* subsp. *canascens* and *S. heldreichiana* are both have diacytic stoma type like the many others members of *Salvia* [27, 38, 39]. *S. heldreichiana* has amphistomatic leaves (number of stomata on the lower surface is equal to stomata number on the upper surface) (Figure 5. J, K, L) and *S. aucheri* subsp. *canascens* has hypostomatic leaves (stomata are just located on the lower surface) (Figure 3. J, K, L). The stems of both *S. aucheri* subsp. *canascens* and *S. heldreichiana* were quadrangular and cortex was composed of one to two layers of collenchyma, which is multilayer at the corners making them quadrangular and several layers of parenchymatic cells. In both species, sclerenchyma cells were visible above the phloem (Figure 2. B, C, D, E, F, I; Figure 4. A, B, E, G) similar to other *Salvia* species [30, 40]. In both examined species, large trachea and smaller tracheid were observed in the xylem (Figure 2. A, C, D, F, I; Figure 4. A, B, C, E, F). Medullary rays in stems of *S. aucheri* subsp. *canascens* and *S. heldreichiana* were visible and the cambium was well distinguished (Figure 2. A, C, D; Figure 4. A, B, C, F) The stem anatomies of both species were more or less similar in previously examined *Salvia* species [1, 2, 12, 26, 27, 37, 40].

5. CONCLUSION

In this study, the stem and leaf anatomy of *Salvia aucheri* subsp. *canascens* and *S. heldreichiana* were studied for the first time. These two endemic species were found to be closely related to each other but *S. aucheri* subsp. *canascens* and *S. heldreichiana* has exhibited many different anatomical characters such as indumentum of stem, glandular trichome, vascular bundle numbers and orientations. Our results provide significant data to the taxonomy of two examined endemic species and the genus *Salvia* and confirm the importance of anatomical structures in the species level.

Funding

The authors have not received any financial support for the research, authorship or publication of this study.

The Declaration of Conflict of Interest/ Common Interest

No conflict of interest or common interest has been declared by the authors.

Authors' Contribution

The first author contributed 60%, the second author 40%.

The Declaration of Ethics Committee Approval

This study does not require ethics committee permission or any special permission

The Declaration of Research and Publication Ethics

The authors of the paper declare that they comply with the scientific, ethical and quotation rules of SAUJS in all processes of the paper and that they do not make any falsification on the data collected. In addition, they declare that Sakarya University Journal of Science and its editorial board have no responsibility for any ethical violations that may be encountered, and that this study has not been evaluated in any academic publication environment other than Sakarya University Journal of Science.

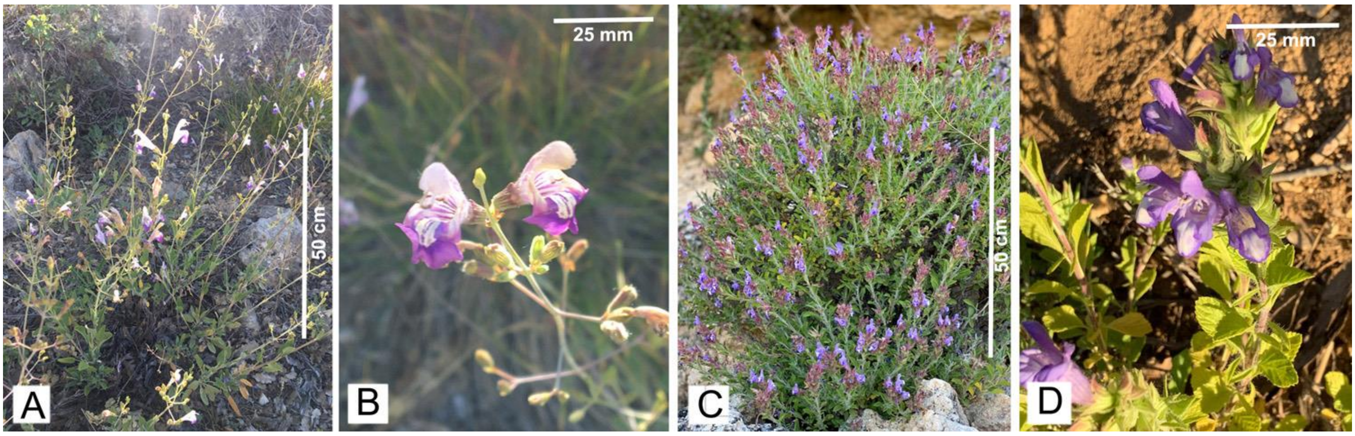

Figure 1 A-B *Salvia aucheri* subsp. *canascens*, C-D *Salvia heldreichiana*.

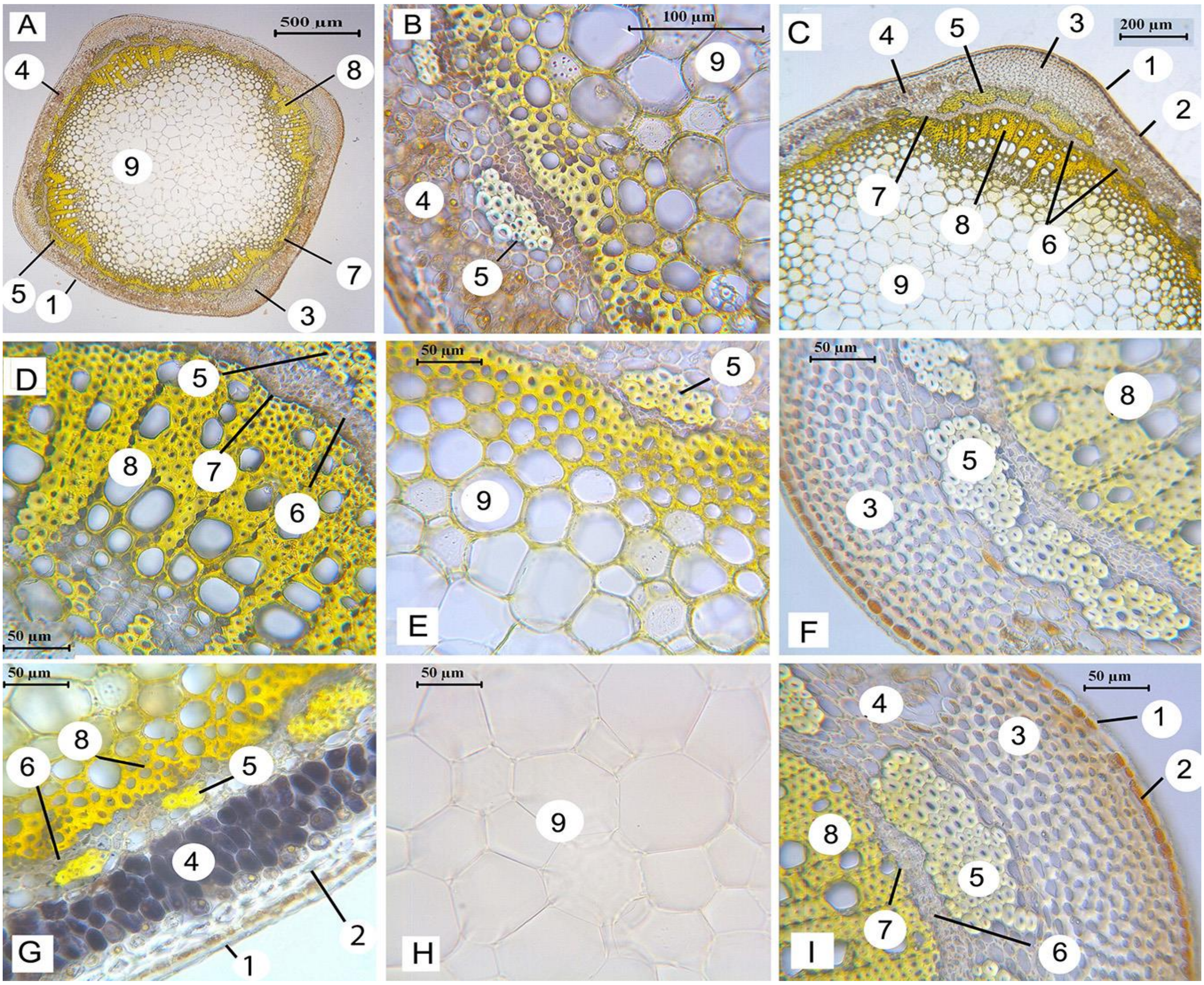

Figure 2 *Salvia aucheri* subsp. *canascens*. (A-I) Stem transverse-section, (1) cuticle, (2) epidermis, (3) collenchyma, (4) parenchyma, (5) sclerenchyma, (6) phloem, (7) cambium, (8) xylem, (9) pith.

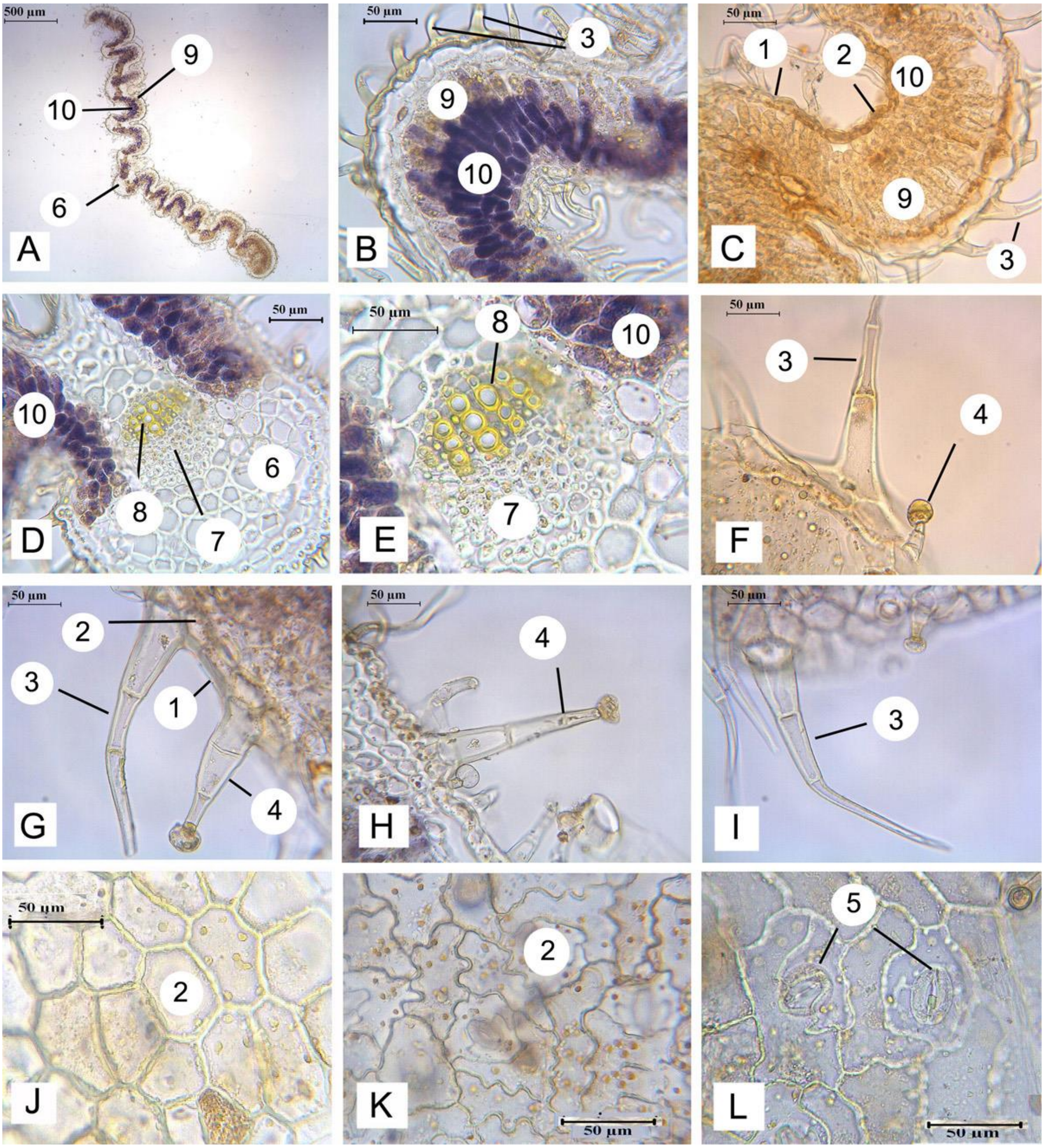

Figure 3 *Salvia aucheri* subsp. *canascens*. (A-I) Leaf transverse-section, (J-L) leaf surface, (1) cuticle, (2) epidermis, (3) non-glandular trichome, (4) glandular trichome, (5) stomata, (6) collenchyma, (7), phloem, (8) xylem, (9) palisade parenchyma, (10) spongy parenchyma.

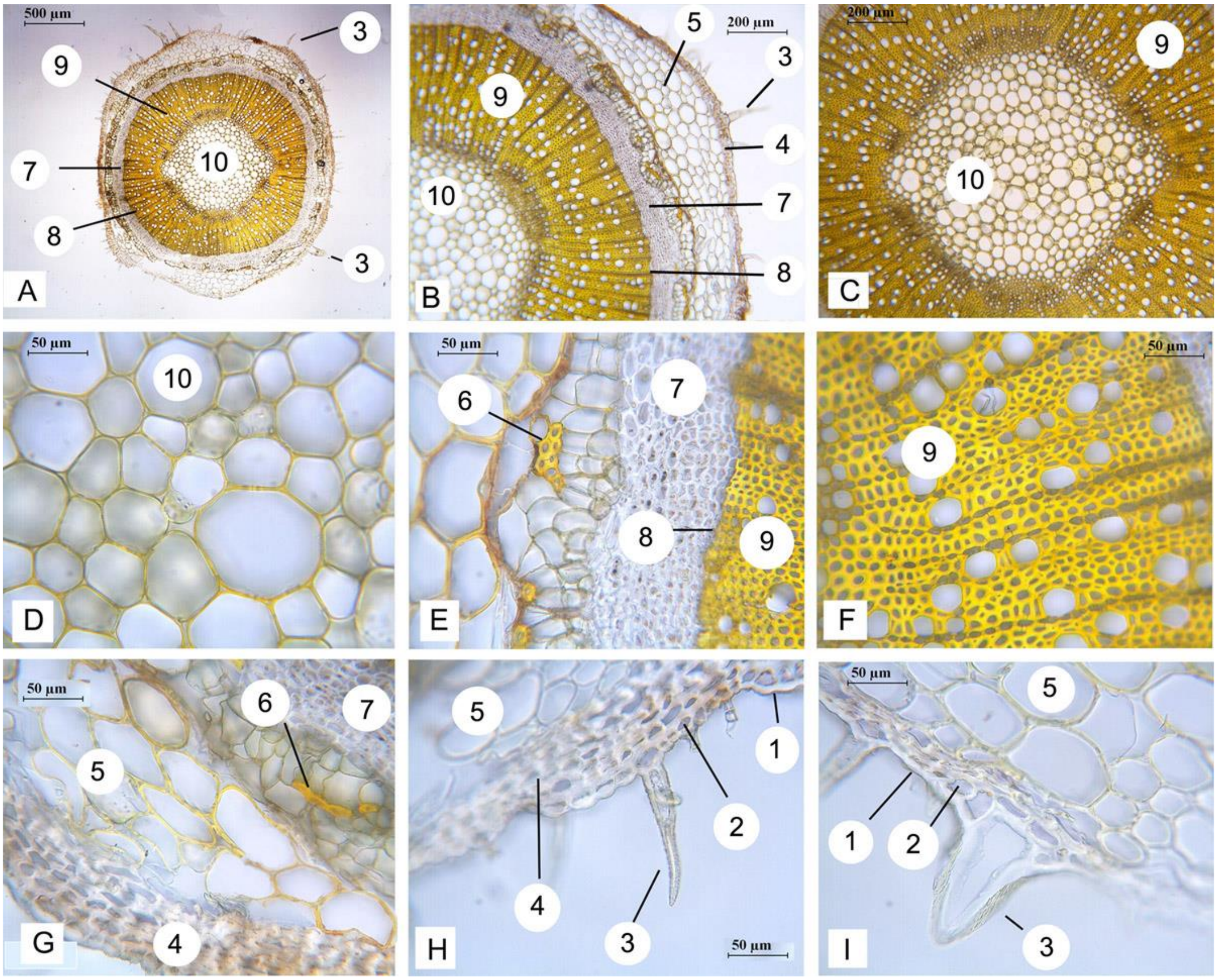

Figure 4 *Salvia heldreichiana*. **(**A-I) Stem transverse-section, (1) cuticle, (2) epidermis, (3) non-glandular trichome, (4) collenchyma, (5) parenchyma, (6) sclerenchyma, (7) phloem, (8) cambium, (9) xylem, (10) pith.

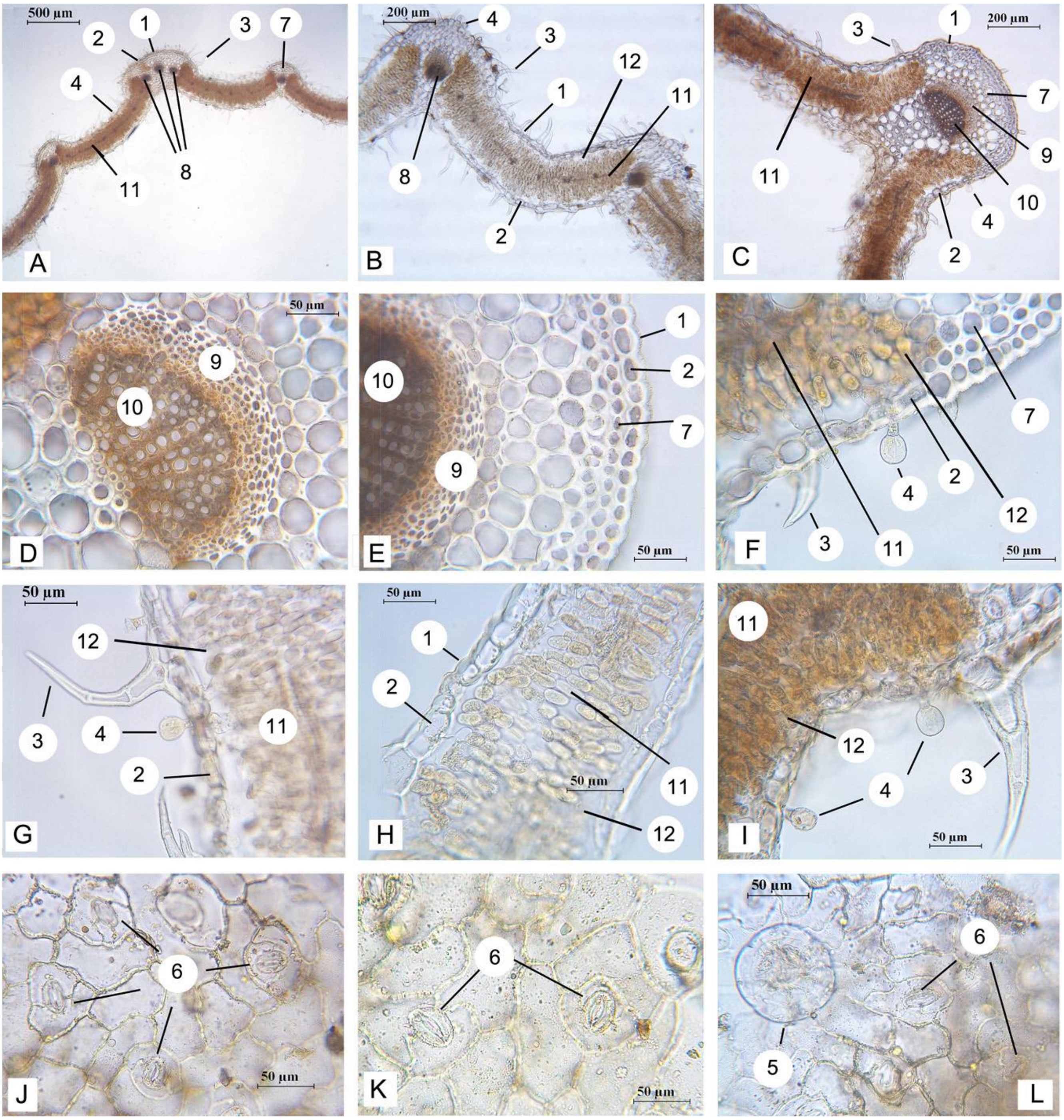

Figure 5 *Salvia heldreichiana*. (A-I) Leaf transverse-section, (J-L) leaf surface, (1) cuticle, (2) epidermis, (3) non-glandular trichome, (4) glandular trichome, (5) Lamiaceae type glandular trichome, (6) stomata, (7) collenchyma, (8) vascular bundle, (9) phloem, (10) xylem, (11) palisade parenchyma, (12) spongy parenchyma.

Table 1 Anatomical measurement of the stem and the leaf characteristic elements of *S. aucheri* subsp. *canascensa* and *S. heldreichiana.*

			Width (µm)		**Length (µm)**	
			Min.–Max.	**Mean ± S.D.**	**Min.–Max.**	**Mean ± S.D.**
S. *aucheri subsp. canascens*	Stem	Cuticle	1.33-7.00	3.83 ± 2.53	2.67-5.00	3.92 ± 0.10
		Epidermis Cell	14.67-23.33	19.00 ± 3.78	18.33-30.00	26.30 ± 5.10
		Trachea Cell	5.35-40.33	17.99 ± 9.48	6.67-33.00	18.12 ± 8.55
		Pith Cell	38.00-86.00	55.524 ± 16.71	30.00-78.67	55.90 ± 18.25
	Leaf	Cuticle	3.75-12.19	8.19 ± 3.20	2.81-9.06	5.88 ± 2.77
		Upper Epidermis Cell	10.94-27.81	18.39 ± 6.84	13.44-20.63	16.88 ± 2.60
		Lower Epidermis Cell	5.63-18.12	12.37 ± 4.87	4.38-10.00	7.99 ± 2.10
		Collenchyma Cell	16.00-36.4	23.54 ± 7.39	12.80-33.20	22.53 ± 7.08
		Mesophyll Region	55.94-110	78.94 ± 20.23	42.81-85	64.56 ± 17.05
		Palisade Parenchyma Cell	3.13-11.56	8.29 ± 2.51	7.50-25.94	16.36 ± 6.10
		Non-glandular Trichome	22.00-29.33	26.67 ± 4.05	127.33-227.63	193.21 ± 57.07
		Glandular Trichome	15.33-27.33	20.666 ± 4.83	19.33-147.33	74.532 ± 55.95
S. heldreichiana	Stem	Cuticle	3.67-1.67	2.75 ± 0.92	1.33-2.67	2.08 ± 0.57
		Epidermis Cell	5.67-17.00	11.22 ± 4.97	6.67-15.33	11.56 ± 3.79
		Trachea Cell	2.67-10.33	5.33 ± 2.43	2.67-9.33	5. 00 ± 2.12
		Pith Cell	20.00-80.00	42.23 ± 19.69	20.67-73.67	41.33 ± 17.99
		Non-glandular Trichome	7.33-74.13	25.18 ± 24.93	23.8-185.71	84.435 ± 61.10
	Leaf	Cuticle	2.14-3.43	2.71 ± 0.66	1.43-2.14	1.81 ± 0.36
		Upper Epidermis Cell	15.00-25.00	20.30 ± 4.05	10.71-26.43	18.88 ± 6.06
		Lower Epidermis Cell	13.57-42.14	26.78 ± 12.04	12.86-19.64	16.29 ± 2.85
		Collenchyma Cell	7.86-39.29	23.04 ± 14.33	11.07-40.71	24. 42 ± 13. 54
		Mesophyll Region	140.71-246.43	191.19 ± 53.02	124.29-216.43	155.80 ± 52.52
		Palisade Parenchyma Cell	5.71-11.79	8.97 ± 2.39	17.5-25.71	22.68 ± 2.79
		Spongy Parenchyma Cell	11.43-14.29	12.45 ± 1.11	12.14-18.57	15.86 ± 2.86
		Non-glandular Trichome	17.5-35.36	24.88 ± 9.32	72.5-128.57	100.54 ± 39.65
		Glandular Trichome	18.57-25	21.70 ± 2.66	31.07-42.5	36.695 ± 5.75
		Lamiaceae Type Glandular Trichome	57.86-98.21	80.89 ± 17.48	64.64-96.07	82.14 ± 13.08

S.D.: Standard Deviation.

Table 2 The leaf anatomical features of *S. aucheri* subsp. *canascens*, *S. heldreichiana* and related taxa.

	Leaf type	Stoma type	Large vascular bundle numbers in the midrib	References
Sect. *Salvia*				
S. aucheri subsp. *canascens* (Boiss. & Heldr.) Celep, Kahraman & Doğan	bifacial	hypostomatic	3	
S. heldreichiana Boiss.	monofacial	amphistomatic	1	
S. macrochlamys Boiss. & Kotschy	monofacial	amphistomatic	1	36
S. ballsiana (Rech.f.) Hedge	monofacial	amphistomatic	1	37
S. potentillifolia Boiss. & Heldr. ex Benth.	bifacial	amphistomatic	1	12
S. nydeggeri Hub.-Mor.	bifacial	amphistomatic	1	12
S. divaricata	bifacial	amphistomatic	1	27
Sect. *Hymenosphace*				
S. euphratica Montbret & Aucher ex Benth.	bifacial	amphistomatic	4	27
Sect. *Aethiopis*				
S. hypargeia Fisch. & C.A.Mey.	bifacial	amphistomatic	4-5	27
S. indica L.	bifacial	amphistomatic	3	38
S. vermifolia Hedge & Hub.-Mor.	bifacial	amphistomatic	3	39
S. argentea L.	bifacial	amphistomatic	1	30
Sect. *Horminum*				
S. viridis L.	bifacial	amphistomatic	1	28
Sect. *Drymosphace*				
S. glutinosa L.	bifacial	hypostomatic	1	26

Tablo 3 The trichome features of *S. aucheri* subsp. *canascens*, *S. heldreichiana* and related taxa.

	Stem Indumentum	**Leaf Indumentum**	**References**
Sect. ***Salvia***			
S. aucheri subsp. *canascens* (Boiss. & Heldr.) Celep, Kahraman & Doğan	glabrous	glandular and non-glandular trichomes	
S. heldreichiana Boiss.	non-glandular trichomes	glandular and non-glandular trichomes	
S. macrochlamys Boiss. & Kotschy	glandular and non-glandular trichomes	glandular and non-glandular trichomes	36
S. ballsiana (Rech.f.) Hedge	glabrous	glandular and non-glandular trichomes	37
S. potentillifolia Boiss. & Heldr. ex Benth.	glandular and non-glandular trichomes	glandular and non-glandular trichomes	12
S. nydeggeri Hub.-Mor.	glandular and non-glandular trichomes	glandular and non-glandular trichomes	12
S. divaricata	glandular and non-glandular trichomes	glandular and non-glandular trichomes	27
Sect. ***Hymenosphace***			
S. euphratica Montbret & Aucher ex Benth.	glabrous	glandular trichomes	27
Sect. ***Aethiopis***			
S. hypargeia Fisch. & C.A.Mey.	glandular and non-glandular trichomes	glandular and non-glandular trichomes	27
S. indica L.	glandular and non-glandular trichomes	non-glandular trichomes	38
S. vermifolia Hedge & Hub.-Mor.	glandular and non-glandular trichomes	non-glandular trichomes	39
S. argentea L.	glandular trichomes	glandular trichomes	30
Sect. ***Horminum***			
S. viridis L.	non-glandular trichomes	glandular trichomes	28
Sect. ***Drymosphace***			
S. glutinosa L.	glandular and non-glandular trichomes	glandular and non-glandular trichomes	26

REFERENCES

[1] K. Aktaş, C. Özdemir, M. Özkan, Y. Akyol, and P. Baran, “Morphological and anatomical characteristics of *Salvia tchihatcheffii* endemic to Turkey,” African Journal of Biotechnology, vol. 8, no. 18, pp. 4519–4528, 2009.

[2] F. Celep, A. Kahraman, Z. Atalay, and M. Doğan, “Morphology, anatomy, palynology, mericarp and trichome micromorphology of the rediscovered Turkish endemic *Salvia quezelii* (Lamiaceae) and their taxonomic implications,” Plant Systematics and Evolution, vol. 300, no. 9, pp. 1945–1958, 2014.

[3] J.B. Walker and K.J. Sytsma, “Staminal evolution in the genus *Salvia* (Lamiaceae): Molecular phylogenetic evidence for multiple origins of the staminal lever,” Ann Bot, vol. 100, pp. 375–391, 2007.

[4] Z. Atalay, F. Celep, F. Bara, and M. Doğan, “Systematic significance of anatomy and trichome morphology in *Lamium* (Lamioideae; Lamiaceae),” Flora: Morphology, Distribution, Functional Ecology of Plants, vol. 225, pp. 60–75, 2016.

[5] M. Vural and N. Adigüzel, “A new species from Central Anatolia: *Salvia aytachii* M. Vural et N. Adigüzel (Labiatae),” Turkish Journal of Botany, vol. 20, no. 6, pp. 531–534, 1996.

[6] I.C. Hedge, “*Salvia* L.,” In: P.H. Davis, Ed. *Flora of Turkey and the East Aegean Islands, Vol. 7*. pp. 400–461. *Edinburgh University Press,* Edinburgh (1982).

[7] S. Baylac and P. Racine, “Inhibition of 5-lipoxygenase by essential oils and other natural fragment extracts,” International Journal of Aromatherapy, vol. 13, no. 2–3, pp. 138–142, 2003.

[8] A.C. Dweck, “The folklore and cosmetic use of various *Salvia* species.,” In: K. SE, Ed. *Sage – the genus Salvia*. pp. 1–25. *Harwood Academic Publishers*, Amsterdam (2000).

[9] J.B. Walker, K.J. Sytsma, J. Treutlein, and M. Wink, “*Salvia* (Lamiaceae) is not monophyletic: Implications for the systematics, radiation, and ecological specializations of *Salvia* and tribe Mentheae,” American Journal of Botany, vol. 91, no. 7, pp. 1115–1125, 2004.

[10] Baytop, *Türkiye’de Bitkiler ile Tedavi, Geçmişte ve Bugün*. *Nobel Tıp Kitapevi*, Istanbul, 1999.

[11] T. Fujita, E. Sezik, M. Tabata, et al., “Traditional medicine in Turkey VII. Folk medicine in middle and west Black Sea regions,” Economic Botany, vol. 49, no. 4, pp. 406–422, 1995.

[12] B. Gürdal, Y. Yeşil, E. Akalın, and N. Tan, “Anatomical features of *Salvia potentillifolia* Boiss. & Heldr. ex Benth. and *Salvia nydeggeri* Hub.-Mor. (Lamiaceae),” İstanbul Journal of Pharmacy, vol. 49, no. 3, pp. 186–190, 2019.

[13] B. Gürdal and Ş. Kültür, “An ethnobotanical study of medicinal plants in Marmaris (Muğla, Turkey),” Journal of Ethnopharmacology, vol. 146, no. 1, pp. 113–126, 2013.

[14] E. Sezik, E. Yeşilada, G. Honda, Y. Takaishi, Y. Takeda, and T. Tanaka, “Traditional medicine in Turkey X. Folk medicine in Central Anatolia,” Journal of Ethnopharmacology, vol. 75, no. 2–3, pp. 95–115, 2001.

[15] E. Sezik, E. Yeşilada, M. Tabata, et al., “Traditional medicine in Turkey VIII. Folk medicine in east anatolia; Erzurum, Erzíncan, Ağri, Kars, Iğdir provinces,” Economic Botany, vol. 51, no. 3, pp. 195–211, 1997.

[16] G. Topçu and A.C. Gören, "Biological Activity of Diterpenoids Isolated from Anatolian Lamiaceae Plants," Records of Natural Products, vol. 1, no. 1, pp. 1–16, 2007.

[17] Y. Yesil and I. Inal, "Traditional knowledge of wild edible plants in Hasankeyf (Batman Province, Turkey)," Acta Societatis Botanicorum Poloniae, vol. 88, no. 3, p. 3633, 2019.

[18] E. Yeşilada, G. Honda, E. Sezik, M. Tabata, K. Goto, and Y. Ikeshiro, "Traditional medicine in Turkey IV. Folk medicine in the Mediterranean subdivision," Journal of Ethnopharmacology, vol. 39, no. 1, pp. 31–38, 1993.

[19] N.P. Bahadirli and F. Ayanoglu, "Genetic diversity of *Salvia* species from Turkey assessed by microsatellite markers," Journal of Applied Research on Medicinal and Aromatic Plants, vol. 20, p. 100281, 2021.

[20] V. Exarchou, L. Kanetis, Z. Charalambous, et al., "HPLC-SPE-NMR characterization of major metabolites in *Salvia fruticosa* Mill. extract with antifungal potential: relevance of carnosic acid, carnosol, and hispidulin," Journal of Agricultural and Food Chemistry, vol. 63, no. 2, pp. 457–463, 2015.

[21] G.P.P. Kamatou, A.M. Viljoen, A.C. Figueiredo, et al., "Trichomes, essential oil composition and biological activities of *Salvia albicaulis* Benth. and *S. dolomitica* Codd, two species from the Cape region of South Africa," South African Journal of Botany, vol. 73, no. 1, pp. 102–108, 2007.

[22] V. Pavlidou, I. Karpouhtsis, G. Franzios, A. Zambetaki, Z. Scouras, and P.M. Tsipidou, "Insecticidal and genotoxic effects of essential oils of Greek sage, *Salvia fruticosa*, and Mint, Mentha pulegium, on *Drosophila melanogaster* and *Bactrocera oleae* (Diptera: Tephritidae)," Journal of Agricultural and Urban Entomology, vol. 21, no. 1, pp. 39–49, 2004.

[23] E. Sarrou, I. Ganopoulos, A. Xanthopoulou, et al., "Genetic diversity and metabolic profile of *Salvia officinalis* populations: implications for advanced breeding strategies," Planta, vol. 246, no. 2, pp. 201–215, 2017.

[24] F.S. Senel, I. Orhan, F. Celep, et al., "Survey of 55 Turkish *Salvia* taxa for their acetylcholinesterase inhibitory and antioxidant activities," Food Chemistry, vol. 12, pp. 34–43, 2010.

[25] S. Karakaya, S.V. Yilmaz, Ö. Özdemir, et al., "A caryophyllene oxide and other potential anticholinesterase and anticancer agent in *Salvia verticillata* subsp. *amasiaca* (Freyn & Bornm.) Bornm. (Lamiaceae)," Journal of Essential Oil Research, vol. 32, no. 6, pp. 512–525, 2020.

[26] A. Kahraman, F. Celep, and M. Dogan, "Morphology, Anatomy and Palynology of *Salvia indica* L. (Labiatae)," World Applied Sciences Journal, vol. 6, no. 2, pp. 289–296, 2009.

[27] A. Kahraman, F. Celep, and M. Dogan, "Comparative morphology, anatomy and palynology of two *Salvia* L. species (Lamiaceae) and their taxonomic implications," Bangladesh Journal of Plant Taxonomy, vol. 16, no. 1, pp. 73–82, 2009.

[28] R. Polat, U. Cakilcioglu, S. Selvi, Z. Türkmen, and A. Kandemir, "The anatomical and micromorphological properties of three endemic and medicinal *Salvia* species (lamiaceae) in Erzincan (Turkey)," Plant Biosystems, vol. 151, no. 1, pp. 63–73, 2017.

[29] R. Polat, F. Satil, and S. Selvi, "Anatomical and ecological Investigations on Some *Salvia* L. (Lamiaceae) species growing Naturally in the vicinity of Balikesir,"

Journal of Applied Biological Sciences, vol. 4, no. 2, pp. 29–33, 2010.

[30] A. Alimpić Aradski, D. Janošević, I. Pećinar, et al., “Micromorphological and anatomical characteristics of *Salvia amplexicaulis* Lam., *S. jurisicii* Košanin and *S. ringens* Sibth. & Sm. (Lamiaceae),” Plant Biosystems, vol. 155, no. 1, pp. 92–108, 2021.

[31] P. Baran, C. Özdemir, and K. Aktaş, “Structural investigation of the glandular trichomes of *Salvia argentea*,” Biologia, vol. 65, no. 1, pp. 33–38, 2010.

[32] S. Gul, M. Ahmad, M. Zafar, et al., “Taxonomic significance of foliar epidermal morphology in Lamiaceae from Pakistan,” Microscopy Research and Technique, vol. 82, no. 9, pp. 1507–1528, 2019.

[33] S. Gul, M. Ahmad, M. Zafar, et al., “Foliar epidermal anatomy of Lamiaceae with special emphasis on their trichomes diversity using scanning electron microscopy,” Microscopy Research and Technique, vol. 82, no. 3, pp. 206–223, 2019.

[34] E. Werker, U. Ravid, and E. Putievsky, “Structure of glandular hairs and identification of the main components of their secreted material in some species of the Labiatae,” Israel Journal of Botany, vol. 34, no. 1, pp. 31–45, 1985.

[35] E. Werker, “Trichome diversity and development,” Advances in Botanical Research, vol. 31, pp. 1–35, 2000.

[36] A. Kahraman, F. Celep, and M. Doğan, “Morphology, anatomy, palynology and nutlet micromorphology of *Salvia macrochlamys* (Labiatae) in Turkey,” Biologia, vol. 65, no. 2, pp. 219–227, 2010.

[37] A. Kahraman, M. Dogan, F. Celep, G. Akaydin, and M. Koyuncu, “Morphology, anatomy, palynology and nutlet micromorphology of the rediscovered Turkish endemic *Salvia ballsiana* (Lamiaceae) and their taxonomic implications,” Nordic Journal of Botany, vol. 28, no. 1, pp. 91–99, 2010.

[38] A. Kahraman, F. Celep, and M. Doğan, “Morphology, Anatomy and Palynology of *Salvia indica* L. (Labiatae),” World Applied Sciences Journal, vol. 6, no. 2, pp. 289–296, 2009.

[39] S. Bagherpour, A. Kahraman, M. Doğan, F. Celep, B. Başer, and S. Pehlivan, “The anatomical and micromorphological characteristics of *Salvia vermifolia* (Section *Aethiopis* Bentham, Lamiaceae) from Central Anatolia, Turkey,” Central European Journal of Biology, vol. 5, no. 6, pp. 872–879, 2010.

[40] A. Kahraman and M. Doğan, “Comparative study of *Salvia limbata* C.A. and *S. palaestina* Bentham (sect. *Aethiopis* Bentham, Labiatae) from East Anatolia, Turkey,” Acta Botanica Croatica, vol. 69, no. 1, pp. 47–64, 2010.

SAKARYA ÜNİVERSİTESİ
FEN BİLİMLERİ ENSTİTÜSÜ
DERGİSİ

Sakarya University Journal of Science
SAUJS

e-ISSN 2147-835X Founded 1997 Period Bimonthly Publisher Sakarya University
http://www.saujs.sakarya.edu.tr/en/

Title: Enhancing The Out-Of-Plane Compressive Performance of Lightweight Polymer Foam Core Sandwiches

Authors: Çağrı UZAY

Recieved: 2021-06-23 00:00:00

Accepted: 2021-10-27 00:00:00

Article Type: Research Article

Volume: 25
Issue: 6
Month: December
Year: 2021
Pages: 1366-1375

How to cite
Çağrı UZAY; (2021), Enhancing The Out-Of-Plane Compressive Performance of Lightweight Polymer Foam Core Sandwiches. Sakarya University Journal of Science, 25(6), 1366-1375, DOI: https://doi.org/10.16984/saufenbilder.956676

Sakarya University Journal of Science 25(6), 1366-1375, 2021

Enhancing The Out-Of-Plane Compressive Performance of Lightweight Polymer Foam Core Sandwiches

Çağrı UZAY*[1]

Abstract

This study investigates the flatwise compressive performance of the developed sandwiches with core stitching modification. Polyvinyl chloride (PVC) foam cores with a density of 0.048 g/cm^3 were stitched with 600-tex glass fiber yarns. Then the core materials were sandwiched with carbon/epoxy and glass/epoxy face sheets, respectively. The composite sandwich structures were produced by applying the vacuum bag method, and the composite layers were co-cured. The non-stitched foam core sandwiches were also manufactured as the benchmark. The developed sandwich panels were subjected to flatwise compression tests per the ASTM C365 Standard to obtain compressive properties. The mechanical testing showed that the stitched foam core sandwiches carried dramatically higher compressive loads and presented additional load peaks. Almost 80% and 90% enhancement were achieved in resistance to compressive forces for the sandwiches made of carbon/epoxy and glass/epoxy face sheets, respectively. Also, the increments in the compressive strength of the developed sandwich panels were found above 80% with a minimum weight penalty. Core stitching, providing the sandwich panels to have better out-of-plane strength, is a simple and less time-consuming through-thickness reinforcement process among the other core modification methods.

Keywords: core stitching, flatwise compression, sandwich composite, strength, modulus

1. INTRODUCTION

Sandwich structures, a kind of hybrid laminated composites, are constructed with two thin and stiff face sheets, which are bonded to relatively thicker and low-density core material by a polymer matrix. While the core materials can be made of honeycomb, corrugated plates, balsa wood, polymer, and aluminum foams, the face sheets are commonly made of very thin metal alloy sheets or fiber-reinforced polymer composites. The core material mainly resists shearing, provides stability of two separated face sheets and load transfer between the face sheets, whereas the face sheets carry the compressive and tensile loads. The sandwich composites have emerged with superior specific strength and the stiffness-to-weight ratio [1-4]. Depending upon the sandwich constituents, they can also resist higher impact loads [5, 6], provide acoustic and vibration damping [7], and have better out-of-plane strength [8]. Therefore, the sandwiches have found widespread application areas in such industries as aerospace, automotive, marine, and

---

* Corresponding author: cagriuzay@ksu.edu.tr

[1] Kahramanmaraş Sütçü İmam University, Faculty of Engineering and Architecture, Department of Mechanical Engineering

ORCID: https://orcid.org/0000-0002-7713-8951

civil infrastructures where lightweight and higher stiffness are the primary design considerations [9-12]. To characterize the mechanical behaviors of the sandwich composites, they are subjected to several testing methods under various loadings, e.g., low-velocity impact [13], flexural [14, 15], edgewise and flatwise compression [9], and tensile [16] loads. The extensively obtained knowledge about the failure modes helps the designers and researchers to reveal optimal sandwich systems satisfying the desired requirements.

The typical failure modes encountered for sandwich structures are core shear, face sheet yielding, indentation, delamination, debonding, and face sheet wrinkling. The initiation and propagation of the failures depend upon the sandwich materials, type of loading, and design geometry [17, 18]. For instance, assuming the sandwiches are irrespective of the manufacturing defects, the core shear and indentation failure modes are commonly encountered under bending loadings, whereas delamination and debonding can be seen under impact loads [19] or flatwise compression [8]. One of the most common failure modes encountered in practice is the debonding or delamination of the core and the face sheets materials [9]. The compressive behavior of the sandwiches has been investigated to analyze these failure modes. Many researchers used high-density core materials to increase shear load carrying capacity, preventing the debonding of the laminates [1, 2, 8, 12, 20]. Some practical approaches for the developments of compressive performance of the sandwich composites are the insertion of shear key elements into the structure [20], z-pinning [16], tufting [21], and through-thickness stitching [16] of the core materials together with or without the face sheets [1]. Abdi et al. [1] obtained a dramatic increase in flatwise compression performance of the sandwiches by inserting polymer pins into the foam core.

Stitching, providing through-thickness reinforcement, can be applied to whole sandwiches, including face sheets and core [22], or applied only to the core material [23]. However, it was stated in the literature that only the core stitching rather than stitching the core with face sheets provided a sandwich panel to had better flatwise compression properties [16]. This might be due to the fiber damages during the stitching process [7]. The stitched core sandwich contributes to the interfacial strength of face sheets to the core leading to obtaining higher out-of-plane properties. The stitching with fiber bundles increases the energy requirement for delamination of the sandwich laminates and prevents face sheet-core debonding. Yalkin et al. [16] reported that core stitching is a simple and less time-consuming process than other through-thickness reinforcement methods such as inserting shear key elements, composite rods, and polymer pins. Malcom et al. [22] stitched the glass/epoxy face sheets and PVC foam core with aramid fiber to increase the shear and compressive properties. Han et al. [4] used 167-tex glass fiber yarns and stitched carbon/epoxy face sheets and polyurethane (PU) foam core with different stitching densities. Drop weight impact test results showed that stitching increased the energy absorption capacity, and also, the delamination area was smaller as the stitched density was increased. Yalkin et al. [23] the PVC foam core glass/epoxy face sheets sandwiches at various tex numbers of glass fiber yarns from 600-tex to 2400-tex. The researchers obtained enhanced compressive, shear, bending, and impact properties. However, they indicated that increasing tex number caused individual fiber damages during the stitching, which made the process more difficult.

In this study, the effects of stitched core on the flatwise compression properties of the low-density polymer foam core sandwich panels were investigated. 15 mm thick, closed-cell, and rigid polyvinyl chloride (PVC) foam cores with a density of 0.048 g/cm^3 were sandwiched with carbon/epoxy and glass/epoxy face sheets. The stitching was applied to the pre-drilled foam core and carried out with glass fiber yarns (600-tex). The vacuum bagging method was applied to manufacture the sandwich panels, in which the laminates were co-cured under a vacuum atmosphere at room temperature. According to ASTM C 365 Standard [24], the flatwise compression tests were performed to discover the developed sandwiches’ compressive properties.

2. MATERIALS AND METHOD

2.1. Materials

Low-density foam core fiber reinforced sandwich panels were fabricated with polyvinyl chloride (PVC) foam core, woven plain glass and carbon fiber fabrics, and polymer epoxy resin set. PVC foam is a linear cross-linked, rigid, closed-cell core material and has widespread application in industrial practice due to its low cost and better environmental resistance like moisture absorption, flammability [25, 26]. Woven plain fiber fabrics were preferred since they provide better fiber yarn stability in both fill and warp directions, which leads to ease of fabrication. They also provide almost equal in-plane elastic properties and high out-of-plane strength compared to unidirectional fibers [27, 28]. In order to obtain the same thickness for the face sheets, 5-ply glass fiber fabrics was used, whereas 4-ply carbon fiber fabrics were used. Although it seems that the use of such ply numbers is not matching the same thickness value, approximately the same face sheet thickness values were obtained as the resin impregnation behaviors are different. The decision made for face sheets' layers was due to the laboratory experiences. The fiber face sheets and the core material were processed with a polymer epoxy resin set. The material properties of the sandwich constituents are given in Table 1.

2.2. Core Stitching and Sandwich Panel Manufacturing

PVC foam core materials were firstly drilled with a CNC milling machine to obtain stitching holes. The diameter of the holes is 2.5 mm. Figure 1 shows the schematic view of the drilled PVC foam core and drilling orientations. The stitching was made manually with a hole density of 0.36 hole/cm^2, which determines the number of stitching holes in a unit cm^2. The core stitching was made on the perforated foam core by using E-glass fiber yarns with 600-tex.

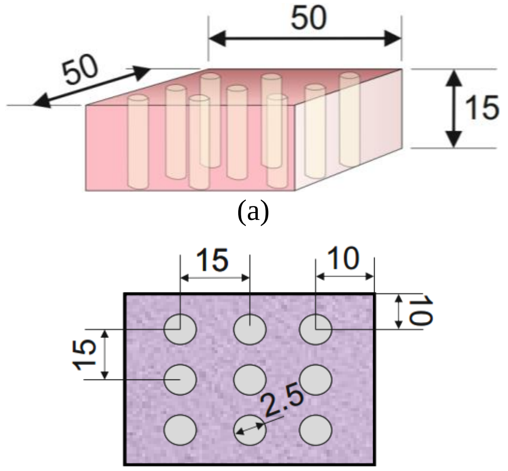

(a)

(b)

Figure 1 a) Schematic view of a drilled PVC core, b) drilling orientation

Table 1 Material properties of the sandwich constituents [29-31]

Material Property	Value
Carbon fiber	
Fabric Description	Woven, 3K plain, continuous
Areal Mass	200 g/m^2
Thickness	0.20 mm
Density	1790 kg/m^3
Tensile Strength	3800 MPa
Tensile Modulus	240 GPa
Tensile Strain	1.6 %
Glass fiber	
Fabric Description	E-glass, woven, continuous
Areal Mass	200 g/m^2
Thickness	0.18 mm
Density	2560 kg/m^3
Tensile Strength	2400 MPa
Tensile Modulus	76 GPa
Tensile Strain	4.8 %
PVC foam core materials	
Description	Rigid, linear, closed-cell
Density	48 kg/m^3
Thickness	14 mm
Compressive strength	0.60 MPa
Compressive modulus	48 MPa
Tensile strength	0.95 MPa
Tensile modulus	35 MPa
Shear strength	0.55 MPa
Shear modulus	16 MPa
Epoxy matrix	
Density	1180-1200 kg/m^3
Resin to hardener ratio	100:25 in weight
Tensile strength	70-80 MPa
Tensile modulus	3.2-3.5 GPa
Tensile strain	5-6.5 %
Compressive strength	80-100 MPa
Impact strength	40-50 kJ/m^2

Sandwich panels’ manufacturing was carried out by applying the vacuum bagging method. The face sheet fabrics were co-cured with the foam cores. Once all the composite layers, including fiber fabrics and core material, were stacked in a specified order, a perforated release film was placed over the resin-impregnated composite sandwich structure to allow the removal of excessive resin and air bubbles. Then, a vacuum breather was placed to collect the excessive resin. Lastly, the composite system was enclosed entirely by a vacuum bag. The non-stitched foam core sandwich panels were also fabricated as the benchmarks. The curing was performed at room temperature under a vacuum pressure of 0.005 mbar. The illustration of the manufacturing method I schematically demonstrated in Figure 2. The total sandwich thickness was obtained at 15.80 mm with a face sheet thickness of 0.9 mm.

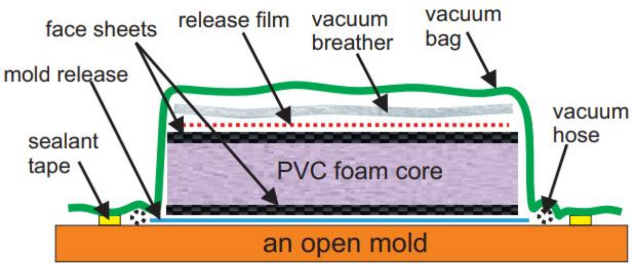

Figure 2 Schematic illustration of the vacuum bag method

2.3. Flatwise Compression Test

The flatwise compression tests were applied since the typical use of sandwich panels are generally under the compressive loads such as bridge decks, floors, roofs, etc. [9]. Therefore, the sandwich panels in the present study were subjected to flatwise compression tests according to ASTM C365 Standard. Dimensions of the testing specimens are 50 mm x 50 mm x 15.80 mm. A universal testing machine named ZwickRoell Z100 was used to perform the compression tests. The cross-head speed was set to 0.5 mm/min. A test specimen under compressive loading was presented in Figure 3. Compressive load and deflection values were recorded by the universal testing machine, and compressive strength and compressive modulus of the sandwich panels were determined based on Equations 1 and 2.

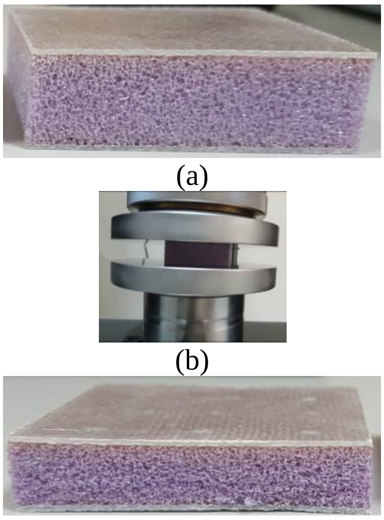
(a)
(b)
(c)

Figure 3 Flatwise compression test of a sandwich specimen; a) before test, b) compression, c) after test

$$\sigma_z = \frac{P}{a.b} \tag{1}$$

$$\varepsilon_z = \frac{\Delta t}{t_c} \tag{2}$$

Where σ_z and ε_z are the thorugh-thickness stress and the strain; a and b are the specimen’s surface dimensions; t_c is the core thickness, and Δ_t is the deflection value of the specimen.

3. RESULTS AND DISCUSSION

Sandwich panels were tested under flatwise-compressive loading with five repetitions. The closest curves to each other were used to present load-deflection (Figure 4 and 5) and stress-strain (Figure 6 and 7) curves. While four specimens are introduced for non-stitched foam core sandwiches, three specimens are introduced for stitched foam core sandwiches. Table 2 presents the average values of compressive load capacity, stress, and modulus data together with their standard deviations. The compressive modulus was calculated by dividing the stress to the corresponding strain value in the linear elastic region. The table also includes the sandwich weights.

As seen in Figure 4a, non-stitched foam core sandwiches with glass/epoxy face sheets exhibited a linear initial elastic zone, followed by a plastic region (a larger plateau), and finally, a densification stage. After the linear elastic zone, the gaps in PVC foam core cells start to close, which carry out in a wide deflection value, and then, densification occurs at last, which the foam core behaves like a solid structure. Similar findings were also obtained by Mostafa [2]. The non-stitched sandwich behaviors under flatwise-compressive loads were found irrespective of the face sheet materials. Because the sandwich with glass/epoxy face sheets carried a compressive load of 1330 N, whereas the sandwich with carbon/epoxy face sheets carried 1270 N. The results are very close to each other. The deflection values where the plastic region initiated were also closer to each other. Garay et al. [9] also obtained similar behaviors even in using both different types of core and face sheet materials. Consequently, the type of fiber reinforcement in face sheets does not significantly affect the failure behavior of the structures when designing a sandwich working under compressive loading.

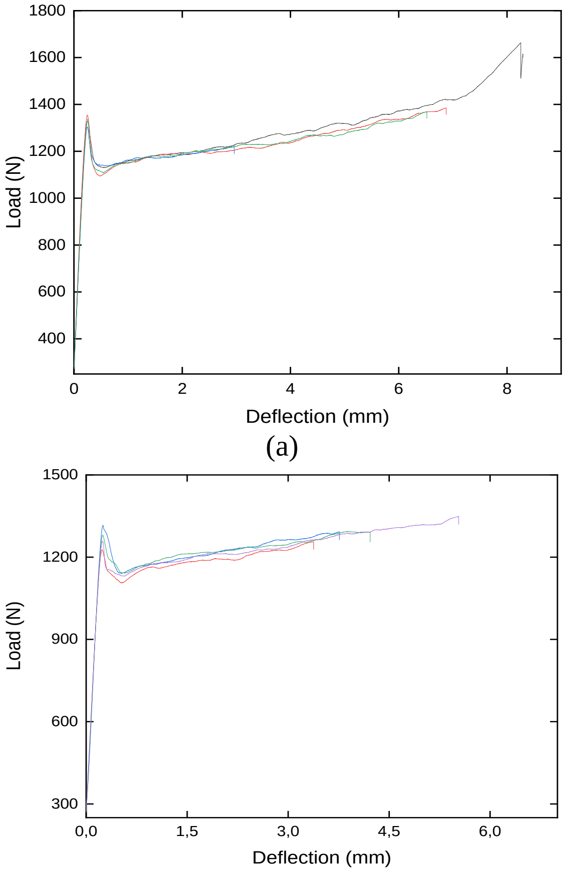

(a)

(b)

Figure 4 Load-deflection of non-stitched foam core sandwiches with; a) glass/epoxy face sheet, b) carbon/epoxy face sheet

Using stitched core provided the sandwich panels to resist higher compressive forces. In the linear elastic region, the increment in compressive load carrying capacity was obtained by 56.02% for the sandwich with glass/epoxy face sheets, whereas it was 77.95% for the sandwich with carbon/epoxy face sheets compared to the non-stitched foam core sandwiches. Contrary to non-stitched foam core sandwiches, the load capacity and compressive behavior were varied for the stitched sandwiches depending upon the face sheets. Moreover, additional force peaks were observed, as seen in Figure 5. The stitched core sandwich with glass/epoxy face sheets carried 2075 N average compressive load, and then after a yielding, it resisted to a force of 2514 N, which is 21.16% higher than the initial peak. On the other hand, in the case of using carbon/epoxy face sheets, the sandwich carried a compressive load of 2260 N, then after a decrease in the force for particular deflection values, the sandwich showed a second peak force of 2256 N, which is almost the same as the first peak force value. This might be due to the better integration of the sandwich layers thanks to the glass/epoxy columns in stitching holes, leading to improved interfacial strength, and the stitching restricted the core movement between the face sheets [23].

Table 2 Compressive properties and weights of the sandwich panels (SC: Stitched core, NSC: Non-stitched core, G/E: glass/epoxy, C/E: carbon/epoxy, FS: Face sheets)

Sandwich configuration	**Load capacity (N)**	**Strength (MPa)**	**Modulus (MPa)**	**Weight (N)**
NSC, G/E FS	1330.25 (18.45)	0.533 (0.007)	47.38 (1.82)	0.0838 (0.0006)
NSC, C/E FS	1269.75 (32.87)	0.508 (0.018)	43.5 (1.12)	0.0767 (0.0014)
SC, G/E FS	1st peak: 2074.33 (23.83) 2nd peak: 2514.33 (173.63)	1st peak: 0.830 (0.009) 2nd peak: 1.006 (0.069)	57.83 (3.79)	0.0905 (0.0008)
SC, C/E FS	1st peak: 2272.00 (21.27) 2nd peak: 2256.67 (123.51)	1st peak: 0.911 (0.008) 2nd peak: 0.918 (0.038)	46.33 (7.77)	0.0839 (0.0020)

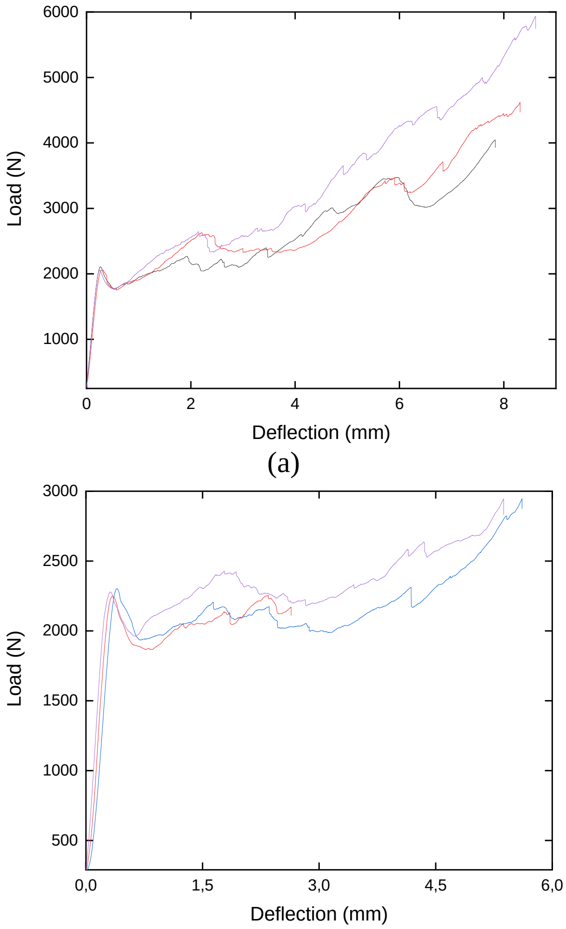

(a)

(b)

Figure 5 Load-deflection of stitched foam core sandwiches with; a) glass/epoxy face sheet, b) carbon/epoxy face sheet

The stress-strain curves of the non-stitched foam core sandwich panels with fiber face sheets (Figure 6) are found similar to the behavior of only the core material. The compressive strength of the sandwiches was obtained closer to that of core material as provided by the manufacturer. Also, in the literature, Mostafa [2] and Yalkin et al. [16] also demonstrated that the compression strength of only the foam core is very close to that of composite sandwich with fiber face sheets. The sandwiches showed a linear elastic phase until the yield stress. Then, the stress value decreased with the increase of strain since the closed cells were exposed to buckling in the core. After certain strain values, no significant change was observed in the compressive stress with increased strain value. Lastly, the sandwiches underwent densification at the end of that stress region since the closed cells were in self-contact in the core. The occurrence of the densification led to an increase in the stress value. The densification strains are about 0.52 mm/mm for the sandwiches. In recent literature, Akar [12] found a strain of 0.60 mm/mm for a 10 mm thick, 0.060 g/cm^3 PVC foam core sandwich with glass/epoxy face sheets. However, the researcher obtained approximately 0.40 MPa compressive strength, whereas it was 0.533 MPa in the present study. In fact, the higher the core density, the higher the compressive strength can be obtained. Compared to ref [12], a relatively thicker core was used in this work and provided the closed cell to resist more buckling loads.

The average values of the compressive strength and compressive modulus are given in Table 2. The standard deviations are given in parenthesis.

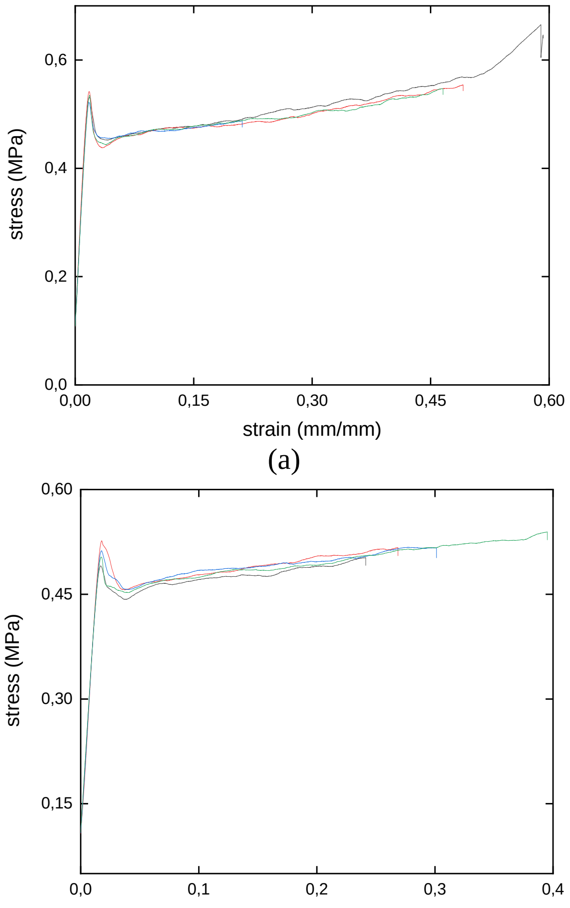

(a)

(b)

Figure 6 Stress-strain curves of non-stitched foam core sandwiches with; a) glass/epoxy face sheet, b) carbon/epoxy face sheet

The stress-strain curves of the stitched core sandwiches are obtained quite differently in the present study, although the shape of the curves of both stitched and non-stitched foam core sandwiches was presented similar to each other in the literature [16, 23, 25]. After the yield stress was reached, the stress value decreased for a particular strain, and then the stress value increased again, reaching the second peak in the stress. The second peak in the stress value was obtained thanks to the glass/epoxy columns in the stitching holes of the core. These through-thickness reinforcements provided to carry most of the compressive loads acting on the sandwich panels. While the failure of the non-stitched core sandwiches was due to only the buckling of the closed cells, the stitched core sandwiches failed due to the damage of both glass/epoxy fiber columns in the stitching holes and the closed cells in the core.

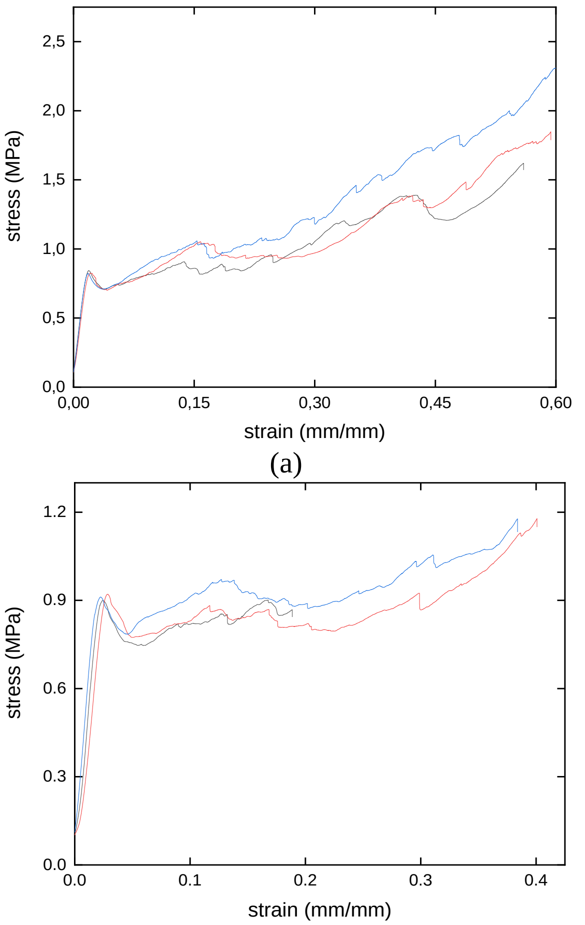

(a)

(b)

Figure 7 Stress-strain curves of stitched foam core sandwiches with; a) glass/epoxy face sheet, b) carbon/epoxy face sheet

When the sandwich weights are considered, it is seen in Table 2 that the core modifications did not make a notable effect on the structural weight. Because core stitching with 600-tex E-glass fiber yarns increased the weight of the sandwich panels by 7.98% and 9.42% for glass/epoxy and carbon/epoxy face sheets sandwiches, respectively. On the other hand, thanks to the stitching process, the compressive strength of the sandwiches was enhanced by 80.71% and 88.74% for carbon/epoxy and glass/epoxy face sheets, respectively.

4. CONCLUSION

In the present study, PVC foam cores were stitched with 600-tex E-glass fiber yarns; then, sandwich composites were manufactured with both carbon/epoxy and glass/epoxy face sheets. The flatwise compression test results showed that using stitched core in a sandwich structure significantly improved the compressive load capacity, strength, and modulus with a minimum weight increase. Because the resin impregnated fiber yarns within the stitching holes acted as the primary load-carrying members. These reinforcements also provided better interfacial bond strength between the core and the face sheets materials leading to high delamination resistance and structural integrity of the sandwiches. Unlike the previous studies, the core stitching provided the sandwich composites to resists additional load peaks, which are higher than the first peaks.

Core stitching is a simple and less time-consuming through-thickness reinforcement process among the other core modifications methods; thus, the stitched core materials with different hole densities can be supplied from the manufacturer or prepared in a laboratory before using them in composite sandwich manufacturing. Therefore, the effects of counts of fiber bundles to make stitching and hole density are potential subjects for future investigations.

Funding

The author has no received any financial support for the research, authorship or publication of this study.

The Declaration of Conflict of Interest/ Common Interest

No conflict of interest or common interest has been declared by the author.

The Declaration of Ethics Committee Approval

This study does not require ethics committee permission or any special permission.

The Declaration of Research and Publication Ethics

The author of the paper declare that he comply with the scientific, ethical and quotation rules of SAUJS in all processes of the paper and that they do not make any falsification on the data collected. In addition, they declare that Sakarya University Journal of Science and its editorial board have no responsibility for any ethical violations that may be encountered, and that this study has not been evaluated in any academic publication environment other than Sakarya University Journal of Science.

REFERENCES

[1] B. Abdi, S. Azwan, M. R. Abdullah, A. Ayob, Y. Yahya, and L. Xin, "Flatwise compression and flexural behavior of foam core and polymer pin-reinforced foam core composite sandwich panels," (in English), Int J Mech Sci, vol. 88, pp. 138-144, Nov 2014. [Online]. Available: <Go to ISI>://WOS:000344428000015.

[2] A. Mostafa, "Numerical analysis on the effect of shear keys pitch on the shear performance of foamed sandwich panels," (in English), Eng Struct, vol. 101, pp. 216-232, Oct 15 2015. [Online]. Available: <Go to ISI>://WOS:000362142200018.

[3] A. Mostafa, K. Shankar, and E. V. Morozov, "Insight into the shear behaviour of composite sandwich panels with foam core," (in English), Mater Design, vol. 50, pp. 92-101, Sep 2013. [Online]. Available: <Go to ISI>://WOS:000320615300014.

[4] F. Y. Han, Y. Yan, and J. Ma, "Experimental study and progressive failure analysis of stitched foam-core sandwich composites subjected to low-velocity impact," (in English), Polymer Composites, vol. 39, no. 3, pp. 624-635, Mar 2018. [Online]. Available: <Go to ISI>://WOS:000426747000004.

[5] J. L. Xu, J. Q. Liu, W. B. Gu, Z. X. Wang, X. Liu, and T. Cao, "Effect of cell size on the energy absorption of closed-cell aluminum foam," (in English), Mater Test, vol. 60, no. 6, pp. 583-590, Jun 2018. [Online]. Available: <Go to ISI>://WOS:000451930900006.

[6] C. Liu, Y. X. Zhang, and R. Heslehurst, "Impact resistance and bonding capability of sandwich panels with fibre–metal

laminate skins and aluminium foam core," Journal of Adhesion Science and Technology, vol. 28, no. 24, pp. 2378-2392, 2014/12/17 2014, doi: 10.1080/01694243.2014.967744.

[7] D. Jebadurai and A. Rose, "Influence of core and matrix modifications on the mechanical characteristics of sandwich composites," IOP Conference Series: Materials Science and Engineering, vol. 912, p. 052026, 09/12 2020, doi: 10.1088/1757-899X/912/5/052026.

[8] Z. Wu, J. Xiao, J. Zeng, and J. Liu, "Compression performance of integrated 3D composite sandwich structures," J Sandw Struct Mater, vol. 16, no. 1, pp. 5-21, 2014/01/01 2013, doi: 10.1177/1099636213501927.

[9] A. C. Garay, J. A. Souza, and S. C. Amico, "Evaluation of mechanical properties of sandwich structures with polyethylene terephthalate and polyvinyl chloride core," (in English), J Sandw Struct Mater, vol. 18, no. 2, pp. 229-241, Mar 2016. [Online]. Available: <Go to ISI>://WOS:000371095700006.

[10] J. Tao, F. Li, D. D. Zhang, J. B. Liu, and Z. B. Zhao, "Manufacturing and mechanical performances of a novel foam core sandwich-walled hollow column reinforced by stiffeners," (in English), Thin Wall Struct, vol. 139, pp. 1-8, Jun 2019. [Online]. Available: <Go to ISI>://WOS:000466257000001.

[11] Z. Salleh, M. Islam, J. Epaarachchi, and H. Su, "Mechanical properties of sandwich composite made of syntactic foam core and GFRP skins," AIMS Materials Science, vol. 3, pp. 1704-1727, 12/01 2016, doi: 10.3934/matersci.2016.4.1704.

[12] A. Dogan, "Low-velocity impact, bending, and compression response of carbon fiber/epoxy-based sandwich composites with different types of core materials," J Sandw Struct Mater, p. 1099636220908862, 2020, doi: 10.1177/1099636220908862.

[13] S. Zangana, J. Epaarachchi, W. Ferdous, and J. Leng, "A novel hybridised composite sandwich core with Glass, Kevlar and Zylon fibres – Investigation under low-velocity impact," International Journal of Impact Engineering, vol. 137, p. 103430, 2020/03/01/ 2020, doi: https://doi.org/10.1016/j.ijimpeng.2019.103430.

[14] Ç. Uzay and N. Geren, "Effect of stainless-steel wire mesh embedded into fibre-reinforced polymer facings on flexural characteristics of sandwich structures," J Reinf Plast Comp, vol. 39, no. 15-16, pp. 613-633, 2020/08/01 2020, doi: 10.1177/0731684420921952.

[15] T. S. Lim, C. S. Lee, and D. G. Lee, "Failure Modes of Foam Core Sandwich Beams under Static and Impact Loads," J Compos Mater, vol. 38, no. 18, pp. 1639-1662, 2004/09/01 2004, doi: 10.1177/0021998304044760.

[16] H. E. Yalkin, B. M. Icten, and T. Alpyildiz, "Tensile and compressive performances of foam core sandwich composites with various core modifications," (in English), J Sandw Struct Mater, vol. 19, no. 1, pp. 49-65, Jan 2017. [Online]. Available: <Go to ISI>://WOS:000391784000003.

[17] I. M. Daniel, E. E. Gdoutos, K. A. Wang, and J. L. Abot, "Failure modes of composite sandwich beams," (in English), Int J Damage Mech, vol. 11, no. 4, pp. 309-334, Oct 2002. [Online]. Available: <Go to ISI>://WOS:000179031500001.

[18] Ç. Uzay, Geren, N, "Failure Analysis of Low-density Polymer Foam Core Sandwich Structures under Three-point Bending Loading," Çukurova Üniversitesi Mühendislik-Mimarlık Fakültesi Dergisi, vol. 35, no. 1, pp. 49-58, 2020.

[19] N. Geren, D. C. Acer, C. Uzay, and M. Bayramoglu, "The effect of boron carbide additive on the low-velocity impact properties of low-density foam core composite sandwich structures," Polymer Composites, https://doi.org/10.1002/pc.25957 vol. 42, no. 4, pp. 2037-2049, 2021/04/01 2021, doi: https://doi.org/10.1002/pc.25957.

[20] N. Mitra, "A methodology for improving shear performance of marine grade sandwich composites: Sandwich composite panel with shear key," Compos Struct, vol. 92, no. 5, pp. 1065-1072, 2010/04/01/ 2010, doi: https://doi.org/10.1016/j.compstruct.2009.10.005.

[21] A. T. Martins, Z. Aboura, W. Harizi, A. Laksimi, and K. Khellil, "Analysis of the impact and compression after impact behavior of tufted laminated composites," Compos Struct, vol. 184, pp. 352-361, 2018/01/15/ 2018, doi: https://doi.org/10.1016/j.compstruct.2017.09.096.

[22] A. J. Malcom, M. T. Aronson, V. S. Deshpande, and H. N. G. Wadley, "Compressive response of glass fiber composite sandwich structures," Composites Part A: Applied Science and Manufacturing, vol. 54, pp. 88-97, 2013/11/01/ 2013, doi: https://doi.org/10.1016/j.compositesa.2013.07.007.

[23] H. E. Yalkin, B. M. Icten, and T. Alpyildiz, "Enhanced mechanical performance of foam core sandwich composites with through the thickness reinforced core," (in English), Compos Part B-Eng, vol. 79, pp. 383-391, Sep 15 2015. [Online]. Available: <Go to ISI>://WOS:000358808300040.

[24] ASTM-C365, Standard Test Method for Flatwise Compressive Properties of Sandwich Cores. USA: Annual Book of ASTM Standards, 2003.

[25] J. Wang, B. X. Chen, H. Wang, and A. M. Waas, "Experimental study on the compression-after-impact behavior of foam-core sandwich panels," (in English), J Sandw Struct Mater, vol. 17, no. 4, pp. 446-465, Jul 2015. [Online]. Available: <Go to ISI>://WOS:000355329600006.

[26] A. K. J. Al-Shamary, R. Karakuzu, and O. Ozdemir, "Low-velocity impact response of sandwich composites with different foam core configurations," (in English), J Sandw Struct Mater, vol. 18, no. 6, pp. 754-768, Nov 2016. [Online]. Available: <Go to ISI>://WOS:000390061800005.

[27] P. Priyanka, A. Dixit, and H. S. Mali, "High-Strength Hybrid Textile Composites with Carbon, Kevlar, and E-Glass Fibers for Impact-Resistant Structures. A Review.," (in English), Mech Compos Mater, vol. 53, no. 5, pp. 685-704, Nov 2017. [Online]. Available: <Go to ISI>://WOS:000416259200010.

[28] A. Dixit, H. Mali, and R. Misra, "A Micromechanical Unit Cell Model of 2 × 2 Twill Woven Fabric Textile Composite for Multi Scale Analysis," Journal of The Institution of Engineers (India): Series E, vol. 95, 03/31 2014, doi: 10.1007/s40034-014-0028-y.

[29] Airex_C70.48-TDS, Universal Structural Foam: Airex C70. . Composites A, 2011.

[30] Dost_Kimya-TDS, Carbon Fabric – 200gr/sqm 3K Plain. Turkey: Dost Kimya Inc., 2014.

[31] Hexion-TDS, Laminating Resin MGSTM L160 and Hardener H160. The Netherlands: Hexion Inc., 2009.

SAKARYA ÜNİVERSİTESİ

FEN BİLİMLERİ ENSTİTÜSÜ
DERGİSİ

Sakarya University Journal of Science
SAUJS

e-ISSN 2147-835X Founded 1997 Period Bimonthly Publisher Sakarya University
http://www.saujs.sakarya.edu.tr/en/

Title: Preparation and Characterization of Biocompatible Membranes Based on TiO2 Nanoparticul

Authors: Gülşen TAŞKIN ÇAKICI

Recieved: 2021-07-13 00:00:00

Accepted: 2021-11-01 00:00:00

Article Type: Research Article

Volume: 25
Issue: 6
Month: December
Year: 2021
Pages: 1376-1385

How to cite
Gülşen TAŞKIN ÇAKICI; (2021), Preparation and Characterization of Biocompatible Membranes Based on TiO2 Nanoparticul . Sakarya University Journal of Science, 25(6), 1376-1385, DOI: https://doi.org/10.16984/saufenbilder.971191

Access link
http://www.saujs.sakarya.edu.tr/tr/pub/issue/66341/971191

Sakarya University Journal of Science 25(6), 1376-1385, 2021

Preparation and Characterization of Biocompatible Membranes Based on TiO_2 Nanoparticul

Gülşen TAŞKIN ÇAKICI*[1]

Abstract

In this study, biocompatible composite membranes of sodium alginate/hydroxypropyl methylcellulose (NaAlg/HPMC) based on nano-titanium dioxide (n-TiO_2) were prepared. Regarding the preparation processes of these membranes, the amount of citric acid [5%, 15%, 30% (w/w)] added to the NaAlg/HPMC blend, the crosslinker type (glutaraldehyde, acetone/water with glutaraldehyde, $CaCl_2$), and the amount of n-TiO_2 [5%, 15%, 20% (w/w)] were studied and optimum conditions were determined. When the equilibrium swelling values were examined, it was observed that the one with the least swelling was the $CaCl_2$ crosslinked membrane. Fourier Transform Infrared (FTIR) Spectroscopy, Differential Scanning Calorimetry (DSC), and Scanning Electron Microscopy (SEM) were used to characterize the modified crosslinked membranes. The FTIR analysis results showed the formation of hydrogen bonds between the hydroxyl groups of the HPMC and NaAlg polymer chains. The DSC analysis showed the existence of single glass transition temperature (Tg) which indicated the compatibility and physical interaction between the NaAlg and HPMC polymer chains for NaAlg / HPMC mixtures.

Keywords: sodium alginate, hydroxypropylmethylcellulose, nanoparticle TiO_2, nanocomposite membrane

1. INTRODUCTION

Today, biodegradable polymers are used especially in shopping bags, food packaging products, agricultural films, and medical instruments. The area, tension, and morphology of the surface of a material are extremely important in terms of biodegradation and colonization of microorganisms on the polymer surface [1]. Different structures can be created using natural-built reinforcement elements based on lignocellulose (starch, wheat stalks, rice halves, cellulose fibers) to meet specific criteria for polymers, to improve mechanical properties, and to cut prices [2]. In general, blend mixtures, which are prepared using the molecular hydrogen bonds formed by two or more polymers, are used in this regard [3]. Petroleum derivatives-polymers are dominantly used in the production of large quantities of plastics worldwide. Because these plastics are not biodegradable, they cause serious environmental problems such as soil poisoning, toxic gases emitted during incineration in landfills. Today, the increase in the use of petroleum-derivative synthetic polymers such as polyethylene (PE), polypropylene (PP),

---

* Corresponding author: gtaskin@cumhuriyet.edu.tr

[1] Sivas Cumhuriyet University, Yıldızeli Vocational School, Chemistry and Processing Technologies
ORCID: https://orcid.org/0000-0001-7564-9777

polystyrene (PS), which are not biodegradable, causes environmental pollution. Therefore, the importance of using biodegradable polymers is increasing day by day.

NaAlg, a biocompatible polymer with good film-forming ability, is used in biomedical applications such as drug release, cell encapsulation systems, tissue and organ regeneration [4-7]. HPMC, a hydrophilic and biocompatible polymer, is widely used in many fields such as drug release, building materials, adhesives, cosmetics, agriculture, and textile [8]. It is a potential polymer used in biomedical applications thanks to its excellent bioavailability and very low toxicity. In the literature, NaAlg and HPMC are generally available in the form of hydrogels, tablets, and matrix systems. Mujtaba and Kohli [9] prepared matrix tablets based on HPMC and NaAlg and examined the release of cefpodoxime. Okeke and Boateng [10] examined the development of tablets and films prepared from HPMC and NaAlg as a mucosadive system on the buccal mucosa for nicotine treatment. Yadava et al. [11] analyzed in vitro diclofenac sodium with gel beads prepared with NaAlg/HPMC/liquid paraffin.

Besides the advantages of biocompatible polymers, they also have some disadvantages such as low mechanical and thermal properties. Recently, polymer nanocomposite technology is used to eliminate these disadvantages of biocompatible polymers [12]. For this purpose, biocompatible nanocomposite polymers are prepared using nanoparticles such as organic and inorganic nanoclay, silicate, TiO_2, and graphene [13]. Kim et al. reported that the mechanical and thermal properties of biodegradable nanocomposite polymers were improved by using graphene nanoparticles [14]. Yun et al. used Chitosan, PVA, and TiO_2 nanoparticles to prepare a nanocomposite film and examined their effects on mechanical and thermal properties [13]. In their study, Işık et al. entrapped commercially obtained ZnO and TiO_2 nanoparticles in calcium alginate beads and carried out adsorption and photochemical experiments to decolorize Reactive Red 180 [15]. Thomas et al. studied the photocatalytic performance of the nanocomposites they synthesized in Sr^{2+} ion crosslinked alginate/carboxymethyl cellulose gels using TiO_2 and graphene nanoparticles [16]. TiO_2 is a nanomaterial of great interest for reasons such as lower costs, high photocatalytic performance, high chemical stability, non-toxicity, and biocompatibility [17-19]. Various polymer/ TiO_2 nanocomposite structures are also available in the literature [20,21].

Chemical cross-linking in the preparation of polymeric materials can affect some properties of polymeric materials such as swelling, drug release, permeability, and chemical stability. Different cross-linking agents are needed to understand the interactions between membrane material and cross-linking agents. For example, glutaraldehyde, epichlorohydrin, Ca^{+2} ions, citric acid, sodium benzoate, boric acid are used as cross-linking agent in typical cross-linking method [22]. The cross-linking improves performance and resistance of biopolymer films.

In this study, the nanocomposite membranes produced from NaAlg and HPMC biocompatible polymers were prepared using n-TiO_2 nanoparticles. Membranes with high mechanical strength have been prepared by using various types of crosslinkers. Depending on their morphological properties, biocompatible membranes have been obtained that can be an alternative in medicine and drug release studies. The hydrophilicity and water absorption tendencies of the membranes were determined by swelling studies. The prepared membranes were characterized by Fourier Transform Infrared (FTIR) Spectroscopy, Differential Scanning Calorimetry (DSC), and Scanning Electron Microscopy (SEM).

2. EXPERIMENTAL

2.1. Materials

Sodium alginate (NaAlg), glutaraldehyde (GA), hydroxypropyl methylcellulose (HPMC), and titanium di oxide (TiO_2) (<100nm particle size) were purchased from Sigma-Aldrich (Germany). Calcium chloride ($CaCl_2$) and citric acid (CA) were all supplied from Merck (Germany).

Hydrochloric acid (HCl) and acetone were provided by Merck (Germany).

2.2. Membrane Formation

Prepared by casting method, NaAlg-HPMC and NaAlg-HPMC -TiO_2 composite membranes were dried at 40 ℃ for 24 hours. For crosslinked process, membranes were immersed in the crosslinking solution for 24 h.

2.3. Techniques Used in The Characterization of Membranes

2.3.1. FTIR Analysis of Membranes

The prepared NaAlg, HPMC, NaAlg/HPMC/CA-30, and NaAlg/HPMC/CA-30/TiO_2-20 membranes were characterized by FTIR spectroscopy. Measurements were performed using a spectrophotometer (Bruker Mode: Tensor II) with potassium chloride pellets.

2.3.2. DSC Analysis of Membranes

DSC analysis of the prepared membranes was performed by DSC Q2000 V24.11 Build 124.

2.3.3. Scanning Electron Microscope (SEM)

For SEM analysis, the dried crosslinked membranes were sputtered with gold in vacuum and then observed under a microscope (TESCAN MIRA3 XMU).

2.4. Determination of Swelling Percentages of Prepared Membranes

The swelling values in water were examined to determine the water absorption tendencies of the crosslinked membranes. The membranes were immersed in water for 24 hours at room temperature. The residual liquid was removed from the swollen membranes and then weighed, dried in an oven and weighed again. Swelling degree percentages (SD%) of the membranes were calculated using Equation (1).

$$SD\%=\frac{Ww-Wd}{Wd}\ x100 \qquad (1)$$

where, W_w and W_d are the wet and dry masses of the membranes, respectively.

3. RESULTS AND DISCUSSION

3.1. Optimum Conditions for The Preparation of Membranes

Prepared membranes from a blend of nanoparticle added HPMC and NaAlg polymers and the effect of crosslinker type on the membrane properties have not been tested before this. Table 1 summarizes some the work done so far.

Table 1 Studies of NaAlg, HPMC and TiO_2 in the literature

Formulation	**Polymer**	**Crosslinking**	**Purpose**	**Ref.**
Composite hydrogel	NaAlg-HPMC	Ca^{+2} ions	Drug release	[23]
Emulsified gel beads	Sodium alginate/ HPMC/ liquid paraffin	Ca^{+2} and Zn^{+2} ions	Drug release	[11]
In situ gelling	NaAlg-HPMC	Ca^{+2} ions	Ophthalmic delivery system	[24]
Matrix tablet	NaAlg-HPMC-microcrystalline cellulose	magnesium stearate	Drug release	[25]
Hydrogel beads	NaAlg-HPMC	Ca^{+2} ions	Drug release	[7]
Films and wafers	NaAlg-HPMC	-	The buccal delivery nicotine.	[10]
Film	HPMC-TiO_2-bovine bone collagen	-	Active packaging in the food industry	[26]
Hydrogel	NaAlg-Pt/TiO_2	Ca^{+2} ions	Photodegradation activity	[27]
Membrane	NaAlg-TiO_2	water/acetone (30:70) 2.5 ml GA, 2.5 ml HCl	Pervaporation	[28]

In this study, HPMC and NaAlg blend aqueous solutions were first prepared in 1:1(w/w) ratio with citric acid (CA). Different amounts of CA (5, 15, and 30 mass % on the weight of HPMC) were added in the polymer blend solution. These blend solutions were designated as NaAlg/HPMC/CA-5; NaAlg/HPMC/CA-15; and NaAlg/HPMC/CA-30, respectively. The CA added to the polymer solution was used to facilitate crosslinking of HPMC [29]. The possible cross-linking mechanism was given in Figure 1. Predetermined amount of blend solution was cast onto glass plates and left for drying at 40 °C for 24 hours (Figure 2). The crosslinked membranes were prepared by immersing the dried membranes in crosslinking solution for 24 h. Then finally they were washed with distilled water and dried.

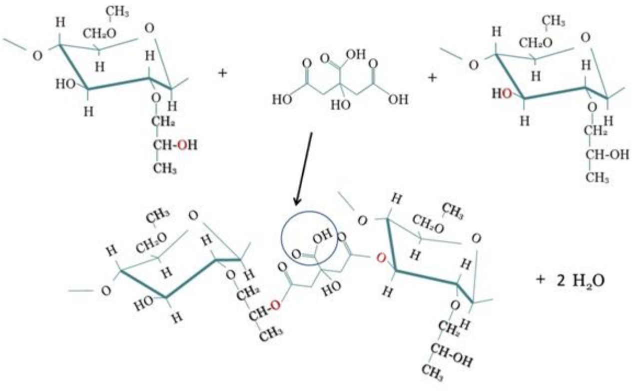

Figure 1 Crosslinking of HPMC with citric acid

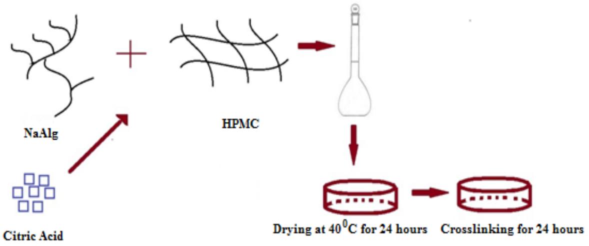

Figure 2 Preparation of NaAlg and HPMC blend solution and membranes

Secondly, nanocomposite solutions were prepared by adding n-TiO_2 (5,15 and 20 mass %) in NaAlg/HPMC blend solutions including citric acid (30 mass %). These solutions were coded NaAlg/HPMC/CA-30/TiO_2-5, NaAlg/ HPMC/ CA-30/ TiO_2-15, and NaAlg/HPMC/CA-30/TiO_2-20, respectively. Predetermined amount of nanocomposite blend solution was cast onto glass plates and left for drying at 40 ºC for 24 hours (Figure 3). The crosslinked nanocomposite membranes were prepared by immersing the dried membranes in crosslinking solution for 24 h. Then finally they were washed with distilled water and dried.

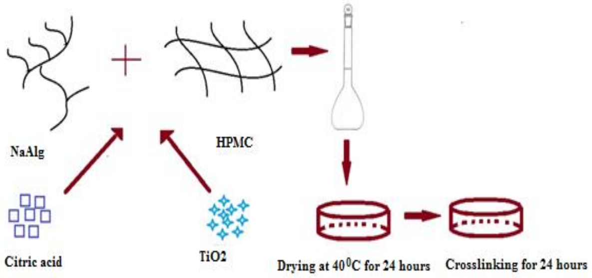

Figure 3 Preparation of NaAlg / HPMC / CA-30/TiO_2 nanocomposite polymer solution and membranes

Figure 4 NaAlg / HPMC / CA-30/ TiO_2 nanocomposite membrane

As seen in Figure 4, a homogeneous membrane was obtained. The membranes obtained were hard but not fragile and easily degradable. They were durable enough to be an alternative especially in transdermal drug systems.

3.2. Effect of Crosslinker Type on The Membrane Morphology

Water-soluble polymers are crosslinked with the help of some crosslinking agents. Crosslinked hydrophilic polymers are especially used for controlled-release preparations. Cross-linking is carried out using heat or chemical binding agents such as glutaraldehyde, formaldehyde, and diacid chloride. Heat denaturation is not suitable for heat-resistant substances. The type of cross-linking agent and the duration of cross-linking are important for the mechanical strength of polymeric materials used in drug release studies [22].

The effect of the cross-linking agent on the strength and morphology of the membranes was investigated by changing the crosslinking type ($CaCl_2$ solution, glutaraldehyde (GA) solution, and acetone/water solution containing 2.5 mL GA and 2.5 mL HCl). The possible cross-linking mechanism was given in the Figures 5 and 6.

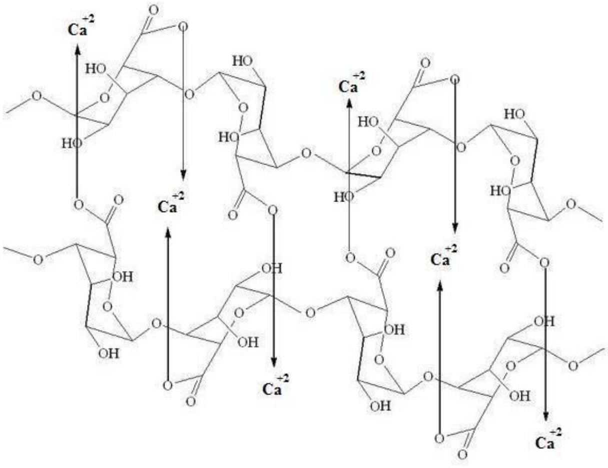

Figure 5 Crosslinking of NaAlg with $CaCl_2$ [30]

Calcium ions bind to carboxyl and hydroxyl groups in the alginate solution.

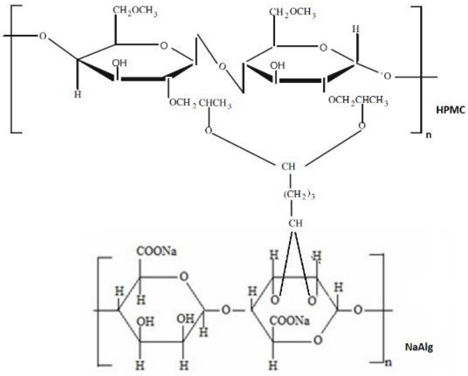

Figure 6 Crosslinking of NaAlg/HPMC blend with GA [31,32]

3.3. Membrane Characterization

3.3.1. FTIR Studies

Figure 7 showed the FTIR spectra of the NaAlg, HPMC, NaAlg/HPMC/CA-30, and NaAlg/HPMC/ CA-30/TiO_2-20 membranes, which were uncrosslinked by $CaCl_2$, GA, and acetone/water solution.

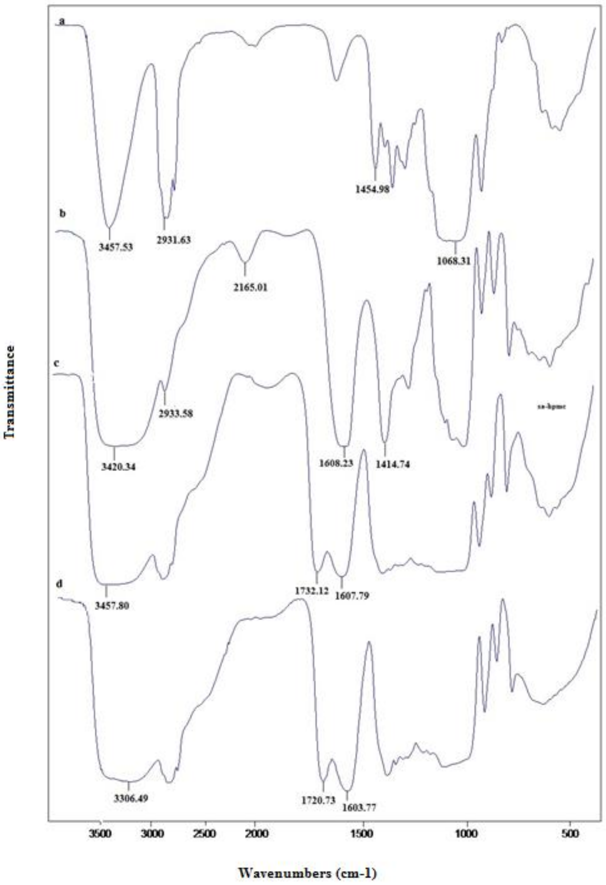

Figure 7 FTIR spectra of membranes [(a) HPMC (b) NaAlg (c) NaAlg/HPMC/CA-30 (d) NaAlg/HPMC/ CA-30/TiO_2-20]

The spectrum of the HPMC membrane (Figure 7a) showed peaks at around 3457.53 cm^{-1} wide band –OH stretching, 2931.63 cm^{-1} band –CH stretching, 1068.31 cm^{-1} band –CO stretching, and 1456 cm^{-1} band CH_3 asymmetric bending vibration [33]. The spectrum of NaAlg (Fig.7b) showed peaks at around 2933.58, 1608.23, 1414.74 and 3420.34 cm^{-1} indicating the stretching vibrations of aliphatic C–H, COO− (asymmetric), COO− (symmetric), and -OH, respectively [34]. The spectrum of NaAlg/HPMC-30 (Fig.7d) showed peaks at around 3457.80, 1607.79 and 1413.04 cm^{-1} indicating the stretching vibrations of -OH, COO− (asymmetric), COO− (symmetric), respectively. The change in these wave values indicates that the intermolecular hydrogen bonds in NaAlg and HPMC blend are formed [33,34]. Furthermore, the presence stretching of carbonyl in the 1723.12cm^{-1} band (C=O) is thought to result from the esterification of hydroxyl groups of HPMC with carboxylic acid groups of citric acids [35]. There is a strong shift in -OH stresses with the addition of TiO_2. This can be attributed to the occurring of hydrogen bond between the n-TiO_2 and polymer molecules [16].

3.3.2. DSC Studies

DSC results of uncrosslinked membranes using $CaCl_2$, GA, and acetone/water solution were given in Figure 8. HPMC showed a wider endothermic peak due to its more amorphous structure than NaAlg. In the NaAlg/HPMC/CA-30 blend, the expansion of the endothermic peak can be attributed to the polymers' having a different degree of crystallization, as well as the polymer –polymer interaction.

The most important factor that determines whether a polymer will crystallize is its geometric structure or chain configuration. NaAlg contains at least three different polymer segments (poly(b-D-mannopyranosyluro-nate), poly(a-L-guluopyranosyluronate), and segments with alternative sugar units. Due to these segment shapes, it has very a weak and small melting peak at 201.15 ºC. In the NaAlg/HPMC blend, the decrease in this melting peak can be attributed to the rigid molecular chain of NaAlg, which affects the overall chain mobility in the blend and crystal growth rate [34].

The reason why a single Tg was observed in the Figure 8 (c and d) may be due to the miscibility of NaAlg and HPMC with TiO_2.

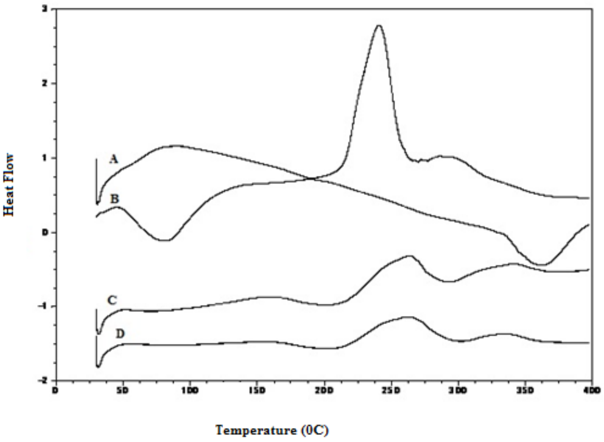

Figure 8 DSC results of membranes [(A) HPMC, (B) NaAlg, (C) NaAlg/HPMC/CA-30, (D) NaAlg/HPMC/CA-30/TiO_2-20]

3.3.3. SEM Studies

In order to investigate the surface morphology of the crosslinked NaAlg/HPMC/CA-30 and NaAlg/HPMC/ CA-30/TiO_2-20 membranes, SEM micrographs were taken and given in the Figures 9 and 10, respectively. Significant morphological differences were observed in SEM images of the membranes depending on the crosslinker used. The surface of the membranes crosslinked with $CaCl_2$ was rough and spongy, while those crosslinked with GA and acetone/water solution had a non-porous and smoother structure. This morphological difference can be attributed to the tighter crosslinking of $CaCl_2$ (crosslinker) membranes.

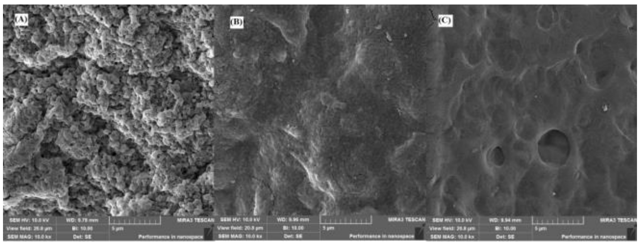

Figure 9 SEM micrographs of NaAlg/HPMC/CA-30 membranes crosslinked with (a) $CaCl_2$, (b) GA, and (c) acetone/water solution

The morphology of NaAlg/HPMC/CA-30 membranes changed depending on the amount of TiO_2 present in the polymer matrix. As can be seen in the images, there are many aggregates or particles dispersed on the top surface, showing that TiO_2 particles tend to form aggregates and are dispersed into the polymer blend matrix [36]. In Figure 10, the aggregation of n-TiO_2 particles was attributed to the tendency of nanoparticles to form aggregates due to their high surface energy [37].

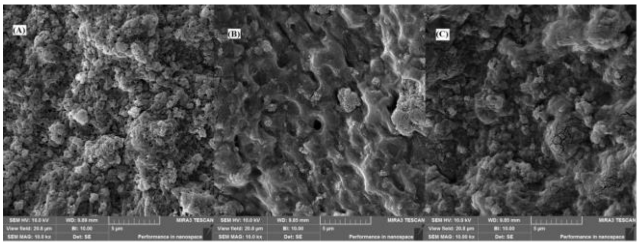

Figure 10 SEM micrographs of NaAlg/HPMC/CA-30/TiO_2-20 membranes crosslinked with (a) $CaCl_2$, (b) GA, and (c) acetone/water solution

3.3.4. Swelling Measurements

The results of swelling experiments for crosslinked NaAlg/HPMC membranes were shown in the Tables 2 and 3. $CaCl_2$ solution, glutaraldehyde (GA) solution, and acetone/water solution containing 2.5 mL GA and 2.5 mL HCl were used as crosslinker. Swelling rates were calculated by averaging at least 5 trials.

Table 2 shows that the membranes crosslinked with $CaCl_2$ have fewer swelling percentages than the membranes crosslinked with other solutions. This can be attributed to the increase in crosslink density and the formation of a more frequent network structure in the membranes. High cross-linking causes a low swelling percentage [38].

Table 2 Swelling percentages of NaAlg/HPMC/ CA membranes

MEMBRANE	$CaCl_2$	Acetone/Water	GA
NaAlg/HPMC/CA-5	210.5	391.8	401.7
NaAlg/HPMC/CA -15	230 .0	239.1	342.3
NaAlg/HPMC/CA -30	171.1	415.5	458.9

The addition of TiO_2 to the polymer matrix not only increased the interaction between hydroxyl groups on the polymer chains, but also reduced the hydrogen bonding effect between the polymer chains. Therefore, the decrease in SD is due to the good dispersion of TiO_2 polymers.

Table 3 Swelling percentages of NaAlg/HPMC/ CA-30/ TiO_2 membranes

Membrane	$CaCl_2$	Acetone/Water	GA
NaAlg/HPMC/CA-30/ TiO_2-5	208.1	345.9	387.8
NaAlg/HPMC/ CA-30/ TiO_2-15	202.5	227.7	334.6
NaAlg/HPMC/ CA-30/ TiO_2-20	139.4	403.4	448.6

4. CONCLUSION

Nanocomposite films were successfully synthesized from NaAlg, HPMC, and TiO_2 nanoparticles using the solutions of $CaCl_2$, GA, and acetone/water with GA as a crosslinker. The prepared membranes were characterized by FTIR, DSC, and SEM. The FTIR results showed strong hydrogen bonds between polymer and nanoparticle. In the DSC results, single Tg temperature showed strong polymer-polymer and polymer-TiO_2 interactions and the blend was miscible. SEM micrographs showed that TiO_2 was evenly dispersed in the NaAlg/HPMC blend. The biocompatible nanocomposite films prepared in this study have qualities that can be an alternative to other films used in the field of medicine.

Funding

This study is supported by Sivas Cumhuriyet University Scientific Research Projects Coordination Unit. Project Number: YMYO-005.

The Declaration of Conflict of Interest/Common Interest

No conflict of interest or common interest has been declared by the authors.

Authors' Contribution

The author solemly performed the computations and wrote the manuscript.

The Declaration of Ethics Committee Approval

The author declare that this document does not require an ethics committee approval or any special permission.

The Declaration of Research and Publication Ethics

The authors of the paper declare that they comply with the scientific, ethical and quotation rules of SAUJS in all processes of the article and that they do not make any falsification on the data collected. In addition, they declare that Sakarya University Journal of Science and its editorial board have no responsibility for any ethical violations that may be encountered, and that this study has not been evaluated in any academic publication environment other than Sakarya University Journal of Science.

REFERENCES

[1] E. Chiellini and R. Solaro, "Biodegradable polymeric materials," Advanced Materials, vol. 8, pp. 305-313, 1996.

[2] M.T. Taghizadeh and N. Sabouri, "Biodegradation behaviors and water adsorption of poly(vinyl alcohol)/starch/carboxymethyl cellulose /clay nanocomposites," International Nano Letters, vol. 51, pp. 1-8, 2013.

[3] Y Sun, Z. Shao, P. Hu, Y. Liu and T. Yu, "Hydrogen bonds in silk fibroin-poly(acrylonitrile-co-methyl acrylate) blends: FT–IR study," Journal of Polymer Science Part B: Polymer Physics, vol. 35, pp. 1405-1414, 1997.

[4] N. Reyes, I Rivas-Ruiz, R. Domínguez-Espinosa and S. Solís, "Influence of immobilization parameters on endopolygalacturonase productivity by hybrid Aspergillus sp. HL entrapped in calcium alginate," Biochemical Engineering Journal, vol. 32, pp. 43–48, 2006.

[5] B.L. Seal, T.C. Otero and A. Panitch, "Polymeric biomaterials for tissue and organ regeneration," Materials Science and Engineering, vol. 34, pp. 147–230, 2001.

[6] M.R. Rasmussen, T. Snabe and L.H. Pedersen, "Numerical modelling of insulin and amyloglucosidase release from swelling Ca-alginate beads," Journal of Controlled Release, vol. 91, pp. 395–405, 2003.

[7] A. Nochos, D. Douroumis and N. Bouropoulos, "In vitro release of bovine serum albumin from alginate/HPMC hydrogel beads," Carbohydrate Polymer, vol. 74, pp. 451–457, 2008.

[8] N. Pekel, F. Yoshii, T. Kume and O. Güven, "Radiation crosslinking of biodegradable hydroxypropylmethylcellulose," Carbohydrate Polymer, vol. 55, pp. 139-147, 2004.

[9] A. Mujtabaa and K. Kohli, "In vitro/in vivo evaluation of HPMC/alginate based extended-release matrix tablets of cefpodoxime proxetil," International Journal of Biological Macromolecules, vol. 89, pp. 434–441, 2016.

[10] O.C. Okeke and J.S. Boateng, "Composite HPMC and sodium alginate based buccal formulations for nicotine replacement therapy," International Journal of Biological Macromolecules, vol. 91 pp. 31–44, 2016.

[11] S.K. Yadava, J.S. Patil, V.J. Mokale and J.B. Naik, "Sodium alginate/HPMC/liquid paraffin emulsified (o/w) gel beads,by factorial design approach; and in vitro analysis," Journal of Sol-Gel Science and Technology, vol.71, pp. 60–68, 2014.

[12] I. Armentano, M. Dottori, E. Fortunati, S. Mattioli and J.M. Kenny, "Biodegradable polymer matrix nanocomposites for tissue engineering: A review," Polymer Degradation and Stability, vol. 95, pp. 2126 -2146, 2010.

[13] Y-H. Yun, J-W. Yun, S-Do Yoon and H-S. Byun, “Physical properties and photocatalytic activity of chitosan-based nanocomposites added titanium oxide nanoparticles.,” Macromolecular Research, vol. 24, pp. 51-59, 2016.

[14] H.W. Kim, A.A. Abdala and C.W. Macosko, “Graphene/ Polymer nanocomposites,” Macromolecules, vol. 43, pp. 6515-6530, 2010.

[15] Z. Isik, Z. Bilici, S. Konen Adiguzel, H.C. Yatmaz and N. Dizge, “Entrapment of TiO_2 and ZnO powders in alginate beads: Photocatalytic and reuse efficiencies for dye solutions and toxicity effect for DNA damage,” Environmental Technology & Innovation, vol. 14, pp. 100358, 2019.

[16] M. Thomas, T.S. Natarajan, M.U.D. Sheikh, M. Bano and F. Khan, “Self-organized graphene oxide and TiO_2 nanoparticles incorporated alginate/ carboxymethyl cellulose nanocomposites with efficient photocatalytic activity under direct sunlight,” Journal of Photochemistry and Photobiology A: Chemistry, vol. 346, pp. 113-125, 2017.

[17] A.L.I. Olad, S. Behboudi and A. Entezami, “Preparation, characterization and photocatalytic activity of TiO_2/ polyaniline core-shell nanocomposite,” Bulletin of Materials Science, vol. 35, pp. 801–809, 2012.

[18] J. Bouclé, S. Chyla, M.S.P. Shaffer, J.R. Durrant, D.D.C. Bradley and J. Nelson, “Hybrid solar cells from a blend of poly(3-hexylthiophene) and ligand-capped TiO_2 nanorods,” Advanced Functional Materials, vol.18, pp. 622–633, 2008.

[19] S.S. Mano, K. Kanehira, S. Sonezaki and A. Taniguchi, “Effect of polyethylene glycol modification of TiO_2 nanoparticles on cytotoxicity and gene expressions in human cell lines,” International Journal of Molecular Sciences, vol. 13, pp. 3703–3717, 2012.

[20] S. Chaudhari, T. Shaikh and P. Pandey, “Review on polymer TiO_2 nanocomposites,” International Journal of Engineering Research and Applications, vol. 3, pp. 1386–1391, 2013.

[21] S. Mallakpour and A. Barati, “Optically active poly(amide-imide)/ TiO_2 bionanocomposites containing L-isoleucine amino acid moieties: synthesis, nanostructure and properties,” Polymer-Plastics Technology and Engineering, vol. 52, pp. 997–1006, 2013.

[22] H.M.C. Azeredo and K. W. Waldron, “Crosslinking in polysaccharide and protein films and coatings for food contact-A review. Trends in,” Food Science & Technology, vol. 52, pp.109-122, 2016.

[23] Y. Hu, S. Zhang, D. Han, Z. Ding, S. Zeng and X. Xiao, “Construction and evaluation of the hydroxypropyl methyl cellulose-sodium alginate composite hydrogel system for sustained drug release,” Journal of Polymer Research, vol. 25, pp.148, 2018.

[24] Z. Liu, J.Li, S. Nie, H. Liu, P. Ding and W. Pan, “Study of an alginate/HPMC-based in situ gelling ophthalmic delivery system for gatifloxacin,” International Journal of Pharmaceutics, vol. 315, pp. 12–17, 2006.

[25] A. Mujtaba, M. Ali and K. Kohli, “Statistical optimization and characterization ofpH-independent extended-release drug delivery ofcefpodoxime proxetil using Box–Behnken design”, Chemical Engineering Research and Design, vol. 92, pp. 156–165, 2014.

[26] X. Shao, H. Sun, R. Zhou, B. Zhao, J. Shi, R. Jiang and Y. Dong, “Effect of bovine bone collagen and nano-TiO_2 on the properties of hydroxypropyl methylcellulose films,” International Journal of Biological Macromolecules, vol. 158, pp. 937–944, 2020.

[27] P. Chen and X. Zhang, "Fabrication of Pt/TiO_2 Nanocomposites in Alginate and Their Applications to the Degradation of Phenol and Methylene Blue in Aqueous Solutions," Clean, vol. 36 no. (5–6), pp. 507 – 511, 2008.

[28] K. Mallikarjuna Reddy, M. Sairam, V. Ramesh Babu, M. C. S. Subha, K. Chowdoji Rao and T. M. Aminabhavi, "Sodium alginate-TiO_2 mixed matrix membranes for pervaporation dehydration of tetrahydrofuran and isopropanol," Designed Monomers and Polymers, vol. 10, no. 4, pp. 297–309, 2007.

[29] L.M. Pedro, G.D. Bloisi and D.F.S. Petri "Hydroxypropylmethyl cellulose films crosslinked with citric acid for control release of nicotine," Cellulose, vol. 22, pp. 3907–3918, 2015.

[30] F. Kurşun, "Grafting of itaconic acid on sodium alginate and use of graft copolymer in drug delivery systems", Kırıkkale University, Kırıkkale,Turkey, (2008).

[31] E. Kondolot Solak, "Preparation and characterization of IPN microspheres for controlled delivery of naproxen," Journal of Biomaterials and Nanobiotechnology, vol. 2, pp. 445-453, 2011.

[32] B. YerriSwamy, C. Venkata Prasad, C.L.N. Reedy, B. Mallikarjuna, K. Chowdoji Rao and M.C.S. Subha, "Interpenetrating polymer network microspheres of hydroxypropyl methyl cellulose/poly (vinyl alcohol) for control release of ciprofloxacin hydrochloride," Cellulose, vol. 18, pp. 349-357, 2011.

[33] C. Ding, M. Zhang and G. Li, "Preparation and characterization of collagen/hydroxypropyl methylcellulose (HPMC) blend film," Carbohydrate Polymer, vol. 119, pp. 194-201, 2015.

[34] S.T.M. Mruthyunjaya, B. Ramaraj and Siddaramaiah, "Thermal and morphological properties of SA/HPMC blends," Journal of Applied Polymer Science, vol. 112, pp. 2235–2240, 2009.

[35] S. Kondaveeti, T.C. Damato, A.M. Carmona-Ribeiro, M.R. Sierakowski and D.F.S. Petri, "Sustainable hydroxypropyl methylcellulose /xyloglucan/gentamicin films with antimicrobial properties," Carbohydrate Polymer, vol. 165, pp. 285-293, 2017.

[36] G.T. Padma, T. Subba Rao and B.N.K. Chandra, "Preparation, characterization and dielectric properties of sodium alginate/titanium dioxide composite membranes," SN Applied Sciences, vol. 1:75, 2019.

[37] Y. Tai, J. Qian, Y. Zhang and J. Huang, "Study of surface modification of nano-SiO_2 with macromolecular coupling agent," Chemical Engineering Journal, vol. 141, pp. 354-361, 2008.

[38] K. Tomihata and Y. Ikada, "Crosslinking of hyaluronin acid with water-soluble carbodiimide," Journal of Biomedical Materials Research; 37: 243-251, 1997.

SAKARYA ÜNİVERSİTESİ
FEN BİLİMLERİ ENSTİTÜSÜ
DERGİSİ

Sakarya University Journal of Science
SAUJS

e-ISSN 2147-835X Founded 1997 Period Bimonthly Publisher Sakarya University
http://www.saujs.sakarya.edu.tr/en/

Title: Reconfigurable and Resource Efficient Implementation of a Parallel FFT Core in FPGA

Authors: Dursun BARAN

Recieved: 2021-02-09 00:00:00

Accepted: 2021-11-02 00:00:00

Article Type: Research Article

Volume: 25
Issue: 6
Month: December
Year: 2021
Pages: 1386-1393

How to cite
Dursun BARAN; (2021), Reconfigurable and Resource Efficient Implementation of a Parallel FFT Core in FPGA. Sakarya University Journal of Science, 25(6), 1386-1393, DOI: https://doi.org/10.16984/saufenbilder.877453

Sakarya University Journal of Science 25(6), 1386-1393, 2021

Reconfigurable and Resource Efficient Implementation of a Parallel FFT Core in FPGA

Dursun BARAN*[1]

Abstract

Resource efficient implementation of a highly reconfigurable, parallel and pipelined FFT core that provides 1.2GS/s throughput rate with 24-bits wide input samples for the real-time spectrum analysis applications is developed and realized. Physical placement constraints are used to improve the timing performance of implemented design in FPGA. Some design techniques to reduce the memory complexities of design are also provided. Full implementation of the design is completed and implementation details are provided.

Keywords: Parallel FFT Core, Real Time Spectrum Analysis, Energy-Efficient Design, FPGA

1. INTRODUCTION

Real time spectrum analysis is a commonly used technique in electronic counter surveillance applications, RF testing and emission measurements. Conventional swept spectrums are failing to demonstrate the intermittent signals that are available very occasionally. Those kind of signals are very critical for the RF emission measurements, the radar signal detection, the signal classification and similar applications. RF emission measurements are also getting more complex and require higher bandwidths as new communication technologies are introduced such as 5G and beyond [1]. In order to support larger RF bandwidths, higher speed ADCs (*__A__nalog to __D__igital __C__onverter*) or parallel RF front ends are needed. The usage of parallel RF frontends becomes costlier and more complex as compared the usage of high speed ADCs. In addition, the sampling rates of current ADC devices already pass 5GSPS (*__G__iga __S__ample __P__er __S__econd*) that enables to digitize more than 2.5GHz bandwidth without any complex RF front ends. After high speed ADCs, backend digital processing blocks must be able to process all digitized samples.

In order to perform spectrum analysis, RF channel power measurements or FFT (*__F__ast __F__ourier __T__ransform*) techniques can be used. For real-time spectrum analysis applications, FFT technique is more suitable since it transforms the input samples from time domain to the frequency domain. Depending on the digital processing power, various FFT speeds, lengths and architectures can be successfully realized [15-16]. To perform FFT algorithm in digital processors efficiently, DFT (*__D__iscrete __F__ourier __T__ransform*) technique is widely used. The DFT for a frame size of N is defined as (where k = 0, 1, …, N-1)

---

* Corresponding author: barandursun@yahoo.com

[1] The Scientific and Technological Research Council of Turkey, Ankara, Turkey

ORCID: https://orcid.org/0000-0001-9277-3796

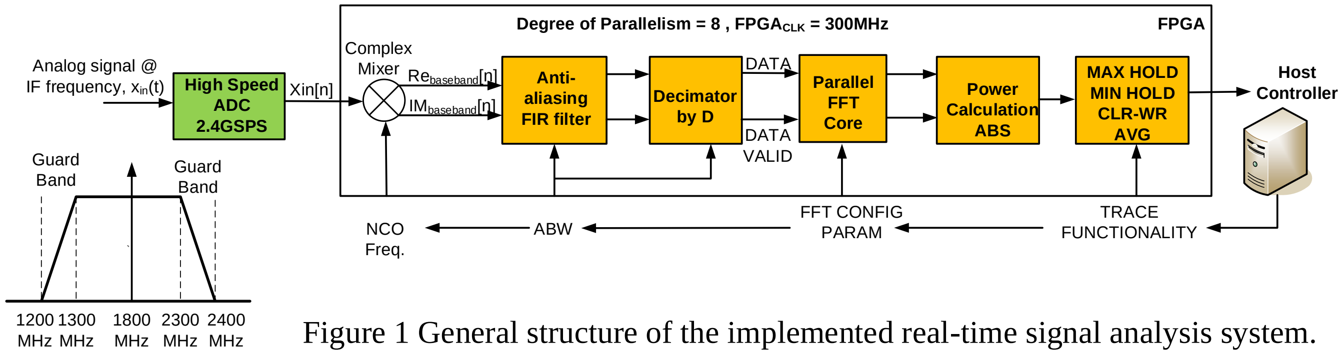

Figure 1 General structure of the implemented real-time signal analysis system.

$$X(k) = \sum_{n=0}^{N-1} x(n) * e^{-j2\pi kn/N} \qquad (1)$$

For custom applications, FPGA (***Field Programmable Gate Array***) is widely used computational environment since they are providing reprogrammable capability to developers with a reasonable cost and performance metrics. In terms of performance and power consumption, FPGA is worse than their corresponding ASIC realization. However, FPGA is able to provide more cost efficient implementation for prototype products since ASIC design requires a high budget for prototype design and tape-out cycles. Current FPGA devices provides lots of resources to designers that can be used to implement the real-time and parallel signal processing algorithms [8]. When a high speed ADC is used in front of FPGA device, FPGA internal clock cannot reach the same speed. This requires to implement a parallel and pipelined FFT core to realize real-time spectrum analysis [2-7] for high bandwidth applications.

In this paper, we provide the implementation details of a highly reconfigurable and resource efficient parallel FFT processing core to be used in spectrum monitoring applications. In addition to the developed parallel FFT core, a digital downconverter block, ADC interface and host controller connectivity circuits are also developed in HDL and realized in FPGA as well. The design detail of those auxiliary circuits will not be demonstrated in this work but they are used to realize the system. In Section II, the general structure of system is given. Section III provides design details of implemented parallel FFT core. Design optimization techniques are detailed in Section IV. Implementation results are given in Section V and Section VI concludes the work.

2. ARCHITECTURE OF THE REAL-TIME SPECTRUM ANALYSIS SYSTEM

The general structure of the implemented real-time signal analysis system for wideband applications is given in Figure 1. Firstly, the analog/RF signal is sampled by using and an ADC that has 2.4GSPS sampling rate that can provide 1.2GHz analysis bandwidth to the overall system if the digital processing hardware is able to support such a speed. Unfortunately, it is not possible to clock any commercially available FPGA device with a 2.4GHz signal. Parallel hardware design technique is used to reduce the FPGA clock requirement to support such demanding applications. The degree of parallelism is selected to be 8 in this design to make FPGA clock is feasible and the FPGA clock becomes 300MHz in this case that is easily supported by the current FPGA ICs.

Sampled signal is moved to the baseband using 8 complex mixers within FPGA. The required NCO (***N****umerically* ***C****ontrolled* ***O****scillator*) signal is generated within FPGA and the NCO frequency is controlled by the host controller to support direct digitization path as well. After complex mixing stages, the signal is fed to anti-aliasing filter stage that is implemented using FIR (***F****inite* ***I****mpulse* ***R****esponse*) filters in FPGA. After this filtering stage, the signal is moved to decimator stage to reduce the signal analysis bandwidth. The degree of decimation D is provided through the host controller as well. After decimation stage, the signal is fed to a parallel FFT core to measure the signal power at each frequency bin index. The bandwidth of each frequency bin is calculated as

$$BW_{FFT-BIN} = \frac{ABW}{N_{FFT}} \qquad (2)$$

where ABW is analysis bandwidth, N_{FFT} is the number of FFT point and $BW_{FFT-BIN}$ is the bandwidth of each FFT-BIN.

After implementing the parallel FFT core, the signal powers at each bin is calculated using an absolute value calculation block. The absolute value calculation simply implemented using two multipliers, an adder and a square root operation. The final stage of the real-time spectrum analysis system is to calculate the max-hold/min-hold/clr-wr/avg trace functions in real time as shown in Figure 1. The block should be able to process all samples without any data loss to provide the real-time spectrum analysis feature. When a new data transfer is requested from the host controller, this block must be able to continue to calculate the trace functionality while transferring data. The data transfer to host PC is implemented using a DMA (**D**irect **M**emory **A**ccess) connectivity to support raw data transfer. The output of parallel FFT core data does not require very high bandwidth connectivity when some trace functionality is selected instead of the raw data transfer.

As seen from Figure 1, the system is highly reconfigurable in terms of the NCO frequency, the analysis bandwidth (ABW), the FFT configuration parameters and the trace functionality. Depending on the ABW configuration, DATA and DATA VALID signal characteristics are changed and FFT core must be able to handle those changes. The summary of design specifications for the spectrum analysis system is given in Table 1. The maximum analysis bandwidth is 1.2GHz and user will use 1GHz bandwidth out of it. 100MHz guard bands (1200MHz to 1300MHz and 2300MHz to 2400MHz) are defined at the left and the right side of IF frequency bands to prevent any signal aliasing may occur between Nyquist bands as shown in Figure 1.

Table 1 Real-Time Spectrum Analysis System Design Specifications

Technical Specifications	Value
ADC Sampling Rate	2.4GHz
SFDR	73dBc (typical)
SNR	58.5dB (typical)
FPGA Clock Frequency	300MHz
ABW	1.2GHz ~ 1MHz
IF Frequency	1800MHz
Sampled IF Bandwidth	1.2GHz - 2.4GHz
Trace Functionalities	MAX-HOLD, MIN-HOLD, AVG, CLR-WR
FFT Core Point	32k - 16
FFT Windowing	Supported
*Spectrum Sweep Speed	73.24THz/Sec

* 32K FFT size and IF bandwidth is 1.2GHz

3. PARALLEL FFT PROCESSING CORE

Four consecutive baseband real and complex data samples are packed into a DATA register and a DATA VALID signal conveys the valid trigger to load data into FFT core. The timing waveform of DATA_VALID signal is shown in Figure 2 for various ABW values. DATA register is 192-bits wide and includes 4 real and 4 imaginary parts of the sampled data as given in Figure 3. DATA_VALID signal depends on the analysis bandwidth and the worst case scenario happens when the analysis bandwidth is set to 1200MHz as shown in Figure 2, DATA and DATA_VALID signals are synchronous with respect to the FPGA_CLK.

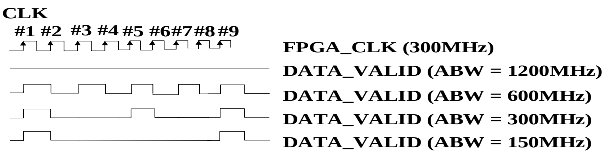

Figure 2 Timing waveform of DATA_VALID signal with respect to FPGA Clock.

DATA [191:168]	DATA [167:144]	DATA [143:120]	DATA [119:96]	DATA [95:72]	DATA [71:48]	DATA [47:24]	DATA [23:0]
IM[n-3]	RE[n-3]	IM[n-2]	RE[n-2]	IM[n-1]	RE[n-1]	IM[n]	RE[n]

Figure 3 Content of DATA register to be processed by parallel FFT core.

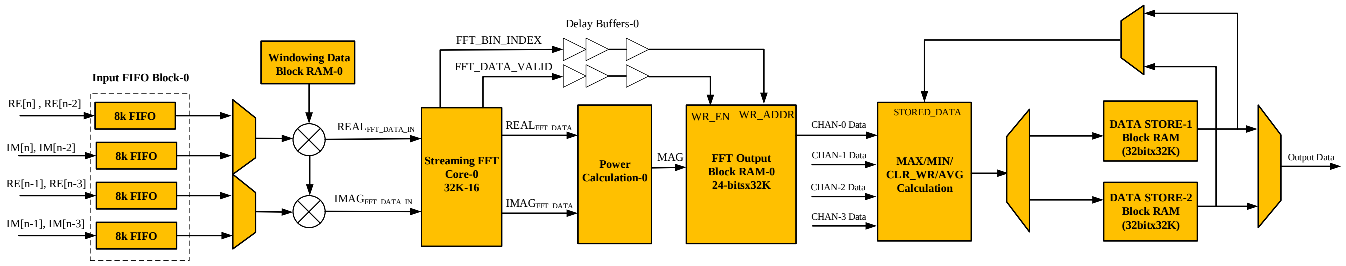

Figure 4 The block diagram of implemented parallel FFT core (one channel out of four is demonstrated)

Parallel FFT core must handle to calculate DFT of incoming data samples without any loss. When the analysis bandwidth is set to 1200MHz, the parallel FFT core must be able to process all sampled data. This requires 4 FFT cores each running at 300MHz FPGA clock. In addition to FFT cores, some memory hardware is required to temporarily store the incoming data. In order to minimize FPGA resource utilization, minimum number of memory should be used. The block diagram for a channel of implemented parallel FFT core is given in Figure 4.

Incoming data is first stored to 8k FIFO (***F****irst* ***I****n* ***F****irst* ***O****ut*) blocks with 24 bits wide. When there is some amount of data available in FIFO, they are moved to FFT cores by the help of empty signal triggers generated from the FIFO blocks. 4 FIFO memory blocks are used for each FFT channel to support 2 Real and 2 Imaginary data samples. When analysis bandwidth is set to 1200MHz, 4 Real and 4 Imaginary data come at each clock cycle that necessitates 8 FIFO memory blocks if they are clocked with the FPGA clock itself. As seen from Figure 4, the need for memory is high in this design and it is important to reduce the amount of memory usage. So, input FIFO is clocked with 2xFPGA_CLK to capture 4 Real and 4 Imaginary data at each FPGA clock when the analysis bandwidth is set to 1200MHz. For other analysis bandwidths, there is no need to clock input FIFO blocks with 2xFPGA_CLK. In those cases, input FIFO clock is derived with FPGA_CLK itself. The clocking scheme of input FIFO block is shown in Figure 5. By using this clocking scheme, 4*8K*24-bits wide memory resources will be saved at expense of a clock multiplier and a BUFG-CTRL that is a controlled clock buffer driver from Xilinx FPGA family [9].

There are various kinds of windowing functions such as Hanning, Blackman Harris and similar coefficient sets that can be applied to DFT calculations [10]. It is very memory consuming to store all windowing coefficients into FPGA memory, therefore a single block RAM is reserved for windowing coefficient set that can be written from host controller to load windowing coefficients before the start of FFT core. The data comes from input FIFO and windowing coefficient RAMs are multiplied before entering FFT blocks. In the system, four block RAMs are reserved for windowing coefficients to support the four parallel cores.

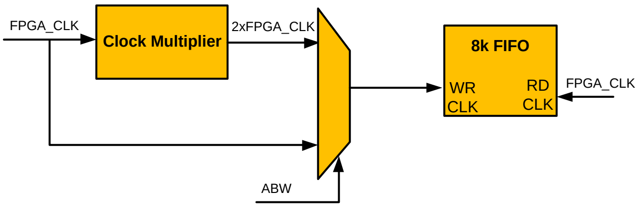

Figure 5 Clocking scheme of input FIFO memory blocks.

A reconfigurable FFT core is used to calculate DFT function as shown in Figure 4 [11]. The outputs of FFT core is provided to power calculation block to convert the complex output of FFT block to signal power amplitude. FFT bin index is used to generate write address of the FFT output block RAM. FFT_DATA_VALID signal is used to generate write enable signal of FFT Output Block RAM as shown in Figure 4.

In order to compensate the delay of power calculation block, delay buffers are added to FFT_BIN_INDEX and FFT_DATA_VALID signals. The amount of delay depends on the implementation of power calculation block. 4

parallel FFT cores are able to fill the FFT Output Block RAMs depending on the FFT configuration register provided from the host controller. If only one channel is sufficient, the rest of channels will be disabled. In order to support 1.2GHz analysis bandwidth case, 4 channel of FFT cores are required. For lower analysis bandwidth cases, the unused FFT channels are reserved for overlapping purpose. The supported overlap percentages for selected analysis bandwidth is provided in Table 2.

Table 2 Supported Overlap Percentages

Analysis Bandwidth	Supported Overlap Percentage
1200MHz	0%
600MHz	0%, 50%
300MHz	0%, 25%, 50%, 75%
Lower Bandwidths	0%, 25%, 50%, 75%

Power calculation block calculates the mathematical operation given in eq. 3. Square root operation is applied to reduce the bit widths of FFT Output Block RAMs. It is an important optimization since this design has a serious bottleneck about the memory resources.

$$\begin{aligned} MAG = SQRT(&REAL_{FFT\_DATA} * REAL_{FFT\_DATA} \\ &+ IMAG_{FFT\_DATA} * IMAG_{FFT\_DATA}) \end{aligned} \quad (3)$$

CHAN-0 Data is the output data from FFT Output Block RAMs that is the magnitude of FFT output data for channel-0 as shown in Figure 4. There will be CHAN-1 Data, CHAN-2 Data and CHAN-3 Data depending on the activated FFT channels. MAX/MIN/CLR_WR/AVG block calculates the trace function selected by the host controller. As name implies, MAX holds the maximal values of data at each FFT_BIN_INDEX and MIN holds the minimal values. CLR_WR function update the content of DATA_STORE block rams with the recent output of FFT cores. AVG function accumulates the values in DATA_STORE rams for a given number of averages. Division operation is completed in host controller side since the division operation is quite costly when implemented in FPGA. Two block RAMs are used to store final output data to prevent any data loss when the data is requested by the host controller. One RAM block stores the current FFT data and other RAM block transfers the stored data to the host controller. Whenever a data read request is generated from the host controller, DATA_STORE ram is switched. One RAM block is cleared and then start to store the new incoming data values. The data in other RAM block will be sent to the host controller.

4. DESIGN OPTIMIZATIONS AND TIMING ENCLOSURE TECHNIQUES

This design requires to use large memory blocks to support 32K FFT size and the real-time analysis features. However, the available memory resources are limited in FPGA [8]. Therefore, the memory usage must be reduced as much as possible to realize the design. There are two resource optimization techniques are applied to design. First one is to drive the clock of input FIFO with 2xFPGA_CLK to write the incoming data for 1.2GHz ABW case. Also, the system starts to operate whenever any data is stored in input FIFO to reduce the size of input FIFO memory as well. This will reduce the FIFO depth to 8K instead of 32K. All RAM memory blocks are implemented using FPGA internal RAM resources.

In order to improve the timing enclosure of the design, physical placement constraints are used. All block RAMs, DSP units and other configurable logic blocks are constrained to fit the specified region of FPGA to get better performance values. In order to implement large block RAMs, synthesizer will use multiple small block RAMs to realize it. As an example, Xilinx Virtex-7 series has internal 18Kb and 36Kb block RAMs to implement larger RAM blocks [8]. Small block RAMs are placed in predetermined regions horizontally or vertically. Therefore, constraining synthesizer to use small block RAMs within the specified regions improve the timing and the implementation time results considerably. Similarly, the FFT cores, the complex multipliers and the power calculation blocks are constrained to be placed to a predetermined region within the target FPGA.

5. RESULTS

The parallel FFT core given in Figure 4 and preceding digital down converter stages are implemented in Xilinx Virtex-7 VX690T model FPGA using HDL. ADC12D800RF model analog to digital converter is used to realize the full system [13]. Target FPGA_CLK period is set to 3.33ns to satisfy 300MHz in Xilinx PlanAhead design environment [14]. Four FFT core blocks are constrained with the physical placement constraints and the final placement result is demonstrated in Figure 6. As shown in this figure, all large RAM blocks are constrained to be placed to nearby small block RAMs. In addition to RAM blocks, four FFT and corresponding power calculation blocks are constrained to place some predefined regions within the FPGA architecture. By using this design technique, the placer successfully meets the timing closures for the complete design. In addition, the buffering technique is commonly used to improve the timing performance of the design similar to ASIC (*Application Specific Integrated Circuit*) counterparts [12]. After determining the failing paths, extra buffers are added to meet the timing constraints. In order to determine the failing paths, the static timing analyzer of Plan Ahead tool is used.

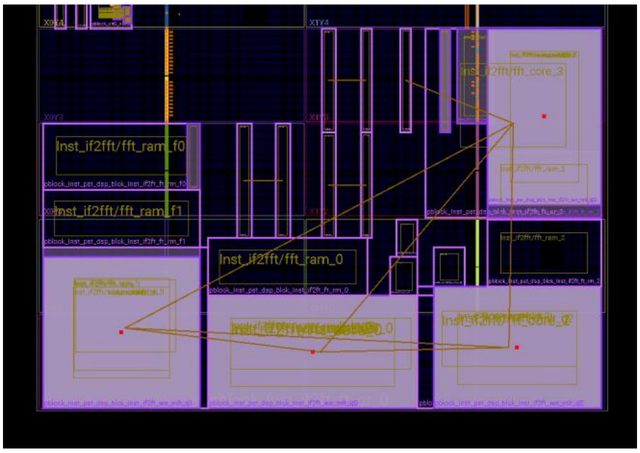

Figure 6 FPGA layout after place and route cycle.

FPGA design steps are followed to generate the final programming file. The resource utilization of parallel FFT core within FPGA is given in Table 3. By placing the FFT cores to specified region of FPGA, routing complexity of the design will be reduced in addition to the timing improvements.

Table 3 Resource utilization of the parallel FFT core

FPGA Resource	Utilization
SLICEL	6839
SLICEM	6119
DSP48E1	508
RAMBFIFO36E1	282
RAMBFIFO18E1	412
BUFGCTRL	1
MMCM (Mixed-Mode Clock Manager)	1

The digitizer board [13] is placed in a PC hardware with a suitable graphic card, a processor and a RAM. The system is connected a HD monitor over HDMI connector. The system is connected to a signal generator using a SMA cable and signal frequency is set to a value within the IF frequency bandwidth. An application program is developed for the parallel FFT core to demonstrate the performance of the system. An example graphic from the developed application is shown in Figure 7.

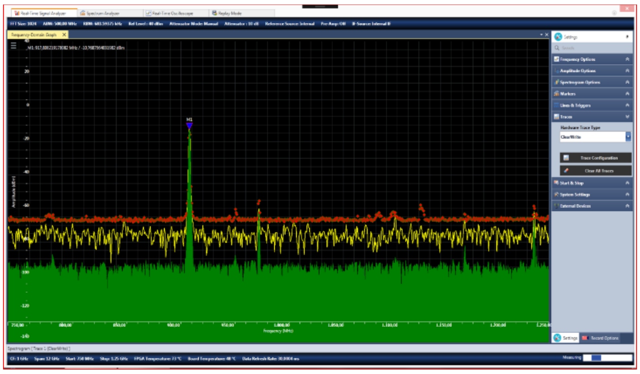

Figure 7 A graphical user interface (GUI) example for the developed FFT core. Each color shows different traces namely max-hold, min-hold, clr/wr and avg.

6. CONCLUSION

A highly reconfigurable and resource efficient implementation of a parallelized FFT core design is demonstrated in this work. The implemented four parallel FFT cores are able to operate simultaneously with 300MHz FPGA clock that provides 1.2GS/s throughput. Various optimization techniques used to reduce the FPGA memory usage and improve the timing enclosure. By using physical placement constraints, the timing performance of the design is improved. The proposed design is implemented in a 7 Series Xilinx FPGA and the final programming file is generated. FPGA is programmed with the generated file to demonstrate successful operation of the developed parallel FFT core. In future, custom coded FFT cores may be developed to improve the performance of the parallel FFT core furthers in terms of speed and RF specifications.

Acknowledgments

Many thanks to Enes Karav and my colleagues in Sensor and Antenna Systems department for their invaluable technical discussions.

Funding

This work is supported by informatics and information and security research center (*BILGEM*).

The Declaration of Conflict of Interest/ Common Interest

“No conflict of interest or common interest has been declared by the authors. ”

Authors' Contribution

The first and only author contributed 100% to this study.

The Declaration of Ethics Committee Approval

“This study does not require ethics committee permission or any special permission.”

The Declaration of Research and Publication Ethics

“The authors of the paper declare that they comply with the scientific, ethical and quotation rules of SAUJS in all processes of the paper and that they do not make any falsification on the data collected. In addition, they declare that Sakarya University Journal of Science and its editorial board have no responsibility for any ethical violations that may be encountered, and that this study has not been evaluated in any academic publication environment other than Sakarya University Journal of Science.”

REFERENCES

[1] C. Fager, T. Eriksson, F. Barradas, K. Hausmair, T. Cunha and J. C. Pedro, "Linearity and Efficiency in 5G Transmitters: New Techniques for Analyzing Efficiency, Linearity, and Linearization in a 5G Active Antenna Transmitter Context," in *IEEE Microwave Magazine*, vol. 20, no. 5, pp. 35-49, May 2019.

[2] C. Eddington, B. Ray, “Using parallel FFT for multi-gigahertz FPGA signal processing”, EE Times Magazine, https://www.eetimes.com/using-parallel-fft-for-multi-gigahertz-fpga-signal-processing/

[3] X. Zou, Y. Liu, Y. Zhang, P. Liu, F. Li and Y. Wu, "FPGA Implementation of Full Parallel and Pipelined FFT," 2012 8th International Conference on Wireless Communications, Networking and Mobile Computing, Shanghai, 2012, pp. 1-4.

[4] H. Kanders, T. Mellqvist, M. Garrido, K. Palmkvist and O. Gustafsson, "A 1 Million-Point FFT on a Single FPGA," in IEEE Transactions on Circuits and Systems I: Regular Papers, vol. 66, no. 10, pp. 3863-3873, Oct. 2019

[5] M. Dreschmann et al., "Implementation of an ultra-high speed 256-point FFT for Xilinx Virtex-6 devices," 2011 9th IEEE International Conference on Industrial Informatics, Caparica, Lisbon, 2011, pp. 829-834.

[6] Shousheng He; Torkelson, M.; “ *A new approach to pipeline FFT processor* ,” Parallel Processing Symposium, 1996, Proceedings of IPPS ’96, The 10th International, April 1996.

[7] V. Iglesias, J. Grajal, M. A. Sánchez and M. López-Vallejo, "Implementation of a Real-

Time Spectrum Analyzer on FPGA Platforms," in IEEE Transactions on Instrumentation and Measurement, vol. 64, no. 2, pp. 338-355, Feb. 2015.

[8] https://www.xilinx.com/products/silicon-devices/fpga.html

[9] https://www.xilinx.com/support/documentation/user_guides/ug472_7Series_Clocking.pdf

[10] S. Rapuano and F. J. Harris, "An introduction to FFT and time domain windows," in *IEEE Instrumentation & Measurement Magazine*, vol. 10, no. 6, pp. 32-44, December 2007.

[11] https://www.xilinx.com/support/documentation/ip_documentation/xfft/v9_1/pg109-xfft.pdf

[12] B. R. Zeydel, D. Baran and V. G. Oklobdzija, "Energy-Efficient Design Methodologies: High-Performance VLSI Adders," in *IEEE Journal of Solid-State Circuits*, vol. 45, no. 6, pp. 1220-1233, June 2010.

[13] https://www.pentek.com/products/detail.cfm?model=78741

[14] https://www.xilinx.com/products/design-tools/planahead.html

[15] Palmer J., Nelson B. (2004) A Parallel FFT Architecture for FPGAs. In: Becker J., Platzner M., Vernalde S. (eds) Field Programmable Logic and Application. FPL 2004. Lecture Notes in Computer Science, vol 3203. Springer, Berlin,

[16] K. Nguyen, J. Zheng, Y. He and B. Shah, "A high-throughput, adaptive FFT architecture for FPGA-based space-borne data processors," 2010 NASA/ESA Conference on Adaptive Hardware and Systems, 2010, pp. 121-126

SAKARYA ÜNİVERSİTESİ

FEN BİLİMLERİ ENSTİTÜSÜ DERGİSİ

Sakarya University Journal of Science
SAUJS

e-ISSN 2147-835X Founded 1997 Period Bimonthly Publisher Sakarya University
http://www.saujs.sakarya.edu.tr/en/

Title: A Multi-task Deep Learning System for Face Detection and Age Group Classification for Masked Faces

Authors: Gozde YOLCU ÖZTEL, İsmail ÖZTEL

Recieved: 2021-08-12 00:00:00

Accepted: 2021-11-03 00:00:00

Article Type: Research Article

Volume: 25
Issue: 6
Month: December
Year: 2021
Pages: 1394-1407

How to cite
Gozde YOLCU ÖZTEL, İsmail ÖZTEL; (2021), A Multi-task Deep Learning System for Face Detection and Age Group Classification for Masked Faces. Sakarya University Journal of Science, 25(6), 1394-1407, DOI: https://doi.org/10.16984/saufenbilder.981927
Access link
http://www.saujs.sakarya.edu.tr/tr/pub/issue/66341/981927

Sakarya University Journal of Science 25(6), 1394-1407, 2021

A Multi-task Deep Learning System for Face Detection and Age Group Classification for Masked Faces

Gozde YOLCU ÖZTEL*[1], İsmail ÖZTEL[2]

Abstract

COVID-19 is an ongoing pandemic, and according to experts, using a face mask can reduce the spread of the disease. On the other hand, masks cause occlusion in faces and can create safety problems such as the recognition of the face and the estimation of its age. To prevent the spread of COVID-19, some countries have restrictions according to age groups. Also, in different countries, people in some age groups have safety restrictions such as driving and consuming alcohol, etc. But these rules are difficult to follow due to occlusion in faces. Automated systems can assist in monitoring these rules. In this study, a deep learning-based automated multi-task face detection and age group classification system is proposed for masked faces. The system first detects masked/no-masked-faces. Then, it classifies them according to age-groups. It works for multi-person regardless of indoor/outdoor environment. The system achieved 92.0% average precision score for masked face detection using YOLO with resnet50 network. Also, 83.87% accuracy for classifying age groups with masked faces and 84.48% accuracy for no-masked faces using densenet201 network have been observed. It produced better results compared to the literature. The results are significant because they show that a reliable age classification for masked faces is possible.

Keywords: age classification, computer vision, COVID-19, deep learning, pretrained networks

1. INTRODUCTION

The Novel Coronavirus Disease (COVID-19) is a worldwide emergency because of its rapid spread and the high death rate. Unfortunately, specific medications are not yet available. Despite some new vaccines, most scientists predict that COVID-19 vaccines will not be 100% effective like most other vaccines [1]. Many studies have been presented to assist the diagnosis of disease. In [2]–[5], the authors have studied on classifying of COVID-19 in chest X-ray images. Also, some studies [6], [7] worked on automatic COVID-19 lung infected region segmentation.

WHO reported that social distancing measures and wearing medical face mask help to slow the spread of disease. In many countries, wearing a medical face mask is obligatory. To prevent the spread of COVID-19, restrictions according to age groups are applied in some countries. For example, according to the restrictions applied in

---

* Corresponding author: gyolcu@sakarya.edu.tr

[1] Sakarya University, Faculty of Computer and Information Sciences, Software Engineering Department
ORCID: https://orcid.org/0000-0002-7841-2131

[2] Sakarya University, Faculty of Computer and Information Sciences, Computer Engineering Department
E-mail: ioztel@sakarya.edu.tr
ORCID: https://orcid.org/0000-0001-5157-7035

the past in Turkey, people over the age of 65 were only allowed to go out between 10:00 and 13:00. Similarly, people under the age of 20 were allowed to go out between 13:00 and 16:00. Also, public transportation was prohibited for these two age groups. Thus, to monitor whether compliance with these rules, there was a need to detect the age group of people wearing masks.

In addition, estimating the age groups of people wearing masks is also important for safety. For example, according to different countries, people in some age groups have restrictions such as driving, consuming alcohol, etc. After the pandemic, age has become hidden due to the mask, and it has become hard to check whether these rules are being followed.

It is quite difficult for the human observer to predict the age groups of masked people. An assistance system can make this observation easier. Thus, there is a need to develop non-invasive, quantitative, and objective automated systems for determining age groups.

This study proposes a deep learning-based multi-task system for face detection and age-group classification using masked face. It classifies human faces into 3 age groups which are teenager (12-20), middle (21-64), and elder (65+). The system can work for multi-person regardless of indoor/outdoor environment. The proposed system is useful for tracking restrictions according to age groups to prevent the spread of coronavirus disease. This tool also can be used for automated age determination of masked people for security purposes. Moreover, it can be an assistant system for suggesting videos/products according to the target age group. The main contributions of this study can be summarized as:

(1) Although the face masks cover the wrinkles in the mouth and cheeks, which play an important role in age determination, such a system that gives promising results has been developed.

(2) Reduced computational cost with fewer face attributes, making the approach advantageous for real-time or resource-limited systems.

The rest of the paper has been organized as follows: Section 2 has the information of related works for age classification. Section 3 includes preparation of the masked images dataset approach, detection and classification methods. Experimental results have been given in Section 4. Finally, the paper has been concluded in Section 5.

2. RELATED WORKS

Recently, many studies have been presented to help reduce the spread of COVID-19 or to assist the diagnosis of disease. In [8]–[10], tools were presented for automated mask detection on human faces. In [11]–[13], the researchers presented tools for automated social distance and mask detection. In [14], the authors presented a formally verified authentication protocol in secure framework for mobile healthcare during the COVID-19-like pandemic. In [15], the authors proposed a masked face recognition system.

This study proposes an assistance system for reducing the spread of COVID-19 using computer vision methods. Owing to computer vision technologies, dealing with many troublesome problems in daily life has become more effortless with automated systems [16]–[25]. The aging process on human facial appearances is affected by many factors such as health, weather, living environment, gender, race, etc. Thus, determining the age of a person may be difficult for an expert, and automated systems can be helpful for this task. Age group classification is one of the challenging tasks of computer vision due to changes in position and orientation, lighting conditions, image resolution, etc. [26].

Over the years, many age classification studies have been presented for different purposes. In the study of [27], the authors used age and gender classification for effective marketing analysis. Also, in [28], the authors used age classification for risk stratification in glioma patients. In [29], an age classification system was used for detecting illicit activity in suspicious sites.

Age group classification was first applied in [30]. In their study, authors classified images into three age groups which are babies, young adults, and senior adults. In the study, six ratios of distances between primary components (e.g., eyes, noses, mouth, etc.) and wrinkles on specific areas of a face were used.

In [31], Sobel edge operator and region labeling were used to locate the positions of eyes, noses, and mouths. Then, geometric and wrinkle features were extracted. Finally, the features were classified using two back-propagation neural networks. In [32], geometric features were extracted from faces and fused the results using five different classifiers. In [33], the authors used local binary patterns (LBP) and the k-nearest neighbor classifiers for the age group classification system. In [34], authors computed the geometric components of facial images; like wrinkle topography, face edge, left eye to right eye separation, eye to nose separation, eye to jaw separation, and eye to lip separation. Then K-means algorithm was used for the classification.

Different from the above studies, age group classification from masked faces due to COVID-19 is the motivation of this study. Because most of the important facial attributes, such as wrinkles on cheeks, nose, etc., are not visible due to the face mask; estimating the age group of people with facial masks becomes more difficult.

On the other hand, Haar Cascade can be another choice for mask detection. In the literature, some studies compare the Haar Cascade and deep learning networks. According to [35], CNN outperforms cascade classifiers in plenty of cases. Generally, Haar Cascade is fast because it uses fewer features. But detection rate is better in a deep learning model because the deep learning system uses many other features [35]. Usage of the Haar Cascade or deep learning model has advantages and disadvantages. A choice can be made based on the current requirements. In this study, deep learning models were preferred.

3. METHODOLOGY

3.1. Preprocessing

Unfortunately, there aren't any age datasets with masked faces. Thus, UTKFace Large Scale Face Dataset [36] images were preprocessed to be placed a medical face mask on each face image. Before placing the mask on the face, the width of the mask was resized to be the *x* distance between the two ears and the length of the mask to be the *y* distance between the nose and the chin. With this step, the system has been made flexible for each face size. Figure 1 shows these distances.

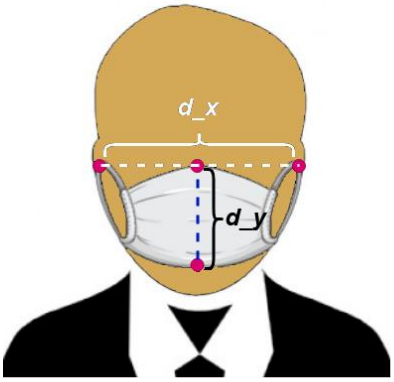

Figure 1 Distances used for mask placed on the face

In order to place the mask on the face with a transparent background, alpha-channel information of the mask image is used. Alpha channel has 0 values in regions associated with the transparent background.

To combine the transparent background mask image with a facial image, firstly, the transposition of the alpha channel (a in Figure 2) of the mask image is multiplied by the corresponding region on the face. The resulting image is then added to the multiplexing of the mask image (b) with its alpha channel (c). Thus, the composite image picks colors from the image when the alpha channel is 1 and picks colors from the facial region when the alpha channel is 0. Eq. 1 defines these processes. Also, these processes are illustrated in Figure 2.

$$C = alpha_m^T * fr + m * alpha_m \tag{1}$$

where C is composite image, $alpha_m$ is alpha channel of the mask image, fr is facial region which is adding the mask, m is the mask image and T represents the transpose process.

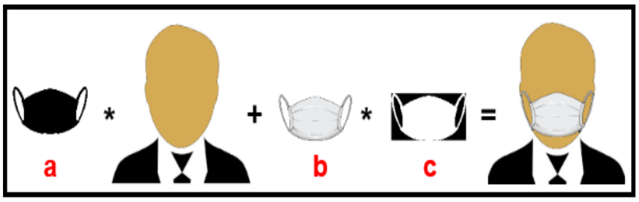

Figure 2 Combining the transparent background mask image with a facial image. a is the transposition of the alpha channel, b is the mask image, and c is the alpha channel of the mask image

3.2. Proposed System

The system pipeline of the proposed age group classification system for masked faces is illustrated in Figure 3. As can be seen in Figure 3, the system first detects faces. For this purpose, a Faster R-CNN and a YOLO detector have been tried, and the YOLO outperformed the Faster R-CNN. After the detection step in real-time, a classification network classifies the cropped faces as masked vs. no masked using the YOLO model.

3.3. Masked Face Detection using Faster R-CNN

The Faster R-CNN [37] architecture contains a pretrained network as a feature extractor and two subnets [37]. For pretrained network, Resnet-50 has been used. The task of the first subnet is to inform the second network of where the object will be searched. The first subnet is a fully convolutional network. It takes an image and outputs rectangular object proposals for that image. Every object proposals have objectness scores. The task of the second subnet is the prediction of the real class labels for object proposals.

For the masked face detection task, the maximum possible proposal number is determined as 3 empirically. That means 3 reference boxes, which are named anchor. Therefore, for all coordinates of 3 boxes, the classification layer outputs 6 score values for each proposal for the probability of object or not object. The loss function of the Faster R-CNN is defined in Eq. 2 [37].

$$L(\{p_i\},\{t_i\}) = \frac{1}{N_{cls}}\sum_i L_{cls}(p_i,p_i^*) + \lambda\frac{1}{N_{reg}}\sum_i p_i^* L_{reg}(t_i,t_i^*) \tag{2}$$

where i is the number of anchor, p_i is anchor's predicted probability, p_i^* is 1 or 0 based on the situation if the anchor is positive or negative, respectively. t_i shows the coordinates of predicted bounding box. t_i^* shows the ground-truth box. L_{cls} represents the classification loss. $L_{reg}(t_i,t_i^*)$ represents the regression loss. The loss of regression can be active with just positive anchors, and this is performed using $p_i^* L_{reg}$ in the equation. N_{cls} and N_{reg} are performed to normalize the two term in the equation using a balancing parameter λ.

3.4. Masked Face Detection using YOLO

The You Only Look Once (YOLO) is an object detection algorithm. It uses a single stage CNN for detection. An object detector decodes the predictions and produces some bounding boxes [38], [39].

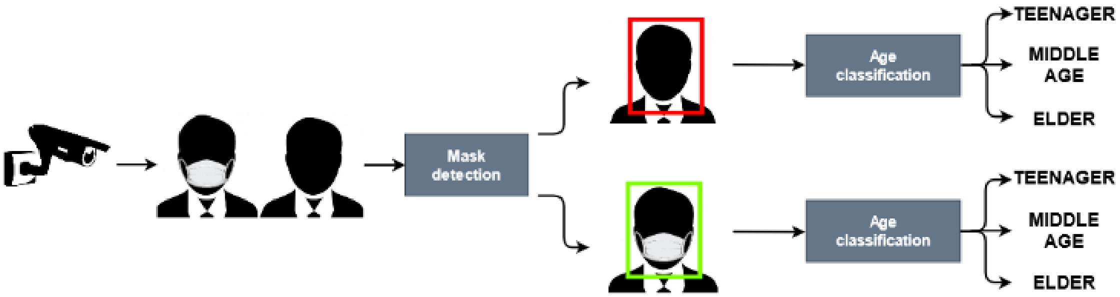

Figure 3 Proposed system pipeline

The anchor boxes are used to detect the object classes. For each anchor box; IoU, anchor box offsets, class probability attributes are predicted. IoU defines the objectness score of the anchor boxes. The anchor box offsets define anchor box position. Class probability defines the class label of each anchor box.

YOLO works on raw images. The input images are divided into grids. Each grid tries to find out if the object is in the field. So, a separate prediction vector is created for each grid. In this study, different feature extractor networks have been used for YOLO, and ResNet showed the best performance.

3.5. Age Group Classification using Deep Transfer Learning

After obtaining masked and no-masked faces from the first stage, the second task is classifying these faces according to age group. For this purpose, a Deep Convolutional Neural Network (DCNN) based approach is used. DCNN is one of the classes of deep neural network approaches used for computer vision problems [40]. It shows outstanding performance in different tasks [41]–[43].

In DCNN, information is transmitted through the layers, with the input of each layer being the output of the next layer. Learning is applied with the backpropagation [44] and stochastic gradient descent [40]. DCNN provides automated learning of discriminant features for a specific task. For the training process, data usually annotated by experts is used [45].

DCNNs are structured with different combinations of convolutions, pooling, dropout, and fully connected layers. In convolution layers, the input is convolved with the learned filters. The filters capture image features. Eq.3 shows the mathematical definition of the convolution process [40].

$$\begin{aligned} S(i,j) &= (I * K)(i,j) \\ &= \textstyle\sum_m \sum_n I(i+m, j+n) K(m,n) \end{aligned} \tag{3}$$

where I is an input image, K is a filter, S is the output after the convolution process and i,j,m,n are the index values.

In pooling layers, inputs are subsampled for reducing the spatial size. Thus, the number of parameters is reduced, and overfitting is controlled. In fully connected layers, classification or regression are performed using the collected features from previous layers. Softmax layer determines which class it belongs to using the values obtained from the fully connected layer. The mathematical equation of the softmax function is given in Eq.4 [40].

$$softmax(x)_i = \frac{\exp(x_i)}{\sum_{j=1}^{n} \exp(x_j)} \tag{4}$$

where x is the output of the fully connected layer, i is the number of samples, and j is the number of the classes.

In dropout layers, input elements are randomly set to zero with a given probability. This is used for preventing overfitting.

Transfer learning allows the parameters of a network learned for a task to be reused as the starting point for another task [46]. Owing to the transfer learning, the performances of various machine learning tasks are improved [47]. In the proposed system, in order to take advantage of transfer learning, pre-trained networks developed for object detection task has been used. To apply these networks in the proposed study, just the fully connected and classification layers of the pretrained network have changed with new ones. The rest of the pretrained network has not been changed. To adapt the networks to the age group classification, the networks are retrained with facial age images. The properties of pretrained networks which are used in this study are given in Table 1.

Table 1 Properties of pretrained networks used for age group classification

Network	**Depth**	**Parameters** $(x10^6)$	**Image input size**	**Size (MB)**
alexnet [48]	8	61.0	227*227	227
vgg16 [49]	16	138	224*224	515
vgg19 [49]	19	144	224*224	535
squeezenet [50]	18	1.24	227*227	5.2
googlenet [51]	22	7	224*224	27
inceptionv3 [52]	48	23.9	299*299	89
densenet201 [53]	201	20	224*224	77
mobilenetv2 [54]	53	3.5	224*224	13
resnet-101 [55]	101	44.6	224*224	167
xception [56]	71	22.9	299*299	85
shufflenet [57]	50	1.4	224*224	5.4
darknet53 [38]	53	41.6	256*256	155

4. EXPERIMENTAL RESULTS

4.1. Datasets

In this study, two different databases were used for two different tasks. For the age group classification stage, UTKFace Large Scale Face Dataset was used. It has the age labels for no-masked human faces. In order to obtain training and test images for the masked age classification pipeline, firstly, masks were placed on the faces in this dataset as mentioned in the method section.

The database has 6631 face images. 1015 images contain faces from 12 to 20 years old, 4503 images from 21 to 64, and 1113 images from 65 to 110. The dataset was divided into 3 parts: training set (%75), validation set (%5), and test set (%20). For the masked faces detection step, the system was trained using Face Mask Dataset from Kaggle [58]. The dataset has 853 masked and no-masked face images. 767 images were used for the training, and 86 images were used for testing purposes. These images mostly include multiple human faces. Totally, the dataset has 3355 samples of faces with mask and 717 samples of faces without a mask. Also, a flipping process was applied to the images for data augmentation in order to increase the performance of the mask detection because of the small dataset size.

4.2. Evaluation of the System

Because classification results are usually evaluated using the Accuracy criteria index in the literature, this index was used for a reliable comparison in this study. The mathematical definition of Accuracy is given in Eq.5.

$$Accuracy = \frac{(TP+TN)}{(TP+TN+FN+FP)} \quad (5)$$

Also, in the literature, object detection performances are usually evaluated with Average Precision (AP), and mean Average Precision (mAP) metrics. Thus, this metric has been used for the mask detection task in this study. Average Precision (AP) is calculated using precision (Eq.6.) and Recall (Eq.7.) as can be seen in Eq 8. mAP is the mean of the APs for all classes.

$$Precision = \frac{TP}{(TP+FP)} \quad (6)$$

$$Recall = \frac{TP}{(TP+FN)} \quad (7)$$

$$Average\ Precision = \sum \frac{Precision}{Recall} \quad (8)$$

where TP is True-Positives, FP is False-Positives and FN is False-Positives.

In order to detect the faces with mask or no-mask, Faster R-CNN and YOLO with resnet50 feature extractor have been used in this study. The training parameters used by resnet50 are as follows: learning rate is 0.005, drop factor is 0.1, mini batch size is 8, momentum is 0.9, and the optimizer is sgdm. The masked face detection system showed 92% AP score for masked faces and 91.50% mAP score in Face Mask Detection Dataset.

For the age group classification task, some popular pretrained networks were retrained with masked and no-masked faces from the dataset. The parameters of the used CNN's are given as follows for 12 different pretrained networks. The optimizer is sgdm, the learning rate is 0.001, minibatch size is 32 and momentum is 0.9. Also, the training and validation data are shuffled once before training.

Classification results are shown in Table 2. As can be seen in this table, densenet201 showed the best performance when considering masked and unmasked face classification joint performance. Although a large part of the face has occlusion with the mask, age group classification in masked faces showed close results to unmasked faces (only slightly lower by 1%). As seen in the table, networks have generally produced similar results.

Table 2 Accuracy of pretrained networks used for age group classification

Pretrained Network	With mask (%)	Without mask (%)
alexnet	75.81	78.82
vgg16	78.37	84.48
vgg19	77.24	83.04
squeezenet	78.30	81.76
googlenet	81.24	81.54
inceptionv3	81.69	85.38
densenet201	83.87	84.48
mobilenetv2	80.78	81.54
resnet-101	83.35	83.57
xception	79.88	83.04
shufflenet	81.16	82.22
darknet53	81.69	83.95

In DCNNs, the first convolutional layers learn basic features. The same situation is observed on the first convolutional filters of densenet201, which has the best score for age group classification. The first convolutional filters of densenet201 are given in Figure 4. As can be seen in this figure, the filters generally learned edges and color information.

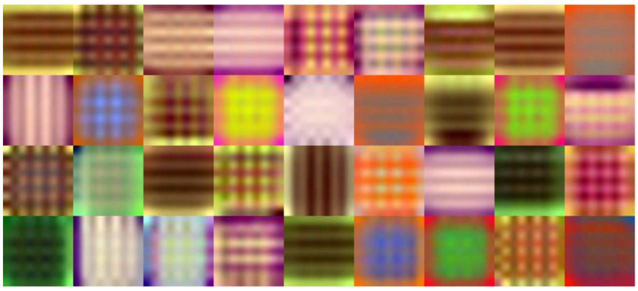

Figure 4 Samples of first convolutional layer filters from densenet201 network

In order to show that how to learn the networks, some output samples of the first convolutional layer of the densenet201 are given in Figure 5. Figure 5, can be interpreted that the filter ignores the mask region and highlight the remaining facial areas in (a). Situation (b) can be interpreted that the filter of the sample (b) becomes apparent in the lines of the figure and it can be related with wrinkles for the age classification.

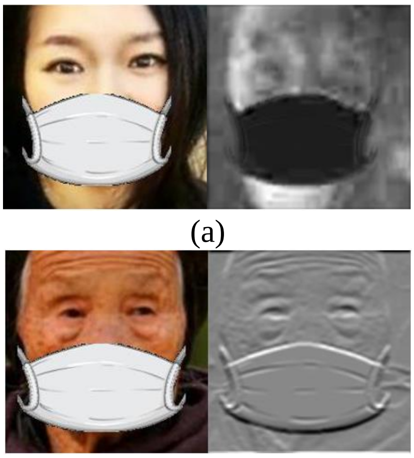

(a)

(b)

Figure 5 Some samples of the outputs of the first convolutional layer from densenet201. (a) and (b) have an original image from UTKFace dataset with implemented face mask and corresponding output that is convolved a filter from the first convolutional layer of densenet201.

Figure 6 shows some sample frames from the system outputs. Figure 6 (a), (b), (c), (d) are from the Face Mask Dataset images and (e), (f) are from real time system. As can be seen in the subfigures, the system produces promising results. Also, Figure 6 (e) and (f), show that the system is not affected by poor lighting conditions and different background conditions in an environment.

4.3. Performance Comparison

The performance of the proposed system has been compared to masked face detection and age group classification systems in the literature, individually. Unfortunately, there is no unified benchmark test set for masked face detection and age group classification; different researchers use different test sets to report their results. Moreover, age classification studies in the literature work on the whole face without a mask. These factors make a fair comparison very hard.

The comparison of proposed masked face detection performance with the literature has been given in Table 3. According to the table, the proposed YOLO has the best performance in terms of AP. Also, in [59], the authors removed some images from the merged database, and the deleted images are not clear. Thus, a fair comparison can not be performed with this study.

Table 4 shows a comparison against age group classification systems using whole face information. In this study, the main motivation is detecting masked face groups in terms of assist controlling COVID-19 restrictions and other security restrictions. Thus, age groups between 12-20, 21-64, and 65+ are key points for this motivation. Unfortunately, there is not a benchmark dataset for this motivation. Thus, the comparison has been applied with-the studies that used the different number of age groups on unmasked faces. Although this is not a fair comparison, there are no other datasets to compare. It was especially shown in the table that the number of classes was different, and other studies worked on the unmasked face.

(a) (b) (c)

(d) (e) (f)

Figure 6 Some samples of the system output from Face Mask Dataset (a,b,c,d) and real time test environment (e,f)

Table 3 Comparison of masked face detection performance with the literature

Method	**Dataset**	**Average Precision**
LLE_CNNs [60]	MAFA	76.4%
YOLO with Resnet [59]	(MMD+FMD) *	81.0%
Proposed Faster R-CNN	FMD	79.0%
Proposed YOLO	FMD	92.0%

*: Note: The authors of Loey2020 removed some images in the merged database.

In this paper, two systems with the same processing steps, one with features from the whole face, one with features from the masked face, have been developed. The results in Table 4 demonstrate that successful age group classification is possible for masked faces. Using both whole face information and masked face information individually, the proposed system produced better results compared to previous studies. Also, using masked face information, the system produced comparable results against the system using whole face information (only slightly lower by ~1% compared to the whole face age group classification system while using only a small part of the face).

5. CONCLUSIONS

This study proposed a multi-task deep learning system for face detection and age group classification from masked faces. Recently, for fighting against COVID-19, people have used face masks. One of the disadvantages of face masks is causing occlusions in the face. Thus it produces difficulties for analyzing the face. But face analysis is essential for security. With this motivation, this study focuses on masked faces.

The proposed system first detects masked and no-masked faces in an environment. Then, it classifies these faces according to three age groups. It can classify age groups for people in front and side profiles, even in crowded areas. It can work regardless of the indoor/outdoor environment. It assists observers to more effortlessly and accurately detect the age group of the masked face. Also, it can quickly detect the people who do not obey the age-related rules in public areas such as markets, streets, shopping centers, airports, etc. and assist the authorities. Thus, more people can be provided to comply with the rules.

One of the study's limitations is that there is no database suitable for motivation, as explained in the experiment section. For this reason, the comparison could be made with studies of different classes of age groups. Also, errors are usually observed in the age borders separating the classes. For example, it is very difficult to distinguish two people's ages that are 20 and 21. But since these two are in separate classes, the correct classification of the system is expected. This is another limitation for the system

The proposed system achieved 92% AP score for masked face detection. Also, it produced 83.87% age group classification accuracy for masked faces. Comparison to the literature showed that the proposed system produces better results against the age group classification system with whole face analysis. These results are significant because they show that a reliable age classification for masked faces is possible. It may be one of the pioneering studies in terms of its motivation.

Acknowledgments

We would like to thank the reviewers and editors for their valuable time.

Funding

This study is supported by Sakarya University Scientific Research Projects Unit (Project Number: 2015-50-02-039).

The Declaration of Research and Publication Ethics

The authors of the paper declare that they comply with the scientific, ethical and quotation rules of SAUJS in all processes of the paper and that they do not make any falsification on the data collected. In addition, they declare that Sakarya University Journal of Science and its editorial board have no responsibility for any ethical violations that may be encountered, and that this study has not been evaluated in any academic publication environment other than Sakarya University Journal of Science.

Table 4 Age group classification accuracies for the proposed system and other studies

Method	Dataset	Age group number	Masked/no-masked	Acc(%)
MTCNN [61]	UTKFace	7	no-masked	70.1
FFNet [61]	UTKFace	7	no-masked	64.0
FaceNet [61]	UTKFace	7	no-masked	59.6
Local age group modelling [62]	Images of Groups	7	no-masked	59.8
Shape and TextureCharacteristic [63]	FG-NET	5	no-masked	79.2
Proposed	UTKFace	3	masked	83.87
Proposed	UTKFace	3	no-masked	84.48

REFERENCES

[1] “World Health Organization.” 2020https://www.who.int/.

[2] A. Abbas, M. M. Abdelsamea, and M. M. Gaber, "Classification of COVID-19 in chest X-ray images using DeTraC deep convolutional neural network," Appl. Intell., vol. 51, no. 2, pp. 854–864, Feb. 2021, doi:10.1007/s10489-020-01829-7.

[3] S. A. B. P and C. S. R. Annavarapu, "Deep learning-based improved snapshot ensemble technique for COVID-19 chest X-ray classification," Appl. Intell., Mar. 2021, doi:10.1007/s10489-021-02199-4.

[4] M. Turkoglu, "COVIDetectioNet: COVID-19 diagnosis system based on X-ray images using features selected from pre-learned deep features ensemble," Appl. Intell., vol. 51, no. 3, pp. 1213–1226, Mar. 2021, doi:10.1007/s10489-020-01888-w.

[5] H. Mittal, A. C. Pandey, R. Pal, and A. Tripathi, "A new clustering method for the diagnosis of CoVID19 using medical images," Appl. Intell., Jan. 2021, doi:10.1007/s10489-020-02122-3.

[6] A. Oulefki, S. Agaian, T. Trongtirakul, and A. Kassah Laouar, "Automatic COVID-19 lung infected region segmentation and measurement using CT-scans images," Pattern Recognit., vol. 114, p. 107747, 2021, doi:10.1016/j.patcog.2020.107747.

[7] D.-P. Fan et al., "Inf-Net: Automatic COVID-19 Lung Infection Segmentation From CT Images," IEEE Trans. Med. Imaging, vol. 39, no. 8, pp. 2626–2637, 2020, doi:10.1109/TMI.2020.2996645.

[8] M. Loey, G. Manogaran, M. H. N. Taha, and N. E. M. Khalifa, "A hybrid deep transfer learning model with machine learning methods for face mask detection in the era of the COVID-19 pandemic," Measurement, vol. 167, p. 108288, 2021, doi:10.1016/j.measurement.2020.108288.

[9] P. Mohan, A. J. Paul, and A. Chirania, "A Tiny CNN Architecture for Medical Face Mask Detection for Resource-Constrained Endpoints," ArVix, 2020http://arxiv.org/abs/2011.14858.

[10] B. Qin and D. Li, "Identifying facemask-wearing condition using image super-resolution with classification network to prevent COVID-19," Sensors (Switzerland), vol. 20, no. 18, pp. 1–23, 2020, doi:10.3390/s20185236.

[11] K. Bhambani, T. Jain, and K. A. Sultanpure, "Real-time Face Mask and Social Distancing Violation Detection System using YOLO," in Bangalore Humanitarian Technology Conference (B-HTC), 2020, pp. 1–6, doi:10.1109/B-HTC50970.2020.9297902.

[12] B. Sathyabama, A. Devpura, M. Maroti, and R. S. Rajput, "Monitoring Pandemic Precautionary Protocols using Real-time Surveillance and Artificial Intelligence," in 3rd International Conference on Intelligent Sustainable Systems (ICISS), 2020, pp. 1036–1041, doi:10.1109/ICISS49785.2020.9315934.

[13] S. Meivel, K. Indira Devi, S. Uma Maheswari, and J. Vijaya Menaka, "Real time data analysis of face mask detection and social distance measurement using Matlab," Mater. Today Proc., 2021, doi:10.1016/j.matpr.2020.12.1042.

[14] S. S. Ahamad and A.-S. Khan Pathan, "A formally verified authentication protocol in secure framework for mobile healthcare during COVID-19-like pandemic," Conn. Sci., pp. 1–23, 2020, doi:10.1080/09540091.2020.1854180.

[15] Y. Li, K. Guo, Y. Lu, and L. Liu, "Cropping and attention based approach for masked face recognition," Appl. Intell., Feb. 2021, doi:10.1007/s10489-020-02100-9.

[16] G. Yolcu, I. Oztel, S. Kazan, C. Oz, and F. Bunyak, "Deep learning-based face analysis

system for monitoring customer interest," J. Ambient Intell. Humaniz. Comput., vol. 11, no. 1, pp. 237–248, Jan. 2020, doi:10.1007/s12652-019-01310-5.

[17] S. Zhang, C. Chi, Z. Lei, and S. Z. Li, "RefineFace: Refinement Neural Network for High Performance Face Detection," IEEE Trans. Pattern Anal. Mach. Intell., p. 1, 2020, doi:10.1109/TPAMI.2020.2997456.

[18] M. Tao et al., "Smartphone-based detection of leaf color levels in rice plants," Comput. Electron. Agric., vol. 173, p. 105431, 2020, doi:10.1016/j.compag.2020.105431.

[19] P. Emami, P. M. Pardalos, L. Elefteriadou, and S. Ranka, "Machine Learning Methods for Data Association in Multi-Object Tracking," ACM Comput. Surv., vol. 53, no. 4, pp. 1–34, 2020, doi:10.1145/3394659.

[20] N. Al-Shakarji, F. Bunyak, H. Aliakbarpour, G. Seetharaman, and K. Palaniappan, "Multi-Cue Vehicle Detection for Semantic Video Compression in Georegistered Aerial Videos," in Proceedings of the IEEE/CVF Conference on Computer Vision and Pattern Recognition (CVPR) Workshops, 2019.

[21] G. V Santiago and A. J. Alvares, "Deployment framework for the Internet of water meters using computer vision on ARM platform," J. Ambient Intell. Smart Environ., vol. 12, no. 1, pp. 35–60, 2020, doi:10.3233/AIS-200544.

[22] K. Trejo, C. Angulo, S. Satoh, and M. Bono, "Towards robots reasoning about group behavior of museum visitors: Leader detection and group tracking," J. Ambient Intell. Smart Environ., vol. 10, no. 1, pp. 3–19, 2018, doi:10.3233/AIS-170467.

[23] H. Wu, L. Yang, S. Fu, and X. (Luke) Zhang, "Beyond remote control: Exploring natural gesture inputs for smart TV systems," J. Ambient Intell. Smart Environ., vol. 11, no. 4, pp. 335–354, 2019, doi:10.3233/AIS-190528.

[24] Y. Sun and Z. Yan, "Image target detection algorithm compression and pruning based on neural network," Comput. Sci. Inf. Syst., vol. 18, no. 2, pp. 499–516, 2021, doi:10.2298/csis200316007s.

[25] J. Ko and K. Cheoi, "A novel distant target region detection method using hybrid saliency-based attention model under complex textures," Comput. Sci. Inf. Syst., vol. 18, no. 2, pp. 379–399, 2021, doi:10.2298/csis200120001k.

[26] K. Ueki, T. Hayashida, and T. Kobayashi, "Subspace-based Age-group Classification Using Facial Images under Various Lighting Conditions," in 7th International Conference on Automatic Face and Gesture Recognition (FGR06), 2006, pp. 43–48, doi:10.1109/FGR.2006.102.

[27] K. S. Htet and M. M. Sein, "Market Intelligence Analysis on Age Estimation and Gender Classification on Events with deep learning hyperparameters optimization and SDN Controllers," in 2020 IEEE Conference on Computer Applications(ICCA), 2020, pp. 1–5, doi:10.1109/ICCA49400.2020.9022854.

[28] Z. Lin et al., "Establishment of age group classification for risk stratification in glioma patients," BMC Neurol., vol. 20, no. 1, p. 310, 2020, doi:10.1186/s12883-020-01888-w.

[29] E. Torres, S. L. Granizo, and M. Hernandez-Alvarez, "Gender and Age Classification Based on Human Features to Detect Illicit Activity in Suspicious Sites," in International Conference on Computational Science and Computational Intelligence (CSCI), 2019, pp. 416–419, doi:10.1109/CSCI49370.2019.00081.

[30] Y. H. Kwon and N. da V. Lobo, "Age Classification from Facial Images," Comput. Vis. Image Underst., vol. 74, no.

1, pp. 1–21, 1999, doi:10.1006/cviu.1997.0549.

[31] W. B. Horng, C. P. Lee, and C. W. Chen, "Classification of age groups based on facial features," Tamkang J. Sci. Eng., vol. 4, no. 3, pp. 183–192, 2001, doi:10.6180/jase.2001.4.3.05.

[32] P. Thukral, K. Mitra, and R. Chellappa, "A hierarchical approach for human age estimation," in IEEE International Conference on Acoustics, Speech and Signal Processing (ICASSP), 2012, pp. 1529–1532, doi:10.1109/ICASSP.2012.6288182.

[33] A. Gunay and V. V Nabiyev, "Automatic age classification with LBP," in 23rd International Symposium on Computer and Information Sciences, 2008, pp. 1–4, doi:10.1109/ISCIS.2008.4717926.

[34] A. K. Soni, R. Kumar, and D. K. Kishore, "Estimation of age groups based on facial features," in 2015 International Conference on Applied and Theoretical Computing and Communication Technology (iCATccT), 2015, pp. 681–687, doi:10.1109/ICATCCT.2015.7456970.

[35] D.-V. Bratu, S.-A. Moraru, and L. Georgeta Guseila, "A Performance Comparison between Deep Learning Network and Haar Cascade on an IoT Device," in 2019 International Conference on Sensing and Instrumentation in IoT Era (ISSI), 2019, pp. 1–6, doi:10.1109/ISSI47111.2019.9043714.

[36] Z. Zhang, Y. Song, and H. Qi, "Age Progression/Regression by Conditional Adversarial Autoencoder," in 2017 IEEE Conference on Computer Vision and Pattern Recognition (CVPR), 2017, pp. 4352–4360, doi:10.1109/CVPR.2017.463.

[37] S. Ren, K. He, R. Girshick, and J. Sun, "Faster R-CNN: Towards Real-Time Object Detection with Region Proposal Networks," IEEE Trans. Pattern Anal. Mach. Intell., vol. 39, no. 6, pp. 1137–1149, Jun. 2017, doi:10.1109/TPAMI.2016.2577031.

[38] J. Redmon, "Darknet: Open Source Neural Networks in C." 2016https://pjreddie.com/darknet/.

[39] J. Redmon and A. Farhadi, "YOLO9000: Better, Faster, Stronger," in 2017 IEEE Conference on Computer Vision and Pattern Recognition (CVPR), 2017, pp. 6517–6525, doi:10.1109/CVPR.2017.690.

[40] I. Goodfellow, Y. Bengio, and A. Courville, Deep learning. MIT Press, 2016http://citeseerx.ist.psu.edu/viewdoc/download?doi=10.1.1.672.7118%7B&%7Drep=rep1%7B&%7Dtype=pdf.

[41] R. Mostafiz, M. S. Uddin, N.-A.- Alam, M. Mahfuz Reza, and M. M. Rahman, "Covid-19 detection in chest X-ray through random forest classifier using a hybridization of deep CNN and DWT optimized features," J. King Saud Univ. - Comput. Inf. Sci., 2020, doi:https://doi.org/10.1016/j.jksuci.2020.12.010.

[42] R. Hafiz, M. R. Haque, A. Rakshit, and M. S. Uddin, "Image-based soft drink type classification and dietary assessment system using deep convolutional neural network with transfer learning," J. King Saud Univ. - Comput. Inf. Sci., 2020, doi:https://doi.org/10.1016/j.jksuci.2020.08.015.

[43] Y. M. Kassim et al., "Clustering-Based Dual Deep Learning Architecture for Detecting Red Blood Cells in Malaria Diagnostic Smears," IEEE J. Biomed. Heal. Informatics, p. 1, 2020, doi:10.1109/JBHI.2020.3034863.

[44] A. Vedaldi and K. Lenc, "MatConvNet," in Proceedings of the 23rd ACM international conference on Multimedia - MM '15, 2015, pp. 689–692, doi:10.1145/2733373.2807412.

[45] J. Roels, J. De Vylder, J. Aelterman, Y. Saeys, and W. Philips, "Convolutional neural network pruning to accelerate membrane segmentation in electron microscopy," in 2017 IEEE 14th International Symposium on Biomedical Imaging (ISBI 2017), 2017, pp. 633–637, doi:10.1109/ISBI.2017.7950600.

[46] L. Torrey and J. Shavlik, "Transfer Learning," in Handbook of Research on Machine Learning Applications and Trends, IGI Global, pp. 242–264, doi:10.4018/978-1-60566-766-9.ch011.

[47] S. J. Pan and Q. Yang, "A Survey on Transfer Learning," IEEE Trans. Knowl. Data Eng., vol. 22, no. 10, pp. 1345–1359, 2010, doi:10.1109/TKDE.2009.191.

[48] A. Krizhevsky, I. Sutskever, and G. E. Hinton, "ImageNet Classification with Deep Convolutional Neural Networks," Adv. Neural Inf. Process. Syst., pp. 1–9, 2012, doi:http://dx.doi.org/10.1016/j.protcy.2014.09.007.

[49] K. Simonyan and A. Zisserman, "Very Deep Convolutional Networks for Large-Scale Image Recognition," Sep. 2014http://arxiv.org/abs/1409.1556.

[50] F. N. Iandola, M. W. Moskewicz, K. Ashraf, S. Han, W. J. Dally, and K. Keutzer, "SqueezeNet: AlexNet-level accuracy with 50x fewer parameters and <1MB model size," CoRR, vol. abs/1602.0, 2016.

[51] C. Szegedy et al., "Going deeper with convolutions," in 2015 IEEE Conference on Computer Vision and Pattern Recognition (CVPR), 2015, pp. 1–9, doi:10.1109/CVPR.2015.7298594.

[52] C. Szegedy, V. Vanhoucke, S. Ioffe, J. Shlens, and Z. Wojna, "Rethinking the Inception Architecture for Computer Vision," in 2016 IEEE Conference on Computer Vision and Pattern Recognition (CVPR), 2016, pp. 2818–2826, doi:10.1109/CVPR.2016.308.

[53] G. Huang, Z. Liu, L. Van Der Maaten, and K. Q. Weinberger, "Densely Connected Convolutional Networks," in 2017 IEEE Conference on Computer Vision and Pattern Recognition (CVPR), 2017, pp. 2261–2269, doi:10.1109/CVPR.2017.243.

[54] M. Sandler, A. Howard, M. Zhu, A. Zhmoginov, and L. Chen, "MobileNetV2: Inverted Residuals and Linear Bottlenecks," in 2018 IEEE/CVF Conference on Computer Vision and Pattern Recognition, 2018, pp. 4510–4520, doi:10.1109/CVPR.2018.00474.

[55] K. He, X. Zhang, S. Ren, and J. Sun, "Deep Residual Learning for Image Recognition," in 2016 IEEE Conference on Computer Vision and Pattern Recognition (CVPR), 2016, pp. 770–778, doi:10.1109/CVPR.2016.90.

[56] F. Chollet, "Xception: Deep Learning with Depthwise Separable Convolutions," 2016http://arxiv.org/abs/1610.02357.

[57] X. Zhang, X. Zhou, M. Lin, and J. Sun, "ShuffleNet: An Extremely Efficient Convolutional Neural Network for Mobile Devices," 2017http://arxiv.org/abs/1707.01083.

[58] Kaggle, "Face Mask Detection," 2020. [Online]. Available: https://www.kaggle.com/andrewmvd/face-mask-detectionhttps://www.kaggle.com/andrewmvd/face-mask-detection.

[59] M. Loey, G. Manogaran, M. H. N. Taha, and N. E. M. Khalifa, "Fighting against COVID-19: A novel deep learning model based on YOLO-v2 with ResNet-50 for medical face mask detection," Sustain. Cities Soc., p. 102600, 2020, doi:10.1016/j.scs.2020.102600.

[60] S. Ge, J. Li, Q. Ye, and Z. Luo, "Detecting Masked Faces in the Wild with LLE-CNNs," in 2017 IEEE Conference on Computer Vision and Pattern Recognition (CVPR), 2017, pp. 426–434, doi:10.1109/CVPR.2017.53.

[61] A. Das, A. Dantcheva, and F. Bremond, "Mitigating Bias in Gender, Age and Ethnicity Classification: a Multi-Task Convolution Neural Network Approach," in Proceedings of the European Conference on Computer Vision (ECCV) Workshops, 2018.

[62] S. H. Lee and Y. M. Ro, "Local age group modeling in unconstrained face images for facial age classification," in International Conference on Image Processing (ICIP), 2014, pp. 1395–1399, doi:10.1109/ICIP.2014.7025279.

[63] L. Liu, J. Liu, and J. Cheng, "Age-Group Classification of Facial Images," in 11th International Conference on Machine Learning and Applications, 2012, pp. 693–696, doi:10.1109/ICMLA.2012.129.

SAKARYA ÜNİVERSİTESİ
FEN BİLİMLERİ ENSTİTÜSÜ
DERGİSİ

Sakarya University Journal of Science
SAUJS

e-ISSN 2147-835X Founded 1997 Period Bimonthly Publisher Sakarya University
http://www.saujs.sakarya.edu.tr/en/

Title: Experimental Study on Composite Floor Panels

Authors: Osman KAYA

Recieved: 2021-03-08 00:00:00

Accepted: 2021-11-04 00:00:00

Article Type: Research Article

Volume: 25
Issue: 6
Month: December
Year: 2021
Pages: 1408-1416

How to cite
Osman KAYA; (2021), Experimental Study on Composite Floor Panels. Sakarya University Journal of Science, 25(6), 1408-1416, DOI: https://doi.org/10.16984/saufenbilder.893070
Access link
http://www.saujs.sakarya.edu.tr/tr/pub/issue/66341/893070

Sakarya University Journal of Science 25(6), 1408-1416, 2021

Experimental Study on Composite Floor Panels

Osman KAYA*[1]

Abstract

This paper presents experimental investigations carried out on various composite floor deck panel systems. The effects of parameters such as concrete shear length, steel thickness, and concrete thickness on the shear and flexural behavior of panels were examined. Shear tests were carried out on identical specimens with four different shear span lengths. Four-point flexural tests were carried out on single-span and double-span specimens. Shear stress-slip, load-deformation, and moment-curvature behaviors were compared. From the test results, the effect of shear strength between the corrugated sheets and concrete governs the failure mechanisms of the flexural test, if there is no shear connector. In all flexural tests the failure is became due to the slippage between the steel panel and concrete.

Keywords: sandwich panels, corrugated steel, shear test, flexural test

1. INTRODUCTION

Due to the effective use of concrete and steel, the use of composite structures in industrial structures becomes more important all over the world. Composite floor slabs consist of concrete blocks and profiled steel sheets. The profiled sheet used in composite flooring systems has two functions. It takes the tensile stresses, so no need to use tensile reinforcement. And it acts as a mold while pouring concrete, so no need for an additional formwork system. Additional wire mesh on top is used to prevent shrinkage and temperature effects.

Under service loading, the sheet and concrete interface is subjected to longitudinal shear stress. To overcome the slip, friction at interface of steel and concrete should be increased. For this reason shear connectors or embossment are implemented on corrugated sheets.

The effects of embossment without shear connectors, on the flexural behavior of deck panel are experimentally investigated in this study

2. LITERATURE REVIEW

Several experimental studies on composite deck panels with shear connectors can be found in the literature [1-10]. However, limited experimental tests have been performed on composite deck panel without shear connectors. Marimuthu et al. [11] studied moment curvature behavior of composite deck slabs with embossed profiled sheets. It was concluded that, shear connectors should be used to increase the shear strength between steel and concrete. In 2007, Ferrer studied use of cold form steel sheet for composite slabs. It is concluded that the critical issue for failure is shear slip [12].

---

* Corresponding author: okaya75@gmail.com
[1] Muğla Sıtkı Koçman University, Faculty of Engineering, Department of Civil Engineering
ORCID: https://orcid.org/0000-0003-3851-3082

Baskar [7, 13] studied on composite deck slabs with and without embossment sheets. It is concluded that using embossed profile increases the load carrying capacity and delays the delamination. In order to improve the shear strength, Lakshmikandhan et al. [14] investigated three different shear transferring mechanisms namely mechanical interlock through indentations, embossments, and fastening studs. The mechanical shear connectors increase the load and bending moment capacity and also increase stiffness.

Hyeong Yeol Kim and Youn Ju Jeong [15] proposed a new type of full-scale composite deck slabs with longer and light-weight span when compared with conventional RC deck slabs. They concluded that the flexural rigidity of the composite deck slabs is approximately twice than that of traditional RC decks. Also the load capacity was increased by two and half times in the composite decks. It is stated by Wright, that the load -deformation behavior of composite deck slab behaves linear elastic until the buckling of corrugated steel. After the buckling, the behavior becomes non-linear. The yielding of steel profile developed in elastic region, so that the load carrying capacity is higher than traditional RC deck slabs [16].

In order to investigate the effects of embossment on the shear capacity and the flexural capacity of floor panels, an experimental study was carried out.

3. EXPERIMENTAL STUDY

The shear capacities and flexural capacities of composite deck panels were investigated experimentally. Test setups and Specimen properties are defined in following section. In Figure 1, dimensions of corrugated sheet were illustrated. The same corrugated sheet was used for both shear and flexural specimens. The photo from production of test specimens was given in Figure 2.

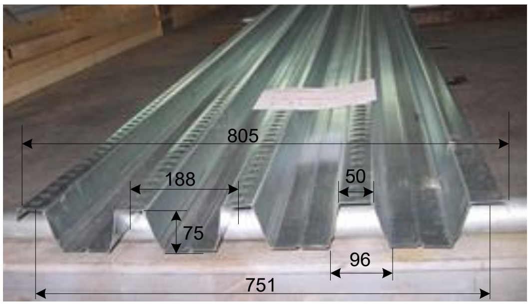

Figure 1 Dimensions of corrugated sheet (in mm)

Figure 2 Production of test specimens

3.1. Shear Tests

The test setup was composed of a trapezoidal steel panel, and a shearing concrete block of specific length and a reaction concrete block. 3m long composite deck panel system were produced. The hydraulic actuator, load cell and displacement transducers were placed in the test area, which is between the shearing concrete block, and the reaction concrete block, as seen in Figure 3.

3.2. Shearing Test Specimens

A total of 4 identical composite deck panel specimens were tested for shear resistance. Four different shearing surface lengths (L) were chosen with constant concrete width (Figure 3).

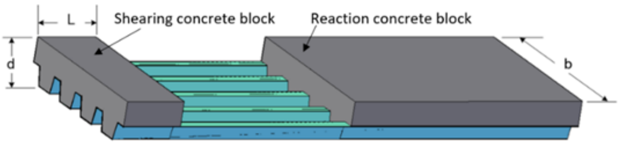

Figure 3 Dimensions of shearing test specimens

In Table 1 and Figure 4, dimensional properties of test specimens are described. Where, d is the overlaying concrete thickness, t is the thickness of steel plate, *b* is width of panel and *L* is the shear length.

Table 1 Description of shearing test specimens

Specimen ID	d *mm*	t *mm*	L *mm*	b *mm*
S1	215	1.0	250	815
S2	215	1.0	500	815
S3	215	1.0	750	815
S4	215	1.0	1000	815

The load was applied by a manually-operated 100 kN capacity hydraulic ram and was measured by a 200 kN capacity load cell. Figure 2 shows the pictures of the test set-up (a), and illustrates schematically the test set-up and the loading applied to the specimen in the test rig (b). All the load and displacement data were recorded by data logger equipment.

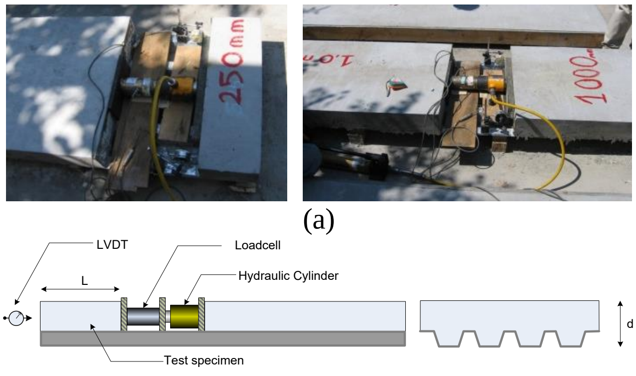

(a)

(b)

Figure 4 Test set-up for shearing test specimens

3.3. Bending Tests

The main components of the test rig included simple supports and rigid beams to distribute the point loads. The main load was applied by a manually-operated 300 kN capacity hydraulic ram and was measured by a 200 kN capacity load cell. The main load was equally distributed via rigid beams and supports underneath the applying point loads at two locations on each span where each point load was applied at 1/3 span distance. Also two LVDTs were used for curvature readings on each span. Figure 5 illustrates schematically the test set-up and instrumentation in the test rig for single span (a) and for double span (b).

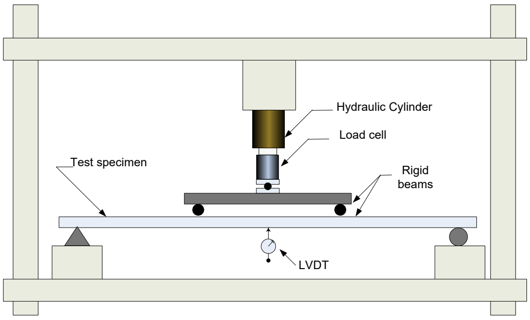

(a) Single Span

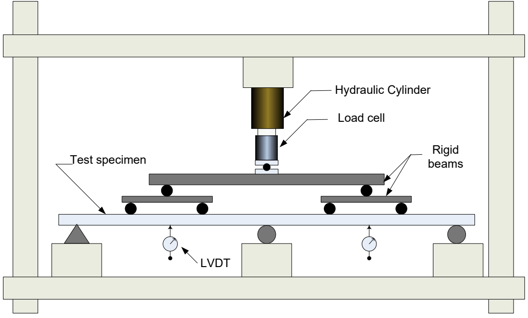

(b) Double Span

Figure 5 Bending Test Set-up

3.4. Bending Test Specimens

A total of 10 single span and 4 double span composite deck panel specimens were tested. Span lengths in double span specimens were kept equal. The overall dimensions of single and double span test specimens are shown in Figure 6 and Table 2.

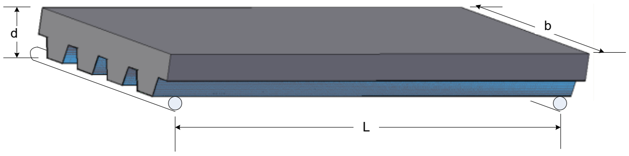

(a) Single Span

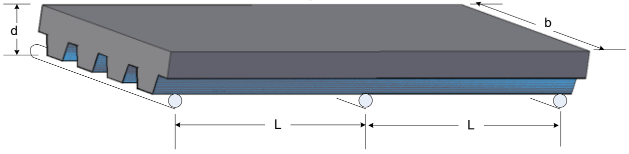

(b) Double Span

Figure 6 Dimensions of bending test specimens

The height of the corrugated steel panel was 75 mm and the overlaying concrete thicknesses, were 125 mm, 175 mm and 215 mm measured from bottom of steel panel. The width of the deck panel in the test rig was taken as 770 mm. The steel panels had a varying thickness of 1.0 and 1.2 mm.

Table 2 Description of bending test specimens

Specimen ID	**Span**	**d** *mm*	**t** *mm*	**L** *mm*	**b** *mm*
F1a	Single	125	1.2	2000	770
F1b	Single	125	1.2	2000	770
F1c	Single	125	1.2	2000	770
F2a	Single	125	1.2	3000	770
F2b	Single	125	1.2	3000	770
F2c	Single	125	1.2	3000	770
F3	Single	215	1.0	3000	770
F4	Single	215	1.0	2750	770
F5	Single	215	1.0	2500	770
F6	Single	215	1.0	2200	770
F7	Double	125	1.2	2000	770
F8	Double	175	1.2	2000	770
F9	Double	125	1.0	2000	770
F10	Double	175	1.0	2000	770

3.5. Material Tests

The tests on 20x20x20 cm concrete cubes were carried out on test dates. An average value of 30 MPa compressive strength was found. The tensile yield strength of corrugated steel material was given by the manufacturer as 280 MPa.

4. TEST RESULTS

4.1. Shear Tests

For each test specimen, slippage between concrete and steel was observed. For specimen S1, which has 250 mm length of shearing block, the maximum load was recorded as 14 kN, whereas for specimen S4, which has 1000 mm shearing block length, the maximum load was recorded as 29 kN. Typical failure mechanism can be seen in Figure 7. Measured load vs. deformation relationships were plotted for shearing tests (Figure 8). For all specimens, the load capacity dropped suddenly after the loss of connection between steel and concrete, however, due to small shearing struts on corrugated steel, shear load capacities do not fall totally down to zero up to 10 mm slip value.

Figure 7 Testing of Specimen S1 and S2

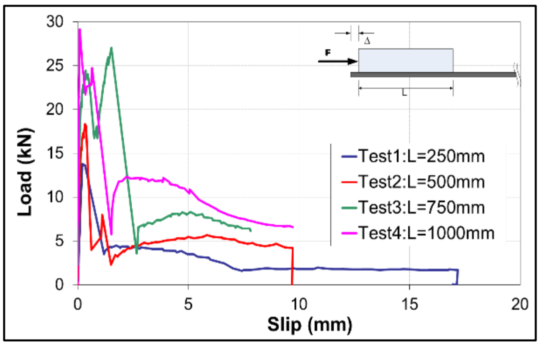

Figure 8 Test results of shearing test

4.2. Single Span Bending Tests

As defined in test setup, four-point loading was applied for single span bending tests. In all specimens, during the loading, first cracking of concrete was observed at the mid span locations. However, the tests were ended by due to the slippage between steel and concrete. In none of the tests did the specimens reach their flexural capacities. In Figure 9, typical failure due to slippage is shown.

Figure 9 Testing of single span bending tests

Also the test results are shown in Figure 10 in terms of applied load and mid span deflection. Three identical specimens for F1 and F2 specimens behave almost similar.

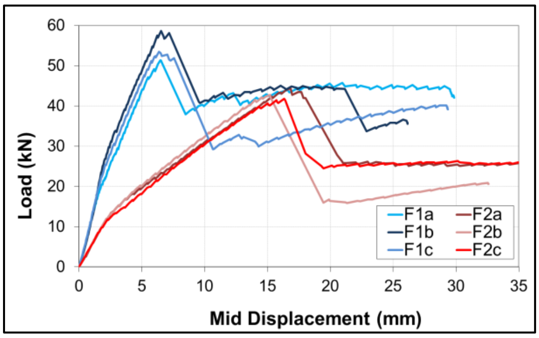

(a) Specimen F1 and F2

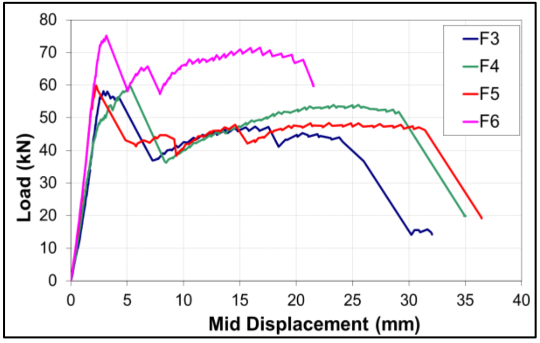

(b) Specimen F3, F4, F5 and F6

Figure 10 Test results of single span bending tests

4.3. Double Span Bending Tests

In double span tests, similar to single span tests, first flexural cracks were observed in each mid span location. Crushing of steel was observed at support region (Figure 11).

Figure 11 Testing of double span bending tests

However, the tests were ended again due to the slippage. The test results are shown in Figure 12 in terms of applied load and two mid span deflections.

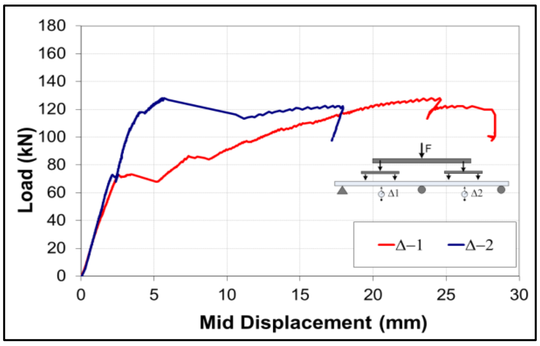

(a) Specimen F7

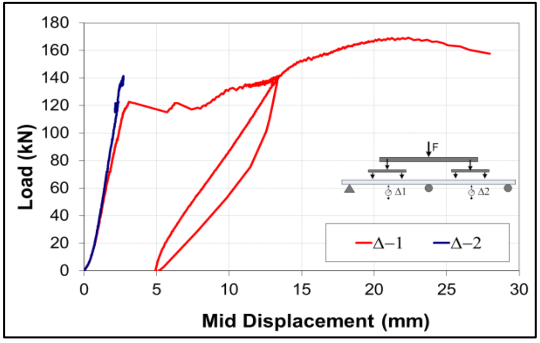

(b) Specimen F8

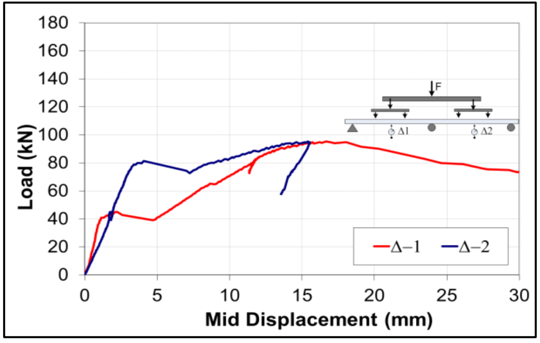

(c) Specimen F9

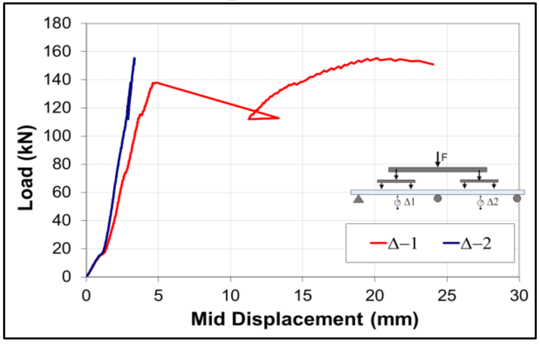

(d) Specimen F10

Figure 12 Test results of double span bending tests

5. ANALYSIS OF TEST RESULTS

5.1. Shear Tests

The objective of this test was to determine the longitudinal shear resistance between concrete block and the corrugated steel panel. Different shear lengths were tried and their corresponding failure loads were measured and thus, shear stresses were calculated. The calculation of shear stresses involved finding the total contact area between the steel and concrete materials in shearing concrete block side and dividing the failure load by that area. Figure 13 shows the variation of the shear stress values vs. slippage of block.

The value of shear stress was found to be between 0.03 MPa and 0.06 MPa, which decreases while shearing length increases.

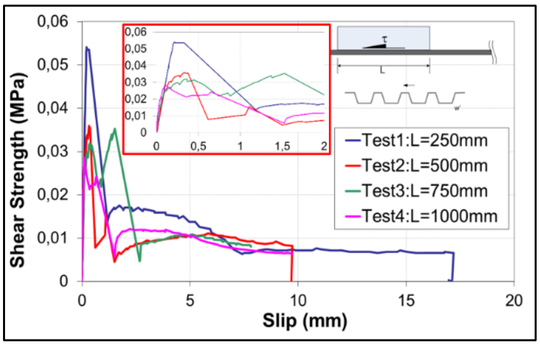

Figure 13 Shear stress vs. slip relationship

5.2. Single Span Bending Tests

A typical four-point load test was conducted in order to determine experimentally the moment-curvature relationship. The moment was calculated for each incremental load application as,

$$M = \frac{1}{2} F \frac{L}{3} = \frac{FL}{6} \qquad (1)$$

where M is the moment and F is the applied load.

Referring to Figure 14, Linear Variable Displacement Transducer (LDVT) 1 and LVDT 2 were used to measure the curvature of the composite panel at mid span location. ε_1 and ε_2 are the strain values within the length of measurement of LVDT 1 and LVDT 2 and are calculated as follows:

$$\varepsilon_1 = \frac{\Delta_1}{e_1} \ , \ \varepsilon_2 = \frac{\Delta_2}{e_2} \qquad (2)$$

where Δ_1 and Δ_2 are the corresponding displacement measurements of LDVTs. e_1 and e_2 are the gage lengths.

Thus the panel curvature, φ, is calculated with the following equation:

$$\varphi = \frac{\varepsilon_1 - \varepsilon_2}{g_1 + g_2 + w_c} \qquad (3)$$

where g_1 and g_2 are the distances of LVDTs from the panel. w_c is panel thickness.

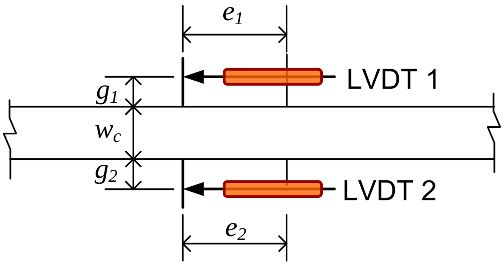

Figure 14 Instrumentation for curvature calculations

Experimentally obtained moment-curvature relationship for each test specimen was plotted in Figure 15. Also, Figure 15 contains theoretical moment-curvature relationship based on full composite action assumption and the nominal material properties of 30 MPa of concrete compressive strength and 280 MPa of steel tensile yield strength, calculated using standard reinforced concrete procedure. The limits of shear stress of 0.03 MPa, which is obtained from shearing tests and the deflection of L/360 were also found corresponding to their respective moment values. These limits are also shown in Figure 15.

The slope of ascending branch of theoretical moment-curvature curve approximately matches to those of experimentally obtained slopes. In theoretical calculation, it is assumed that the concrete and the steel work together without any slippages. However, in the experiments, a separation between concrete and steel was observed indicating shear failure before full composite action was taken in place. These observations along with theoretical calculations are verified in Figure 15.

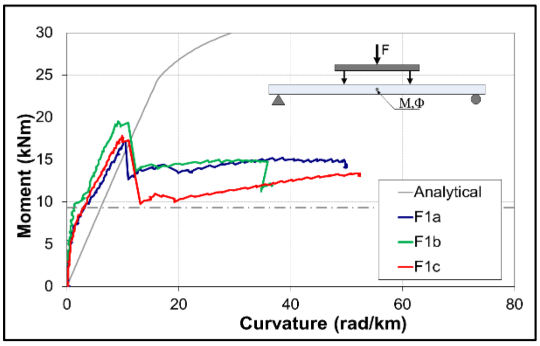

(a) Specimen F1

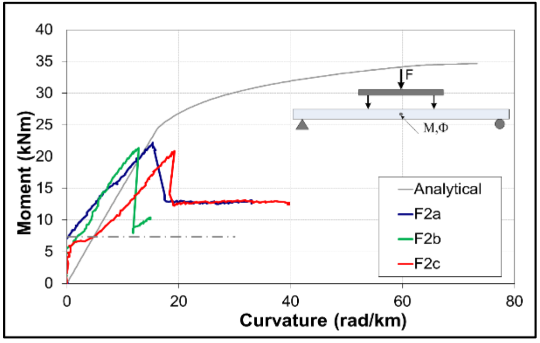

(b) Specimen F2

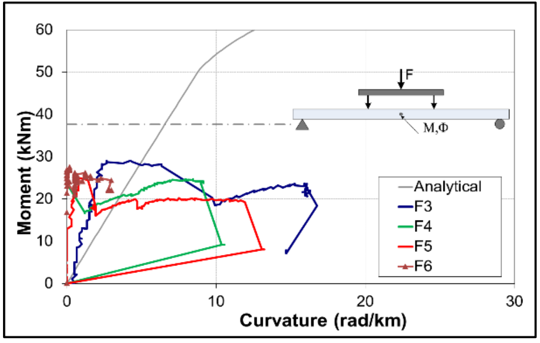

(c) Specimen F3, F4, F5 and F6

Figure 15 Analysis of single span bending tests

5.3. Double Span Bending Tests

The analyses were carried out similar to single span case and as it is seen from Figure 16, same conclusions could be drawn as the case of single span test.

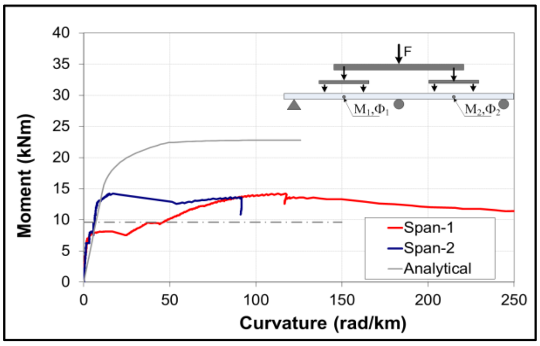

(a) Specimen F7

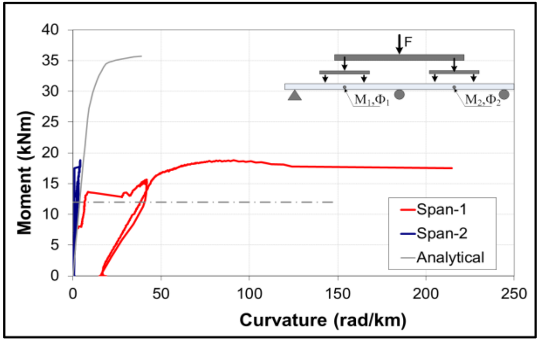

(b) Specimen F8

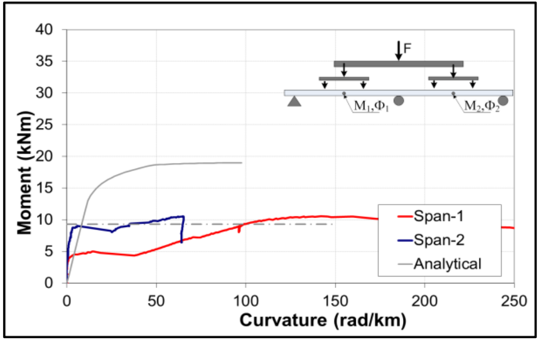

(c) Specimen F9

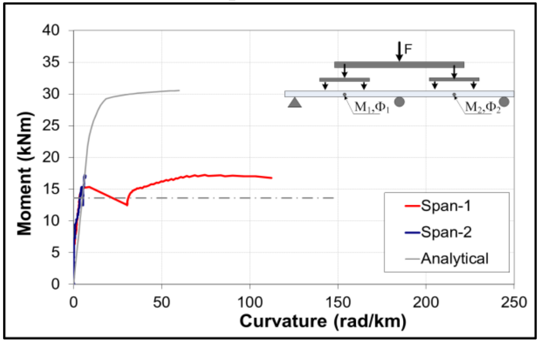

(d) Specimen F10

Figure 16 Analysis of double span bending tests

The moment in this case was calculated as the maximum positive moment for each span which is

$$M = 0.222\left(\frac{F}{4}\right)L = 0.056FL \tag{4}$$

where M is the maximum span moment, F is the applied load mid span and L is the length of span.

As in single span test, a separation between concrete and steel was observed in the tests of double span specimens. That separation causes a slip so that full composite action was not taken in place.

When the thickness of concrete layer is increased, the theoretical moment capacity is increased as expected. However, for the thicker member, the slippage occurs at small curvature level.

6. CONCLUSIONS

Experimental investigation conducted on composite floor panels without shear connectors has been presented. 4 longitudinal shear tests with different shearing length, 10 single-span simply supported flexural tests and 4 two-span flexural tests on Composite Floor Panels were carried out. From the shear tests, It is found that shear strengths at steel-concrete interface varies between 0.03 MPa to 0.06 MPa for 250 mm and 1000 mm shear length respectively. And the longitudinal shear strength between the steel and concrete has significant effect on flexural capacity. In all flexural tests, the specimens show semi-composite behavior due to slip between concrete and steel layer. The maximum moment value shown in M-Φ curves are almost half of the flexural capacity of the composite panels. Due to the slip, yielding of steel panel is not developed.

REFERENCES

[1] PCI Committee on Precast Concrete Sandwich Wall Panels, “State of the art of precast/ pre-stressed sandwich wall panels,” PCI Report, 1997.

[2] M. J Burnet, D. J Oehlers, “Rib shear connectors in composite profiled slabs,” Journal of Constructional Steel Research, vol. 57, Issue 12, pp. 1267-1287, 2001.

[3] ASTM C393-00, “Standard Test Method for Flexural Properties of Sandwich Constructions,” ASTM International, West Conshohocken, PA, 2000.

[4] A. Benayoune, A. Aziz A. Samad, D. N. Trikha, A. Abdullah Abang Ali, A. A. Ashrabov, “Structural behaviour of eccentrically loaded precast sandwich panels,” Construction and Building Materials, vol. 20, issue 9, pp. 713-724, 2006.

[5] A. Benayoune, A. A. Abdul Samad, D. N. Trikha, A. A. Abang Ali, S. H. M. Ellinna, “Flexural behaviour of pre-cast concrete sandwich composite panel – experimental and theoretical investigations,” Construction and Building Materials, vol. 22, Issue 4, pp. 580–592, 2008.

[6] D. C. Salmon, M. K. Einea, A. Tadros, T. D. Culp. “Full scale testing of precast concrete sandwich panels,” ACI Structural Journal, vol. 94, issue 4, pp. 354-362, 1997.

[7] R. Baskar, A. C. Jeyasehar, “Experimental and Numerical Studies on Composite Deck Slabs,”. International Journal of Engineering Research and Development, vol. 3, issue 12, pp.22-32, 2012.

[8] K. K. Prajapati, M. G. Vanza, M. D. Vakil, “Behavior of Cold-formed Stainless Steel Composite Deck,” International Journal of Earth Sciences and Engineering, vol. 4, pp. 616–618, 2011.

[9] F. J. Plantema, “Sandwich Construction,” John Wiley, New York, USA, 1967.

[10] S. Avudaiappan, E. I. S. Flores, G. A. Letelier, W. J. Thomas, S. N. Raman, G. Murali, M. Amran, M. Karelina, R. Fediuk, N. Vatin, “Experimental Investigation on Composite Deck Slab Made of Cold-Formed Profiled Steel Sheeting,” Metals, vol. 11, no. 229, 2021.

[11] V. Marimuthu, S. Seetharaman, S. A. Jayachandran, S., A. Chellappan, T. K. Bandyopadhyay, D. Dutta, “Experimental studies on composite deck slabs to

determine the shear-bond characteristic (m–k) values of the embossed profiled sheet," Journal of Constructional Steel Research, vol. 63, issue 6, pp. 791–803, 2007.

[12] M. Ferrer, F. Marimon, M. Crisinel, "Designing cold-formed steel sheets for composite slabs: An experimentally validated FEM approach to slip failure mechanics," Thin-Walled Structures, vol 44, Issue 12, pp. 1261-1271, 2006.

[13] R. Baskar, "Experimental and numerical studies on composite deck slabs," International Journal of Engineering and Technology, vol. 2, no. 7, pp. 1116–1125, 2012.

[14] K. N. Lakshmikandhan, P. Sivakumar, R. Ravichandran, S. A. Jayachandran, "Investigations on efficiently interfaced steel concrete composite deck slabs," Journal of Structures, vol. 2013, id. 628759, 2013.

[15] H. Y. Kim, Y. J. Jeong, "Ultimate strength of a steel–concrete composite bridge deck slab with profiled sheeting," Engineering Structures, vol. 32, issue 2, pp. 534-546, 2010.

[16] H. D. Wright, H. R. Evans, P. W. Harding, "The Use of Profiled Steel Sheeting in Floor Construction," Journal of Constructional Steel Research, vol. 7, issue 4, pp. 279-295, 1987.

SAKARYA ÜNİVERSİTESİ

FEN BİLİMLERİ ENSTİTÜSÜ
DERGİSİ

Sakarya University Journal of Science
SAUJS

e-ISSN 2147-835X Founded 1997 Period Bimonthly Publisher Sakarya University
http://www.saujs.sakarya.edu.tr/en/

Title: Analysis of the Saliency Ratio Effect on the Output Torque and the System Efficiency in IPM Drives

Authors: Osman Emre ÖZÇİFLİKÇİ, Mikail KOÇ

Recieved: 2021-06-14 00:00:00

Accepted: 2021-11-15 00:00:00

Article Type: Research Article

Volume: 25
Issue: 6
Month: December
Year: 2021
Pages: 1417-1426

How to cite
Osman Emre ÖZÇİFLİKÇİ, Mikail KOÇ; (2021), Analysis of the Saliency Ratio Effect on the Output Torque and the System Efficiency in IPM Drives. Sakarya University Journal of Science, 25(6), 1417-1426, DOI: https://doi.org/10.16984/saufenbilder.952222
Access link
http://www.saujs.sakarya.edu.tr/tr/pub/issue/66341/952222

Sakarya University Journal of Science 25(6), 1417-1426, 2021

Analysis of the Saliency Ratio Effect on the Output Torque and the System Efficiency in IPM Drives

Osman Emre ÖZÇİFLİKÇİ*[1], Mikail KOÇ[1]

Permanent magnet synchronous motors (PMSM) can be classified into two groups based on the rotor saliency structure as surface mounted permanent magnet synchronous motors (SPM) and interior mounted permanent magnet synchronous motors (IPM). Saliency ratio is defined as the ratio of q- axis inductance to d- axis inductance. While SPMs with the same d- and q-axis inductance values have the capacity to generate only the magnet-based torque IPMs are salient machines and they also produce reluctance torque due to the difference in inductances. This study analyses the influence of the saliency ratio on the drive system efficiency and the torque production capability of salient machines. First, efficient torque control systems have been implemented and successfully achieved for two identical IPMs with only difference in saliency ratios. Then, tests were carried out on the drive systems for two IPMs. It has been validated by extensive simulation results that the torque production capacity and the efficiency of the drive system can be increased considerably if the saliency ratio can be increased at the stage of machine design.

Keywords: IPM, PMSM, saliency ratio, torque control

1. INTRODUCTION

PMSMs attract attention due to their superior features such as high efficiency, low acoustic noise, low rotor losses, and wide speed range [1]. Accordingly, they are widely used in industry such as machine tools, robotics, aeronautics, automotive [2]. Its popularity has increased in recent years with applications such as the increasing use in electric vehicle technology compared to other motors [3] and the increasing use in railway systems due to their high power density and wide speed range of operation [4]. Therefore, the design and modern control strategies for PMSMs are an important research topic.

PMSMs can be divided into two groups based on the rotor structure as salient and non-salient machines. While surface mounted permanent magnet synchronous motors (SPMs) are non-salient machines, interior mounted permanent magnet synchronous motors (IPMs) are known as salient brush-less AC machines. SPMs are motors designed by mounting permanent magnets on the rotor surface and do not contain saliency in the rotor [5]. Therefore, it has the capacity to generate only the magnet based electromagnetic torque. However, in IPMs, magnets are mounted in the rotor and there is a saliency in the rotor structure. When motor modelled with coordinate transformations in d- and q- rotary axes, inductance values in d- and q- axes are different.

---

* Corresponding author: osman.ozciflikci@ahievran.edu.tr
[1] Ahi Evran University, Faculty of Engineering and Architecture, Electrical - Electronics Engineering
E-Mail: mkoc@ahievran.edu.tr
ORCID: https://orcid.org/0000-0001-8770-020X, https://orcid.org/0000-0003-1465-1878

While there is a difference between inductance values in d- and q- axes in IPMs, d- and q- axes inductance values are the same in SPMs. Saliency ratio in PMSMs refers to the ratio of L_q to L_d. Since IPMs have saliency, they have the ability to produce reluctance torque as well as magnet-based torque. Thus, the torque output that can be obtained from IPMs is higher than that of SPMs [6].

There are scalar and vector approaches in control methods used in motor drive systems. Although the scalar control technique is a low-cost method, it is only effective in steady state because it exhibits very poor dynamic performance. Vector control approach has advantages over standard techniques such as full torque capacity at low speed, better dynamic performance, higher efficiency for each operating point in a wide speed range [7]. Vector control techniques are basically divided into two categories as Field Oriented Control (FOC) and Direct Torque Control (DTC). FOC and DTC are widely used in both PMSM and induction motor drive systems [8-11]. In the FOC control technique, the current errors are driven to zero while the torque and the stator flux magnitude errors are driven to zero in DTC drives [12]. Since DTC drives rely on observer accuracy and the current limits cannot be posed directly, the machine is controlled with FOC strategy in the case study in which the current limits can directly be posed and the drive is exempt from flux and torque observers.

After adopting the motor control with coordinate transformations in the drive systems, d- and q-axis reference voltage components are obtained. Although the reference voltages in d- and q- axis can be transformed into three phase components to directly being applied to the machine by the use of coordinate transformations in the simulation environment, this is not feasible in real life since a modulation strategy for an inverter is a must in practice. Therefore, the inverter structure and pulse width modulation technique has been modelled and employed in the simulated drives to better represent the drives as in real world. Sinusoidal pulse width modulation (SPWM) [13] and space vector pulse width modulation (SVPWM) are commonly used in motor drive systems [14-16]. The SVPWM technique is superior to SPWM with its features such as 15% more output voltage, lower total harmonic distortion, and low switching losses [17-18]. Hence, SVPWM switching technique is employed to trigger the inverter gates in this study.

Efficient torque control systems have been developed for two IPMs with different saliency ratios for the purpose of comparing the two machines. Since the available battery voltage is finite, SVPWM technique is limited by the over-modulation block in the simulation. Two IPM drives with different saliency ratios have been compared broadly in terms of torque output capabilities and overall system efficiencies. From the realistic simulation results, it has been validated that the IPM machine with a high saliency ratio has higher output torque capability and the drive achieves higher efficient operation.

2. MATHEMATICAL EXPRESSIONS

2.1. Coordinate transformations and IPM model

In order to control three-phase PMSMs like a DC motor, equations in the abc reference system are expressed in d- and q- rotary frames with the help of coordinate transformations. Firstly, Clarke matrix in (1) is applied to the equations in the abc reference system and defined in the stationary frame. The equations defined in the stationary frame are defined by the Park transformations given in (2) in the d- and q- axes according to the rotor angle θ_e. By taking the inverse of the matrices given in (1) and (2), I_{abc} currents at the inverter output to be used in the control system are transformed into d- and q- axes with the matrix in (3).

$$\begin{bmatrix} I_\alpha \\ I_\beta \end{bmatrix} = \frac{2}{3} * \begin{bmatrix} 1 & -\frac{1}{2} & -\frac{1}{2} \\ 0 & \frac{\sqrt{3}}{2} & -\frac{\sqrt{3}}{2} \end{bmatrix} \begin{bmatrix} I_a \\ I_b \\ I_c \end{bmatrix} \tag{1}$$

$$\begin{bmatrix} V_d \\ V_q \end{bmatrix} = \begin{bmatrix} \cos\theta & \sin\theta \\ -\sin\theta & \cos\theta \end{bmatrix} \begin{bmatrix} V_\alpha \\ V_\beta \end{bmatrix} \tag{2}$$

$$\begin{bmatrix} I_d \\ I_q \end{bmatrix} = \frac{2}{3} * \begin{bmatrix} \cos\theta & \cos\theta - \frac{2*\pi}{3} & \cos\theta + \frac{2*\pi}{3} \\ -\sin\theta & -\sin\theta - \frac{2*\pi}{3} & -\sin\theta + \frac{2*\pi}{3} \end{bmatrix} \begin{bmatrix} I_a \\ I_b \\ I_c \end{bmatrix} \tag{3}$$

When the coordinate transformations are applied to the three phase equations of the motor, the voltage equations in the d- and q- axis of the IPM are as in (4) and (5).

$$V_d = R_s * I_d + L_d * \frac{dI_d}{dt} - L_q * \omega_e * I_q \tag{4}$$

$$V_q = R_s * I_q + L_q * \frac{dI_q}{dt} + L_d * \omega_e * I_d + \Psi_m * \omega_e \tag{5}$$

IPM torque and mechanical equations are given by (6) and (7). In (8) and (9), torque components are separated as torque due to magnets and reluctance torque. As can be seen from (8) and (9), the magnet-based torque depends on the magnetic flux linkage, and the reluctance torque depends on the difference of the d- and q- axis inductances.

$$T_e = \frac{3*p}{2} \left[\Psi_m * i_q + \left(L_d - L_q \right) * i_d * i_q \right] \tag{6}$$

$$\omega_m = \int \frac{T_e - T_m - B * \omega_m}{J} * dt \tag{7}$$

$$T_e^{Magnet} = \frac{3*p}{2} \left[\Psi_m * i_q \right] \tag{8}$$

$$T_e^{Reluctance} = \frac{3*p}{2} \left[\left(L_d - L_q \right) * i_d * i_q \right] \tag{9}$$

V_d,V_q are voltage magnitudes (Volt) and I_d, I_q are current magnitudes in dq- frame, ω_e and ω_m are the electrical and mechanical speed in rad/s, respectively, p is the pole-pair number, L_d and L_q are the inductance values of d- and q- axis, respectively, Ψ_m is the permanent magnet flux linkage (Weber) and R_s is the stator resistance (ohm). T_e is the electromagnetic torque in N.m. The saliency ratio of the motor is defined as the ratio of the q- axis inductance to the d- axis inductance and it is expressed by (10) [19].

$$\rho = \frac{L_q}{L_d} \tag{10}$$

In this study, it is aimed to analyse the torque production capability and the system efficiency of two IPM machines with different saliency ratios. In Figure 1, the schematic of the proposed control system for both motors is given.

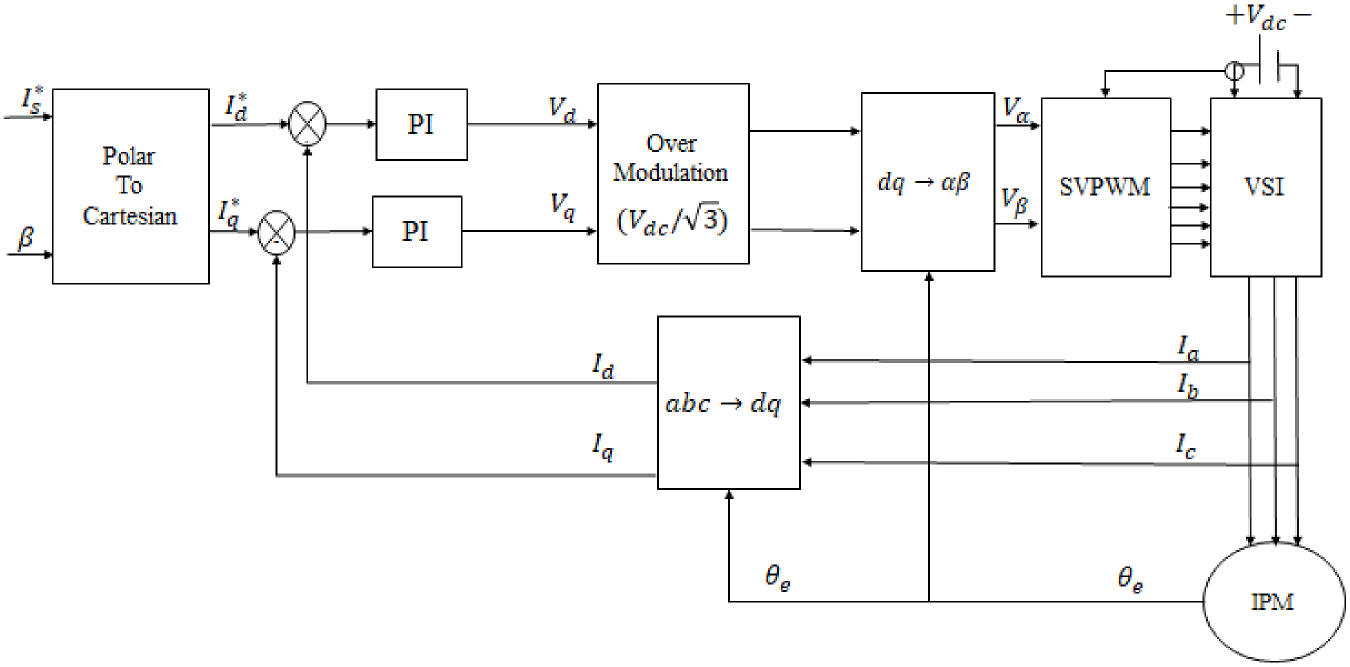

Figure 1 The proposed drive system schematic for both motors

2.2. Inverter and SVPWM technique

In (11-13), the function of the output phase voltages of the ideal inverter depending on the switching states are given. S_1, S_2 and S_3 represent the switching states.

$$V_a = \frac{V_{dc}}{3} * (2S_1 - S_2 - S_3) \tag{11}$$

$$V_b = \frac{V_{dc}}{3} * (2S_1 - S_2 - S_3) \tag{12}$$

$$V_c = \frac{V_{dc}}{3} * (2S_1 - S_2 - S_3) \tag{13}$$

After the control process is performed with PI controllers, voltage values are obtained in the d - and q- axes. For the application of the SVPWM technique, the voltage values in the d- and q- axes are transformed into the $\alpha\beta$ frame by inverse Park transformation. The angle of the voltage vector in the axes of the $\alpha\beta$ lies in the hexagonal structure in Figure 2. Sectors are determined according to the angle of the reference vector by dividing the 360° rotation path into 6 equal parts. Switching times are calculated according to sector information through equation (14-16).

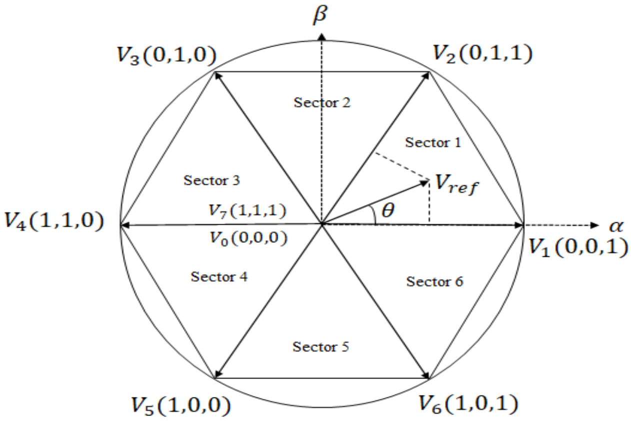

Figure 2 Hexagonal structure where the reference vector lies in

$$T_1 = \frac{\sqrt{3} * V_{ref}}{V_{DC}} * T_s * \sin((n * \frac{\pi}{3}) - \theta) \tag{14}$$

$$T_2 = \frac{\sqrt{3} * V_{ref}}{V_{DC}} * T_s * \sin((n * \frac{\pi}{3}) - \theta) \tag{15}$$

$$T_0 = T_s - (T_1 + T_2) \tag{16}$$

where, V_{dc} represents the battery voltage, V_{ref} is the magnitude of the reference vector, n is the sector information, T_S is the switching period, and θ is the angle of the reference vector.

3. SIMULATION RESULTS

The improved system performance with the increased saliency ratio is validated through the simulation studies in this section. The specifications of the two IPM motors are listed in Table 1. Two drives to be compared are implemented as shown in Figure 1. The two motors are operated at the 1000 rpm speed and the inverter switching frequency is set to 5 kHz. The motors with low and high saliency ratios are compared based on torque capability and the system efficiency in the following sections.

Table 1 The specifications of the two IPM motors

Motor Type	**IPM Machine 1**	**IPM Machine 2**
Phase Number/ Pole Number	3/8	
Nominal Speed	2500 rpm @120V DC	
Continuous Torque	15.7 Nm @51.6 Arms	
Continuous Power	4.1 kW @120V DC	
Input Voltage Range	12V-600 V	
Nominal d- Axes Inductance	0.282 mH	
Nominal q- Axes Inductance	0.828 mH	1.656 mH
Nominal PM Flux Linkage	0.0182 Weber	
Nominal Phase Resistance	0.0463 ohm	
Inertia	0.0072 kg.m^2	
Saliency Ratio	2.936	5.872

3.1. Torque production capabilities of the two motors

The two motors are operated at the same stator current magnitude values and the maximum produced electromagnetic torque with the two machines are presented in Figure 3. As can be seen from the Figure 3, the motor model with high saliency ratio is capable to generate higher output torque in the drive system.

In the motor drive system with low saliency ratio, 8.3 N.m average torque output is obtained when machine operates at 30 A, while the average torque production achieved by the higher salient machine is approximately 12.5 N.m. This implies that the twice the increase of the saliency ratio increases the torque production capability of the machine at the rate of 33.6% for the 30 A stator current magnitude operation.

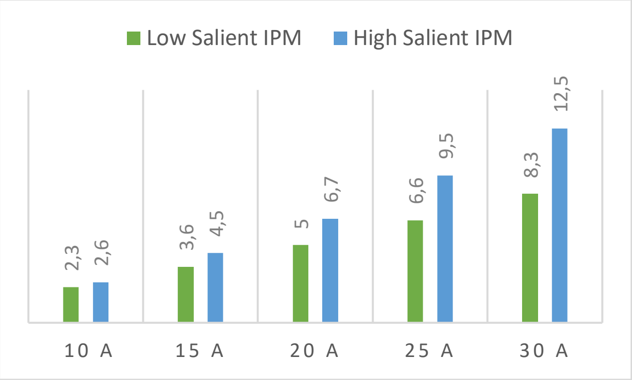

Figure 3 Torque production capabilities of the two machines (N.m)

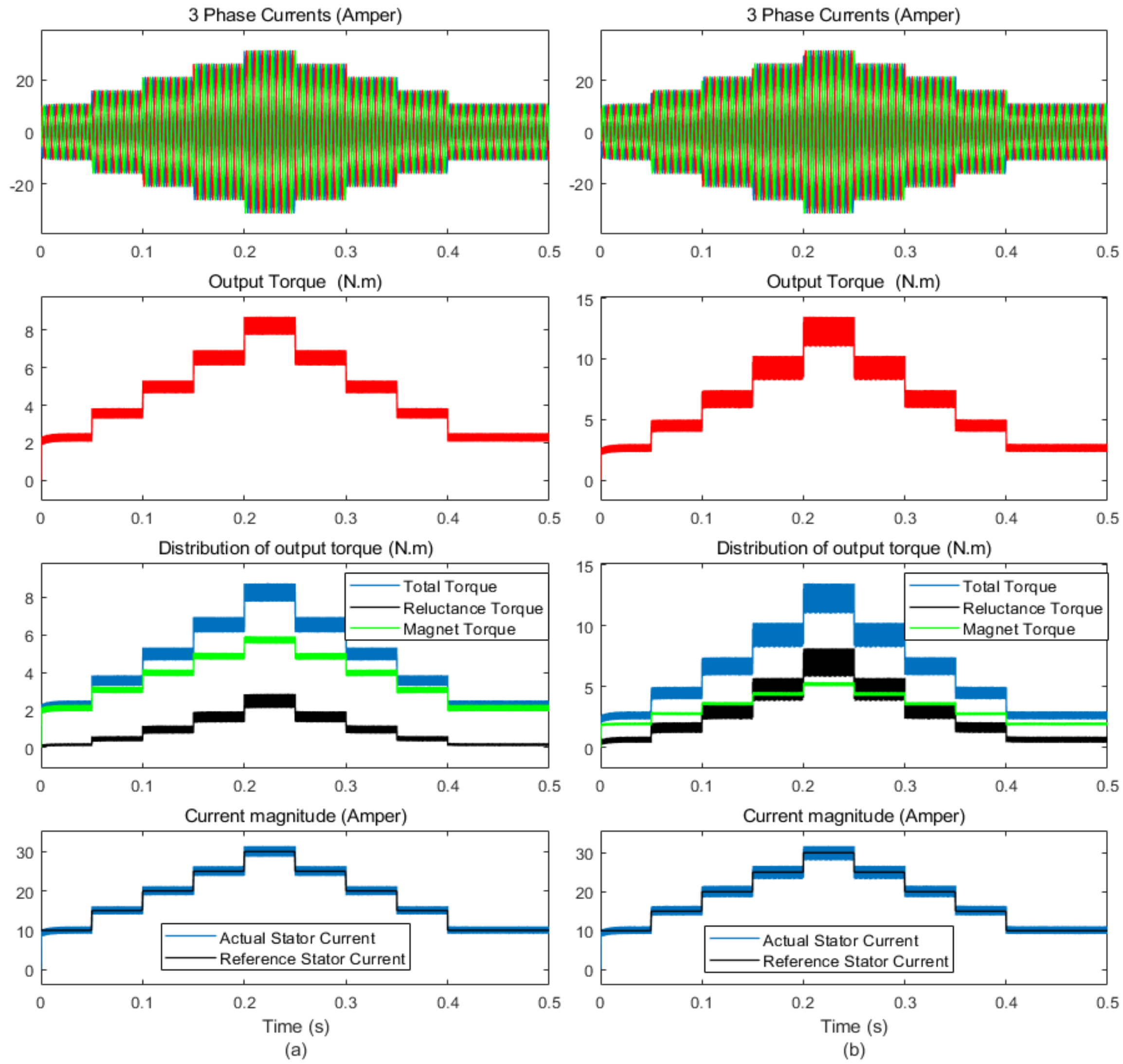

Figure 4 Maximum electromagnetic torque production with the two machines. (a) Low salient IPM (b) High salient IPM

The two machines have been operated to generate the maximum electromagnetic torque for given stator current magnitude commands and the results are illustrated in Figure 4. It is evident that the maximum electromagnetic torque production is higher in high salient machine than that of low salient machine since the utilization from the reluctance torque component increases in high salient machines while the magnet-based torque production slightly reduces. This implies that the achievement of the increased saliency ratio in IPM machines is a desired machine design criteria as the total torque can be increased by the utilization of the reluctance torque.

3.2. Efficiency analysis

Input and output powers of IPM machines are given in (17) and (18), respectively [20].

$$P_{input} = \frac{3}{2} * (V_d * I_d + V_q * I_q) \quad (17)$$

$$P_{output} = w_m * T_e \quad (18)$$

$$\eta(\%) = \frac{P_{output}}{P_{input}} * 100 \quad (19)$$

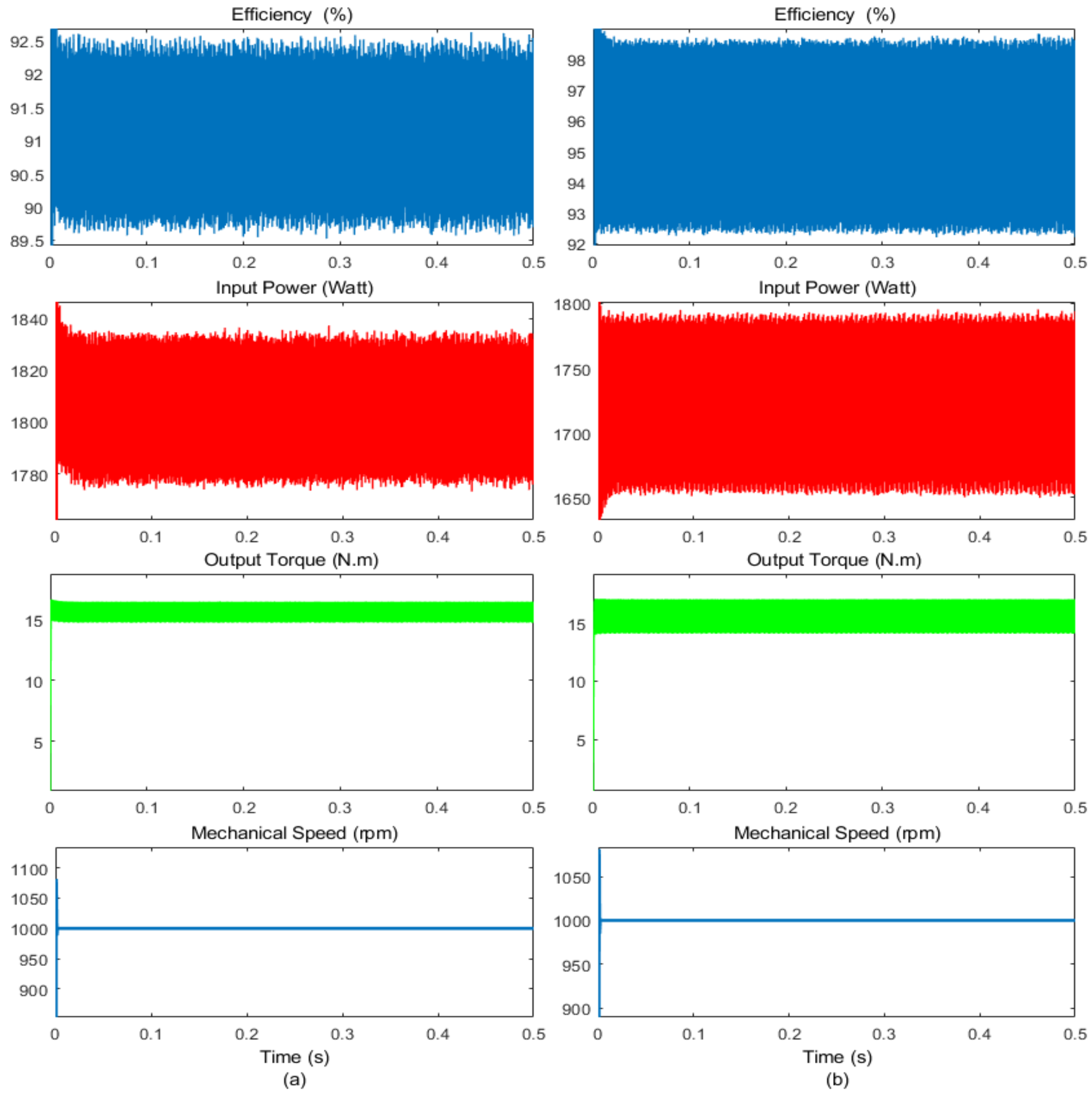

Figure 5 (a)Results with IPM Machine 1 (b) Results with IPM Machine 2

Figure 5 shows the efficiency results by operating the drive systems implemented for two different IPM models at continuous torque output (15.7 N.m) and 1000 rpm mechanical speed. Output powers of the two machines are the same based on (18) since the two drives are operated at the same speed and the same electromagnetic torque. On the other hand, the input powers of the two system show significant difference at the same certain operating point. While the average input power of the system is 1810 W for low salient drive, it is 1730 W for high salient machine. In the light of these results, the efficiency of the drive systems are 91% and 96% for low and high salient machines, respectively. Hence, 5% increase in the efficiency would be a significant improvement for high salient machines. Considering the two drive systems generate the same output torque production continuously at 1000 rpm, a battery pack of capacity 10 kWh would be consumed at 5 hours 31.5 minutes for low salient machines whereas it would be consumed at 5 hours 46.8 minutes for high salient machines. This implies that the high salient machine drive achieves the same output torque production 15.3 minutes longer than that of the low salient machine for the case study. Overall, the results validate how important it is to achieve the increased saliency ratio during machine design process.

4. CONCLUSION

The two IPM machines with a saliency ratio of 2.93 and 5.86 have been compared and its effect on output torque production and on the efficiencies of the drive systems have been analysed comprehensively. The comparisons are made by realistic high performance IPM drives and the results have been discussed in detail. It has been validated that the increase of the saliency ratio increases the torque production capability of the drive system while the operation speed and the stator current magnitude are the same. Accordingly, the system efficiency increases dramatically by the increase of the saliency ratio. It has been shown that the torque production capability of the machine would increase 33.6% while the machine operates at 30 A stator current magnitude. Also, system efficiency increased by 5% when tested at 1000 rpm speed and continuous torque (15.7 N.m). The results validate how significant it is to achieve the increased saliency ratio as an attractive design criterion.

Acknowledgement

The authors would like to thank the Scientific and Technological Research Council of Turkey (TUBITAK) for contributing to the financial portion of the project.

Funding

This study has been supported by the Scientific and Technological Research Council of Turkey (TUBITAK) through the Scientific and Technological Research Projects Funding Program (1001) with a project numbered as 118E858.

The Declaration of Conflict of Interest/ Common Interest

No conflict of interest or common interest has been declared by the authors.

Authors' Contribution

The authors contributed equally to the study.

The Declaration of Ethics Committee Approval

The authors declare that this document does not require an ethics committee approval or any special permission.

The Declaration of Research and Publication Ethics

The authors of the paper declare that they comply with the scientific, ethical and quotation rules of SAUJS in all processes of the article and that they do not make any falsification on the data collected. In addition, they declare that Sakarya University Journal of Science and its editorial board have no responsibility for any ethical violations that may be encountered, and that this study has not been evaluated in any academic publication environment other than Sakarya University Journal of Science.

REFERENCES

[1] M. Koç, “Efficiency Optimised Control Of Interior Mounted Permanent Magnet Machines For Electric Vehicle Traction”, PhD. Thesis in Department of Electronic and Electrical Engineering. 2016, The University of Sheffield, p.219.

[2] M. Abassi, A. Khlaief, O. Saadaoui, A. Chaari and M. Boussak, "Performance analysis of FOC and DTC for PMSM drives using SVPWM technique," 2015 16th International Conference on Sciences and Techniques of Automatic Control and Computer Engineering (STA), pp. 228-233, 2015.

[3] Z. Wang, T. W. Ching, S. Huang, H. Wang and T. Xu, "Challenges Faced by Electric Vehicle Motors and Their Solutions," in IEEE Access, vol. 9, pp. 5228-5249, 2021.

[4] Z. Zhang et al., "A Deadbeat PI Controller With Modified Feedforward for PMSM Under Low Carrier Ratio," in IEEE Access, vol. 9, pp. 63463-63474, 2021.

[5] D. Yu, X. Y. Huang, Y. T. Fang and J. Zhang, "Design and comparison of interior permanent magnet synchronous

traction motors for high speed railway applications," 2017 IEEE Workshop on Electrical Machines Design, Control and Diagnosis (WEMDCD*)*, pp. 58-62, 2017.

[6] S. K. Dwivedi, M. Laursen and S. Hansen, "Voltage vector based control for PMSM in industry applications," 2010 IEEE International Symposium on Industrial Electronics, pp. 3845-3850, 2010.

[7] L. K. Jisha and A. A. Powly Thomas, "A comparative study on scalar and vector control of Induction motor drives," 2013 International conference on Circuits, Controls and Communications (CCUBE*)*, pp. 1-5, 2013.

[8] A. Oprea and D. Floricau, "Field Oriented Control of Permanent Magnet Synchronous Motor with Graphical User Interface," 2021 12th International Symposium on Advanced Topics in Electrical Engineering (ATEE*)*, pp. 1-4, 2021.

[9] M. S. Reddy, V. S. R. Subrahmanyam, C. S. Prakash and G. V. S. U. Shankar, "Performance analysis of Fuzzy and Neural controller implementation in permanent magnet synchronous motor," 2021 5th International Conference on Intelligent Computing and Control Systems (ICICCS), pp. 566-574, 2021.

[10] A. Srivastava, A. Chauhan and A. Tripathi, "Comparative Analysis Of Two-Level &; Three-Level Svpwm Based DTC IM Drives," 2021 International Conference on Artificial Intelligence and Smart Systems (ICAIS), pp. 1612-1618, 2021.

[11] P. Yunhao, Y. Dejun and H. Yansong, "The stator flux linkage adaptive SVM-DTC control strategy of permanent magnet synchronous motor," 2021 6th Asia Conference on Power and Electrical Engineering (ACPEE), pp. 826-831, 2021.

[12] F. Korkmaz, İ. Topaloğlu, M. F. Çakir and R. Gürbüz, "Comparative performance evaluation of FOC and DTC controlled PMSM drives," 4th International Conference on Power Engineering, Energy and Electrical Drives, pp. 705-708, 2013.

[13] M. K. Waghmare and S. V. Patil, "Speed Control Strategy of Permanent Magnet Synchronous Motor Drive Using SPWM Technique," 2019 4th International Conference on Recent Trends on Electronics, Information, Communication & Technology (RTEICT), pp. 1328-1332, 2019.

[14] Z. Han and J. Liu, "Comparative Analysis of Vibration and Noise in IPMSM Considering the Effect of MTPA Control Algorithms for Electric Vehicles," in IEEE Transactions on Power Electronics, vol. 36, no. 6, pp. 6850-6862, 2021.

[15] X. Li, D. Xi and Y. Zhang, "Permanent magnet synchronous motor vector control based on MATLAB/Simulink," 2017 First International Conference on Electronics Instrumentation & Information Systems (EIIS), pp. 1-6, 2017.

[16] L. Yu, C. Wang, H. Shi, R. Xin and L. Wang, "Simulation of PMSM field-oriented control based on SVPWM," 2017 29th Chinese Control And Decision Conference (CCDC), pp. 7407-7411, 2017.

[17] D. Rathnakumar, J. LakshmanaPerumal and T. Srinivasan, "A new software implementation of space vector PWM," Proceedings. IEEE SoutheastCon, 2005. pp. 131-136, 2005.

[18] S. Srivastava and M. A. Chaudhari, "Comparison of SVPWM and SPWM Schemes for NPC Multilevel Inverter," 2020 IEEE International

Students' Conference on Electrical,Electronics and Computer Science (SCEECS), pp. 1-6, 2020.

[19] P. Yulong, L. Yue., Y. Yanjun., S. Yanwen., C. Feng., “Increasing the saliency ratio of fractional slot concentrated winding interior permanent magnet synchronous motors.” IET Electric Power Applications, vol. 9, pp. 439-448, 2015.

[20] M. Koç, S. Emiroğlu, B. Tamyürek. "Analysis and simulation of efficiency optimized IPM drives in constant torque region with reduced computational burden." Turk J Elec Eng & Comp Sci vol. 29, pp. 1643 – 1658, 2021.

SAKARYA ÜNİVERSİTESİ
FEN BİLİMLERİ ENSTİTÜSÜ
DERGİSİ

Sakarya University Journal of Science
SAUJS

e-ISSN 2147-835X Founded 1997 Period Bimonthly Publisher Sakarya University
http://www.saujs.sakarya.edu.tr/en/

Title: Development and Validation of RP-HPLC Method for the Determination of Dexrabeprazole Sodium

Authors: Semra YILMAZER KESKİN, Ebru Nurdan ŞENTÜRK, Cihansel UNLU

Recieved: 2021-09-24 00:00:00

Accepted: 2021-11-15 00:00:00

Article Type: Research Article

Volume: 25
Issue: 6
Month: December
Year: 2021
Pages: 1427-1431

How to cite
Semra YILMAZER KESKİN, Ebru Nurdan ŞENTÜRK, Cihansel UNLU; (2021), Development and Validation of RP-HPLC Method for the Determination of Dexrabeprazole Sodium. Sakarya University Journal of Science, 25(6), 1427-1431, DOI: https://doi.org/10.16984/saufenbilder.999458
Access link
http://www.saujs.sakarya.edu.tr/tr/pub/issue/66341/999458

Sakarya University Journal of Science 25(6), 1427-1431, 2021

Development and Validation of RP-HPLC Method for the Determination of Dexrabeprazole Sodium

Semra YILMAZER KESKİN*[1], Ebru Nurdan ŞENTÜRK[1], Cihansel UNLU[1]

Abstract

A rapid and simple liquid chromatographic method was developed for the quantitative determination of dexrabeprazole sodium in the tablet dosage form. The reverse-phase chromatographic analysis was carried out by using a C-18 column. The acetonitrile-phosphate buffer mixture was used as the mobile phase. The obtained retention time was 4.33 ∓ 0.02 min. by using 50:50 (v:v) acetonitrile:phosphate buffer(pH 7) and 1.0 mL/min. flow rate. Quantification of the analyte was based on measuring the peaks areas at 272 nm. The analytical performance of the developed RP-HPLC method was validated with respect to accuracy, precision, linearity, stability, and robustness. The obtained linearity range was 77-143 mg/L and the correlation coefficient was 0.9989. The obtained LOD and LOQ values were 0.010 mg/L and 0.034 mg/L, respectively.

Keywords: Dexrabeprazole, RP-HPLC, validation

1. INTRODUCTION

Dexrabeprazole sodium (DEX) is R (+)-isomer of rabeprazole. Rabeprazole has been used in the treatment of gastroesophageal reflux disease by suppressing gastric acid secretion. It acts as a proton pump inhibitor of the H^+/K^+ ATPase enzyme [1,2]. Several methods were described for the analyses of the racemic mixture of rabeprazole in pharmaceutical formulations and plasma samples. HPLC techniques are the best methods due to their rapid, low cost, and selective properties. These techniques are very useful for the simultaneous determination of pharmaceutically active compounds and ingredients in drugs, biological fluids and tissues [3]. Kim et al. [4] used a chiral column. The stationary phase of the chiral column was modified with cellulose. A mixture of ethanol, hexane, and ethylenediamine solutions was used as a mobile phase. The developed HPLC method assayed rabeprazole enantiomers determination in commercial tablets. The reported LOQ value was and 0.03 μg/mL and the LOD value was 0.01 μg/mL. Similarly, Miura et al. [5] investigated quantitative enantiomers of rabeprazole and their metabolites determination in human plasma. A chiral column was used. The mobile phase consisted of acetonitrile and $NaClO_4$. The achieved LOQ was 5 ng/mL. Su et al. [6] proposed an SFC-MS method to determine

---

* Corresponding author: syilmazer@sakarya.edu.tr
[1] Sakarya University, Faculty of Arts and Sciences, Department of Chemistry
E-mail: senturkkebruu@gmail.com, cihnsel.unlu@ogr.sakarya.edu.tr
ORCID: https://orcid.org/0000-0002-9467-3171, https://orcid.org/0000-0003-1496-4284, https://orcid.org/0000-0001-5676-4323

enantiomers of rabeprazole in dog plasma. They used using a supercritical fluid compatible chiral column. The used mobile phase consists of CO_2 and methanol. The obtained linearity was in the range of 1–1000 ng/mL. Also, some studies are available using the drugs' name as dexrabeprazole. Shedpure et al. [7] developed a first-order derivative spectroscopic method to determine domperidone maleate and dexrabeprazole sodium in capsule and bulk forms. The reported LOQ and LOD values were 1.28 µg and 0.75 µg, respectively. Khadangale et al. [8] determined impurities in dexrabeprazole sodium with an RP-UPLC. A C18 column was used as a stationary phase. The developed method was based on a gradient program. A mixture of phosphate buffer and acetonitrile was used as the first mobile phase. The second mobile phase contained acetonitrile and methanol. The reported LOD was 0.0075 ppm and LOQ was 0.023 ppm for the determination of dexrabeprazole sodium. Chitlange et al. [9] investigated simultaneous determination of domperidone and dexrabeprazole in the pharmaceutical dosage form. They used RP-HPLC method with a C-18 column as a stationary phase. The used mobile phase was a mixture of potassium dihydrogen orthophosphate buffer and acetonitrile.

In this study, dexrabeprazole sodium was determined in single dosage tablet form by the RP-HPLC method. A C18 column was used in the method. The developed RP-HPLC method was optimized and validated with accuracy, precision, linearity, and robustness according to the International Conference on Harmonization (ICH) guidelines [10].

2. MATERIALS AND METHODS

The stock solution (100 mg/L) of DEX was prepared in 50 mL acetonitrile. The serial concentrations of the calibration standard solutions (77 - 143 mg/L) were prepared from the stock solution by dilution. A calibration graph was obtained by using peak areas of the DEX. The commercial pharmaceutical analysis was performed in drug tablets containing 10 mg DEX. 20 tablet forms of the drug were taken, then weighed and powdered. The sample solutions were prepared by weighting two tablets amount and dissolving them in acetonitrile. The obtained solutions were filtered with 0.45 µm membrane filter. The final solutions were diluted to concentration of 100 mg/L DEX.

A Shimadzu UV 2401PC UV-VIS spectrophotometer with a 1 nm slit width was used for the absorption measurements. Chromatography was performed with an HPLC system (Shimadzu, Japan) equipped with an automated sample injector, a pump, and a UV–Vis DAD detector. The used stationary phase was a reverse-phase C18 column (250 mm × 4.6 mm × 5 µm, GL Sciences) and the temperature of the column oven was fixed 25 °C. The isocratic mode was used with 1.0 mL/min flow rate and the sample injection volume was 10 µL. A mixture of acetonitrile and phosphate buffer (pH 7) (50:50 v/v) was used as the mobile phase that was freshly prepared and filtered with a 0.45 µm membrane filter. Data treatments, regressions and statistical analysis were performed using EXCEL software.

3. RESULTS AND DISCUSSION

3.1. Optimization of experimental conditions

The UV–Vis absorption of DEX was measured between 200 and 800 nm region to find maximum absorption wavelength. The maximum absorption band was observed at 272 nm. The optimum experimental conditions of RP-HPLC were determined by examining flow rate, mobile phase composition, detector wavelength, and sample injection volume. The tested mobile phase compositions were 50:50 (v/v), 70:30 (v/v), 80:20 (v/v) of acetonitrile:phosphate buffer(pH 7) and the flow rates were ranging from 0.8 to 1.5. The peak of DEX was obtained in a short time with high intensity in 50:50 (v/v) acetonitrile:phosphate buffer as the mobile phase (Figure 1) at 1.0 mL/min flow rate. The found retention time was 4.2 min. at these conditions. The system suitability parameters (retention time, RT; theoretical plate, N and tailing, T) were calculated by six replicate injections of 10 µL standard solution. The found RT, N, and T values were 4.323, 5532, and 1.169, respectively. The calibration curve was obtained by plotting peak areas versus concentrations of DEX solutions (Figure 2). The used DEX concentrations were range from 77 to 143 mg/L. The calibration equation and statistical parameters are summarized in Table 1.

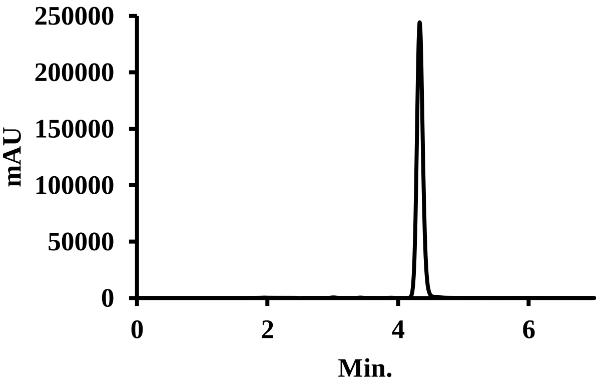

Figure 1 HPLC chromatogram of DEX (100 mg/L) at 272 nm

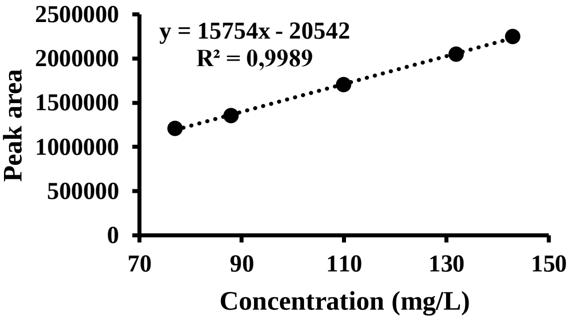

Figure 2 Calibration curve of DEX at 272 nm

Table 1 Statistical results of calibration curve

Method	RP-HPLC
λ (nm)	272
Regression equation	y=15753602.55x-20541.75
r	0.9989
SE(m)	303.70
SE(n)	34264.44
SE(r)	17034.23

r = Regression coefficient; SE(r) = Standard error of linear regression; SE(m) = Standard error of slope; SE(n) = Standard error of intercept.

3.2. Method validation

Linearity, precision, accuracy, solution stability, and robustness parameters were tested for the validation of the proposed method. The obtained linearity of the method was in the range of 77-143 mg/L. The calculated LOD and LOQ values were 0.010 mg/L and 0.034 mg/L, respectively. The method precision was performed with six replicates of 100 mg/L standard solution DEX. The intra-day and inter-day assays were carried out. The calculated standard deviations and relative standard deviations are shown in Table 2. Accuracy studies were carried out using standard solutions of 88 mg/L, 110 mg/L, and 132 mg/L DEX concentrations. The calculated recoveries and relative standard deviations are shown in Table 3. The standard solution (100 mg/L DEX) stability tests were carried out at room temperature (25 °C) for 24 hours and +4 °C for 30 days. No significant peak was observed in the chromatogram kept at room temperature (Figure 3a). Therefore, it can be stated that the standard solution of DEX could remain stable for 24 hours at room temperature. However, the degradation occurred in the other solution, which was kept at +4 °C after 30 days. New peaks were observed in the chromatogram (Figure 3b). The robustness of the proposed method was investigated by changing chromatographic conditions such as mobile phase compositions, column oven temperature, and flow rate. The mobile phase composition was changed from 50:50 (ACN : phosphate buffer, v:v) to 44:56 (v:v) and 36:64 (v:v). The column oven temperature was adjusted to 20.5, 22.5, and 25 °C and the flow rate was set to 0.9 mL/min., 1.0 mL/min. and 1.1 mL/min. The obtained retention times under the examined conditions are shown in Table 4.

Table 2 Results of intra-day and inter-day assays

Concentration (mg/L)	**Intra-day (mg/L)**	**Inter-day (mg/L)**
100	99	99
100	100	99
100	100	99
100	100	99
100	99	100
100	100	99
Mean	99.67	99.17
SD	0.471	0.373
RSD	0.473	0.376

SD = Standard deviation; RSD = Relative standard deviation

Table 3 Recoveries of DEX

Added mg/L	**Found mg/L**	**% Recovery**
0.088	0.090	102.27
0.088	0.089	101.14
0.088	0.089	101.14
0.110	0.111	100.91
0.110	0.109	99.09
0.110	0.111	100.91

0.132	0.131	99.24
0.132	0.132	100.00
0.132	0.134	101.52
	Mean:	100.69
	SD	1.05
	RSD	1.04

SD = Standard deviation; RSD = Relative standard deviation

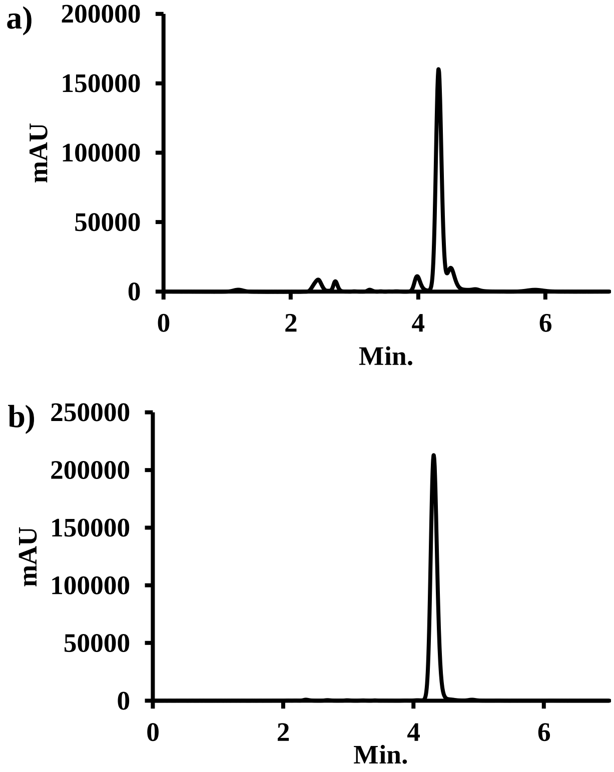

Figure 3 HPLC chromatograms of solution kept in room temperature for 1 day (a), in +4 °C for 30 days (b)

Table 4 The retention times at different chromatographic conditions

Mobile phase (ACN:buffer) v:v	Flow rate mL/min	Temperature °C	RT min
50:50	1.0	25.0	4.33
44:56	1.0	25.0	4.34
36:64	1.0	25.0	4.21
50:50	0.9	25.0	4.36
50:50	1.1	25.0	4.12
50:50	1.0	20.5	4.31
50:50	1.0	22.5	4.32
		Mean	4.28
		SD	0.08
		RSD	1.88

SD = Standard deviation; RSD = Relative standard deviation

3.3. Analyses of Pharmaceutical Tablet Samples

The optimized HPLC method was evaluated in the commercial tablets' assay to determine DEX in drug form. Six replicate determinations were carried out. The obtained results (Table 5) were in good agreement with the label claims. The recovery percentages were range from 90% to 100%.

Table 5 Analysis results of DEX in pharmaceutical tablets

Claimed value mg	Found mg
10	9.951
	10.042
	10.048
	9.971
	10.049
	9.939
Mean	10.000
SD	0.047
RSD	0.473

SD = Standard deviation; RSD = Relative standard deviation

4. CONCLUSIONS

A simple and rapid RP-HPLC procedure was developed for DEX determination in synthetic solution and commercial tablet form. The proposed chromatographic method was validated with respect to linearity, robustness, precision, and accuracy as per ICH guidelines. The calibration curve was obtained in 77–143 mg/L with a correlation coefficient of 0.9989. The calculated LOD and LOQ values were 0.010 mg/L and 0.034 mg/L, respectively. The calculated RSDs of all examined parameters were less than 2.00%. The optimized method was also successfully applied to the tablet form.

Funding

The authors have not received any financial support for the research, authorship, or publication of this study.

The Declaration of Conflict of Interest/ Common Interest

No conflict of interest or common interest has been declared by the authors.

Authors' Contribution

The first author contributed 40%, the second author 40%, the third author 20%.

The Declaration of Ethics Committee Approval

This study does not require ethics committee permission or any special permission.

The Declaration of Research and Publication Ethics

The authors of the paper declare that they comply with the scientific, ethical and quotation rules of SAUJS in all processes of the paper and that they do not make any falsification on the data collected. In addition, they declare that Sakarya University Journal of Science and its editorial board have no responsibility for any ethical violations that may be encountered and that this study has not been evaluated in any academic publication environment other than Sakarya University Journal of Science.

REFERENCES

[1] X. M. Xia, H. Wang, "Gastroesophageal reflux disease relief in patients treated with rabeprazole 20 mg versus omeprazole 20 mg: a meta-analysis, Gastroenterol. Res. Pract. **2013**.

[2] S. S. Chitlange, A. I.Mulla, G. R. Pawbake, S. B. Wankhede, "Simultaneous spectrophotometric estimation of telmisartan and ındapamide in capsule dosage form," Int. J. Pharm. Qual. Assur., vol. 2, no. 2, pp. 31–34, 2010.

[3] M. Gülfen, Y. Canbaz, A. Özdemir, "Simultaneous determination of amoxicillin, lansoprazole, and levofloxacin in pharmaceuticals by HPLC with UV–Vis detector," J. Anal. Test. vol. 4, no. 1, pp. 45-53, 2020.

[4] M. Kim, S. K. Yu, Q. K. Truong, X. L. Mai, H. K. Chung, J. S. Kang, K. H. Kim, "Determination of rabeprazole enantiomers in commercial tablets using ımmobilized cellulose-based stationary phase," Arch. Pharm. Res., vol. 40, no. 3, pp. 373-381, 2017.

[5] M. Miura, H. Tada, S. Satoh, T. Habuchi, T. Suzuki, "Determination of rabeprazole enantiomers and their metabolites by high-performance liquid chromatography with solid-phase extraction," J. Pharm. Biomed. Anal. vol. 41, no. 2, pp. 565-570, 2006.

[6] C. Su, H. Yang, X. Meng, J. P. Fawcett, J. Cao, Y. Yang, J. Gu, "Determination of Rabeprazole enantiomers in dog plasma by supercritical fluid chromatography tandem mass spectrometry and ıts application to a pharmacokinetic study," J. Sep. Sci., vol. 40, no. 4, pp. 1010-1016, 2017.

[7] P. S. Shedpure, P. A. Patel, S. D. Sawant, M. N. Dole, "Spectrophotometeric determination of dexrabeprazole sodium and domperidone maleate in bulk and capsule dosage form by first order derivative spectroscopy," Res. J. Pharm. Technol., vol. 4, no. 7, pp. 10886-1089, 2011.

[8] S. T. Khadangale, V. M. Dhalape, R. V. Pinjari, "Development and validation of rapid, sensitive RP-UPLC method for determination of related ımpurities in dexrabeprazole sodium," Orient. J. Chem. vol. 34, no. 5, pp. 2425-2434, 2018.

[9] S. S. Chitlange, A. I. Mulla, G. R. Pawbake, S. B. A. Wankhede, "A validated RP-HPLC method for simultaneous estimation of dexrabeprazole and domperidone in pharmaceutical dosage form," Der Pharm. Sin., vol. 1, no. 1, pp. 42-47, 2010.

[10] E. M. European Medicines Agency: An Unacceptable Choice Prescrire Int. vol. 20, no. 121, pp. 278, 2011.

SAKARYA ÜNİVERSİTESİ
FEN BİLİMLERİ ENSTİTÜSÜ
DERGİSİ

Sakarya University Journal of Science
SAUJS

e-ISSN 2147-835X Founded 1997 Period Bimonthly Publisher Sakarya University
http://www.saujs.sakarya.edu.tr/en/

Title: Spectrophotometric Determination of Losartan Potassium and Hydrochlorothiazide in tablets by Wavelet Transform Approach

Authors: Özgür ÜSTÜNDAĞ, Erdal DİNÇ

Recieved: 2021-09-01 00:00:00

Accepted: 2021-11-16 00:00:00

Article Type: Research Article

Volume: 25
Issue: 6
Month: December
Year: 2021
Pages: 1432-1437

How to cite
Özgür ÜSTÜNDAĞ, Erdal DİNÇ; (2021), Spectrophotometric Determination of Losartan Potassium and Hydrochlorothiazide in tablets by Wavelet Transform Approach. Sakarya University Journal of Science, 25(6), 1432-1437, DOI: https://doi.org/10.16984/saufenbilder.989654

Sakarya University Journal of Science 25(6), 1432-1437, 2021

Spectrophotometric Determination of Losartan Potassium and Hydrochlorothiazide in tablets by Wavelet Transform Approach

Özgür ÜSTÜNDAĞ*[1], Erdal DİNÇ[1]

Abstract

A precise, rapid and simple spectrophotometric method development with continuous wavelet transform technique was described in this paper for the simultaneous determination of losartan potassium and hydrochlorothiazide in tablets. The continuous wavelet transform approach based on the application of Symlets5-CWT. If the original UV spectra of losartan potassium and hydrochlorothiazide are examined, it is seen that the spectra of these two substances strongly overlap. With the developed Symlets5-CWT method, the analysis was carried out successfully without any pre-separation process. The calibration equations were obtained at 247.7 nm for the losartan potassium determination and at 259.1 nm for the hydrochlorothiazide determination, respectively. The developed methods were tested in terms of validity and applicability.

Keywords: Spectrophotometry, Continuous wavelet transform, Losartan potassium, Hydrochlorothiazide, Quantitative determination

1. INTRODUCTION

Nowadays, researchers seek to meet the needs of better scientific measurements or to evolve more efficient procedures and increase the reliability of existing analytical methods to achieve the desired analytical results in many disciplines and the aforementioned fields [1-3].

For analytical studies, LC and CE methods have been used in conjunction with different spectroscopic systems (separate techniques, namely LC-MS and CE-MS) to obtain more chemical data and reduce the complication of multicomponent substance analysis. Furthermore, these combined unit methods involve high costs and time for analysis [4-6]. Analytical methods such as spectrophotometry [7], mass-spectrometry [8], chromatography [9] and electrophoresis [10], electrochemistry [11] and their joint devices have been used for analytical purposes. Herewith the disadvantages of the mentioned separation techniques or combination analyzers, analytical chemists opt to use spectroscopic methods (rather than separation techniques) to enable rapid analysis at low cost. Nowadays, applications of continuous wavelet transform (CWT) methods to the spectrophotometric data gaining popularity because it can be used in the analysis of components in complex systems without the need for any separation process. Therefore, CWT methods can offer suitable solutions for such cases. [12-14]. In this paper, the aim is is to

---

* Corresponding author: ustundag@pharmacy.ankara.edu.tr

[1] Ankara University, Faculty of Pharmacy, Department of Basic Pharmaceutical Sciences

E-mail: dinc@ankara.edu.tr

ORCID: https://orcid.org/0000-0001-9611-4210, https://orcid.org/0000-0001-6326-1441

develop new signal processing method based on the combined use of CWT with zero crossing technique simultaneous quantitative determination of losartan potassium (LOS) and hydrochlorothiazide (HCT) in tablets without the use of a separation step. Several analytical methods for the analysis of LOS and HCT have been reported in pharmaceutical and biological studies, including spectrophotometric methods [15-18], spectrofluorometric method [19] and chromatographic methods [20-24].

2. MATERIAL AND METHOD

The absorption spectra of mixtures and tablet solutions in the spectral range 200-305 nm were measured by a Shimadzu UV-1601 dual-beam UV-VIS spectrophotometer with a constant gap width (2 nm).

2.1. Commercial Tablet

A pharmaceutical tablet (HYZAAR® Tablet, MSD Ind., Istanbul, Turkey) including 50 mg LOS and 12.5 mg HCT per tablet was gathered from the Turkish market.

2.2. Standard solutions

Standard LOS and HCT stock solutions were arranged respectively by dissolving 25 mg of each drug in 100 mL of methanol. A calibration ranges between 4.0-26.0 μg ml^{-1} for LOS and 2.0-24 μg ml^{-1} HCT in solvent was prepared for spectrum analysis from standard stock solutions for each active ingredient.

2.3. Sample solutions preparation

For testing tablets; twenty tablets of LOS and HCT were weighed and powdered. Transfer an equal amount of powder to a 100 ml volumetric flask and solved with methanol. The contents of the flask were mechanically stirred. After filtration, the supernatant is diluted with methanol to an ultimate concentration. This procedure was repeated ten times.

3. RESULTS AND DISCUSSION

The purpose of this work is to apply the Symlets5-CWT (SYM5-CWT) method to the spectra of LOS and HCT in mixtures and preparations for the simultaneous assay. The LOS and HCT standards and the UV spectra of the tablet solution were measured between 200 and 305 nm as can be seen in Figure 1.

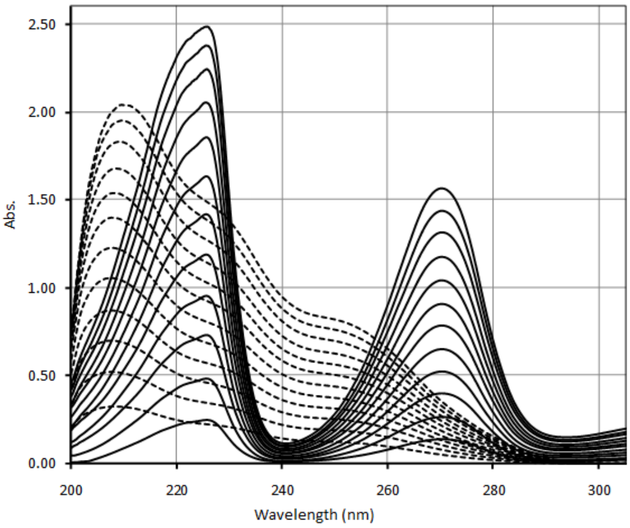

Figure 1 The UV-Absorption spectra of 4.0-26 μg mL^{-1} LOS (---) and 2.0-24 μg mL^{-1} HCT (—) in methanol

3.1. Symlets5 Continuous Wavelet Transform Method (SYM5-CWT)

For the analysis of artificial mixtures and tablets containing LOS and HCT compounds by the SYM5-CWT method, calibration mixtures were prepared as described in the above section, using methanol as a solvent in a linear concentration range of 4.0-26 μg mL^{-1} for LOS and 2.0-24 μg mL^{-1} for HCT. The original UV spectra of these calibration solutions were recorded in the 200-305 nm wavelength range with $\Delta\lambda = 0.1$ nm intervals. The SYM5-CWT method applied to the spectra of LOS and HCT (Figure 2). Regression equation, correlation coefficient and their statistical data were shown in Table 1. The calibration equation of the SYM5-CWT method was validated by using the quantitative assay of artificial mixtures. Recovery results and with relative standard deviation were shown in Table 2.

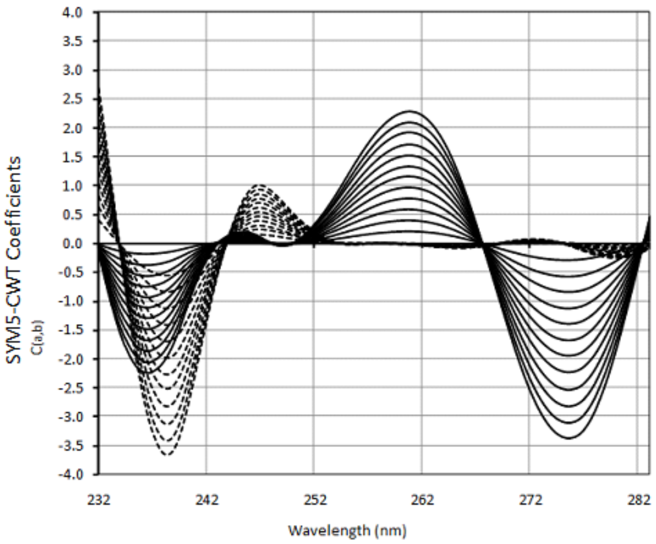

Figure 2 SYM5-CWT spectra obtained by transforming the UV absorption spectra of LOS (---) and HCT (—)

The outcome of the regression analysis obtained are shown in Table 1. The amounts of LOS and HCT in the samples were computed using the calibration equations obtained from the linear regression analysis in Table 1.

Table1 Statistical outcome for the SYM5-CWT method

Method	**SYM5-CWT**	
Parameter	**LOS**	**HCT**
λ (nm)	247.7	259.1
m	3.63×10^{-2}	8.93×10^{-2}
n	5.06×10^{-4}	1.74×10^{-2}
r	0.9999	0.9998
SE(m)	1.76×10^{-3}	1.90×10^{-4}
SE(n)	1.06×10^{-4}	2.79×10^{-3}
SE(r)	2.54×10^{-3}	4.54×10^{-3}
LOD	0.54	0.35
LOQ	1.81	1.17

3.2. Validation of the Proposed Methods

A validation kit consisting of 16 artificial solutions of dissimilar concentrations in methanol in a working range of 4.0-36.0 µg ml^{-1} for LOS and 2.0-9.0 µg ml^{-1} HCT was produced. This validation set tested the accuracy and precision of the SYM5-CWT method. The results gathered by performing the SYM5-CWT method to artificial mixtures prepared as a verification set are shown in Table 2.

Table 2 Recovery outcome calculated by using artificial mixtures

	Intra-day Results					
	Added (µg mL^{-1})	**Found (µg mL^{-1})**	**SD**	**RSD**	**RE**	**Recovery (%)**
LOS	4	3.95	0.09	2.21	-0.90	98.8
	16	15.91	0.14	0.91	-0.37	99.5
	20	21.06	0.15	0.70	0.29	105.3
HCT	4	4.08	0.05	1.27	0.52	101.9
	16	15.71	0.25	1.60	-0.65	98.2
	20	19.75	0.21	1.07	-0.44	98.8
	Inter-day Results					
LOS	4	4.02	0.04	0.92	0.38	100.4
	16	15.97	0.29	1.83	-0.75	99.8
	20	20.45	0.52	2.53	1.03	102.2
HCT	4	4.07	0.04	0.89	0.36	101.7
	16	15.90	0.19	1.20	-0.49	99.4
	20	20.28	0.36	1.76	0.72	101.4

Table 3 Intra-day and inter-day outcome by the SYM5-CWT method

SYM5-CWT					
Added (µg mL^{-1})		**Found (µg mL^{-1})**		**Recovery (%)**	
LOS	**HCT**	**LOS**	**HCT**	**LOS**	**HCT**
4	6	4.02	5.90	100.5	98.4
6	6	5.93	5.90	98.9	98.3
8	6	7.97	5.89	99.6	98.2
10	6	10.01	5.94	100.1	98.9
12	6	11.91	5.87	99.2	97.8
14	6	13.90	5.78	99.3	96.4
16	6	15.89	5.86	99.3	97.7
18	6	18.17	5.99	100.9	99.9
20	6	19.92	5.75	99.6	95.8
22	6	21.92	5.89	99.6	98.1
24	6	23.83	5.90	99.3	98.4
26	6	25.74	5.90	99.0	98.4
24	2	23.94	1.95	99.7	97.7
24	4	23.95	3.95	99.8	98.6
24	6	24.02	5.88	100.1	98.1
24	8	23.89	7.84	99.5	98.0
24	10	24.07	9.91	100.3	99.1
24	12	24.00	11.90	100.0	99.2
24	14	24.18	13.87	100.7	99.1
24	16	24.20	15.87	100.8	99.2
24	18	24.30	17.62	101.3	97.9
24	20	24.43	19.76	101.8	98.8
24	22	25.18	21.70	104.9	98.6
24	24	24.85	23.55	103.5	98.1
			Mean	100.3	98.3
			SD	1.42	0.88
			RSD	1.42	0.87

To appraise the accuracy and precision of the SYM5-CWT method, precision and accuracy survey were applied daily at three dissimilar concentrations and the prepared solutions were used for intra-day and inter-day studies. The results can be seen in Table 3.

Before the SYM5-CWT method was implemented to the commercial tablet preparation, a standard addition technique was used to test the interference effects of tablet excipients on LOS and HCT. The results can be seen in Table 4.

Table 4 Standard addition outcome by the SYM5-CWT method

	LOS			**HCT**		
			Added (µg mL^{-1})			
	2	6	10	2	8	12
No.			**Found (µg/mL)**			
1	1.99	6.06	9.92	2.07	8.02	11.59
2	2.03	6.42	9.97	2.19	8.03	11.62
3	1.97	6.07	9.95	2.13	8.00	12.04
4	2.02	5.95	10.02	2.07	8.04	11.92
5	2.04	5.87	10.06	2.08	8.03	11.74
			Recovery (%)			
No.	**LOS**			**HC**		
1	99.4	101.1	99.2	103.4	100.2	96.6
2	101.6	107.0	99.7	109.5	100.3	96.9
3	98.4	101.1	99.5	106.4	100.0	100.3
4	101.1	99.2	100.2	103.4	100.5	99.3
5	101.9	97.9	100.6	103.8	100.4	97.9
Mean	100.5	101.3	99.8	105.3	100.3	98.2
SD	1.51	3.48	0.53	2.68	0.19	1.62
RSD	1.50	3.44	0.53	2.55	0.19	1.65
RE	0.49	1.25	-0.16	5.28	0.29	-1.81

Recovery and other calculations for LOS and HCT were performed by subtracting the quantity of LOS and HCT from the tablets. These surveys were performed with five replicas at three dissimilar concentration grades.

3.3. Tablet Analysis

The outcomes gathered by applying the proposed technique to the LOS-HCT commercial preparation solutions are shown in Table 5. Accomplished results have been gathered for the quantification of tablets containing LOS and HCT. In the determination of tablets, no interference with the tablet excipients in the determination of the concerned compounds was monitored when the SYM5-CWT method was applied to commercially available tablets.

Table 5 Tablet assay by the SYM5-CWT method (50.0 mg LOS and 12.5 mg HCT per tablet)

Method	**SYM5-CWT**	
	LOS (mg)	**HCT (mg)**
Mean	49.70	12.45
SD	0.26	0.10
RSD	0.53	0.79
SE	0.08	0.03
CL	0.16	0.06

4. CONCLUSION

To summarize the study briefly, the SYM5-CWT method we have developed has been successfully applied to the spectral analysis of artificial mixtures and tablet formulations containing LOS and HCT. This method we have developed can be applied without requiring any pre-separation in cases where the spectra overlap each other in the same spectral region as in this study (see Figure 1). It was performed with analytical validation parameters to indicate the validity and applicability of the method. We think that this developed SYM5-CWT method is a promising approach for the quantification of the related compounds.

Funding

The author (s) has no received any financial support for the research, authorship or publication of this study.

The Declaration of Conflict of Interest/ Common Interest

No conflict of interest or common interest has been declared by the authors.

Authors' Contribution

The authors contributed equally to the study.

The Declaration of Ethics Committee Approval

This study does not require ethics committee permission or any special permission.

The Declaration of Research and Publication Ethics

The authors of the paper declare that they comply with the scientific, ethical and quotation rules of SAUJS in all processes of the paper and that they do not make any falsification on the data collected. In addition, they declare that Sakarya University Journal of Science and its editorial board have no responsibility for any ethical violations that may be encountered, and that this study has not been evaluated in any academic publication environment other than Sakarya University Journal of Science.

REFERENCES

[1] M. Siddiqui, Z. AlOthman, N. Rahman, "Analytical techniques in pharmaceutical analysis: A review," Arabian Journal of Chemistry, vol. 10, pp. 1409-1421, 2017.

[2] R. Valagaleti, P. Burns, M. Gill, "Analytical support for drug manufacturing in the United States—from active pharmaceutical ingredient synthesis to drug product shelf life," J. Drug. Inform., vol. 37, pp. 407-438, 2003.

[3] H. Ju, "Grand challenges in analytical chemistry: towards more bright eyes for scientific research, social events and human health," Front. Chem., 2013, https://doi.org/10.3389/fchem.2013.00005.

[4] Y. Chhonker, C. Edi, D. Murry, "LC–MS/MS method for simultaneous determination of diethylcarbamazine, albendazole and albendazole metabolites in human plasma: Application to a clinical pharmacokinetic study," J. Pharm. Biomed. Anal., vol. 20, no. 151, pp. 84–90, 2018.

[5] J. Sáiz, C. García-Ruiz, B. Gómara, "Comparison of different GC-MS configurations for the determination of prevalent drugs and related metabolites," Analytical Methods, vol. 9, pp. 2897-2908, 2017.

[6] H. Maurer, "Toxicological analysis of drugs: GC-MS screening and confirmation," Acta Medicinæ Legalis, vol. XLIV, pp. 489-492, 1994.

[7] F. Rocha, L. Teixeira, "Strategies to increase sensitivity in UV-VIS spectrophotometry," Quimica Nova, vol. 27, no. 5, pp. 807-812, 2004.

[8] T. Thiem, "Comparison of optical-emission mass-spectroscopy utilizing laser vaporization of solid samples for inorganic analysis," American Laboratory, vol. 26, no. 3, pp. 48-52, 1994.

[9] Z. Deyl, J. Janak, V. Schwarz V. "Bibliography section - Liquid column chromatography - Gas chromatography - Planar chromatography - Gel chromatography - Capillary electrophoresis and electrokinetic chromatography," Journal of Chromatography A, vol. 940, no. 2, pp. 119-219, 2001.

[10] A. Otieno, S. Mwongela S, "Capillary electrophoresis-based methods for the determination of lipids - A review," Analytica Chimica Acta, vol. 624, no. 2, pp. 163-174, 2008.

[11] A. Naggar, A. Kotb, A. Abdelwahab, "Graphite studded with facile-synthesized cu2o nanoparticle-based cubes as a novel electrochemical sensor for highly sensitive voltametric determination of mebeverine hydrochloride," Chemosensors, 2021, https://doi.org/10.3390/chemosensors9020035.

[12] I. Daubechies, "Ten Lectures on Wavelets, Society for Industrial and Applied Mathematics," Philadelphia, pp. 1-357, 1992.

[13] E. Dinç, D. Baleanu, "Continuous wavelet transform applied to the overlapping absorption signals and their ratio signals for the quantitative resolution of mixture of oxfendazole and oxyclozanide in bolus," J. Food. Drug. Anal., vol. 15, no. 2, pp. 109-117, 2007.

[14] Ö. Üstündağ, E. Dinç, "Continuous wavelet transforms and ultra performance liquid chromatography applied to the simultaneous quantitative determination of candesartan cilexetil and hydrochlorothiazide in tablets," Monatshefte für Chemie, 2021, https://doi.org/10.1007/s00706-021-02822-7.

[15] M. Toral, O. Saldias, C. Soto, “Strategies used to develop analytical methods for simultaneous determination of organic compounds by derivative spectrophotometry,” Quimica Nova, vol. 32, no. 1, pp. 257-282, 2009.

[16] D. Nagavalli, V. Vaidhyalingam, O. Divya, “Simultaneous spectrophotometric determination of losartan potassium, amlodipine besilate and hydrochlorothiazide in pharmaceuticals by chemometric methods,” Acta Pharmaceutica, vol. 60, no. 2, pp. 141-152, 2010.

[17] C. Vetuschi, A. Giannandrea, “Anti-beer evaluation of Hydrochlorothiazide and Losartan by UV derivative spectrophotometry,” Analytical Letters, vol. 36, no. 5, pp. 1051-1064, 2003.

[18] T. Binh, L. Tram, N. Trang, “Simultaneous Determination of Hydrochlorothiazide and Losartan Potassium in Pharmaceutical Product by UV-Vis Spectrophotometric Method with Kalman Filter Algorithm,” Journal of Analytical Methods in Chemistry, 2021, https://doi.org/10.1155/2021/2754133.

[19] A. Youssef, “Spectrofluorimetric Assessment of Hydrochlorothiazide Using Optical Sensor Nano-Composite Terbium Ion Doped in Sol-Gel Matrix,” Journal of Fluorescence, vol. 22, no. 3, pp. 827-834, 2012.

[20] K. Marghany, R. Abdelsalam, G. Haddad, “HPLC method transfer study for simultaneous determination of seven angiotensin II receptor blockers,” Journal of Separation Science, vol. 43, no. 8, pp. 1398-1405, 2020.

[21] S. Rahaman, K. Micheal, “A new RP-HPLC method for the simultaneous estimation of hydrochlorothiazide and losartan potassium in bulk and pharmaceutical dosage forms,” International Journal of Life Science and Pharma Research, vol. 10, pp. 648-653, 2020.

[22] N. Mohammed, H. Abdo, H. Hassan, “Method development and validation of simultaneous determination of hydrochlorothiazide and losartan in tablet dosage form by RP-HPLC,” International Journal of Pharmaceutical Sciences and Research, vol. 10, no. 1, pp. 227-231, 2019.

[23] C. Vishnuvardhan, P. Radhakrishnanand, N. Satheeshkumar, “RP-HPLC Method for the Simultaneous Estimation of Eight Cardiovascular Drugs,” Chromatographia, vol. 77, no. 3-4, pp. 265-275, 2014.

[24] R. Maggio, P. Castellano, T. Kaufman, “A multivariate approach for the simultaneous determination of losartan potassium and hydrochlorothiazide in a combined pharmaceutical tablet formulation,” Analytical and Bioanalytical Chemistry, vol. 391, no. 8, pp. 2949-2955, 2008.

SAKARYA ÜNİVERSİTESİ
FEN BİLİMLERİ ENSTİTÜSÜ
DERGİSİ

Sakarya University Journal of Science
SAUJS

e-ISSN 2147-835X Founded 1997 Period Bimonthly Publisher Sakarya University
http://www.saujs.sakarya.edu.tr/en/

Title: Application of an Epidemic Model to Turkey Data and Stability Analysis for the Covid-19 Pandemic

Authors: Nejdet KÖKER, Ömer Faruk GÖZÜKIZIL

Recieved: 2021-08-17 00:00:00

Accepted: 2021-11-19 00:00:00

Article Type: Research Article

Volume: 25
Issue: 6
Month: December
Year: 2021
Pages: 1438-1445

How to cite
Nejdet KÖKER, Ömer Faruk GÖZÜKIZIL; (2021), Application of an Epidemic Model to Turkey Data and Stability Analysis for the Covid-19 Pandemic. Sakarya University Journal of Science, 25(6), 1438-1445, DOI: https://doi.org/10.16984/saufenbilder.980797
Access link
http://www.saujs.sakarya.edu.tr/tr/pub/issue/66341/980797

Sakarya University Journal of Science 25(6), 1438-1445, 2021

Application of an Epidemic Model to Turkey Data and Stability Analysis for the Covid-19 Pandemic

Nejdet KÖKER*[1], Ömer Faruk GÖZÜKIZIL[1]

Abstract

An epidemic disease caused by a new coronavirus has spread all over the world with a high rate of transmission. The main purpose of this article is to define an epidemic model for the Covid-19 pandemic, to apply it to Turkey's data and to interpret it. Accordingly, a SEIR model was created to calculate the infected population and the number of deaths caused by this epidemic, and the stability of the model was examined. Since all the parameters affecting the stability cannot be calculated clearly, it cannot be expected to reach a realistic result. For this reason, a model was created with accessible parameters. Later, the diseased and non diseased equilibrium points of the model were discussed. The Hurwitz theorem is used to find the local stability of the model, while the Lyaponov function theory is used to investigate its global stability. Finally, some numerical results are given with the help of MATLAB program.

Keywords: SEIR Model, Covid-19 Pandemic, Stability.

1. INTRODUCTION

Ordinary Differential Equations are the types of equations that appear and are widely used in applications in many Applied Sciences as well as the Department of Mathematics. The concept of stability, which constitutes a wide research area in differential equations, was put forward by the Soviet mathematician A. M. Lyapunov in the early 1900s [1]. Stability has applications in many applied sciences such as physics, engineering, medicine. Mathematical biology is a broad branch with many applications. Viruses are the most abundant species in nature, some viruses cause serious infectious diseases in humans. One of these types is coronavirus. The epidemic caused by a new coronavirus (COVID-19) has spread rapidly all over the world. A study was conducted by José M. Carcione et al. to determine the course of the epidemic in Italy in 2020 [2]. Although there are many studies on the subject around the world, there are not many studies specific to Turkey. In this direction, it is aimed to create and interpret an epidemic model by using Turkey Covid-19 data within the scope of this article.

2. MATHEMATICAL MODEL

2.1. Model Formation

We divided the population into five classes. X(t), E(t), I(t), N(t), R(t) as susceptible vulnerable population class, exposed class, infected (infectious) class, intubated (severely ill) class, recovered class, Model created at time (t).

---

* Corresponding author: necokoker@gmail.com

[1] Sakarya University, Faculty of Arts and Sciences, Department of Mathematics

E-mail: farukg@sakarya.edu.tr

ORCID: https://orcid.org/0000-0003-0585-0314, https://orcid.org/0000-0002-5975-6430

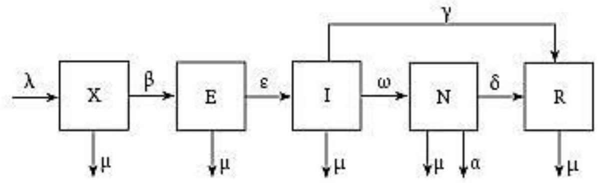

Figure 1 Schematic Diagram of the Model

The differential equations that make up the model are as follows and all of the parameters used are positive real numbers and are explained in Table 1.

$$\begin{cases} \frac{dX}{dt} = \lambda - \mu X - \beta XE \\ \frac{dE}{dt} = \beta XE - \varepsilon EI - \mu E \\ \frac{dI}{dt} = \varepsilon EI - (\mu + \omega + \gamma)I \\ \frac{dN}{dt} = \omega I - (\mu + \alpha + \delta)N \\ \frac{dR}{dt} = \gamma I + \delta N - \mu R \end{cases} \qquad (1)$$

Table 1 Parameters and description.

symbols	Definition
λ	Birth rate per capita.
μ	Natural death rate per capita.
α	Average death rate from the virus.
β	The rate at which the susceptible population moves to the exposed class.
ε	Rate of progression from exposure to infection.
ω	The rate at which the infected become intubated (severely ill).
γ	The rate of recovery of those infected.
δ	Recovery rate of intubated patients.

Since the first four equations of system (1) are independent, we skip R(t) without losing generality, and then system (1) is reduced to the following system of differential equations.

$$\begin{cases} \frac{dX}{dt} = \lambda - \mu X - \beta XE \\ \frac{dE}{dt} = \beta XE - \varepsilon EI - \mu E \\ \frac{dI}{dt} = \varepsilon EI - (\mu + \omega + \gamma)I \\ \frac{dN}{dt} = \omega I - (\mu + \alpha + \delta)N \end{cases} \qquad (2)$$

2.2. Equilibrium Points of the Differential Equation System

2.2.1. Disease Free Balance Point

For the absence of a diseased individual; if $E = I = N = 0$ is taken and the expressions on the right side of the system are equal to zero, $\lambda - \mu X = 0 \rightarrow X = \frac{\lambda}{\mu}$ is obtained, and the equilibrium point $E_0 = \left(\frac{\lambda}{\mu}, 0,0,0\right)$ is obtained.

The Jacobian matrix of system (2);

$$J = \begin{bmatrix} -\mu - \beta E & -\beta X & 0 & 0 \\ \beta E & \beta X - \varepsilon I - \mu & -\varepsilon E & 0 \\ 0 & \varepsilon I & \varepsilon E - (\mu + \omega + \gamma) & 0 \\ 0 & 0 & \omega & -(\mu + \alpha + \delta) \end{bmatrix}$$

is found.

When the Jacobian matrix E_0 is at equilibrium point

$$J(E_0) = \begin{bmatrix} -\mu & -\frac{\beta\lambda}{\mu} & 0 & 0 \\ 0 & \frac{\beta\lambda}{\mu} - \mu & 0 & 0 \\ 0 & 0 & -(\mu + \omega + \gamma) & 0 \\ 0 & 0 & \omega & -(\mu + \alpha + \delta) \end{bmatrix}$$

The following matrices are written for the reproduction number.

$$F = \begin{pmatrix} \frac{\beta\lambda}{\mu} & 0 & 0 \\ 0 & 0 & 0 \\ 0 & 0 & 0 \end{pmatrix}, \qquad V = \begin{pmatrix} \mu & 0 & 0 \\ 0 & \mu + \omega + \gamma & 0 \\ 0 & -\omega & \mu + \alpha + \delta \end{pmatrix}$$

Here $\frac{\beta\lambda}{\mu^2}$ is the dominant eigenvalue of the matrix FV^{-1}. That is, required reproduction number

$$R_0 = \frac{\beta\lambda}{\mu^2} \tag{3}$$

is obtained in the form [3-4].

2.2.2. Diseased Equilibrium Point

Theorem 2.1. If $R_0 > 1$, infectious disease has a positive equilibrium point.

Proof: Let's find the positive equilibrium point E_0^*, (2) by equating the left side of the system of differential equations to zero, the following statements are obtained.

(2) from the first equation of the system of differential equations,

$$\lambda - \mu X^* - \beta X^* E^* = 0$$
$$X^*(\mu + \beta E^*) = \lambda$$
$$X^* = \frac{\lambda}{\mu + \beta E^*}$$

(2) from the second equation of the system of differential equations,

$$\beta X^* E^* - \varepsilon E^* I^* - \mu E^* = 0$$
$$E^*(\beta X^* - \varepsilon I^* - \mu) = 0$$
$$\beta X^* - \varepsilon I^* - \mu = 0$$
$$I^* = \frac{\beta X^* - \mu}{\varepsilon}$$

(2) from the third equation of the system of differential equations,

$$\varepsilon E^* I^* - (\mu + \omega + \gamma) I^* = 0$$
$$I^*[\varepsilon E^* - (\mu + \omega + \gamma)] = 0$$
$$\varepsilon E^* - (\mu + \omega + \gamma) = 0$$
$$E^* = \frac{\mu + \omega + \gamma}{\varepsilon}$$

(2) from the fourth equation of the system of differential equations

$$\omega I^* - (\mu + \alpha + \delta) N^* = 0$$
$$N^* = \frac{\omega I^*}{\mu + \alpha + \delta}$$

is found. From here,

$$I^* = \frac{\beta X^* - \mu}{\varepsilon} = \frac{\beta \frac{\lambda}{\mu + \beta E^*} - \mu}{\varepsilon} =$$
$$\frac{\beta \frac{\lambda}{\mu + \beta \frac{\mu + \omega + \gamma}{\varepsilon}} - \mu}{\varepsilon} =$$
$$\frac{\frac{\beta\lambda\varepsilon}{\mu\varepsilon + \beta(\mu + \omega + \gamma)} - \mu}{\varepsilon} =$$
$$\frac{\beta\lambda\varepsilon - \mu^2\varepsilon - \beta\mu(\mu + \omega + \gamma)}{\varepsilon^2\mu + \varepsilon\beta(\mu + \omega + \gamma)} =$$
$$\frac{\mu^2\varepsilon\left(\frac{\beta\lambda}{\mu^2} - 1\right) - \beta\mu(\mu + \omega + \gamma)}{\varepsilon^2\mu + \varepsilon\beta(\mu + \omega + \gamma)} =$$
$$\frac{\mu^2\varepsilon(R_0 - 1) - \beta\mu(\mu + \omega + \gamma)}{\varepsilon^2\mu + \varepsilon\beta(\mu + \omega + \gamma)} =$$

It is obtained from (3).

For $\mu^2\varepsilon(R_0 - 1) > \beta\mu(\mu + \omega + \gamma)$, $R_0 > 1$ must be present. Thus, the value of I^* becomes positive.

That is, if $R_0 > 1$, the required positive balance point

$$E_0^* = (X^*, E^*, I^*, N^*) = \left(\frac{\varepsilon I^* + \mu}{\beta}, \frac{\mu + \omega + \gamma}{\varepsilon}, \frac{\mu^2\varepsilon(R_0 - 1) - \beta\mu(\mu + \omega + \gamma)}{\varepsilon^2\mu + \varepsilon\beta(\mu + \omega + \gamma)}, \frac{\omega I^*}{\mu + \alpha + \delta}\right) \text{ [4].}$$

2.3. Stability of the Model

2.3.1. Local Stability

Theorem 2.2. If $R_0 < 1$, at equilibrium point E_0, the system of differential equations (2) is locally stable. If $R_0 > 1$, the system of (2) differential equations is unstable.

Proof: Let's write the jacobian matrix of the system of differential equations when E_0 is at equilibrium point (2)

$$J(E_0) = \begin{bmatrix} -\mu & -\frac{\beta\lambda}{\mu} & 0 & 0 \\ 0 & \frac{\beta\lambda}{\mu} - \mu & 0 & 0 \\ 0 & 0 & -(\mu + \omega + \gamma) & 0 \\ 0 & 0 & \omega & -(\mu + \alpha + \delta) \end{bmatrix}$$

The eigenvalues of the matrix are as follows.

$$\lambda_1 = -\mu < 0$$

$$\lambda_2 = \frac{\beta\lambda}{\mu} - \mu = \mu^2(R_0 - 1)$$

$$\lambda_3 = -(\mu + \omega + \gamma) < 0$$

$$\lambda_4 = -(\mu + \alpha + \delta) < 0$$

If all eigenvalues are negative, the system of differential equations is stable. For $\lambda_2 < 0$ to be $R_0 < 1$. If $R_0 = 1$ or $R_0 > 1$, then $\lambda_2 < 0$ cannot be so (2) the system of differential equations becomes unstable. It is necessary proof.

Theorem 2.3. If $R_0 > \frac{\varepsilon\lambda}{\mu(\mu+\omega+\gamma)}$, at equilibrium point E_0^*, the system of differential equations (2) is locally stable. Otherwise, at equilibrium point E_0^*, the system of differential equations (2) is unstable.

Proof: When E_0^* is at the equilibrium point, let (2) Write the jacobian matrix of the system of differential equations.

$$J(E_0^*) = \begin{bmatrix} \mu - \beta E^* & -\beta X^* & 0 & 0 \\ \beta E^* & \beta X^* - \varepsilon I^* - \mu & -\varepsilon E^* & 0 \\ 0 & \varepsilon I^* & \varepsilon E^* - (\mu + \omega + \gamma) & 0 \\ 0 & 0 & \omega & -(\mu + \alpha + \delta) \end{bmatrix}$$

$$J(E_0^*) = \begin{bmatrix} \mu - \beta E^* & -\beta X^* & 0 & 0 \\ \beta E^* & 0 & -\varepsilon E^* & 0 \\ 0 & \varepsilon I^* & 0 & 0 \\ 0 & 0 & \omega & -(\mu + \alpha + \delta) \end{bmatrix} \begin{matrix} \underline{R_2 \rightarrow R_2 + R_1} \\ \underline{R_3 \rightarrow R_2 + R_3} \end{matrix}$$

$$J(E_0^*) = \begin{bmatrix} \mu - \beta E^* & -\beta X^* & 0 & 0 \\ -\mu & -\beta X^* & -\varepsilon E^* & 0 \\ \beta X^* & \varepsilon I^* & -\varepsilon E^* & 0 \\ 0 & 0 & \omega & -(\mu + \alpha + \delta) \end{bmatrix} \underline{R_2 \rightarrow R_2 + \frac{\mu R_3}{\beta E^*}}$$

$$J(E_0^*) = \begin{bmatrix} \mu - \beta E^* & -\beta X^* & 0 & 0 \\ 0 & -\beta X^* + \frac{\mu\varepsilon I^*}{\beta E^*} & -\varepsilon E^* - \frac{\mu\varepsilon}{\beta} & 0 \\ \beta X^* & \varepsilon I^* & -\varepsilon E^* & 0 \\ 0 & 0 & \omega & -(\mu + \alpha + \delta) \end{bmatrix}$$

To be simpler, we can write this matrix as follows.

$$J(E_0^*) = \begin{bmatrix} A & B \\ C & D \end{bmatrix}$$

Here, $A = \begin{bmatrix} \mu - \beta E^* & -\beta X^* \\ 0 & -\beta X^* + \frac{\mu\varepsilon I^*}{\beta E^*} \end{bmatrix}$,

$B = \begin{bmatrix} 0 & 0 \\ -\varepsilon E^* - \frac{\mu\varepsilon}{\beta} & 0 \end{bmatrix}$,

$C = \begin{bmatrix} \beta X^* & \varepsilon I^* \\ 0 & 0 \end{bmatrix}$,

$D = \begin{bmatrix} -\varepsilon E^* & 0 \\ \omega & -(\mu + \alpha + \delta) \end{bmatrix}$ [6].

The eigenvalues of the $J(E_0^*)$ matrices vary depending on the eigenvalues of the A and D matrices. The eigenvalues of the matrix A are obtained as follows.

$$\lambda_1 = -\mu - \beta E^* < 0$$

$$\lambda_2 = -\beta X^* + \frac{\mu\varepsilon I^*}{\beta E^*} =$$

$$-\beta\frac{\varepsilon I^* + \mu}{\beta} + \frac{\mu\varepsilon I^*}{\beta E^*} =$$

$$-\varepsilon I^* - \mu + \frac{\mu\varepsilon I^*}{\beta E^*} =$$

$$-\mu + \frac{\mu\varepsilon I^*}{\beta E^*\lambda}\left(\lambda - \frac{\beta E^*\lambda}{\mu}\right) =$$

$$-\mu + \frac{\mu\varepsilon I^*}{\beta E^*\lambda}\left(\lambda - \frac{\beta\frac{(\mu + \omega + \gamma)}{\varepsilon}\lambda}{\mu}\right) =$$

$$-\mu + \frac{\mu\varepsilon I^*}{\beta E^*\lambda}\left(\lambda - \frac{\mu(\mu + \omega + \gamma)}{\varepsilon}\frac{\beta\lambda}{\mu^2}\right) =$$

$$-\mu + \frac{\mu\varepsilon I^*}{\beta E^*\lambda}\left(\lambda - \frac{\mu(\mu + \omega + \gamma)}{\varepsilon}R_0\right)$$

If $R_0 > \frac{\varepsilon\lambda}{\mu(\mu+\omega+\gamma)}$ then $\lambda_2 < 0$.

The eigenvalues of the matrix D are obtained as follows.

$$\lambda_3 = -\varepsilon E^* < 0$$

$$\lambda_4 = -(\mu + \alpha + \delta) < 0$$

Thus, the proof is completed.

2.3.2. Global Stability

Theorem 2.4. If $R_0 < 1$ then (2) the system of differential equations is spherically stable.

Proof: To prove this theorem, let's first construct the Lyapunov function as L,

$$L = ln\frac{X}{X_0} + ln\frac{E}{E_0} + I + N \qquad (4)$$

(4) if the derivative of the equation is taken according to time; according to the Lyapunov stability criterion ,

$$L' = \frac{X'}{X} + \frac{E'}{E} + I' + N'$$

$$L' = \frac{\lambda}{X} - \mu - \beta E + \beta X - \varepsilon I - \mu + \varepsilon EI - (\mu + \omega + \gamma)I + \omega I - (\mu + \alpha + \delta)N$$

$$L' = \frac{\lambda}{X} - 2\mu - \beta E + \beta X + \varepsilon EI - (\mu + \varepsilon + \gamma)I - (\mu + \alpha + \delta)N$$

, are obtained. Typing instead of E_0 in the above equation,

$$L' = \mu - 2\mu + \beta\frac{\lambda}{\mu} = \beta\frac{\lambda}{\mu} - \mu = \mu\left(\frac{\beta\lambda}{\mu^2} - 1\right) = \mu(R_0 - 1)$$

can be found.

For $L' < 0$ it must be $R_0 < 1$. In this case (2) the system of differential equations is globally stable.

3. RESEARCH FINDINGS

3.1. Application Of Model To Turkey Data

In this part of our study, Turkey data dated 25.10.2020 and 03.07.2021 corresponding to the parameter values of the model created in Section 2 are given in Table 2 the classification of the population of Turkey is also given in table 3 [5,6,7,8].

Table 2 Parameters and Turkey data.

symbols	Definition	Turkey Data (25.10.2020)	Turkey Data (03.07.2021)
λ	Birth rate per capita..	0.015	0.013
μ	Natural death rate per capita.	0.053	0.053
α	Average death rate from the virus.	0.084	0.062
β	The rate at which the susceptible population moves to the exposed class.	0.192	0.078
ε	Rate of progression from exposure to infection.	0.166	0.023
ω	The rate at which the infected become intubated (severely ill).	0.033	0.010
γ	The rate of recovery of those infected.	0.843	0.887
δ	Recovery rate of intubated patients.	0.687	0.785

Table 3 Classification Of Turkish Population

class	Definition	Turkey Data (25.10.2020)	Turkey Data (03.07.2021)
X(t)	susceptible population	57.999.210 (0.987)	52.875.643 (0.829)
E(t)	exposed class	361.801 (0.006)	5.440.368 (0.085)
I(t)	infected (infectious) class	47.411 (0.001)	129.599 (0.002)

N(t)	intubated (severely ill) class	15.751 (0.0003)	75.293 (0.001)
R(t)	recovered class	314.390 (0.0057)	5.310.769 (0.083)

3.1.1. Disease-Free Equilibrium Point According To Turkey Covid-19 Data

Equilibrium point according to the data in Table 2 $E_0 = \left(\frac{\lambda}{\mu}, 0, 0, 0\right) = \left(\frac{0.013}{0.053}, 0, 0, 0\right) = (0.245, 0, 0, 0)$. Accordingly, the jacobian matrix of the system, at the equilibrium point, if the data dated 25.10.2020 is written

$$J(E_0) = \begin{bmatrix} -0.053 & -0.054 & 0 & 0 \\ 0 & 0.001 & 0 & 0 \\ 0 & 0 & -0.927 & 0 \\ 0 & 0 & 0.033 & -0.824 \end{bmatrix}$$

can be found.

From here, the reproduction number is found $R_0 = \frac{\beta\lambda}{\mu^2} = \frac{0.015\,.0.192}{(0.053)^2} \cong 1.025$ according to (3).

If data dated 03.07.2021 is written

$$J(E_0) = \begin{bmatrix} -0.053 & -0.019 & 0 & 0 \\ 0 & -0.034 & 0 & 0 \\ 0 & 0 & -0.94 & 0 \\ 0 & 0 & 0.01 & -0.89 \end{bmatrix}$$

can be found.

From here, the reproduction number is found $R_0 = \frac{\beta\lambda}{\mu^2} = \frac{0.078\,.0.013}{(0.053)^2} \cong 0.361$ according to (3).

3.1.2. Diseased Equilibrium Point According To Turkey Covid-19 Data

Since $R_0 \cong 1.025$, which we found according to data dated 25.10.2020 for Turkey, the system of differential equations has a positive equilibrium point.

This point

$$E_0^* = \left(\frac{\varepsilon I^* + \mu}{\beta}, \frac{\mu+\omega+\gamma}{\varepsilon}, \frac{\mu^2\varepsilon(R_0-1) - \beta\mu(\mu+\omega+\gamma)}{\varepsilon^2\mu + \varepsilon\beta(\mu+\omega+\gamma)}, \frac{\omega I^*}{\mu+\alpha+\delta}\right)$$

$E_0^* \cong (0.277\,, 5.596\,, -0.125\,, 0.000037)$ can be found.

According to the data dated 03.07.2021 for Turkey, since$R_0 \cong 0.361 < 1$, The System (2) does not have a positive equilibrium point.

3.2. Stability Of The Model

3.2.1. Local stability

According to the data dated 03.07.2021 for Turkey, at the equilibrium point $E_0 = (0.245, 0, 0, 0)$, the jacobian matrix of the (2) system $J(E_0) = \begin{bmatrix} -0.053 & -0.019 & 0 & 0 \\ 0 & -0.034 & 0 & 0 \\ 0 & 0 & -0.94 & 0 \\ 0 & 0 & 0.01 & -0.89 \end{bmatrix}$ found.

Eigenvalues of this matrix;

$\lambda_1 = -0.053 < 0$

$\lambda_1 = -0.034 < 0$

$\lambda_1 = -0.940 < 0$

$\lambda_1 = -0.890 < 0$

it is calculated in the form of. Since $R_0 \cong 0.361 < 1$ is what we find, the (2) system is locally stable according to Theorem 2.2.

For the values $R_0 \cong 1.025$ and $\frac{\varepsilon\lambda}{\mu(\mu+\omega+\gamma)} = \frac{0.166\,.0.015}{0.053\,.0.929} \cong 0.051$ that we find at the equilibrium point $E_0^* \cong (0.277\,, 5.596\,, -0.125\,, 0.000037)$ according to the data dated 25.10.2020 for Turkey, the system (2) is locally stable, since $R_0 > \frac{\varepsilon\lambda}{\mu(\mu+\omega+\gamma)}$ according to Theorem 2.3.

3.2.2. Global Stability

By Lyapunov function,

$$L' = \frac{X'}{X} + \frac{E'}{E} + I' + N'$$

$$L' = \frac{\lambda}{x} - \mu - \beta E + \beta X - \varepsilon I - \mu + \varepsilon EI - (\mu + \omega + \gamma)I + \omega I - (\mu + \alpha + \delta)N$$

$$L' = \frac{\lambda}{x} - 2\mu - \beta E + \beta X + \varepsilon EI - (\mu + \varepsilon + \gamma)I - (\mu + \alpha + \delta)N$$

By writing instead of $E_0 = (0.245, 0, 0, 0)$ in the equation, $L' = \beta\frac{\lambda}{\mu} - \mu = \beta . 0.245 - \mu$ is found, where $L' = \beta\frac{\lambda}{\mu} - \mu = \beta . 0.245 - \mu$ is obtained if the values β and μ are written. According to the Lyapunov stability criterion, the (2) system of differential equations is globally stable.

Also, since $R_0 \cong 0.361 < 1$ according to Theorem 2.4, the system (2) is globally stable.

4. CONTROVERSY AND CONCLUSION

One of the major concerns with any infectious disease is its ability to invade the population. Many epidemiological models have a disease-free balance, in which the population remains disease-free. These models usually have a threshold parameter, R_0, known as the basic breeding number, is defined as this threshold parameter. The R_0 reproduction number of a mathematical model submits us very important information about the increase and decrease of the epidemic. R_0 consists of the parameters of the model. In our model, $R_0 = \frac{\beta\lambda}{\mu^2}$ is found. If $R_0 < 1$, the epidemic is close to ending over time. If $R_0 = 1$, the epidemic never disappears, it is in balance. If $R_0 > 1$, contagion increases as time passes. R_0 also provides us with information about the stability of the model. If $R_0 < 1$, then the system of differential equations is stable. If $R_0 = 1$ or $R_0 > 1$, the system is unstable. The number of R_0 reproductions to be calculated for the Covid–19 global pandemic can guide us in the measures to be taken. The R_0 value can be analyzed for decisions on increasing or reducing constraints.

4.1. Appendices

Acknowledgments

We would like to thank our journal editors, referees and journal secretary who contributed to the publication of our article.

Funding

The authors have no received any financial support for the research, authorship or publication of this study.

The Declaration of Conflict of Interest/ Common Interest

No conflict of interest or common interest has been declared by the authors.

Authors' Contribution

The authors contributed equally to the study.

The Declaration of Ethics Committee Approval

This study does not require ethics committee permission or any special permission.

The Declaration of Research and Publication Ethics

The authors of the paper declare that they comply with the scientific, ethical and quotation rules of SAUJS in all processes of the paper and that they do not make any falsification on the data collected. In addition, they declare that Sakarya University Journal of Science and its editorial board have no responsibility for any ethical violations that may be encountered, and that this study has not been evaluated in any academic publication environment other than Sakarya University Journal of Science.

REFERENCES

[1] Lyapunov, A.M., “The General Problem of the Stability of Motion,” University of Kharkov, PhD thesis, 1892.

[2] Carcione José M. and others, “A Simulation of a COVID-19 Epidemic Based on a Deterministic SEIR Model,” Frontiers in Public Health, vol. 8, pp. 2296-2565, 2020.

[3] Edwards C.M. and Penney D.E., “Differential Equations and Boundary Value Problems (Translation Prof. Dr. Ömer Akın),” Palme Publishing, Ankara, pp. 366-434, 2005.

[4] Boyce W. E. and DiPrima R. C., “Elementary Differential Equations and Boundary Value Problems (Translation Uğuz M. and Ürtiş Ç.),” Palme Publishing, Ankara, pp. 495-527, 2016.

[5] Haran M., “An introduction to models for disease Dynamics,” SAMSI, pp. 5-25, 2009.

[6] Van den Driessche P., Watmough J., “Reproduction numbers and sub-threshold endemic equilibria for compartmental models of disease transmission,” vol. 1-2, pp. 29-48, 2002.

[7] Alzahrani E., Zeb A., “Stability analysis and prevention strategies of tobacco smoking model,” Bound Value Problems, pp. 3, 2020.

[8] https://corona.cbddo.gov.tr/Home/DeathConfirmedRatio, Access Date: 04.07.2021.

[9] https://data.tuik.gov.tr/Bulten/Index?p=Dogum-Istatistikleri-2020-33706, Access Date: 04.07.2021.

[10] https://www.nufusu.com/turkiye-nufusu-yas-gruplari, Access Date: 04.07.2021.

[11] https://data.tuik.gov.tr/Bulten/Index?p=Olum-ve-Olum-Nedeni-Istatistikleri-2019-33710, Access Date: 04.07.2021.